University of Naples Federico II

Ph.D program in
Ingegneria Strutturale, Geotecnica e Rischio Sismico

THESIS FOR THE DEGREE OF DOCTOR OF PHILOSOPHY

Pseudo-dynamic tests for seismic performance assessment: infrastructure development, verification and test reliability

by
Carmine Molitierno

Advisor: Prof. Andrea Prota

Co-advisor: Prof. Ciro Del Vecchio

2024

SCUOLA POLITECNICA E DELLE SCIENZE DI BASE
DIPARTIMENTO D STRUTTURE PER L'INGEGNERIA E L'ARCHITETTURA

A journey of thousand miles
Begin with a single step
(Lao Tzu)

Pseudo-dynamic tests for seismic performance assessment: infrastructure development, verification and test reliability

Ph.D. Thesis presented

for the fulfillment of the Degree of Doctor of Philosophy

in Ingegneria Strutturale, Geotecnica e Rischio Sismico

by

Carmine Molitierno

2024

Approved as to style and content by

____

Prof. Andrea Prota, Advisor

____

Prof. Ciro Del Vecchio, Co-advisor

Università of Naples Federico II
Ph.D. Program in Ingegneria Strutturale, Geotecnica e Rischio Sismico
XXXVI cycle - Chairman: Prof. Iunio Iervolino

www.dist.unina.it/dottorati-di-ricerca/dottorati

Candidate's declaration

I hereby declare that this thesis submitted to obtain the academic degree of Philosophiæ Doctor (Ph.D.) in Ingegneria Strutturale, Geotecnica e Rischio Sismico is my own unaided work, that have not used other than the sources indicated, and that all direct and indirect sources are acknowledged as references.

Parts of this dissertation have been published in international journals and/or conference proceedings (see list of the author's publications at the end of the thesis).

Napoli, March 05, 2024

Carmine Molitierno

Carmine Molitierno

Abstract

The existing infilled reinforced concrete (RC) buildings belonging to the Mediterranean area are vulnerable to moderate-to-severe earthquakes. This is demonstrated by the damage on structural and non-structural components observed in the aftermath of recent seismic events. In this context, the experimental investigations of seismic performances are crucial to enhance the knowledge on the mechanical response and to develop/validate innovative strengthening solutions. In addition, the test results provide a reliable data for the calibration of numerical building models aimed at predicting earthquake damage. The mechanical response is often characterized by a brittle response of the infills or the structural system, thus experimental tests on full-scale prototype are needed to correctly reproduce damage propagation and the hysteretic response. However, only a few tests on full-scale infilled RC multi-storey structures are carried out because of the limitation in the testing facilities. Recently, a pseudo dynamic (PsD) testing framework has been implemented at the Laboratory of testing on real-scale STRUcTures (LaSTRUT) within the center CeSMA of the University of Naples Federico II to enable researchers to conduct experiments on full-scale building prototypes or subassemblies. This thesis presents the testing infrastructure and the control system properly developed to conduct PsD tests. A four-storey infilled RC building damaged by the 2009 L'Aquila earthquake is selected as case study. A reference perimetral frame, the most damaged, is selected and faithfully reproduced in the laboratory environment to conduct the tests considering three different infill-to-frame connections. The substructuring approach and the testing set-up are presented and discussed. Nonlinear models of the building and the frame are proposed and experimentally calibrated. They were used to confirm the results of experimental tests and to extent the results at building level. Finally, the research activities conducted at the European Laboratory of Structural Assessment (ELSA) at the Joint Research Centre (JRC) of the European Commission on the effects of errors on the reliability of the tests are presented and a proposal to improve the UNINA PsD testing framework is made.

Keywords: infilled RC frames, seismic assessment, nonlinear time history, substructuring, pseudo-dynamic testing, test reliability.

Sommario

Gli edifici tamponati in cemento armato (C.A) esistenti appartenenti all'area Mediterranea sono vulnerabili ai terremoti di medio-alta intensità. Questo è il dato che emerge dall'analisi dei danni osservati sugli su elementi strutturali e non a seguito dei recenti eventi sismici. In questo contesto, l'analisi delle prestazioni sismiche attraverso prove di laboratorio è cruciale per migliorare la conoscenza della risposta meccanica e per sviluppare/validare delle soluzioni innovative di rinforzo. Inoltre, i risultati delle prove forniscono dei dati affidabili per la calibrazione dei modelli numerici utilizzati allo scopo di predire il danneggiamento delle strutture. La risposta meccanica è spesso caratterizzata da una risposta fragile delle tamponature o del sistema strutturale. Tali meccanismi possono essere condizionati dall'effetto scala, quindi si rendono necessarie prove sperimentali realizzate su provini in scala reale per riprodurre correttamente la propagazione del danno e la risposta isteretica. Tuttavia, in letteratura sono presenti poche prove su strutture tamponate in C.A. in scala reale a più piani a causa delle limitazioni delle strutture di prova. Recentemente, una struttura di prova pseudo-dinamica (PsD) è stata implementata nel laboratorio di prove su strutture in scala reale (LaSTRUT) del centro CeSMA dell'Università di Napoli Federico II per consentire ai ricercatori di condurre esperimenti su prototipi di edifici in scala reale o sottostrutture. Questa tesi presenta la struttura di prova e il sistema di controllo sviluppati per condurre le prove PsD. Un edificio tamponato in cemento armato di quattro piani danneggiato dal terremoto de L'Aquila 2009 è stato selezionato come caso studio. Un telaio perimetrale di riferimento, il più danneggiato, è stato selezionato e riprodotto fedelmente in laboratorio per condurre le prove considerando tre differenti connessioni telaio-tamponatura. L'approccio di sottostrutturazione ed il set-up di prova sono presentati e discussi. Sono stati proposti e calibrati sperimentalmente dei modelli non lineari dell'edificio e del telaio sono. Questi sono stati poi usati per verificare i risultati sperimentali e per estendere tali risultati a livello di edificio. Infine, sono presentate delle attività di ricerca condotte presso l'European Laboratory of Structural Assessment (ELSA) del Joint Research Centre (JRC) per migliorare la conoscenza sugli effetti degli errori di controllo sull'affidabilità delle prove poi implementate nel sistema di prove PsD proposto.

Parole chiave: strutture esistenti, analisi sismica, analisi non lineari time history, sottostrutturazione, prove pseudo-dinamiche, affidabilità prove.

Acknowledgements

This study was performed within the framework of the PE 2022–2023 joint program DPC-ReLUIS, WP5: “Fast and Integrated Retrofit Interventions”.

The collaboration of the ELSA laboratory staff and resources are acknowledged specially regarding the contents of chapter 6 of this dissertation.

Contents

List of Figures

List of Tables

Chapter 1

1. Introduction

Experience is the hardest kind of teacher: it gives you the test first and the lesson afterward.

Oscar Wilde

In the last decade, devastating seismic events in the Mediterranean area remarked the high vulnerability of existing infilled reinforced concrete (RC) buildings. Many buildings exhibited damage to structural and non-structural components when subjected to moderate-to-severe earthquakes [1, 2, 3]. Post-earthquake field surveys showed that most of the damage was concentrated on infill panels [1, 4]. Diagonal cracking, crushing of corner bricks, and overturning of some panels were observed during the inspections. Furthermore, experimental and analytical studies demonstrated that stiff infills, as those made with hollow clay bricks, may significantly change the response of the structural system [5, 6, 7, 8]. High shear forces are carried by the infills before the significant cracking and strength degradation. This load is transferred to the surrounding frames and may lead to the shear cracking at the top of the columns and in the beam-column joints [6, 8, 5]. In this context, the assessment of seismic performance of existing infilled RC buildings is fundamental to characterize the damage on structural and non-structural components and to investigate the role of the infills in the structural response.

The testing methods implemented in the laboratories worldwide enable the researchers to evaluate the seismic performance of reduced or full-scale systems. The most used is the quasi-static testing method since it requires simple test-setup and control systems, low performance actuators and can be carried-out with a limited budget [9]. The test consists in the application of a pre-defined loading protocol to evaluate the stiffness, the strength and the energy dissipation (i.e., the hysteresis) of small substructures or components. However, the dynamic effects are neglected due to the low loading-rate commonly used in such tests. To overcome these limitations and to accurately reproduce the dynamic effects of earthquakes on structural systems, the dynamic testing methods are used. Among these, the shaking table testing method allow to reproduce the dynamic response of structural systems and to identify the dynamic characteristics of structural and non-structural components accounting for strain-rate effects [10, 11]. Many facilities are available in the laboratories worldwide. They differ in the number of degrees of freedom that can be reproduced, in the size of the table and in the maximum payload [12]. However, the shaking table testing method is not the most accurate in many cases due to the difficulties for the control to reproduce the specified accelerogram, especially for large and heavy structures and when several degrees of freedom are controlled. Except for few large testing facilities available in some laboratories, the main limitations of common shaking tables are the limited size of the table and the maximum payload. In addition, the force transmitted to the structure by the earthquake cannot be monitored during the tests, this limits the use of the test results in the validation/calibration of accurate numerical models.

In this context, the pseudo-dynamic (PsD) testing method allow to overcome the limitations of the previous testing methods (i.e., pre-defined protocol, the table size and the maximum payload) and in the test configuration (i.e., reduced scale and single-storey specimen). It allows to consider the step-by-step experimental/numerical variability of specimen's mechanical behaviour within the control process in which the inertia and the viscous damping forces are numerically simulated while the stiffness and the hysteretic damping are acquired directly from the specimen [13]. The testing method allows to test small-to-large size specimens with multi-storey accounting for the stiffness degradation and the damage evolution on the displacement demand. Furthermore, when the structural system exceeds the dimensions of the laboratory facilities a substructuring approach can be used [14, 15, 16]. It allows to concentrate the physical test only on the portion of the whole structure (physical substructure) that is more susceptible to damage, while the response of the remaining part of the structure (numerical substructure) is numerically simulated in a remote process. The definition of a substructuring approach is crucial to accurately reproduce the effects of an earthquake on the physical specimen. The approaches used for this purpose are generally complex, but a simplified approach can be adopted if the reliability of its assumptions is numerically and experimentally assessed.

The results of the PsD tests performed on full-scale multi-storey infilled RC frames represents a reliable data to calibrate and validate the nonlinear model of buildings capable of reproducing the actual displacement demand and accounting for stiffness degradation and damage evolution. In this way, the results of a nonlinear time-history analysis can be useful to predict the global and the local response of the building [5]. In addition, the calibrated model can be implemented in a losses-assessment framework to be used as a tool to predict losses at regional scale [1]. However, the reliability of the test results may be affected by the presence of errors that may occur in the response during the test [17, 18]. The sources of errors are related to the control parameters and on the physical parts of the experimental set-up [18, 19]. The effects of the errors may appear in the frequency or damping distortion in the response that can be identified using an identification model based on the test results [19]. Therefore, the presence of potential errors in the response must be identified and the reliability of the tests assessed to guarantee the quality of the test results.

The present thesis deals with the development and validation of a pseudo dynamic testing framework realized in the large-scale structures laboratory of Centro Servizi Metereologici e Tecnologici Avanzati (CeSMA) and managed by the Department of Structures for Engineering and Architecture (DiST) of the University of Naples Federico II. The development of the control system, the desing of the test setup and the reference prototypes used for the test validation are reported and discussed. PsD tests on a physical substructure representing a portion of a multi-stories existing infilled RC building tested considering different infill-to-frame connections are used for the validation. The test results are used to calibrate a refined nonlinear numerical models used to predict the global and the local response of the building. In addition, further activities are carried out at the European Laboratory for Structural Assessment (ELSA) of the Joint Research Centre (JRC) at European Commission to study the effects of errors on the test results and the assessment of the reliability of the tests. In particular, the presence of control errors during the tests is investigated and the reliability of the test is assessed identifying the effects introduced by errors in the response.

1.1 Scope and Objectives

This thesis deals with the development of a pseudo-dynamic testing framework for seismic performance assessment of full-scale structural systems, its validation through the testing of multi-storey infilled RC frames and the study of the test reliability. The objectives of the research works can be divided into three main groups.

The first group refers to the implementation of the PsD testing method in the large-scale structures laboratory of the CeSMA and the main objectives are: i) the development of a PsD testing framework, of the control system and the coordination software; ii) the implementation of a simplified substructuring approach to perform the tests; iii) the numerical validation of the proposed approach.

The second group refers to the experimental tests and the main objectives are: iv) the design of experimental test campaigns on a full-scale multi-storey infilled RC frames ; v) the analysis of experimental results and the study on the influence of the infill-to-structure connection; vi) the comparison between the numerical and the experimental results to validate the substructuring approach and the nonlinear models.

The third group includes the study of the effects of control errors on the reliability of the PsD test. It reports the activities carried out during the visiting period at the ELSA of the JRC in Ispra.

The first objective is fundamental to enable the researchers to perform PsD tests on full-scale specimens in the DiST-CeSMA laboratory of the University of Napoli Federico II. To this end, the research activities focused on the design of the testing facilities (i.e. pumping system, manifold, connection system to the reaction wall, etc.), on the development of control system, and the programming of a coordinator system. The latter was programmed in a MATLAB environment in agreement with recent research advances on PsD tests. The equation of motion at each step is solved by an integration algorithm that provide as outputs the displacement profile to be imposed at each DOF of the specimen. In addition, different scripts were created to define the input parameters and to visualize in real-time the output of the test. Instead, the upgrade implemented in the control system consists of a hardware-in-the-loop (HIL) interface that allow to communicate with the coordinator system. This allows to receive the displacement profile computed by the coordinator system then applied to the specimen by hydraulic actuators controlled through the existing control system. Furthermore, a dedicated window is implemented in the HIL interface to visualize the main information received from the system coordinator.

The second objective is the development of a simplified substructuring approach to perform PsD tests. This is because the limited dimension of the laboratory allows only a portion of a selected structural system to be physically reproduced in full-scale. The substructuring approach is fundamental to ensure that the displacement applied on the physical substructure is a realistic displacement that the substructure included in the whole building experienced during the earthquake. To this end, a linear and a nonlinear model of the whole structural system and the selected substructure are realized. Then, a modal analysis and a nonlinear static analysis are carried out to define the properties of the physical substructure required as input to perform the tests using the assumptions of the proposed simplified approach. In this study, a 4-storey infilled reinforced concrete building subjected to a real earthquake was selected as a case study from a database and the most damaged frame, representing the test specimen, was selected from this building and reproduced in the laboratory environment.

The third objective is the validation of the proposed substructuring approach. To this end, the nonlinear models realized for the second objective are used to perform nonlinear time history analyses. The dynamic properties defined as input for the physical substructure are used in the corresponding frame numerical model. An accelerogram is defined as input to perform the analyses. The vertical loads are estimated by means of a gravity load analysis, considering dead loads and live loads in the seismic combination defined according to the standards. Then, the results in terms of displacement time histories of the numerical analyses performed using both models are used to verify that the displacements applied to the frame are comparable with those applied on the same frame, when considering that the whole building is subject to the earthquake shaking.

The fourth objective is the development of experimental tests on a full-scale one-bay two-storey infilled RC frame using the developed PsD testing framework and the proposed substructuring approach. These tests allowed to study the contribution in terms of stiffness and strength of the infill in the lateral response of the frame and to characterize the damage exhibited during the test by structural and non-structural components. To this end, the properties of the specimen defined using the proposed substructuring approach and the record used to perform nonlinear time history analyses are used as input to perform the tests. Three specimens with different connection between the infill panels and the surrounding frame are realized to investigate on the effect of the connection on the lateral response. An experimental set-up was designed and realized in the laboratory to apply the displacement to be imposed on the specimen and the vertical load. Furthermore, to monitor global and local deformations on the specimen and strain on internal reinforcements, high precision LVDTs, classic LVDTs, strain gauges, and potentiometers are installed on the specimen and their measures are recorded by a data acquisition system (DAQ).

The fifth objective is the analysis of the experimental results obtained from the PsD tests carried out on the full-scale infilled RC frame. To this end, the results in terms displacement time-histories and interstorey shear-displacement or base shear-displacement obtained for each specimen are compared to study the effects of the beam-infill connection on the lateral response of the specimen. In particular, the initial stiffness, the maximum strength and the maximum displacement evaluated for each specimen are compared for the purpose. In addition, the damage experienced by the specimen during the tests is compared to the damage observed during post-earthquake inspection on the case study building to assess the reliability of the PsD testing method in reproducing the damage observed on the real structure.

The sixth objective is the comparison of numerical and experimental results to validate the substructuring approach, and to calibrate and validate the nonlinear models. To this end, the results of the experimental tests in terms of displacement time histories are used to verify that the displacements applied to the test specimen are comparable with those applied on the same frame, when considering that the whole building is subject to the earthquake shaking. Then, to calibrate the numerical model used to reproduce the nonlinear response of infills implemented in the building model, the global hysteresis obtained from both experimental and numerical analysis are compared and several iterations are performed to achieve the matching. In addition, the results of the numerical analysis are used to validate the nonlinear building model in terms of damage by comparing the damage assessed from the results of the numerical analysis with the damage observed on the real structure.

The last objective is the study of the effects of errors on the experimental response. To this end, a series of tests are carried out at the European Laboratory for Structural Assessment (ELSA) of the Joint Research Centre (JRC) at the European Commission. The experimental tests are performed on a new bench test, called PONYBENCH, conceived for demonstration, training, research and knowledge handover. The test results are used to identify the dynamic properties of the specimen and to investigate the presence of control errors to assess the reliability of the tests. In particular, the control parameters and the effects of their change on the response of the PsD system are investigated.

1.2 Thesis outline

According to the scope and the objectives presented in this chapter (Chapter 1), the thesis is organized in the following Chapters.

Chapter 2 introduces the testing methods available in earthquake engineering. The PsD testing methods are presented with emphasis on the infrastructure available worldwide, the characteristics of the control system, the integration algorithms that can be implemented to solve the equation of motion and the experimental and control errors that can affect the reliability of the test results. Finally, the distributed and hybrid testing methods are introduced.

Chapter 3 presents the pseudo-dynamic testing infrastructure, the solution algorithm, the control and the coordinator system implemented in the DiST-CeSMA the laboratory to enable the researchers to perform tests on full-scale structures . An overview of the laboratory along with the available facilities, devices and instruments is shown. Then, the control system and the upgrade implemented to enable the PsD test to be performed in the laboratory is discussed. Finally, the code implemented in the laboratory which allow to perform the PsD test solving the equation of motion is described in detail along with the scripts which constitute this code and their functions.

Chapter 4 presents the 4-storey existing infilled reinforced concrete (RC) building selected as a case study building. The geometrical details, the material properties, the reinforcement details and the damage observed on the case study during the post-earthquake inspection are shown. The selection criteria used to define the record motion used for the experimental tests and the numerical analyses is discussed. The models adopted to reproduce the linear and nonlinear behaviour of structural and non-structural components included in the numerical building model are described in detail. The selection of physical substructure from the case study building and reproduced in the laboratory environment is discussed. Then, the nonlinear model of the selected substructure is realized according to the characteristics numerical model of the building. The proposed substructuring approach and the corresponding assumptions considered to define the properties of the substructure are described. Finally, the numerical validation of the proposed substructuring approach based on the results of numerical analyses performed using the nonlinear models of the building and the frame is shown.

Chapter 5 presents the experimental tests carried out on the physical substructure. The test set-up designed and realized to perform the tests, the testing procedure and the characteristics of the tested specimens are shown. The analysis of the experimental results in terms of displacement time histories, interstorey and global hysteresis and observed damage is presented. The test verification and the experimental validation of the substructuring approach based both on the test results are discussed. The calibration of numerical model adopted to reproduce the nonlinear behaviour of infills is also shown. Finally, loss-assessment framework used to evaluate the losses at regional scale in which the simplified model experimentally calibrate is implemented is introduced.

Chapter 6 the research activities conducted at the European Laboratory for Structural Assessment (ELSA) at the Joint Research Centre (JRC) of the European Commission are presented. The testing infrastructure and the new bench test set-up, the PONYBENCH, conceived for demonstration, training, research and knowledge handover are presented. The numerical models representative of the specimen adopted for the analysis and implemented to perform the experimental tests are described. Finally, the results of a dynamic snap-back test and of PsD tests are analysed with emphasis on the study of the effects of errors introduced in the response that can affect the test reliability .

Chapter 2

2. Literature review on testing methods in earthquake engineering

Different testing methods are available in earthquake engineering to assess the seismic performance of structures. Among these, those commonly adopted in major laboratories worldwide can be classified according to the loading protocol in quasi-static tests, dynamic tests, pseudo-dynamic tests. Other differences between the aforementioned testing methods are related to the operation cost, and the effects of the earthquake effectively reproduced. In this chapter, the properties of each testing method are discussed, with particular emphasis on the pseudo-dynamic testing method that represent the core of this thesis.

2.1 Quasi-static tests

Quasi-static testing method represents the simplest method to statically assess the seismic performance of structural systems under imposed (pre-defined) loading protocols. This is because it requires simple control systems, small facilities and reduced operation costs to perform the tests. It is generally used to mechanically characterize small-to-large size structural systems or structural and non-structural components such as reinforced concrete (RC) frames [6], RC beam-column joints [9], RC columns [20] and masonry walls [7] and to investigate the effectiveness of innovative retrofit solutions [21].

Figure 2.1.1 shows a typical test set-up used to perform quasi-static test on RC beam-column joints. It consists of an oil pumping system which supply the hydraulic actuator and the hydraulic jacks. The hydraulic actuator is installed on the reaction structure, clamped to the strong floor and designed ad-hoc for this test, to apply the horizontal load while the hydraulic jacks are installed at the top of the columns to apply the axial load. Each hydraulic piston is equipped with a load cell to measure the reaction force of the specimen and an internal displacement transducer to measure the rod movement. When the tests are performed in displacement control, an additional displacement transducer may be installed on the specimen to monitor the displacement at the reference point. In addition, the global or local behaviour of the specimen is monitored using an additional instrumentation managed by the data acquisition system (DAQ) shown in Figure 2.1.1.

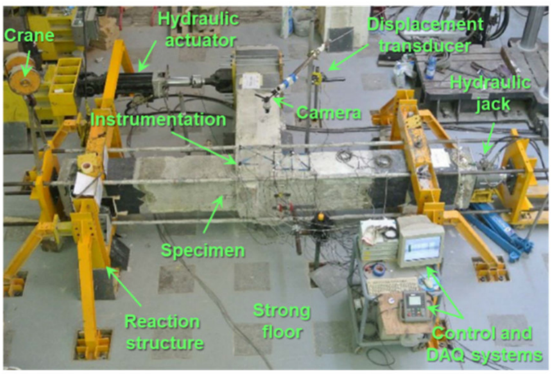

(a)

(b)

Figure 2.1.1. Quasi-static (or cyclic) test set-up of real beam-column joint (a) [9] and a full-scale column (b) [20].

The test consists in the application of a pre-defined loading protocol (Figure 2.1.2) on the specimen by the hydraulic actuator, while the vertical load applied by the hydraulic jacks is kept constant. The loading protocol consists of a load pattern with a defined number of stages. Loading protocol can be defined according to available testing standards [22, 23] or literature studies [24, 25, 26]. Figure 2.1.2 shows a loading protocol [6] where during the same stage the displacement amplitude is constant and repeated three times in both directions, while the displacement amplitude increases when the test come the next stage.

The quasi-static testing method allow to perform tests with at reduced costs to analyse the response of structural system in terms of strength, stiffness and hysteresis. It is commonly used in large experimental program with relevant number of specimens with the scope of compare the influence of different construction details, material properties or to study the effects of a strengthening solution at component level. It allows to clearly identify the hysteretic response. The main limitations are: neglect the influence of strength, stiffness and other dynamic properties on the displacement demand; neglect the effect of velocity on the mechanical response.

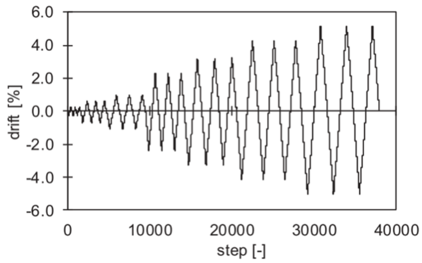

Figure 2.1.2. Example of displacement loading protocol [6].

2.2 Dynamic tests

The dynamic testing method is an advanced experimental method which allows to reproduce the dynamic effects on the reference prototype. Such a type of test often requires the ad-hoc design of a complex infrastructure and the use high-performance equipment and instrumentation. This testing method is used for testing small-to-large size structural systems, e.g., RC bridges [27], framed structures [28], masonry buildings [11] and non-structural components [29].

Among the available dynamic testing methods, the shaking table is the commonly used to reproduce earthquake loads on structural and non-structural components. The dynamic shaking table tests consist of the horizontal and vertical components of a natural or artificial earthquake applied at the base of the specimen to investigate the dynamic response. The rotation motions (i.e., roll, pitch and yaw) can be reproduced by the shaking table operating along all the six degrees of freedom (DoFs) available in a 3D environment. The strain rate effects and inertial/damping forces are accounted. However, most of the shaking table available worldwide have significant limitation in the table size and payload or a limited number of DoFs (in most of the cases only the translational motion is allowed). In addition, the testing method does not allow to directly measure the global and the local reaction forces and to observe the damage mechanism during the tests due to the speed execution.

Table 2.2.1. Characteristics of shaking table available worldwide.

institution	payload [tons]	dimensions [m^2]	DoFs	max. acc.*[g]
National research Institute for Earth science and Disaster prevent (Japan)	1200	15.0 x 20.0	3	1.7
University of California San Diego (USA)	400	12.0 x 7.6	1	4.7
EUCENTRE (Italy)	60	5.6 x 7.0	1	6.0
Laboratorio National de Enganbaria Civil (Portugal)	40	5.6 x 4.6	3	1.8
National Technical University Athens (Greece)	10	4.0 x 4.0	6	2.0
Faculty of Engineering University of Bristol (UK)	15	3.0 x 3.0	6	3.7
University of Naples Federico II (Italy)**	20	3.0 x 3.0	2	1.0

*the maximum acceleration must be intended in horizontal direction without payload
**the characteristics are referred to two shaking table available in the laboratory

To date, various shaking tables are available in the laboratories worldwide. Table 2.2.1 provides an overview of the shaking tables presented in this study. The largest shaking tables have been realized indoor and outdoor at the National Research Institute for Earth science and disaster prevent (NIED) in Japan [10] and the University of California of San Diego [30]. The EUCENTRE shake table has the highest allowable horizontal acceleration (without payload) of the facilities presented. The shake tables of the National Technical University of Athens (Greece) [31] and the Faculty of Engineering of the University of Bristol (UK) [32] allow the reproduction of translational and rotational motions, as six degrees of freedom (or axes) can be controlled.

The laboratory of the Department of Structures for Engineering and Architecture (DiSt) of University of Naples Federico II [12] has two shaking tables. The tables allow to reproduce two translational DoFs and can be controlled in synchronously or asynchronously. The Laboratorio National de Engarbaria Civil (LNCE) [28] in Portugal has a shake table allow the reproduction of three DoFs and intermediate characteristics.

The characteristics of the available shaking tables differ in terms of dimensions, maximum payload, shaking direction (or number of degrees of freedom), frequency range, maximum displacement, maximum acceleration, maximum load and bending moment (Table 2.2.1). The table size limits the dimensions of the specimen while the maximum payload limits the specimen weight. The number of operational DoFs allows the test to be performed by combining the translational motions (longitudinal, transverse and vertical) with the rotational motions (roll, pitch and yaw). The number of DoFs can be increased by adding or combining the number of hydraulic actuators installed on the test set-up. For instance, a shake table with two hydraulic actuators installed in the longitudinal and transverse directions can be used to perform the uniaxial and bi-axial test. If additional hydraulic actuators are added in the vertical direction, the vertical load can also be applied. Furthermore, the roll, the pitch and the yaw can be reproduced by combining additional hydraulic actuators to those present in the translational directions. The frequency range depends on the performance of the control systems and the equipment installed on the test-up while the maximum displacement, maximum acceleration and maximum load depends on the payload present on the table during the test and on the actuator stroke.

Figure 2.2.1 a) shows the E-Defense shake table of the National research Institute for Earth science and Disaster prevent (NIED) in Japan, which is the world's largest indoor shake table. Measuring 20 m x 15 m and with a maximum payload of 12 MN, the shaking table allows a large specimen to be tested operating along all six degrees of freedom. The frequency ranges from 0 Hz to 15 Hz with reasonable accuracy while the maximum allowable acceleration is ±9.0 m/s horizontally and ±15.0 m/s vertically [10].

The world's largest outdoor shake table is the Large High-Performance Outdoor Shake Table (LHPOST) which was developed at University of

California in San Diego (see Figure 2.2.1, b). Designed as uniaxial system. The shaking table has been upgraded to operate along all six degrees of freedom. The table measures 12.2 m x 7.6 m and has a maximum payload of 20 MN. The frequency bandwidth ranges from 0 Hz to 33 Hz while the maximum allowable acceleration at 4 MN payload is ±1.28 g [30].

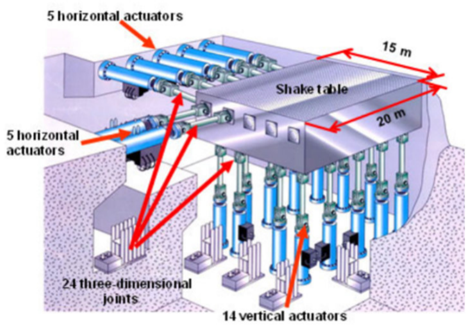

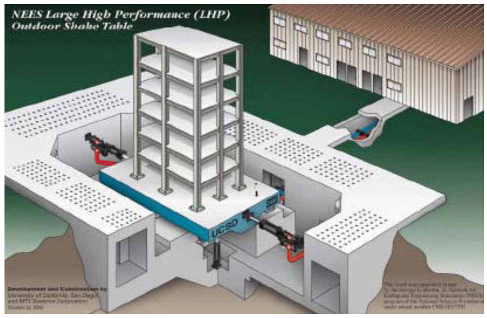

(a) (b)

Figure 2.2.1. Shake table largest facilities available worldwide: E-Defense shake table of NIED in Japan [10]; LHPOST outdoor shake table of NHERI at San Diego [30].

2.3 Pseudo-dynamic tests

The pseudo-dynamic testing method is a simultaneous simulation and control process, in which the inertia and viscous damping properties are numerically simulated, while the stiffness and the hysteretic damping properties are measured directly from the structure [13]. This test method represents an attractive alternative to reproduce the effect of an earthquake on small-to-large structural systems. It combines the advantages of the quasi-static tests with the possibility of applying earthquake-representative loading protocol account for the damage evolution and the deriving stiffness degradation. The rising attention of the research community to such a type of test is related to the simplicity of the seismic testing of large-scale specimens without using complex and expensive dynamic facilities with the main advantage of overcoming the limitations related to the quasi-static predefined loading protocols and shaking table payload. In addition, the damage scenario e.g., cracking, yielding or failure can be followed during the test due the slow loading rate. However, the main limitation could be that the strain-rate effects are not accounted during the test.

In the pseudo-dynamic (PsD) tests, an idealized lumped mass model with a limited number of degrees of freedom (DoFs) is adopted to define the response of the specimen. The equation of motion valid for this type of model is second order differential equation system which can be expressed in matrix form as in the following (2.1):

$$[\mathrm{M}] \cdot \{\ddot{\mathrm{x}}(\mathrm{t})\} + [\mathrm{C}] \cdot \{\dot{\mathrm{x}}(\mathrm{t})\} + \{\mathrm{R}(\mathrm{t})\} = \{\mathrm{F}(\mathrm{t})\} \tag{2.1}$$

where $[\mathrm{M}]$ is the mass matrix, $[\mathrm{C}]$ is the viscous damping matrix (typically assumed null in the PsD tests), $\{\mathrm{R}(\mathrm{t})\}$ is the restoring force vector (measured from the structure), $\{\mathrm{F}(\mathrm{t})\}$ is the external force applied to the structure (e.g., earthquake load), $\{\ddot{\mathrm{x}}(\mathrm{t})\}$ is the acceleration vector and $\{\dot{\mathrm{x}}(\mathrm{t})\}$ is the velocity vector (both numerically simulated). The equation of motion can be solved using the integration algorithms available in the literature [33].

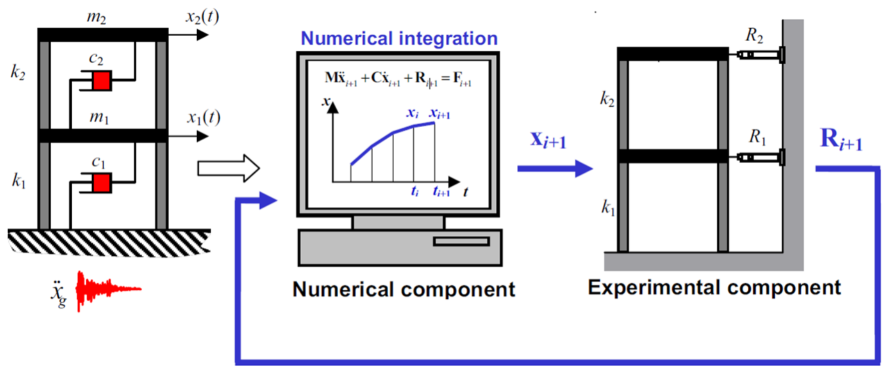

Figure 2.3.1. Reference pseudo-dynamic testing framework [16].

Figure 2.3.1 shows a reference scheme of a pseudo-dynamic testing procedure. It consists of an experimental component that is physically built in the laboratory and of a numerical part simulated on a remote PC or on the controller, in which an integration algorithm is implemented to solve the equation of motion. The input record signal, the dynamic properties of the specimen (i.e., mass and viscous damping) and the integration algorithm parameters, must be defined at the beginning of the test. Then the displacement profile, which must be applied to the specimen by using an hydraulic actuators, is computed by solving the equation of motion using the integration algorithm. The restoring force is measured on the specimen at the target displacement and sent to the controller to compute the next step of the record. In this way, the actual displacement demand of the earthquake can be reproduced considering the strength and stiffness degradation.

The development of the pseudo-dynamic testing framework requires the realization of a facility, the implementation of a testing method and an integration algorithm to perform the test. In this paragraph, the characteristics of the available facilities, the testing infrastructure and the controller are discussed. The available PsD testing method with the integration algorithm and the errors that can affect the reliability of the test are then presented.

2.3.1 The pseudo-dynamic facilities available world-wide

Pseudo-dynamic testing facilities are realized in different countries to enable the researchers to assess the seismic performance of small-to-large structural system. An overview of the pseudo-dynamic testing facilities available worldwide is provided by Calvi et al. [34].

Table 2.3.1, indicates the institution, the shape and the height of the reaction wall and the strong floor area of these facilities. Furthermore, the facilities are classified according to the height of the reaction wall. The characteristics of the most significative laboratories reported in the

Table 2.3.1 are presented in this paragraph. The laboratory of the Department of Structures for Engineering and architecture (DiSt) at the University of Napoli Federico II and of the European Laboratory for Structural Assessment (ELSA) of Joint Research Centre will be presented in the paragraphs 3.1 and 6.

Table 2.3.1. Pseudo-dynamic facilities available worldwide [34].

	Institution	H [m]	A [m^2]	Type
1	Building research Institute (Japan)	25.50	N.A.	L-shaped two sides
2	Hazama Technical Research Institute, Hazama Corp. Ltd. (Japan)	18.00	423	-
3	European Laboratory for Structural Assessment – JRC Ispra (Italy)	16.00	281	L-shaped two sides
4	ATLSS and Fritz Laboratories, Lehigh University (USA)	15.20	381	L-shaped
5	Structural Systems Laboratory, University of California at San Diego (USA)	15.00	946	-
6	Bristol Laboratory for Advance Dynamic Engineering (UK)	15.00	-	-
7	Building and Fire Research Laboratory, National Institute of Standards and Technology (USA)	14.00	345	-
8	Earthquake Engineering Research Centre, UC Berkeley Pacific (USA)	13.30	590	Reconfigurable
9	Cornell University (USA)	12.00	300	L-shaped
10	University of Minnesota – Twin Cities (USA)	12.00	297	-
11	Faculty of Science and Engineering, Nihon University at Tokyo (Japan)	12.00	285	L-shaped
12	European Centre for Training and Research in Earthquake Engineering - EUCENTRE, Pavia (Italy)	12.00	138	L-shaped
13	Ecole Polytechnique, Montreal (Canada)	10.00	500	-
14	Technical Research Institute, Shimizu Corporation Ltd. (Japan)	10.00	N.A.	-
15	Nabor Carrillo y R J Marsal del Instituto de Ingenieria, Universidad Nacional Autonoma de Mexico (Mexico)	10.00	N.A.	-
16	Structural Engineering and Materials Laboratory, Georgia Tech (USA)	9.80	764	-
17	Large Scale Structures Laboratory, University of Nevada at Reno (USA)	9.50	765	L-shaped - one side
18	Materials and Structural Testing – University of Trento	9.50	407	-
19	Constructed Facilities Laboratory, North Carolina State University (USA)	7.60	418	-
20	Full-Scale Structure Laboratory, Chulalongkom University (Thailand)	7.00	300	-
21	**Department of Structures for Engineering and Architecture (DiSt), University of Napoli Federico II (Italy)**	**7.00**	**260**	**L-shaped - two sides**

22	Structures Test Hall, University of California, Irvine (USA)	6.70	325	-
23	Materials and Structural Testing – University of Basilicata (Italy)	6.00	-	-
24	Structures Laboratory, University of Patras (Greece)	5.50	288	L-shaped - one side

Building Research Institute (Japan) – PsD facility

Figure 2.1.1 show the large-structural testing laboratory facility of the Building Research Institute (BRI) of Japan [15]. It was built in 1979 and consist of a reaction wall 25.5 m high, 20.0 m wide and 6.6 m thick served on both sides of a strong floor with the same width and 24.6 m long. The laboratory is equipped with a several hydraulic actuators and displacement transducers to perform tests on large structure up to seven floors. Furthermore, a pumping system is provided to supply the hydraulic actuators. More details about the BRI testing facility can be found in [35].

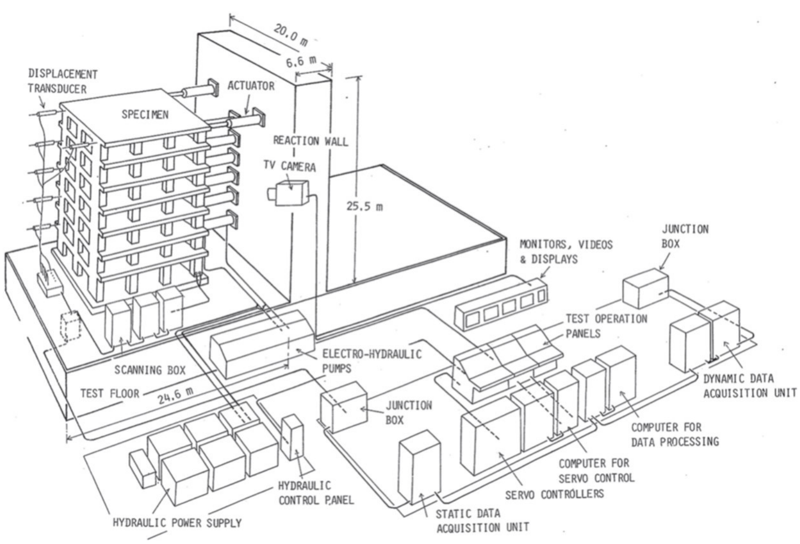

Figure 2.3.2. Large-scale structural testing laboratory built by the Building Research Institute (BRI) of Japan [15].

European Laboratory for Structural Assessment (EU) – PsD Facility

The European laboratory for Structural Assessment (ELSA) was inaugurated located in Ispra (VA) in 1992 and consist of a reaction wall 16.0 m high, 20.0 m long and 4.0 m thick. The reaction wall was built on a strong floor 4.2 m high with an irregular shape in plane. It was designed to resist a bending moment of 200 MNm and a base shear of 20 MN, while the strong floor was designed to resist a bending moment of 240 MNm. To install testing set-ups, an anchor-hole regular grid with a spacing of 1.0 m was realized on both the reaction wall and the strong floor. Figure 2.3.3 shows the dimensions and the capacity load of the reaction wall and the strong floor [36].

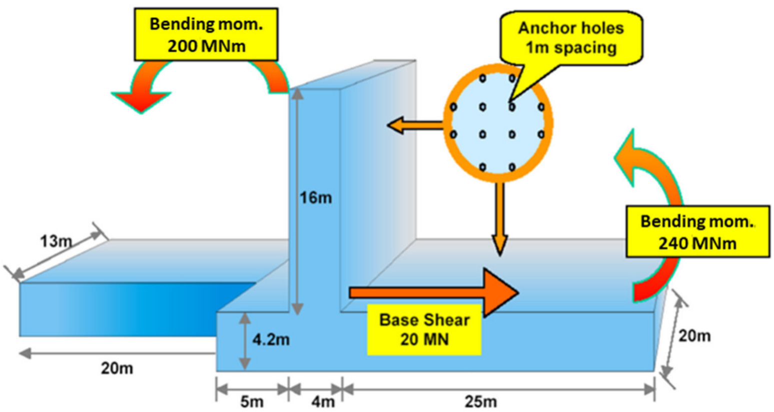

Figure 2.3.3. European Laboratory for Structural Assessment (ELSA) reaction wall and strong floor [36].

To perform cyclic, dynamic and pseudo-dynamic test on small-to-large size specimens, the laboratory is equipped with hydraulic-actuators and a pumping system. The tests are performed using the in-house developed control system, ELSAREC, presented in the Chapter 6. More details about the ELSA facility can be found in [37].

ATLSS laboratory at Lehigh University(USA) – PsD facility

The Real-Time Multi-Directional Earthquake Simulation Facility has been established in 2004 at the Lehigh University ATLSS Engineering Research Center and is an equipment site within the Network for Earthquake

Engineering Simulation (NEES) [38]. The ATLSS Laboratory is equipped with a strong floor that measures 31.1 m by 15.2 m in plan, and a multi-directional reation wall that measured up to 15.2 m in height (see Figure 2.3.4). Anchor points are spaced on a 1.5 m grid along the floor and the walls. Each ancor point can resist 1330 kN tension force and 2220 kN shear force. Additional steel framing is used in combination with the strong floor and reaction wall to create a wide variety of test configurations.

Figure 2.3.4. Real-Time Multi-Directional (RTDM) Earthquake Simulation Facility reaction wall and strong floor [39].

To create the RTDM facility, several pieces of equipment have been installed in the ATLSS Laboratory. This equipment includes five, dynamic, double rodded hydraulic actuators with a $\pm$ 500 mm stroke. Two of these actuators have a 2300 kN maximum load capacity, with the remaining three having 1700 kN maximum load capacity. Each of the actuators is ported for three 1500 l/min servo-valves, enabling them to achieve a maximum nominal velocity of 840 mm/sec (2300 kN actuators) and 1140 mm/sec (1700 kN actuators). The existing hydraulic power supply system at ATLSS consisted of five 2550 l/min pumps. A hydraulic oil reserve and two banks of accumulators were added to enable strong ground motion effects to be sustained for up to 30 sec. More details of this facility are reported in [38].

Earthquake Engineering Research Centre, UC Berkeley Pacific (USA) – PsD facility

The test floor of the NEES Berkely facility, shown in Figure 2.3.5, consists of a main center bay and two side bays. The full length of the main bay is serviced by an overhead bridge crane with capacity of 12 tons. A paved area 15.2 x 30.4 m located on the east side of the laboratory is used as a construction area. The structural tie-down floor is located on the east end of the main bay of the laboratory. The overall plan dimensions of the tie-down slab are 6.1 x 18.3 m. The slab has 63.5 mm diameter holes located in an array at 0.914 m on center over the 6.1 x 18.3 m^2 area. The test floor provides a completely versatile facility for testing large structural assemblies. Static or dynamic loads may be applied to specimens using tie rods, hydraulic actuators, and the reconfigurable reaction wall. The test floor was designed to act as a hollow box girder in the longitudinal direction and as a Vierendeel girder in the transverse direction.

Figure 2.3.5. UC Berkeley wall and frame test [40].

The reconfigurable reaction wall or walls is made up of 24 individual reinforced concrete blocks that are designed to be post tensioned to each other and to the test floor. The blocks are 3.05 m by 2.74 m in plan and 0.76 m high. Each block contains 10 vertical holes @ 0.91 m on center around its perimeter for post tensioning to the test floor. Similarly, each block contains horizontal holes for tying blocks together. The maximum stackable height of the wall is 12.8 m and the wall capacities for two principal configurations. More details about the NEES Berkeley facility can be found in [40].

EUCENTRE SHAKE (Italy) - PsD facility

The EUCENTRE laboratory in which the PsD facility is realized, is the SHAKE LAB. It is equipped with a shaking table to test the large-size specimen, a testing machine with a 5 DoFs to test isolator devices and an L-shaped reaction wall and strong floor to perform quasi-static and pseudo-dynamic tests. An overview of the laboratory is shown in Figure 2.3.6. The reaction walls are 9.6 m and 14.4 m long and 12.0 m high, allowing to test structure more than three stories high. The thickness of both reaction wall and strong floor is 2.4 m in order to resist the forces which are necessary to deform and damage full-scale specimens.

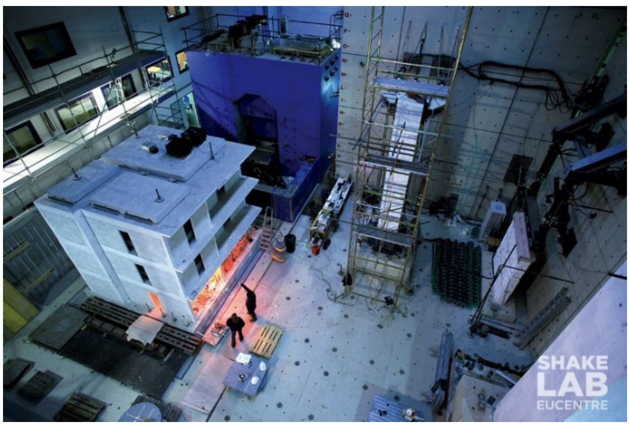

Figure 2.3.6. EUCENTRE SHAKE LAB reaction wall and strong floor.

The reaction wall and the strong floor are realized through an in-situ post-tensioned system of tendons designed to ensure the high performance of the PsD facility. The maximum base moments that can be resisted by the two reaction walls are 46120 kNm for the longest wall and 30748 kNm for the shorter one. To perform quasi-static and pseudo-dynamic test, a pressure of 280 bars is the maximum pressure guaranteed during the test. In addition, the piping system is designed to ensure a maximum flow of 1360 l/min. More details on the design and the characteristics of the EUCENTRE SHAKE LAB PsD facility can be found in [34].

University of Trento (Italy) - PsD facility

The Pseudo-dynamic facility is located in the laboratory of the Department of Mechanical and Structural Engineering (DIMS) belong to the University of Trento. The laboratory is equipped with a bi-directional reaction wall, consisting of a 9.5 m tall pre-stressed concrete wall and a 42 m long strong floor, provided of a regular hole grid for fast and effective connections of the testing set-up. The overall dimensions of the PsD facility are 42.00 x 16.60 x 9.5 m.

Figure 2.3.6 shows the 3D laboratory sketch. The maximum load acting on the reaction wall depends on the considered load combination. In the case of an Earthquake load combination, the maximum load, in tension and in compression, is 2250 kN at 9.0 m, and decreases at lower height.

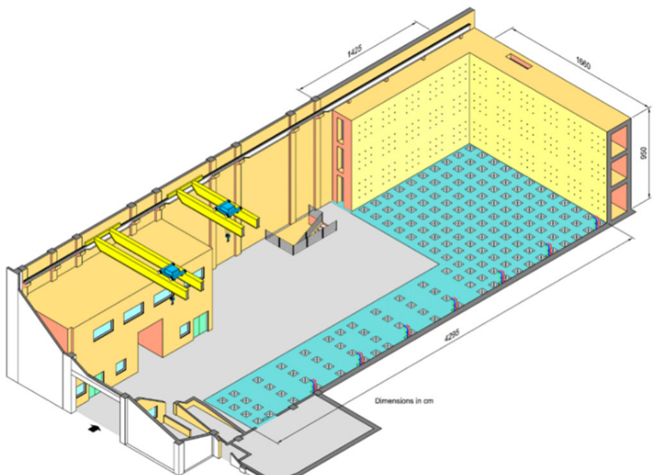

Figure 2.3.7. University of Trento 3D Laboratory sketch.

The laboratory is also equipped with two 10 tons bridge-cranes that permit the movement and positioning of test structures. By means of computer controlled hydraulic actuators it is possible to expose full scale structures to dynamic strong forces and control the resulting displacements with high precision. In addition to static and cyclic tests on large structures and components, the facility is equipped for the so-called pseudo-dynamic test (PsD) technique, enabling the simulation of earthquake loading of full-scale buildings.

The hydraulic system of the laboratory has the following general characteristics: (i) header pipeline flow of 1500 l/min, (ii) riser pipeline flow of 1200 l/min and (iii) engaged power of 600 kW and work (high) pressure of 21 MPa. In addition, the following equipment is available in the laboratory: (i) oleodynamic universal testing machine - Metrocom - 1000 kN, (ii) mechanical universal testing machine - Galdabini - 100 kN, (iii) compression test rig - controls - 300 tons; (iv) +1000/-1000 kN MTS dynamic actuator, (v) +1000/-640 kN MTS actuator, (iv) jacks and reaction frames up to 2000 kN. The details of the PsD testing facility of the University of Trento are reported on the website [41].

University of Patras (Greece) - PsD facility

The facility of the Structures Laboratory (STRULAB) belongs to the University of Patras consists of a reaction walls 5.5 m high, 6.0 m and 4.0 m long with a thickness of 1.0 m. The walls, solid and vertically pre-stressed, have an L-shape arrangement so that they can be used for bidirectional testing. The reaction wall is served by a strong floor 18.0 m by 16.0 m in plan, with a regular anchor hole grid of 0.5 m in both directions to install the equipment and the devices.

The system is used for pseudo-dynamic testing of earthquake-resistant components, subassemblies or small structures. To this end, the laboratory has a pump with a capacity of 500 l/min and eight servo-hydraulic actuators (ranging from 250 to 1000kN capacity), one of which is dynamic (1600l/min). The oil-supply system provides a total of 500 l/min all around the strong floor and to the top of the reaction walls, assisted by three banks of accumulators. State-of-the-art digital controllers with a total of eight channels are employed for a large spectrum of tests, including hybrid (pseudo-dynamic) with sub-structuring (including geographically distributed tests). Figure 2.3.8 shows a test set-up realized to PsD testing a reduced scale RC frame in the STRULAB.

Figure 2.3.8. Pseudo-dynamic test of a reduced-scale RC frame at STRULAB.

University of Minnesota – MAST laboratory

The Multi-Axial Subassemblage Testing (MAST) laboratory belongs to the University of Minnesota allow to test structures up to 6.1 x 6.1 m in plan and up to 8.6 m high imposing 6-degree-of-freedom (6-DoFs) loading or deformation. It is a large structural testing machine that is able to load structures attached between the stiff top crosshead (in the shape of a cruciform) and strong floor through movement of the machine's top crosshead (see Figure 2.3.9).

The strong floor is 10.7 m x 10.7 m in plan and consists of an array of 140 mm thick threaded steel plates post-tensioned to a 2.1 m thick concrete slab. The threaded holes in the steel plate consist of a regular grid of anchor points at a center-to-center spacing of 460 mm. More closely spaced holes are located directly below the centered placement of the top crosshead. The service load capacity of each threaded hole in the strong floor is 560 kN in the vertical (axial) direction and 560 kN in the horizontal (shear) direction.

Each inside leg of the L-shaped reaction (strong) wall is 10.7 m wide and 10.7 m tall. The wall is post-tensioned to the foundation to increase its stiffness. A regular grid of anchor points is provided with a 460 mm center-to-center spacing. Each leg of the reaction wall can resist lateral forces of ±3910 kN each at two elevations along the wall height, 4.9 m and 9.8 m above the top of the strong floor), for a total of ±7830 kN.

Figure 2.3.9. Multi-Axial Subassemblage Testing (MAST) System [42].

The crosshead has a cruciform shape in plan, measuring 8.93 m tip to tip, with a 1.42 m x 1.65m box-shaped cross section, resulting in a span to depth (L/d) ratio of 2.2. It is fabricated with 38 mm thick plates, with the bottom plate being 50 mm thick. Design constraints included a weight limit not to exceed the 445 kN capacity of the crane such that the crosshead could be lifted by the crane.

Two sets of actuator pairs with strokes of ±400 mm provide lateral loads up to ±3910 kN in the orthogonal directions. Four ±1470 kN vertical actuators, capable of applying a total force of ±5870 kN with strokes of ±510 mm, connect the crosshead and the strong floor. Hydrostatic bearings are used in conjunction with the vertical actuators to reduce friction loads. Vertical spacers can be mounted between the bearings and the vertical actuators for gross height clearance adjustment. The actuators are powered by a combination of four hydraulic service manifolds, attached to 680 l/min hydraulic power supply. Each actuator is configured with a 57 l/min servo valve to support quasi-static testing. More details on the Multi-Axial Subassemblage Testing (MAST) laboratory are reported in [42].

2.3.2 Testing infrastructure

Figure 2.3.10 shows a laboratory model used as reference, to discuss the equipment required to realize a PsD testing facility [42]. It consists of a reaction wall and a strong floor that can be made of reinforced concrete or steel. An anchor-hole grid with a defined spacing must be realized on both the reaction wall and the strong floor in order to fast install testing set-up and the specimen. The dimensions (height, width and grid spacing), the number and the capacity (maximum shear and bending moment) of the reaction wall and the strong floor must be designed according to the size of the specimens to be tested and the maximum load that must be applied. The rear of the reaction wall can be realized as accessible to accommodate the plant systems.

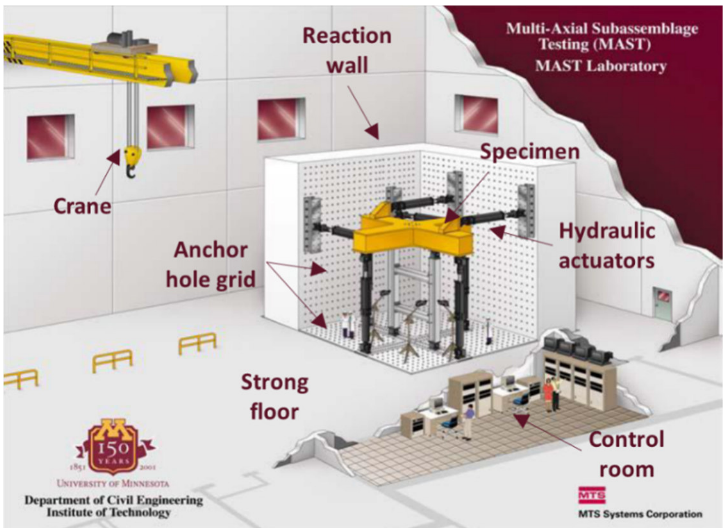

Figure 2.3.10. Reference pseudo-dynamic testing facility [42].

A main entrance with proper dimensions must be provided to allow the access of the truck or to move the specimen in the laboratory (if it is built outside). In this specific case, a pulling system must be designed to entering the specimen into the laboratory. The laboratory must be served by a crane, an electrical system and an oil pumping system. A separate room should be provided for the pump and its water-cooling unit, the electrical cabinet and to the control room. The control room will contain the control system, the data acquisition system (DAQ) and the equipment required to perform the test.

The hydraulic actuators and hydraulic jacks are installed on the reaction wall and on the strong floor in order to apply both the horizontal and vertical load to the specimen. Each actuator is equipped with a load cell and an internal displacement transducer to measure the applied force and the displacement of the rod. If the test is conducted in displacement control with a control point on the specimen, a displacement transducer can be installed on the structure.

The equipment presented in this paragraph represents the minimum required to perform a pseudo-dynamic test. The additional devices depend on the configuration of the test set-up, on the budget and on the aim of the research activities.

2.3.3 Control system

For the pseudo-dynamic test, a digital controller is required to manage the actuators. The controller may be developed by the owners (in-house) or by a provider (commercial). The main advantage of an in-house developed controller is the possibility to upgrade the system without additional costs. However, the upgrade and the maintenance of the system require a specific skill. Figure 2.3.11 shows a reference scheme of an in-house digital controller implemented in the European Laboratory for Structural Assessment (ELSA) of the European Commission [33]. The digital controller allows to manage the actuators in force control or in displacement control. It is equipped with a personal computer (PC) that allows to set the control parameters, the interlocks and the alarm and to visualize in real-time the feedback sent to the controller by the load cell and the displacement transducers installed on the actuator. The response of the actuator depends on the parameters of the Proportional-Integrative-Derivative (PID) algorithm [43] defined in the controller for the selected control mode. The interlocks are set on the force or the displacement of the actuator in order to shut-down the pump system in the case of dangerous situations. The controller allows to apply the load in terms of displacement both in local mode (manual) and remote mode (automatic). The remote mode is used to perform the PsD test.

The integration algorithm that solves the equation of motion can be implemented in the controller or in a remote PC. Figure 2.3.11 shows a control system in which the integration algorithm is implemented in the controller. In this configuration, the target displacement computed by the controller is converted in an analogic signal and sent to the actuator to be applied to the specimen. The restoring force and the applied displacement measured by the load cell and the displacement transducers are then converted into a digital signal and sent to the controller to compute the next step of the record. In particular, the measured displacement allows to check the correct application of the computed displacement, while the measured restoring force is used to perform the next step of integration.

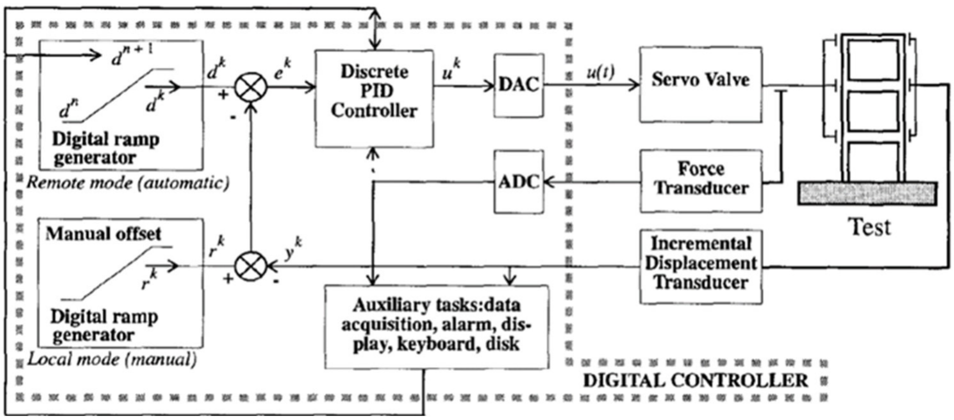

Figure 2.3.11. Digital controller for pseudo-dynamic test [33].

Figure 2.3.12 shows the pseudo-dynamic testing framework presented in [44]. The difference respect to the previous scheme (Figure 2.3.11) consists in the use of a remote PC to solve the equation of motion. The remote PC sent to the controller at every step the target displacement to be applied to the specimen by the actuators and receives from it the measured restoring force. Furthermore, this scheme shows an additional instrumentation is also installed on the specimen and the measurements are recorded by a data acquisition system (DAQ) to monitoring the specimen response.

The control systems presented in this paragraph are an example of an in-house control system that can be used to perform pseudo-dynamic test. The architecture of the commercial control system is the same as that of an in-house control system. However, the commercial control system requires additional costs for the implementing functions, and degrees of freedom as well as for upgrading and maintaining the control system.

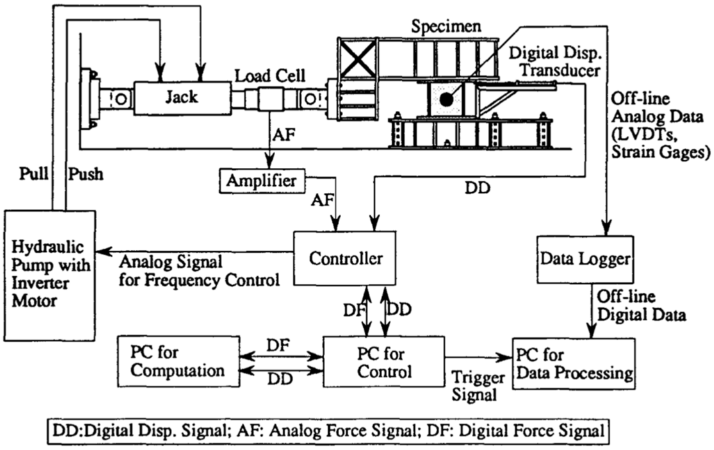

Figure 2.3.12. Pseudo-dynamic testing framework [44].

2.3.4 Testing methods

The pseudo-dynamic (PsD) test was performed for the first time by Takanashi et al. [45] solving the equation of motion by using a digital computer. The method adopted by the authors numerically simulates the inertia and the viscous damping while the stiffness and the hysteretic damping is directly acquired on the specimen during the test.

Different nouns were assigned to this testing method to designate the combination of the experimental test with the numerical simulation: pseudo-dynamic test method, hybrid testing and computer-actuator on-line testing [46]. Many researchers contributed to the improvement of this test method during the years. The Continuous method was proposed for the first time by Takanashi and Ohi [47] as an alternative to the Classical (or Step) method. The substructuring technique was first proposed by Demitzakis and Mahin [48] in order to test in the laboratory, only the physically substructure that experience the damage while the remaining portion of the structural system is numerically simulated.

Watanabe et. al [49] and Mosqueda et al. [50] proposed a distributed substructuring technique to test in different location the physical and the numerical substructures. Figure 2.3.13 shows a flow chart in which various types of testing methods are reported.

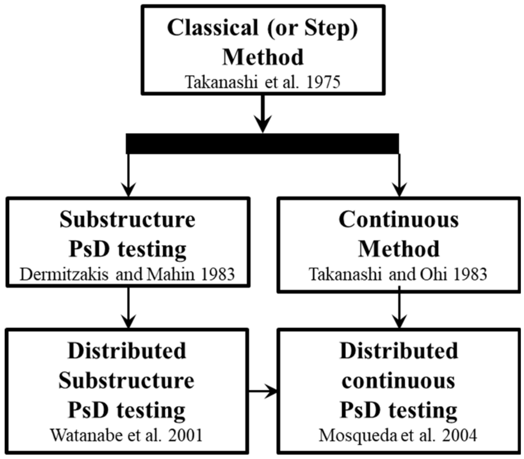

Figure 2.3.13. Flow chart of various types of PsD testing methods.

2.3.4.1 Classical (or step) method

The Classical or Step method, is the most commonly used in the research field to perform PsD test. The equation of motion is solved at every step of the record selected as the input using an integration algorithm implemented in the controller or in a remote PC to compute the target displacement. The test is performed in displacement control sending the target displacement to be imposed on the specimen to the actuators through the controller. The application of the target displacement covers a time increment Δt for the integration of the equation of motion in the prototype time and consists of four phases in the experimental time [36].

Figure 2.3.14 shows a time increment calculated using the Classical method, passing from the step n with an acceleration equal to a_g^n to the step n+1 with an acceleration equal to a_g^{n+1} of the accelerogram. The prototype time t is related to the duration of the accelerogram record, while the experimental time T is related to the duration of the test. The size of the time increment Δt

in the prototype time t must be chosen according to the integration algorithm adopted to solve the equation of motion. This is because the time increment influences the stability and the accuracy of the method while increase the numbers of steps (i.e., the test duration) when it has a small size. The factor λ represents the time scale factor defined as the ratio between the experimental time T, and the prototype time t. Typically, the time scale factor value for the PsD test ranges from 200 to 1000. This means that a PsD test with λ of 200 is performed 200 times slower than the real-time.

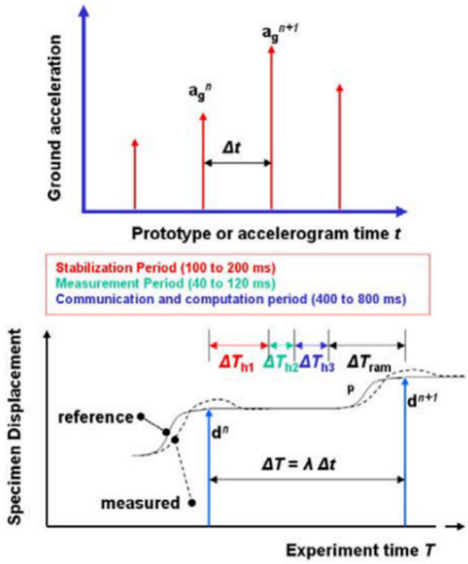

Figure 2.3.14 Classical (or Step) PsD method [36].

Once the target displacement is calculated, this is sent to the controller that generates a ramp (ΔT_{ramp}) to smoothly achieve the target. The duration and the slope of the ramp depends on the loading rate defined in the controller and on the displacement increment to be imposed. A stabilising hold period (ΔT_{h1}) consents to achieve with an acceptable accuracy the target displacement. The duration of the stabilising hold period is fundamental to measuring the restoring force corresponding to the target displacement. If the displacement measured on the specimen differs from the target displacement, the restoring force measured does not correspond to the target, introducing an error in the solution. The measuring hold period (ΔT_{h2}) following the stabilising, consenting to reduce the signal noise of the load cell by averaging a number of measures. This is important to avoid the introduction of random errors in the solution. Finally, during the computation hold period (ΔT_{h3}), the restoring force measured from the specimen is sent to the solver to calculate the next step. The duration of this period depends on the computation and communication time delay. The sum of the time delay of all the periods is the experimental time required to execute a single prototype step.

The Classical method is used for the PsD testing especially when using substructuring and distributed techniques. This is because the method accounting for the time delay in the computation and the communication between the controller and the remote processes. The disadvantage of the method resided in the force relaxation that may occur during the test when the displacement is held constant [51]. As a result, the measured restoring force does not correspond to the imposed displacement introducing an error in the solution.

2.3.4.2 Continuous method

In the Continuous method [16, 36, 52] the integration of a single step of the record requires the measuring and the computation hold periods, while the stabilising period and the ramp period are reduced to zero (see Figure 2.3.15). This is because the accelerogram is discretized using a linear interpolation, subdividing every time increment Δt into a selected number of internal substeps N_{int}.

The time delay in the experimental time T is given by the sum of the controller sampling period δT (typically of 2 ms) and the computation time period, which depends on the performances of the computer used to solve the equation of motion. If the integration algorithm is implemented in the controller, the time delay is given by the controller sampling period δT. In this way, the test is performed in a range of frequency of 500 Hz, in which the hydraulic system and the actuators are unable to respond. As a consequence, the missing periods of the ramp and stabilising are unnecessary. With this condition, the occurrence of the force relaxation during the test is reduced in comparison to the Classical Method.

The number of steps necessary to perform the PsD test using the Continuous test is greater than those computed using the Classical method. Nonetheless, the test duration is reduced due to the absence of the ramp and the stabilising hold periods.

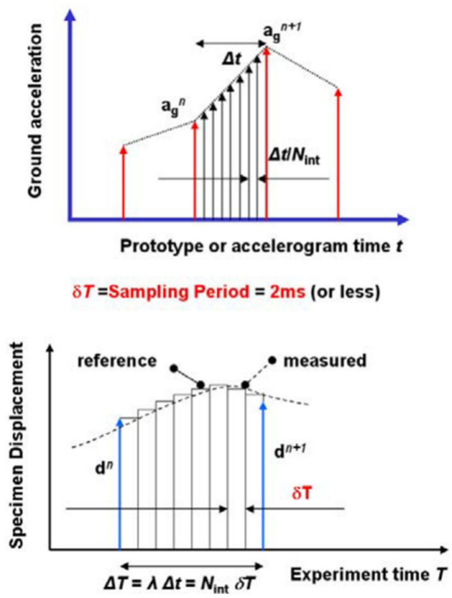

Figure 2.3.15 Continuous PsD method [36].

In addition, the use of an increment time of substeps, that is of the order of 2 ms, consent to always use an explicit algorithm without concern about the stability and accuracy of the method. In this way, the stability and the accuracy of the test depend exclusively on the time scale factor λ that regulates the test speed. This factor depends on the number of substeps N_{int} selected to discretize the time increment Δt (2.2):

$$\lambda = \frac{\Delta T}{\Delta t} = \frac{\delta T \cdot N_{int}}{\Delta t} \tag{2.2}$$

Based on the (**2.2**), the time scale λ increases when the number of substep increases while decreases when the number of substeps decreases. When λ is equal to 1 the test is performed in real-time (dynamic test).

The Continuous method can be used to perform PsD test also with substructure and distributed techniques. However, when the integration algorithm is implemented in a remote PC, the method does not account for the communication and computation time delay.

2.3.4.3 Substructure PsD testing

The Classical and the Continuous method are useful for PsD testing of a structural system physically realized in the laboratory. However, if the size of the specimen exceeds the laboratory dimensions or if the aim of the research is the investigation of the response of a component of the whole structural system, the substructuring technique must be used.

The pseudo-dynamic test with substructuring technique represents an advanced testing method that was implemented for the first time by Dermitzakis and Mahin [48] and subsequently has been widely used [53, 54]. Figure 2.3.16 shows a reference scheme of pseudo-dynamic testing framework with substructure.

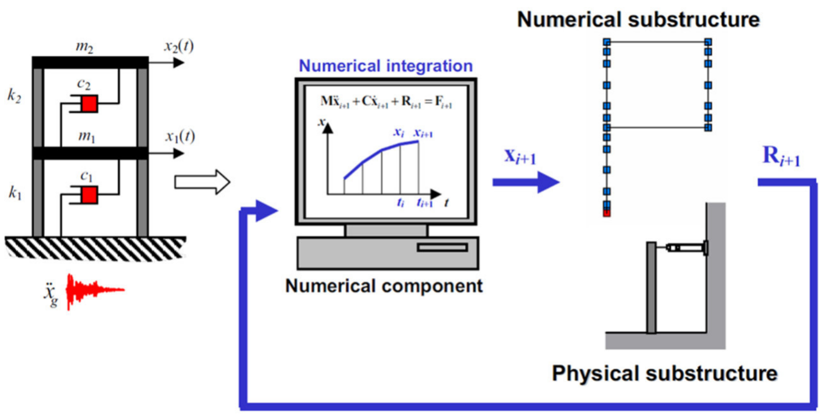

Figure 2.3.16. Pseudo-dynamic testing framework using substructuring technique [16].

The substructuring technique allows to test in the laboratory the physically portion that may experience the damage or the portion of research interest, while the response of the remaining part of the structure is numerically modelled. For instance, it is possible to physically test a full-scale reinforced concrete (RC) beam-column joint while the response of remaining part of the building is numerically simulated. The test starts with the computation through the resolution of the equation of motion of the target displacement to be imposed on the structure. The computed displacement is applied to the specimen through the hydraulic actuators and the corresponding restoring force is measured by the load cells installed on the actuators. At the same time, the displacement of the numerical DoFs is applied to the numerical model which allows determining the corresponding restoring force. At the end of the step, the restoring force obtained from the process is fed back to the algorithm in order to compute the target displacement at the next time step.

Figure 2.3.17. Experimental set-up of physical piers physically built in the laboratory [54].

Figure 2.3.17 shows the pseudo-dynamic test set-up on a large-scale model of an existing six-pier bridge performed using the substructuring technique at the European Laboratory for Structural Assessment (ELSA) of the Joint Research Centre (JRC) of European Commission [54]. Two physical piers were constructed in reduced scale and tested in the laboratory, while the deck, the abutments and the remaining four piers were numerically modelled. More details on the test set-up and the used substructuring technique are reported in Pinto et al. [54]. The pseudo-dynamic test with substructuring technique can be performed using the Classical method as well as the Continuous method. In addition, two different approaches can be followed to perform the test: the monolithic approach (see Figure 2.3.18) and the partitioned approach (see Figure 2.3.20).

2.3.4.4 Substructure PsD testing (monolithic approach)

In the monolithic approach, the integration algorithm for both the physical and the numerical substructures is implemented in the same process. This process, in which the time domain integration scheme of the physical substructure and the numerical substructure is the same, can be implemented in a remote PC, which sent to the controller the target displacement to be applied to the specimen while receiving from it the restoring force measured on the specimen (Figure 2.3.18, a), or in the controller (Figure 2.3.18, b).

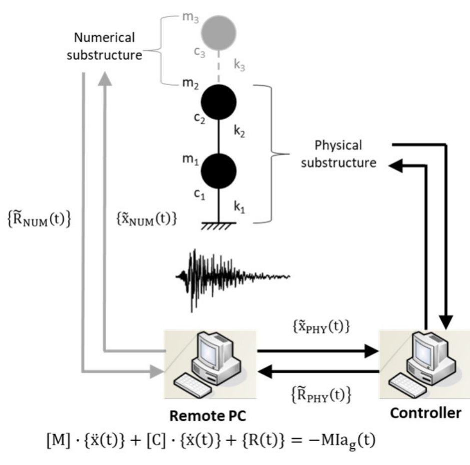

(a)

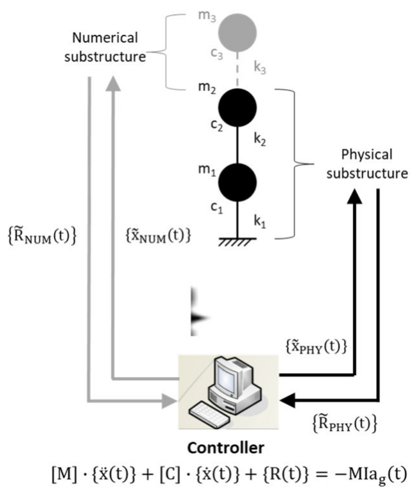

(b)

Figure 2.3.18. PsD testing with substructuring technique using a monolithic approach with process implemented in a remote PC (a) or in the controller (b).

The use of the Classical method is suggested when to perform the PsD test with substructuring is adopted, a monolithic approach in which the integration algorithm is implemented in a process running on a remote PC that communicates with the controller. This is because, the Classical method accounting for the computation hold period and the and communication hold period [36]. Instead, the use of the Continuous method is suggested when a monolithic approach with the integration algorithm implemented in a process running on the controller is used.

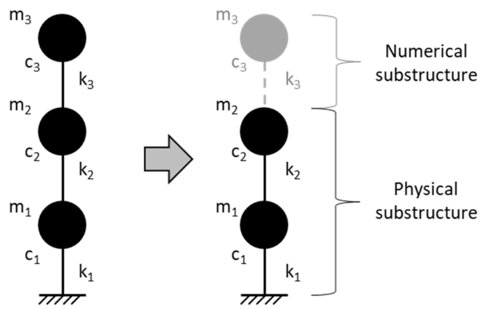

$$[M]\cdot\{a(t)\}+[C]\cdot\{v(t)\}+\{r(t)\}=-MIa_g(t)$$

Figure 2.3.19. Example of substructuring technique used to define the substructure's matrices in the monolithic approach.

In the case of the PsD test with substructuring techniques performed using the monolithic approach, the elements of the force vectors (inertial, viscous damping and restoring) of the system of equation (2.1) are obtained as the sum of the forces of the physical substructure and of the numerical substructure. For example, considering a linear system (Figure 2.3.19) with 2 DoFs physically built in the laboratory and 1 DoF numerically simulated (i.e., 3 DoFs in total), the result would be equivalent as having the mass matrix (2.3), the viscous damping matrix (2.4), and the stiffness matrix (2.5) assuming the following form:

$$[\mathrm{M}] = [\mathrm{M_{PHY}}] + [\mathrm{M_{NUM}}] = \begin{bmatrix} \mathrm{m_1} & 0 & 0 \\ 0 & \mathrm{m_2} & 0 \\ 0 & 0 & 0 \end{bmatrix} + \begin{bmatrix} 0 & 0 & 0 \\ 0 & 0 & 0 \\ 0 & 0 & \mathrm{m_3} \end{bmatrix} \tag{2.3}$$

$$[\mathrm{C}] = [\mathrm{C_{PHY}}] + [\mathrm{C_{NUM}}] = \begin{bmatrix} c_1 + c_2 & -c_2 & 0 \\ -c_2 & c_2 & 0 \\ 0 & 0 & 0 \end{bmatrix} + \begin{bmatrix} 0 & 0 & 0 \\ 0 & c_3 & -c_3 \\ 0 & -c_3 & c_3 \end{bmatrix} \tag{2.4}$$

$$[\mathrm{K}] = [\mathrm{K_{PHY}}] + [\mathrm{K_{NUM}}] = \begin{bmatrix} k_1 + k_2 & -k_2 & 0 \\ -k_2 & k_2 & 0 \\ 0 & 0 & 0 \end{bmatrix} + \begin{bmatrix} 0 & 0 & 0 \\ 0 & k_3 & -k_3 \\ 0 & -k_3 & k_3 \end{bmatrix} \tag{2.5}$$

2.3.4.5 Substructure PsD testing (partitioned approach)

The partitioned approach is the more complex of the presented approaches. It is used for the PsD test with substructuring technique where one or more degrees of freedom are solved using an integration algorithm implemented in a process running on a remote PC, that exchanges data with the controller during the test via a pre-defined protocol (Figure 2.3.20). The numerical substructure can be modelled using a simplified lumped mass system or a Finite Element Model (FEM) realized in a common modelling programme (e.g. OpenSees [55], SAP2000 [56], MATLAB [57], etc.). In the partitioned approach the time domain integration scheme of the structure is divided in two algorithms that belong to each substructure. The main challenge of this approach is to merge the algorithms of each substructure that are implemented in two parallel processes.

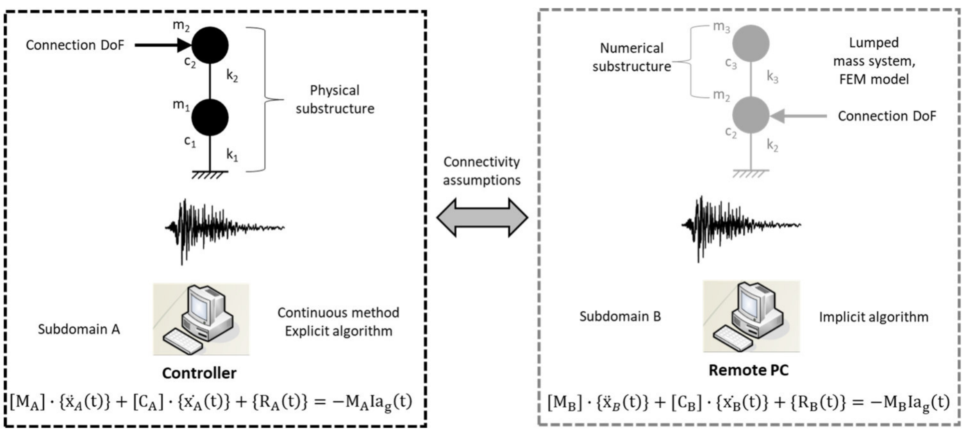

Figure 2.3.20. PsD testing with substructuring technique using a partitioned approach.

The algorithms corresponding to the substructures can be connected assuming certain conditions [36]. Various substructuring techniques have been used by many researchers for PsD testing of large structures using a partitioned approach. For reference, the studies by Nakashima [58], Shing and Mahin [59], Pegon [14], Mercan and Ricles [38], Kwon and Kammula [60], Reinhorn [61], Abbiati et al. [62] Tornaghi [63] and Kallioras [64] can be mentioned here. These studies show that the techniques adopted to perform the PsD test differ from one test to another, as the implementation of the substructuring techniques depends on the complexity of the tested structures and the configuration of the control system.

For the development of the pseudo-dynamic testing framework for the large structures laboratory of the Department of Structures for Engineering and architecture (DiSt) of University of Napoli Federico II, a simplified substructuring assumptions were preferred to more complex ones (e.g. hybrid simulations) in order to easily identify the source of possible errors in the PsD tests.

2.3.5 Integration algorithms

An integration algorithm is required for PsD testing to solve step-by-step the equation of motion (2.1) of the structure subjected to an acceleration history with a duration t divided in equal time increment Δt. Generally, the selected algorithms are based on the Newmark method [65]. In this method, the acceleration is assumed to vary with a predefined trend (e.g., constant, linear, quadratic, etc.) over the time increment. Starting from the knowledge of the displacement vector $\{x_i\}$, the velocity vector $\{\dot{x}_i\}$ and the acceleration $\{\ddot{x}_i\}$ at time step i, it is possible to calculate these vectors at time step $t_{i+1} = t_i + \Delta t_i$, according to (2.6) and (2.7):

$$\{x_{i+1}\} = \{x_i\} + \Delta t \cdot \{\dot{x}_i\} + \Delta t^2 \left[\left(\frac{1}{2} - \beta\right) \cdot \{\ddot{x}_i\} + \beta \cdot \{\ddot{x}_{i+1}\}\right] \tag{2.6}$$

$$\{x_{i+1}\} = \{\dot{x}_i\} + \Delta t[(1-\gamma) \cdot \{\ddot{x}_1\} + \gamma \cdot \{\ddot{x}_{i+1}\}] \tag{2.7}$$

where, β and γ are the Newmark integration parameters which govern the stability and the numerical damping (or dissipation) of the integration algorithm. The numerical damping can be introduced in the algorithm through the parameter γ: it is positive when γ is greater than 1/2 while it is negative with γ smaller than 1/2. When this parameter is assumed to be equal to 1/2 no numerical damping is introduced. This property of the Newmark methods is fundamental to continuously control the amount of numerical damping [66].

The introduction of a numerical damping is fundamental to damp out the presence of the spurious higher modes in the response that may affect the stability of the method. It is fundamental for PsD testing where the higher modes of the system are more sensitive to the experimental errors than the lower ones [67]. This is because the response of the lower modes of the system is much more accurately reproduced than the response of the higher modes. However, the introduction of numerical damping into the integration method leads to significantly reduction in the accuracy order of the method.

Depending on the value assumed for the integration parameters β and γ, the integration algorithm can be explicit or implicit. Assuming $\beta = 0$ and $\gamma = 1/2$ the Central Difference Method (CDM) is recovered. This method consents to calculate the displacement at the next step knowing the information on the previous and the current step according to (2.8):

$$
\begin{aligned}
\{x_{i+1}\} = \left[\frac{1}{\Delta t^2}[M] + \frac{1}{2\Delta t}[C]\right]^{-1} \Bigg[& \frac{2}{\Delta t^2}[M]\{x_i\} \\
& - \left(\frac{1}{\Delta t^2}[M] + \frac{1}{2\Delta t}[C]\right)\{x_{i-1}\} - \{R_i\} + \{F_i\}\Bigg]
\end{aligned}
\tag{2.8}
$$

The advantage of this method is that it is an explicit non-iterative method which automatically filtering out the integration any high-frequency noise present in the experimental tests (e.g., noise at the load cells). However, the method is conditionally stable and become unstable when the size of time increment is too large Δt. This is because the stability criterion of the method is based on the following expression (2.9):

$$\omega_0 \cdot \Delta t \leq 2 \tag{2.9}$$

where ω_0 is the highest natural angular frequency of the tested structural system. It is important to note that in the case of the PsD test performed using the Continuous method this integration algorithm is always stable, since the size of the internal substeps used to linearly interpolate the accelerogram is of the order of 2 ms.

The constant-average-acceleration method is recovered with $\beta = 1/4$ and $\gamma = 1/2$ [67, 16]. The method, implicit and unconditionally stable, requires any iterations to calculate the response at the next step. The use of an iterative procedure is not preferable for PsD testing due to the complexity of the method. Therefore, the presented method is not used as integration method.

Hilber et al. [66] proposed a modification of the Newmark method, introducing of a parameter α that control the amount of numerical damping without degrading the accuracy order of the method. The equation of motion valid for the proposed method is the following (2.10):

$$\begin{aligned}[M]\{\ddot{x}_{i+1}\} + (1+\alpha)[C]\{\dot{x}_{i+1}\} - \alpha[C]\{\dot{x}_i\} + (1+\alpha)\{R_{i+1}\} - \alpha\{R_{i+1}\} \\ = (1+\alpha)\{F_{i+1}\} - \alpha\{F_{i+1}\}\end{aligned} \tag{2.10}$$

where the displacement vector $\{x_{i+1}\}$ and the velocity vector $\{\dot{x}_{i+1}\}$ are given by the expressions (2.6) and (2.7), while α, β and γ are defined according to (2.11), (2.12) and (2.13):

$$\beta = \frac{1}{4}(1-\alpha^2) \tag{2.11}$$

$$\gamma = \frac{1}{2}(1-2\alpha) \tag{2.12}$$

$$-\frac{1}{3} \leq \alpha \leq 0 \tag{2.13}$$

The proposed method is unconditionally stable and provides a numerical damping controlled by the introduced parameter α. If this parameter is equal to 0 (i.e., $\beta = 1/4$ and $\gamma = 1/2$), the Constant-Average-Acceleration method is recovered. However, although the proposed method improves the previous method providing a second order of accuracy, it remains still iterative.

In order to implement the α-Newmark method proposed by Hilber et al. [66] without an iteration procedure, Nakashima et al. [68] and Combescure & Pegon [69] proposed an Operator Splitting (OS) method. The method is based on an approximation of the restoring force shown (see Figure 2.3.21) and based on the following expression (2.14):

$$\{R_{i+1}\} \approx \{\tilde{R}_{i+1}\} + [K_0] \cdot (\{x_{i+1}\} - \{\tilde{x}_{i+1}\}) \tag{2.14}$$

where $[K_0]$ is the stiffness matrix. With this approximation, the algorithm applies an implicit method for the elastic part of the response, without requiring any iteration, and an explicit method for the nonlinear part of the response. The stiffness matrix $[K_0]$ must be as close as possible to the elastic stiffness of the tested structure to guarantee the stability of the algorithm. In particular, the algorithm is unconditionally stable when the stiffness of the system is not greater than the initial elastic stiffness. In addition, the presence of the spurious higher modes in the response can be damp out through the numerical damping introduced by the parameter α.

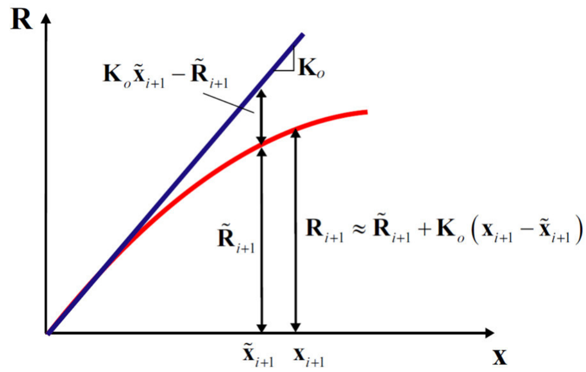

Figure 2.3.21. Operator Splitting method for PsD testing [16].

The implementation of the α-OS method for the PsD testing is presented in Figure 2.3.22. A preliminary test can be performed in the elastic range (to avoid the damage of the specimen) in order to identify the initial stiffness matrix $[K_0]$ [70] and the viscous damping matrix $[C]$ (generally considered null). The matrices can be identified, based on the results obtained from the preliminary test, using an identification model (e.g., linear regression, spatial model, filtered model, etc. [19, 70]). These methods will be presented in the paragraph regarding the experimental and control errors. Once the initial stiffness $[K_0]$ and the viscous damping $[C]$ matrices are known, it is possible to calculate the pseudo-mass matrix $\left[\widehat{M}\right]$ according to (2.15) :

$$\left[\widehat{M}\right] = [M] + \gamma\Delta t(1+\alpha)C + \beta\Delta t^2(1+\alpha)[K_0] \tag{2.15}$$

which is constant during the test (Figure 2.3.22). The test starts at step i+1 when the external force vector $\{F_{i+1}\}$ and the response at step i are known. It is worth remembering that the definition of the parameter α, β and γ is also required if the numerical damping must be introduced in the solution. At this point, it is possible to calculate the predictor (target) displacement vector $\{\tilde{x}_{i+1}\}$ to be imposed on the specimen in order to measure the restoring force vector $\{\widetilde{R}_{i+1}\}$ and the predictor velocity vector $\{\tilde{\dot{x}}_{i+1}\}$ according to (2.16) and (2.17):

$$\{\tilde{x}_{i+1}\} = \{x_i\} + \Delta t\{\dot{x}_i\} + \frac{\Delta t^2}{2}(1-2\beta)\{\ddot{x}_{i+1}\} \tag{2.16}$$

$$\{\tilde{\dot{x}}_{i+1}\} = \{\dot{x}_i\} + \Delta t\,(1-\gamma)\{\ddot{x}_{i+1}\} \tag{2.17}$$

The measured restoring force vector $\{\widetilde{R}_{i+1}\}$ is used in the expression (2.14) to compute the actual restoring force vector $\{R_{i+1}\}$. From this, it is possible to compute the pseudo-force vector $\{\hat{F}_{i+1}\}$ as following (2.19):

$$\begin{aligned}\{\hat{F}_{i+1}\} = (1+\alpha)\{F_{i+1}\} - \alpha\{F_{i+1}\} + \alpha\{\widetilde{R}_{i+1}\} - (1+\alpha)\{\widetilde{R}_{i+1}\} + \alpha[C]\{\tilde{\dot{x}}_{i+1}\} \\ - (1+\alpha)\{\tilde{\dot{x}}_{i+1}\} + \alpha(\gamma\Delta t[C] + \beta\Delta t^2[K_0]\{\ddot{x}_i\})\end{aligned} \tag{2.18}$$

in order to calculate the acceleration vector $\{\ddot{x}_{i+1}\}$ of the current step (2.19):

$$\{\ddot{x}_{i+1}\} = \{\hat{F}_{i+1}\}[\widehat{M}]^{-1} \tag{2.19}$$

The loop is concluded with the calculation of the corrector displacement vector $\{x_{i+1}\}$ (2.27) and the corrector velocity vector $\{\dot{x}_{i+1}\}$ (2.21) using the acceleration vector previously defined:

$$\{x_{i+1}\} = \{\tilde{x}_{i+1}\} + \Delta t^2\beta\{\ddot{x}_{i+1}\} \tag{2.20}$$

$$\{\dot{x}_{i+1}\} = \{\tilde{\dot{x}}_{i+1}\} + \Delta t\,(1-\gamma)\{\ddot{x}_{i+1}\} \tag{2.21}$$

Once the response at the step i+1 is defined, it is possible to proceed to the next step of the integration. More details about this method can be found in Combescure & Pegon [69].

The Central Difference method (CDM) and the α-Operator Splitting (α-OS) method are the most widely used for the PsD testing between the method available in the literature. On the one hand, the CDM method, which require low computational costs while filtering out the high-frequency noise present in the experimental tests, is always used when the stability of the method is guaranteed (i.e., time increment Δt with small size). This condition is ensured for example when the Continuous method is used for the PsD testing. On the other hand, when the size of the time increment becomes large and the stability of the CDM is not guaranteed PsD test, the α-OS is used. In addition, if the substructuring techniques is required to perform the PsD tests, the use of α-OS is useful to damp out the response of spurious higher modes through the numerical damping introduced by the parameter α.

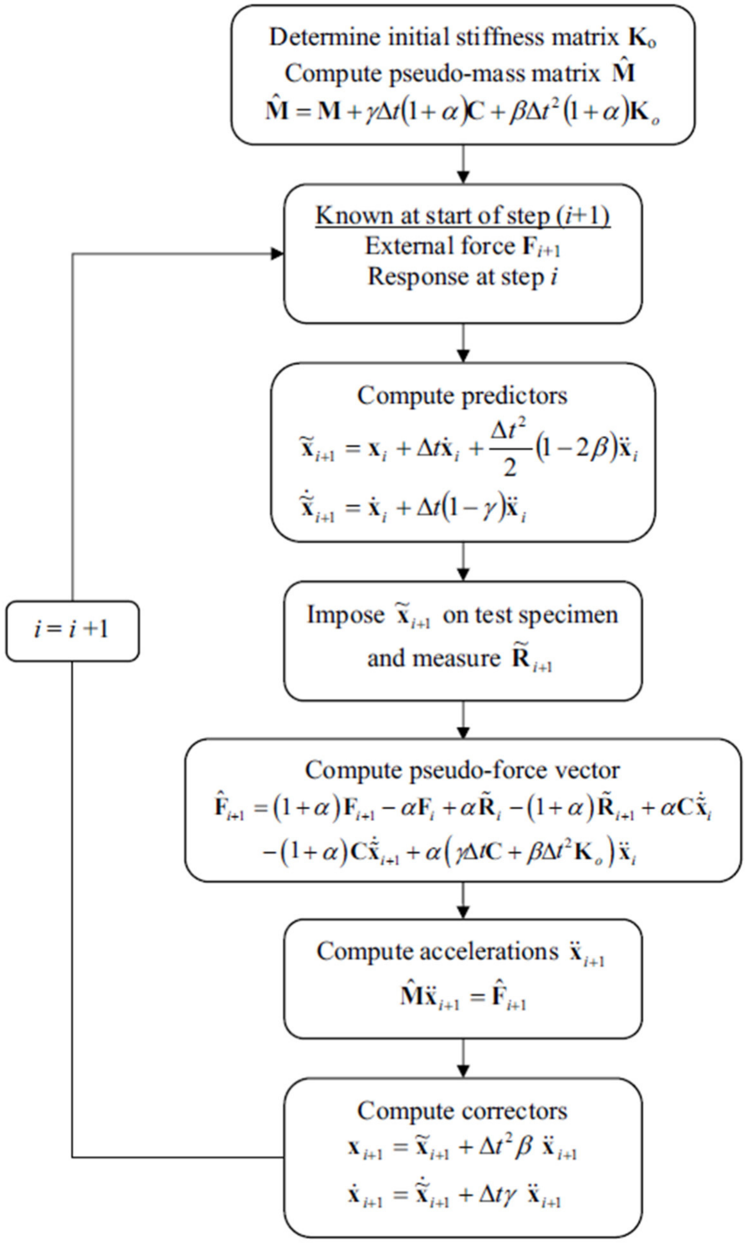

Figure 2.3.22. Implementation of the **α**-OS method for the PsD testing [16].

2.3.6 Experimental and control errors

The pseudo-dynamic testing method is used to reproduce the dynamic effects of a selected earthquake on a tested structural system. The method allows to test a whole structural system or subassemblies in reduced or full scale. However, the assessment of the reliability of the test is required to investigate the presence of errors generated from various sources that can enter in the structural response invalidating the test outcomes. Different error sources are identified by many researchers [67, 70, 19, 51, 46] studying the reliability of the PsD testing method: the modelling and numerical errors, the experimental errors and the control errors.

The modelling errors, resulting from the assumptions considered in the modelling of the tested specimen. The specimen, which is generally consists of a continuous mass system, is usually discretized using an idealized lumped mass system. In addition, an equivalent viscous damping is modelled when it is necessary to reproduce the strain-rate effects of missing devices or structural mechanisms that cannot be reproduced by the PsD testing method. On the other hand, the numerical errors result from the discretization of the system of the equation of motion (2.1) with respect to the time domain and the resolution of this system as differential equations. However, the amplitude of the errors resulting from these simplifications is acceptable and does not lead to a distortion of the structural response.

The experimental errors are directly related to the characteristics of the test set-up. The erroneous installation, the erroneous calibration, the precision, and the accuracy of the transducer used to feedback the measured displacement and the restoring force, the high-frequency noise in experimental measurement, the presence of clearance in the actuator-structure connection, are just some of the possible sources that can introduce errors in the structural response. The experimental errors can be made less important than the control errors by improving the performance of the test set-up facilities or by regular maintenance. In addition, using the numerical damping provided for some integration algorithms the high-frequency noise in the measurement can be damp out.

The control errors have a greater influence on the experimental response. These errors are defined as the difference between the computed (target) displacement and the measured displacement. They generally depend on the working frequencies and amplitude, the specimen type, the hydraulic actuators, the transducers, and the control system including the control algorithm and its parameters [19].

The control errors occur when the displacement imposed (measured) on the specimen is different to the computed (target) displacement. As a result, the measured restoring force does not correspond to the computed displacement introducing an error in the structural response. As a simplification, the difference between the computed displacement and the measured displacement could be delay or an anticipation [70, 51, 19]. Figure 2.3.23 shows the effects of control errors on the response of an elastic system with a single degree of freedom. The black straight line represents the measured response of the system while the sinusoidal red line represents the command response. A delay in the control system, generates a counterclockwise hysteresis (see Figure 2.3.23, a), which adds energy to the structural response (without some physical meaning). In contrast, if the control system is in advance, the error is positive (the imposed displacement is greater than the computed displacement), generating a clockwise hysteresis and the energy is absorbed by the structure (see Figure 2.3.23, b).

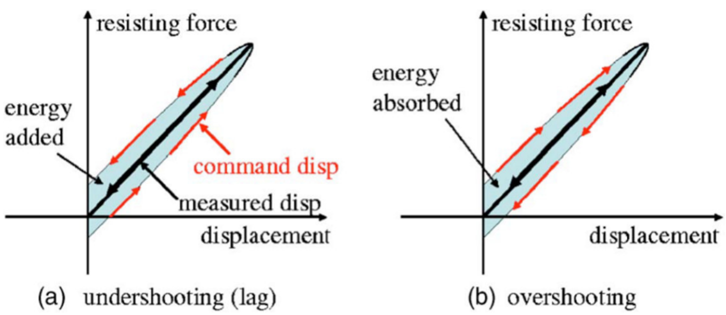

Figure 2.3.23. Effects of the control errors on the structural response: (a) restoring force delay; (b) restoring force anticipation [51].

In PsD test performed using the Classical method, the control errors can be also occur during the alternation of the ramp hold period and the stabilising hold period (i.e., force relaxation). The introduction of errors can be reduced using the Continuous method in which these hold periods are reduced to zero. The present study will be discussed with reference to the Continuous method.

Assuming that the other sources of error are negligible and the Continuous method is used for PsD testing, the consequences of control errors are larger at larger testing speed (depending on the scale factor λ) and depending on the calibration of the gain parameters of the Proportional-Integrative-Derivative algorithm (PID) [43]. In particular, the proportional and the integrative gain parameters significantly influence the stability and the accuracy of the control system while the derivative gain parameter is generally defined equal to 0. The time scale factor λ control the speed of the execution of the test. The control errors related to the testing speed and the PID gain parameters introduce a frequency and damping distortion that could bring the response to become unstable even with a stable control.

Preliminary PsD test performed in the elastic range using a low intensity accelerogram record, are fundamental to investigate the effects on the control system of the control parameters as well as their limit range. In this way, it is possible to define the optimal set of these parameters. At every attempt, the PID parameters must be chosen by a compromise between accuracy and stability of the control [71] while the time scale factor λ must be chosen in order to allow during the test the possibility to observe the response performing the test in safety conditions. The results of the test are used to assess the frequency and the damping distortion in the structural response using an identification method. The optimal set of control parameters is defined as the set of control parameters for which the control errors amplitude assessed during the preliminary tests is acceptable. In addition, the defined set of parameters should guarantee the reliability of the PsD test also at higher intensities due to the reduction of the frequencies related to the specimen degradation. However, at larger amplitudes, the control system may show non-liearities that can introduce larger errors in some cases as, for example, when servo-valves get closer to saturation.

The presence and amplitude of control errors in the response can be monitored in real-time during the test or assessed at the end. In particular, the comparison between the absorbed energy and the energy error calculated at each integration step allow to monitor the errors during the test, while the frequency and damping distortion affecting the response can be assessed based on the test results using an identification method. Among these, the Spatial model and the Filter model are here presented [19].

2.3.6.1 Evaluation of the Energy Error

The energy absorbed by the structure during the test can be computed from the measured restoring force R and the measured displacement x as (2.22):

$$E = \int R \cdot dx \tag{2.22}$$

or from the measured restoring force R and the computed displacement x_m (2.23):

$$E_m = \int R \cdot dx_m \tag{2.23}$$

The difference between the (2.22) and (2.23) represent the energy error ΔE calculated as follows (2.24):

$$\Delta E = E_r - E = \int R \cdot dx_m - \int R \cdot dx = \int R \cdot d(x_m - x) = \int R \cdot d\varepsilon \tag{2.24}$$

The comparison between the (2.22) and the (2.24) provide a global indicator of significant damping distortion introduced by the control errors. Based on the experience gained from the several tests performed during the years, the authors recommend that for an acceptable quality of the test results, the energy error should not exceed, say, a 5% of the total absorbed energy at any moment [17]. In addition, as suggested before, a preliminary test performed in elastic range using a low intensity accelerogram record is fundamental to verify the presented criterion and to define the optimal set of the control parameters.

2.3.6.2 Spatial model for Identification of Response frequency and damping

An equivalent linear model is considered to identify the stiffness and the viscous damping matrices using the Spatial model [72]. The identification is based on a short window of the measured restoring forces, the measured displacements and the computed displacement selected from the experimental results. This model, assumes that the restoring force, the displacement and the corresponding velocity are linked for every discrete time n of the original acceleration record, according to (2.25):

$$R(n) = K \cdot x(n) + C \cdot \dot{x}(n) + o \tag{2.25}$$

Where $R(n)$, $x(n)$, and $\dot{x}(n)$ are the results of the test, K and C are the unknown matrices and o is an unknown vector of residual forces. In this case, the velocity $\dot{x}(n)$ is evaluated as differentiation of the displacement $x(n)$. The expression (2.25) can be rewritten as follows (2.26):

$$\begin{bmatrix} x^T(n) & \dot{x}^T(n) & 1 \end{bmatrix} \cdot \begin{bmatrix} K^T \\ C^T \\ o^T \end{bmatrix} = R^T(n) \tag{2.26}$$

The minimum number of discrete-time data sets N required for the identification is based on the number of DoFs (n_{DoF}) of the structure.

Considering that K, C and o contain $2n_{DoF}^2 + n_{DoF}$ unknown elements and the number of available equations is Nn_{DoF}, the minimum number of discrete-time data sets N is (2.27):

$$N \geq 2n_{DoF} + 1 \tag{2.27}$$

The matrices K and C and the vector o can be estimated using a least squares solution. Once they are defined, the complex eigenfrequencies and mode shapes can be obtained by solving the generalized eigenvalue problem (2.28) [72]:

$$s\begin{bmatrix} C & M \\ M & 0 \end{bmatrix}\varphi + \begin{bmatrix} K & 0 \\ 0 & -M \end{bmatrix}\varphi = 0 \tag{2.28}$$

where M is the theoretical mass matrix of the structure. The complex conjugate eigenvalue couples can be evaluated according to (2.29):

$$s_i, s_i^* = \omega_i\left(-\zeta_i \pm j\sqrt{1-\zeta_i^2}\right) \tag{2.29}$$

where ω_i is the natural frequency and ζ_i the damping ratio. The corresponding ith mode shape is also given by the first n_{DoF} rows of the associated eigenvector φ. For the assessment of the effects of the control errors on the structural response, the identification process is repeated for two sets of variables. The first set is constituted by the measured restoring forces, the measured displacements and derived velocities, while the second set is constituted by the measured restoring forces, the computed displacements and derived velocities. The stiffness and the viscous damping identified using the first set of parameters are considered the real ones of the specimen not affected by the control errors, while those identified using the second set may provide a distortion in the structural response. The difference between the frequency and the damping ratio identified with the defined sets of variables using the Spatial model characterizes the errors introduced in the response by the control system. More details about the Spatial model for the identification of frequency and damping distortion can be found in [19].

2.3.6.3 Filter model for Identification of Response frequency and damping

The Filter model is used as an alternative to the Spatial model for the testing method in which the restoring force cannot be measured [19], such as for shaking table test or dynamic snap-back test. Considering a system with $x(n)$ the input and $y(n)$ the output, the filter model of orders p and q can be defined using the constant-coefficient difference equation [73]:

$$y(n) = a_1 y(n-1) + \cdots + a_p y(n-p) + b_0 x(n) + \cdots + b_q x(n-q) \tag{2.30}$$

This equation will be adapted for a system containing n_{in} inputs (2.31):

$$x^T(n) = \left[x_1(n) \cdots x_{n_{in}}(n)\right] \tag{2.31}$$

and n_{out} outputs (2.32):

$$y^T(n) = \left[y_1(n) \cdots y_{n_{out}}(n)\right] \tag{2.32}$$

formulating the matrix equation (2.33):

$$y^T(n) = [y^T(n-1) \cdots y^T(n-p)] \begin{bmatrix} A_1 \\ \vdots \\ A_p \end{bmatrix} + [x^T(n) \cdots x^T(n-q)] \begin{bmatrix} B_0 \\ \vdots \\ B_q \end{bmatrix} + o^T \qquad (2.33)$$

in which a constant offset term o has been added. The defined filter model may be estimated from the input and output data at N time instants if the number of the equation is equal or larger than the number of the unknown coefficients (2.34):

$$n_{out}(N - \max(p,q)) \geq n_{out}(pn_{out} + (q+1)n_{in} + 1) \qquad (2.34)$$

or equivalently, if (2.35):

$$N \geq pn_{out} + (q+1)n_{in} + 1 + \max(p,q) \qquad (2.35)$$

The unknown coefficients can be estimated using the least squares method applied to (2.33).

After that, by setting to zero every input and offset in (2.33), the free response of the system is defined as (2.36):

$$y^T(n) = [y^T(n-1) \cdots y^T(n-p)] \begin{bmatrix} A_1 \\ \vdots \\ A_p \end{bmatrix} \qquad (2.36)$$

or, in order to obtain natural frequencies and mode shapes (2.37):

$$[\mathrm{y^T(n)}\ \ \mathrm{y^T(n-1)} \cdots \mathrm{y^T(n-p+1)}] = [\mathrm{y^T(n-1)} \cdots \mathrm{y^T(n-p+1)}\ \ \mathrm{y^T(n-p)}] \begin{bmatrix} A_1 & I & & \\ \vdots & & \ddots & \\ A_{p-1} & & & I \\ A_p & 0 & \cdots & 0 \end{bmatrix} \tag{2.37}$$

This expression can be written as (2.38):

$$\mathrm{Y^T(n)} = \mathrm{Y^T}(n-1)A^T \tag{2.38}$$

or, by successively transposing, recursively substituting, and eigenvalue decomposing:

$$\mathrm{Y(n)} = \mathrm{AY(n-1)} = \mathrm{A^nY(0)} = \mathrm{V\Lambda^nV^{-1}Y(0)} \tag{2.39}$$

where:

$$\Lambda = \mathrm{diag}\{\lambda_1 \cdots \lambda_{\mathrm{pn_{out}}}\} \tag{2.40}$$

contains the eigenvalues of A (poles of the filter) and V contains the eigenvectors. In this form, the conjugate couples of poles contained in (2.40) can be evaluated as (2.41):

$$\lambda_{\mathrm{i}}, \lambda_{\mathrm{i}}^* = e^{\omega_{\mathrm{i}}\left(-\zeta_{\mathrm{i}} \pm \mathrm{j}\sqrt{1-\zeta_{\mathrm{i}}^2}\right)\Delta t} \tag{2.41}$$

Where ω_i and ζ_i are the associated natural frequencies and damping ratio. The corresponding ith mode shape is given by the first n_{out} rows of the associated eigenvector φ. For this method, even if the number of input variables has to be complete, the number of output variables can differ to the number of DoFs of the tested system. The order of filter is generally set equal to 2, i.e., p = q = 2. However, the authors recommend a higher-order of filter model when the number of the DoFs is larger than the number of outputs or if some spurious harmonics coming from nonlinearities or noise need to be discriminated. More details about the Filter model for the frequency and damping distortion identification can be found in [19].

2.4 Distributed and Hybrid testing

In the case of complex structural systems, the distributed substructure and hybrid PsD testing allows to perform a test connecting on-line a laboratories group that are geographically located in different sites to facilitate the collaboration between them. The facilities required to perform this test are the same of those seen in the PsD test. In addition, a laboratory network must be realized to connect the different sites involved to perform the test.

The distributed substructure technique was used for the first time by Watanabe et al. [49] to perform a parallel pseudo-dynamic seismic loading test on elevated bridge system through the internet between the Japan and Korea. With this technique, it is possible to test a structural system in which a portion of structure is tested in a laboratory equipped to perform a PsD test, while another portion of the structure is contemporary tested in a laboratory equipped to apply a thermal load for example. Otherwise, the remaining portion of the structure can be also numerically simulated with a hybrid simulation using a software package from a site without laboratory. In this way, the distributed and hybrid PsD testing allows to use the devices that are provided in the other laboratories while allows to use the laboratory located in another site by an institution without laboratory.

To date, several laboratories initiated a research project to create a laboratories network that allow to perform distributed tests. For instance, the U.S. federal government provided a commitment to the advancement of earthquake engineering research within the George E. Brown, Jr. Network for Earthquake Engineering Simulation (NEES) initiated by the National Science Foundation (NSF) [42]. The objective of the program was to develop a network of advanced integrated and interconnected facilities to transform earthquake engineering research so that it relies on the integration and coordination of experimentation, computation, and model-based simulation. Through NEES, fifteen geographically distributed laboratories (see Figure 2.4.1) are integrated and interconnected through Internet2 to facilitate collaboration and to readily make these resources available to institutions that otherwise do not have access to experimental facilities.

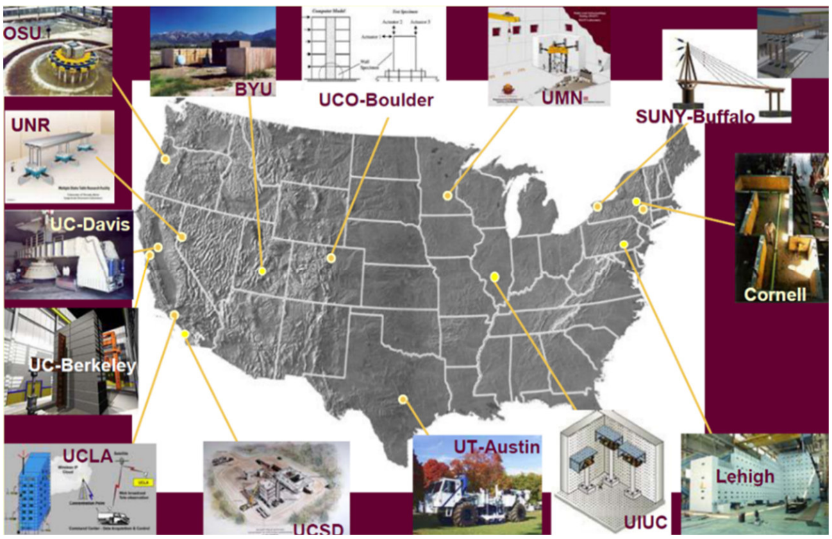

Figure 2.4.1. Geographical distribution of fifteen NEES equipment sites [42].

With regard to the software packages used for the distributed and hybrid testing, the UI-SIMCORE [74] and the OpenFresco [75] are the most known in the research field to perform this kind of test. Figure 2.4.2 shows a distributed test performed of a bridge using the UI-SIMCORE with the Multi-Site Soil-Structure-Foundation Interaction Test (MISST) project.

The bridge was divided into three modules; (i) left pier, (ii) deck and middle pier, and (iii) right pier as shown in Figure 2.4.2 (a), (b) and (c), respectively. For the purposes of testing the developed framework, the left pier, Figure 2.4.2

(a) was tested using physical experiment, while two piers and soil foundation were at three NEES sites and the deck and middle column were numerically simulated.

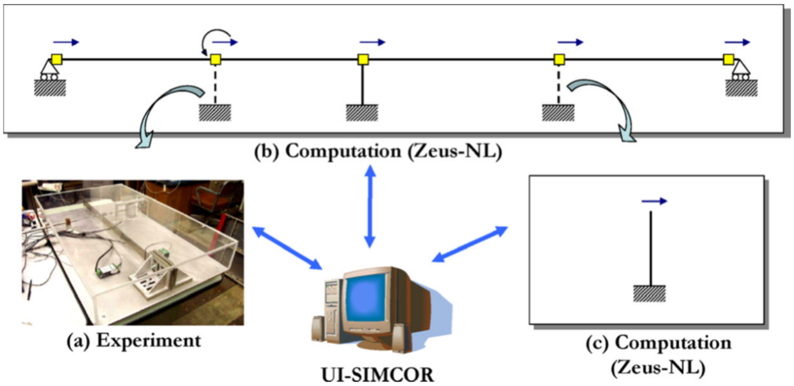

Figure 2.4.2. An example of distributed test performed using the UI-SIMCORE software packaging [74].

Both UI-SIMCORE and Openfresco, allow hybrid simulations to be performed using a wide variety of computational software commonly used in research field (e.g. Opensees, Matlab, Abaqus etc.). In addition, OpenFresco and UI-SIMCORE can be used together to perform hybrid simulation as an interface that enables the communication between them is implemented in both software packages.

Chapter 3

3. Pseudo-dynamic (PsD) testing infrastructure and code implemented at UNINA

In the last decade, the Department of Structures for Engineering and Architectures (DiSt) at the University of Napoli Federico II invested many resources to enable researchers to conduct quasi-static [9, 6] and dynamic shaking table tests [11]. However, the limitation in the payload of the tables to 20 tons, does not allow to conduct full-scale tests on multistorey RC buildings. To overcome this limitation and enable researchers to perform full-scale test on large prototypes, a research infrastructure consisting in a RC strong wall and strong floor was built in the Center of Advanced Measurement Services (CeSMA) and it is managed by the DiSt [76]. It has been recently equipped with a PsD testing framework, which has been numerically and experimentally validated.

In this chapter, the laboratory environment is presented together with the facilities, the devices and the instrumentation. Furthermore, the control system and the implemented PsD testing framework is presented, with emphasis on the features implemented in the control system and on the code developed in-house to carry out PsD tests.

3.1 The CeSMA-UNINA laboratory environment

3.1.1 Facilities

The CeSMA laboratory of testing on real-scale structures for large-scale test at University of Naples Federico II, is an indoor laboratory with a floor area about 260 m^2. It is equipped with an L-shape reaction wall 7.25 m high, 12.40 m long and 1.80 thick and with a strong floor. A plan view of the reaction wall is shown in Figure 3.1.1.

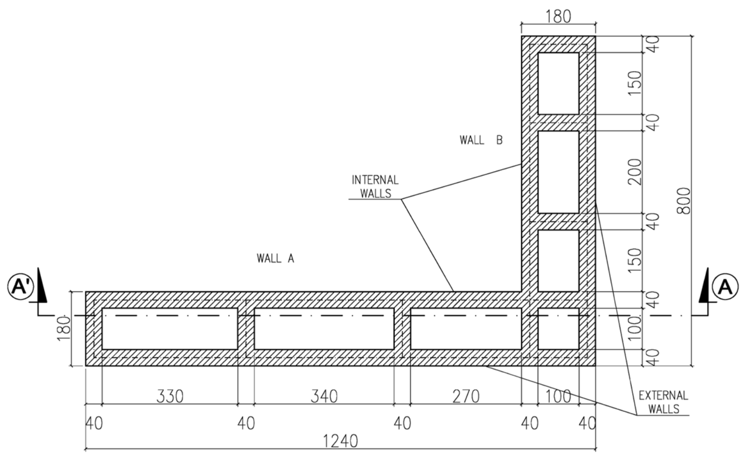

Figure 3.1.1. Reaction wall plan view.

The reaction wall has a hollow cross-section made of cast-in-place reinforced concrete with post-tensioned bars to improve its strength and stiffness. The base of the wall is connected to the existing foundation and the reinforced concrete walls belonging to strong floor (see Figure 3.1.2). It is designed to sustain a maximum load of 1500 kN at 6.3 m of height and 800 kN at 3.0 m of height, both in tension and in compression. An anchor hole grid with a hole diameter of 0.06 m and spacing of 0.60 m is realized on the wall to allow the installation of the testing set-up (e.g., steel plates, actuators, frames). The strong floor has a hollow cross-section made of reinforced concrete to be accessible. The thickness of the upper and the bottom slab (foundation) are 0.50 m and 1.20 m, respectively. The interstorey height is 2.40 m while the spacing between the RC walls ranges from 2.40 m to 2.80 m. An anchor hole grid is also provided for the strong floor, with a hole diameter of 0.10 m and spacing of 1.90 m in the direction orthogonal to the reaction wall and 1.25 m in the direction parallel to the wall.

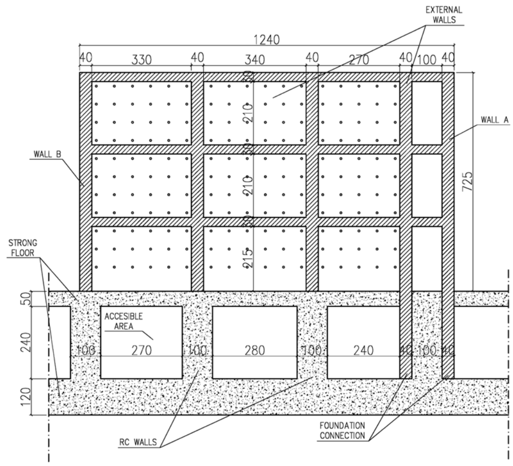

Figure 3.1.2. Reaction wall A-A' section.

Figure 3.1.3 shows a picture of the reaction wall and the strong floor before the implementation of the PsD testing framework.

Figure 3.1.3. Reaction wall and strong floor before the implementation of the PsD testing framework.

To guarantee an adequate working pressure to the hydraulic actuators and jacks during the test, the laboratory is equipped with an electric oil pumping system consisting of two hydraulic pumps (Figure 3.1.4, a). The maximum allowable oil flow is of 200 l/min at a working pressure of about 210 bars. The oil temperature is controlled by means of a cooling tower located outside the laboratory (Figure 3.1.4, b).

(a)

(b)

Figure 3.1.4. (a) oil pumping system; (b) water cooling unit.

Steel pipes, located under the strong floor, connect the oil pump with the two manifolds positioned on the strong floor (Figure 3.1.5, a).

(a)

(b)

Figure 3.1.5. (a) Oil pumping system manifold; (b) electrical cabinets.

The manifolds allow to connect the actuators with the pumping system by means of flexible pipes. The pumping system is connected to the control system to allow the automatic management of the oil pressure and to interrupt the oil flow in case of emergency or system interlock. In addition, a crane of 10 tons lifting capacity and different electrical sockets (Figure 3.1.5, b) serve the area.

3.1.2 Device and instrumentation

The device and instrumentation available in the CeSMA laboratory allow to conduct large scale tests. In particular, four ITALSIGMA hydraulic actuators and one MTS hydraulic actuator are available in the laboratory to apply the horizontal load. Figure 3.1.6 shows a picture of the ITALSIGMA hydraulic actuator. Two ITALSIGMA actuators are installed on the reaction wall at 3.4 m and 6.5 m of height, corresponding to the typical interstorey height of the existing RC buildings. A steel hinge installed at both ends, allow to connect the actuator to the specimen and the steel plate installed on the reaction wall. Each actuator has a total load capacity of 1200 kN and a total stroke of 750 mm. It is equipped with a load cell and an internal displacement transducer to measure the applied force and displacement.

Figure 3.1.6. ITALSIGMA hydraulic actuator for horizontal load application.

An MTS actuator is also installed on the reaction wall in a different position, at a height of 2.9 m, to apply the horizontal load on a bench test set-up. Figure 3.1.7 shows a picture of the actuator on the reaction wall. It has a steel hinge installed at both ends that allows to connect the actuator to the specimen and to the reaction wall. The actuator has a capacity of 364 kN in compression and 240 kN in tension and a total stroke of 500 mm. It is equipped with a load cell and an internal displacement transducer to measure the applied force and displacement.

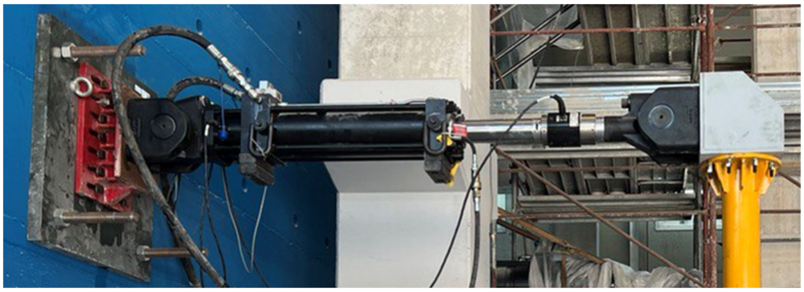

Figure 3.1.7. MTS hydraulic actuator for horizontal load application.

The vertical (or axial) load is applied by means of two BOVIAR hydraulic jacks reported in Figure 3.1.8. They have a total load capacity of 750 kN and a total stroke length of 300 mm. At the top end, it is equipped with a load cell, on which a steel hinge can be positioned, while at the bot end a steel plate with a pre-defined holes consent to install the hydraulic jack on the specimen. Generally, the load is applied in force control and kept constant during the test.

Figure 3.1.8. BOVIAR hydraulic jacks for the application of the vertical load.

The displacement imposed to the specimen is monitored during the test using a Temposonics displacement transducer. It is a high-precision sensor with profile extrusion housing that provides a captive-sliding magnets which utilize slide bearings of special material that reduce friction, and help mitigate dirt build up. Figure 3.1.9 shows the characteristics of the sensor with the reference dimensions.

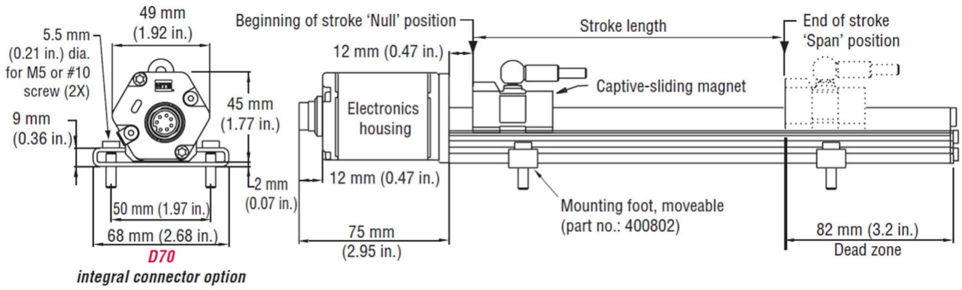

Figure 3.1.9. Temposonics R-Series Model RP Profile-style sensor dimension reference.

Two of them with a stroke length of 750 mm and a resolution of 0.5 µm are available in the laboratory environment. The transducers are generally installed on a reference frame (or structure) provided for the test set-up to perform PsD tests (Figure 3.1.10).

Figure 3.1.10. Temposonics transducer installed on a reference frame and connected to the specimen.

To monitor global and local deformations on the specimen and strain on internal reinforcements, high precision LVDTs, classic LVDTs, strain gauges, and potentiometers are used. Figure 3.1.11 shows the HBM QuantumX data acquisition system used to record the measured data. It is based on EtherCAT technology and provides 32 channels for connecting LVDTs, laser transducers, accelerometers, inclinometers and potentiometers and further 16 channels for connecting strain gauges. The system allows to start the acquisition independently or simultaneously to the control system using a pre-defined trigger implemented in the controller.

Figure 3.1.11. HBM Quantum X data acquisition system.

3.2 The developed pseudo-dynamic testing framework

Figure 3.2.1 shows the PsD testing framework developed in the CeSMA laboratory to enable researchers to perform full-scale test on large prototypes. It consists of an electronic-based control system (B) allowing the communication between the system coordinator (A) and the physical specimen (C). The coordinator system (A) is a Matlab [57] code consisting of an input suite, integration algorithm to solve the equation of motion, communication suite (sending and receiving data to/from the control system (B)), and a real-time output interface. The α-OS Splitting Method algorithm [69] is used to perform the PsD tests in the laboratory of CeSMA. The interface for the input definition allows to define the mass matrix $[M]$, the initial stiffness matrix $[K_0]$, the initial and boundary conditions (B.C.), the numerical algorithm parameters α (to introduce a numerical damping), the viscous damping ζ, and the acceleration history $\ddot{x}_g(t)$ with its scaling factor (S.F.) and time increment Δt. Among these, the viscous damping plays a crucial role in the stability of the control system and in the accuracy of the results.

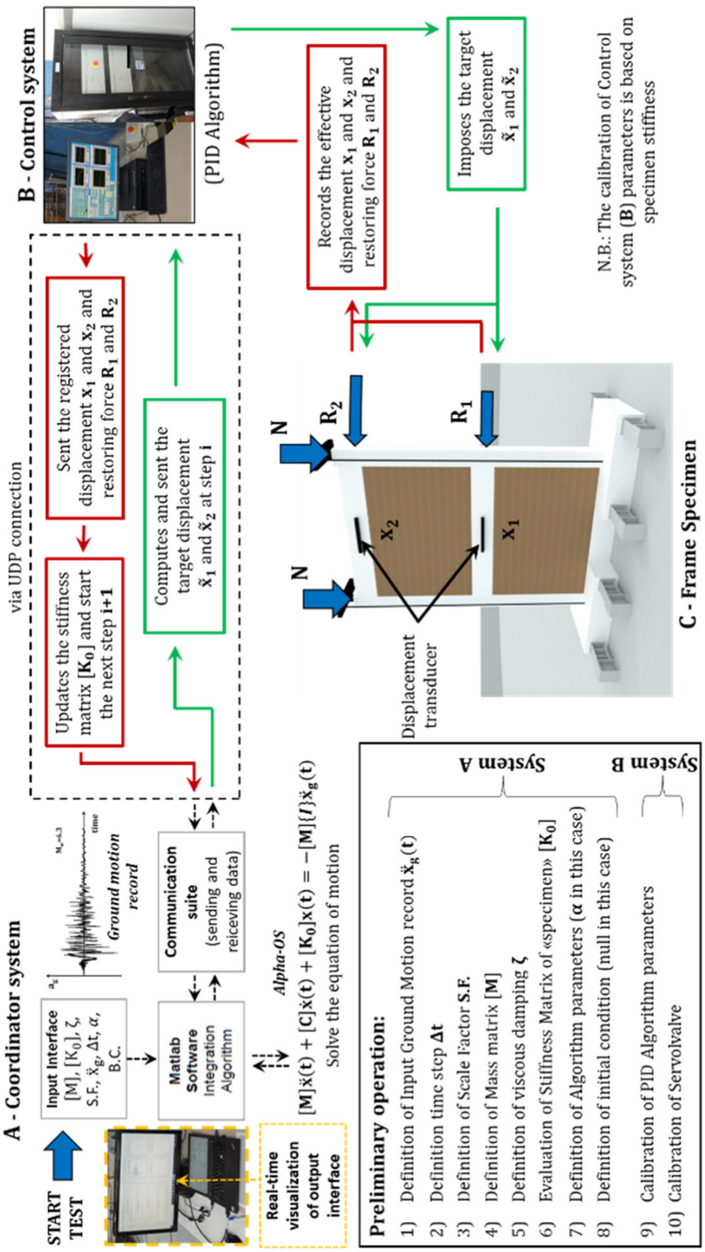

Figure 3.2.1. Pseudo-dynamic testing framework implemented in the CeSMA laboratory.

This parameter should be properly selected to balance between the accuracy and the stability of the tests [19]. The real-time visualization of output interface allows to visualize the displacement imposed at each DoF, the control errors and the interstorey shear-displacement hysteresis during the test.

The control system (B) consists in the controller and a personal computer. It allows to manage input/output, the gain parameters, the interlocks and the data recorded during the tests by means of a real-time graphical user interface. A Proportional Integrative Derivative (PID) algorithm [43] is used to guarantee a real-time direct control of actuators. A Hardware-in-the-loop (HIL) interface has been developed in the controller to communicate, via an UDP connection, with the coordinator system (A) for the specific purpose of conducting PsD tests.

In the preliminary phase of tests, the definition of some parameters and boundary conditions is needed to have accurate and reliable results as-well-as to guarantee the stability of the control. In particular, the calibration of the gain parameters of the PID algorithm and of the servo valve of the actuators is needed at each stage of the test. This is because they depend on the initial stiffness of the specimen. After definition of the input variables and calibration of the gain parameters of each actuator in the selected control mode, the connection between coordinator (A) and control systems (B) can be established. In particular, the connection is established after the vertical load (N) has been applied using the hydraulic jacks. It is kept constant during the test and is not controlled by the coordinator system (A). This is because the control system receives from the coordinator system only the displacements to be imposed to the specimen.

The adopted PsD testing procedure, in which the Classical (or step) method is used, is summarized in Figure 3.2.2. A data acquisition system (D) is also provided to measure the global or local deformation of the specimen. At the first step, the coordinator system, based on the acceleration input, $\ddot{x}_g(t)$, solves the equation of motion, computes the target displacements $\tilde{x}(t)$ and sends them to the control system using the communication suite. The target displacements $\tilde{x}(t)$ are applied to the specimen by the actuator and controlled by means of displacement transducers. After application of displacements, i.e., ramp and stabilising hold periods, the system measures the actual displacement and corresponding restoring force at the DoF by means of displacement transducers installed on the specimen (Figure 3.2.2) and load cells installed on the hydraulic actuator.

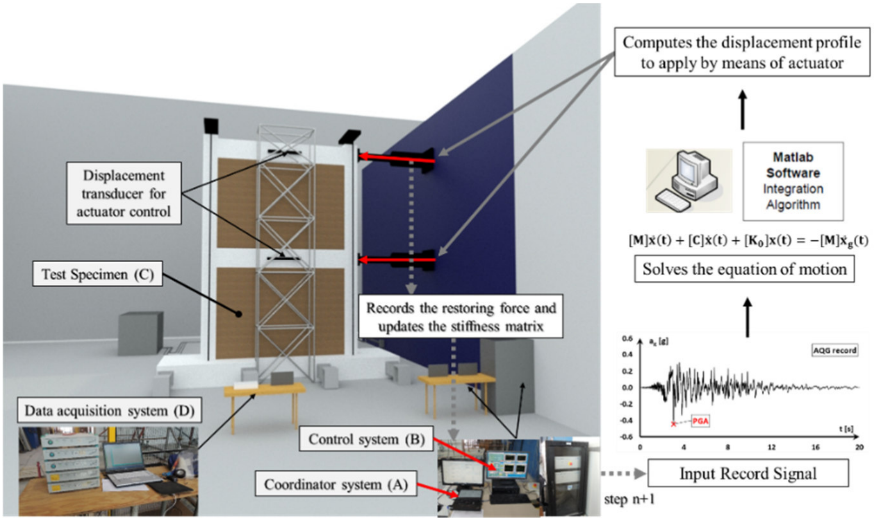

Figure 3.2.2. Classical PsD testing method implemented in the CeSMA laboratory.

The measured quantities are acquired by the control system and sent to the coordination system and processed by the integration algorithm. This allows to compute the target displacements at the following step accounting for the stiffness degradation and for the progressive damage of the tested specimen. The duration of the test depends on the load application ratio (or set point rate), on the intensity of the record, on the size of the calculated displacement increment sent as set point to the controller and on the length and the time step Δt selected for the accelerogram record $\ddot{x}_g(t)$. In particular, the tests with an intensity of the record of 10% and 25% have a length between 50 min and 100 min, the test with an intensity of 50%, 75% and 100%, has a length between 100 min and 170 min and the test with an intensity of 125% and 150% has a length between 170 min and 180 min.

The characteristics of control system (B) and the algorithm implemented in the coordinator system (A) are presented in detail in this Chapter. The numerical and experimental validation of the PsD testing framework is discussed in the Chapters 4 and 5, respectively.

3.2.1 Control system

The control system, available in the laboratory of CeSMA, is developed by Trio Sistemi e misure S.R.L. for the DiSt. It consists of two RT3 controllers, linked between them, and a personal computer, in which the control software is implemented (Figure 3.2.3).

Figure 3.2.3. RT3 control system.

The control system has a total of 6 force channels, 6 displacement channels, 6 servo valve channels, 1 read-out channel, 1 trigger channel, 1 pump channel, 1 emergency channel (for an additional mushroom) and 1 TCP/IP port. Furthermore, two additional Synchronous Serial Interface (SSI) encoders (i.e., Temposonics transducers) can be connected to the control system using an auxiliary channel on which a D/A and A/D converter is installed.

Two I/O mushrooms are available for the control system to shut-down the pumping system in the case of danger (Figure 3.2.3): one on the control panel and one on the desk. The personal computer, placed on the desk, is connected to the control system via a TCP/IP protocol. The software included in the computer, allows to manage input/output, the system configurations and the data recorded during the tests by means of a real-time graphical user interface. Figure 3.2.4 shows the control interface implemented in the personal computer.

The software implemented in the control system is programmed in the LabView environment [77]. With this software the control system can be used in local mode (manual) and in remote mode (automatic) to control a total number of 6 actuators (see Figure 3.2.5). If the control system is used in local mode, it is possible to impose a load (in force or in displacement control) to the specimen or to apply a pre-defined loading protocol defined using the generator function implemented in the system. Instead, if the control system is used in remote mode (i.e., a connection is established between the coordinator system and the control system), the control system exchanges data to the coordinator system and the devices cannot be managed on the control panel unless the connection between the systems is interrupted.

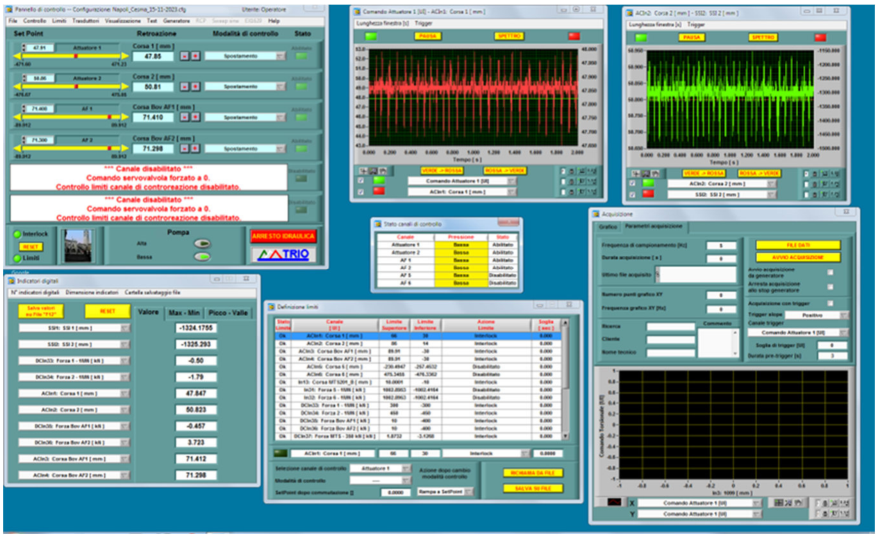

Figure 3.2.4. RT3 controller interface panel.

The pump system can be managed on the control panel to supply the system with low-pressure or high-pressure (Figure 3.2.5). Once the pressure is provided, the load can be imposed to the hydraulic actuators defining a set point on the control panel in the desired control mode (e.g., displacement control, force control or mixed control).

The response of the actuators is controlled using the Proportional-Integrative-Derivative (PID) [43] algorithm. The gain parameters (i.e., P, I, while D is reduced to zero) can be defined for each control mode in a proper menu. The definition of these parameters is fundamental to guarantee the stability and the accuracy of the response of devices.

Figure 3.2.5. RT3 control panel.

Two levels of interlock are defined in the control system. The first level, allow to define a limit range for all the devices connected to the control system. If one of the defined interlocks is exceeded at any time, the system shuts down the pumping system. The second level of interlocks, implemented in the Hardware-In-the-Loop (HIL) interface, is discussed successively.

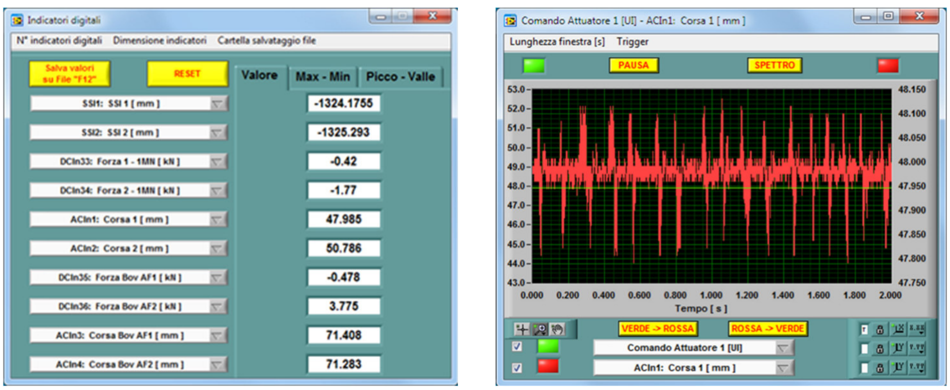

(a) (b)

Figure 3.2.6. RT3 Real-time feed-back visualization**:** (a) digital display; (b) digital oscilloscope.

The feed-back sent from the devices (e.g., load cell, displacement transducer, SSI encoder) to the control system, can be visualized in real-time using the digital display (Figure 3.2.6, a) and the graphical user interfaces that can be added and customized on the desktop (Figure 3.2.6, b). The feed-back can be recorded at a defined frequency (typically of 5Hz) using the data acquisition system included in the controller. In addition, the control system is equipped with a trigger channel that allow to simultaneously start its acquisition and the acquisition configurated in an additional system used for the test.

An Hardware-in-the-loop (HIL) interface, was developed in collaboration with the Department of Structures for Engineering and Architecture (DiSt), to allow the communication between the control system and the coordinator system for the specific purpose of conducting PsD tests. Figure 3.2.7 shows the communication between the two system during a PsD test. The UDP port, which consent the communication, is provided on the personal computer of the control system.

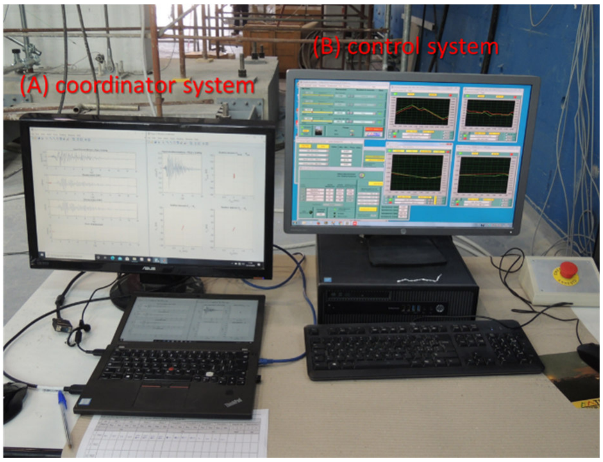

Figure 3.2.7. RT3 control system connected to the coordinator system during a PsD test.

The advantages of the developed HIL interface reside in:

- the record of the variables involved in the integration of equation of motion (e.g., the computed displacement, the measured displacement and the measured restoring force) at each step, according to the prototype time. This acquisition runs in parallel with the continuous acquisition included in the control system.

- the real-time visualization in a graphical user interface of the computed and measured variables (i.e., displacement and restoring force) at each step of integration.
- a layer of interlocks defined for the computed displacement and for the displacement error (i.e., control errors). This interlock layer allows to pause the system without shutting down the pumping system, when one of the defined interlocks is exceeded during the test.
- the possibility to pause and restart the test in order to adjust the interlocks or, more interestingly, to observe the damage scenario on the tested specimen.

Figure 3.2.8 shows the main menu of the HIL interface. The digital button a), opens the UDP port available on the personal computer to establish communication between the coordinator system and the control system. When the button is pressed, the control system prompts the user to specify the path b) where the data recorded is to be saved and the name of the file. The c) can be used to activate the control channel to be controlled during the test.

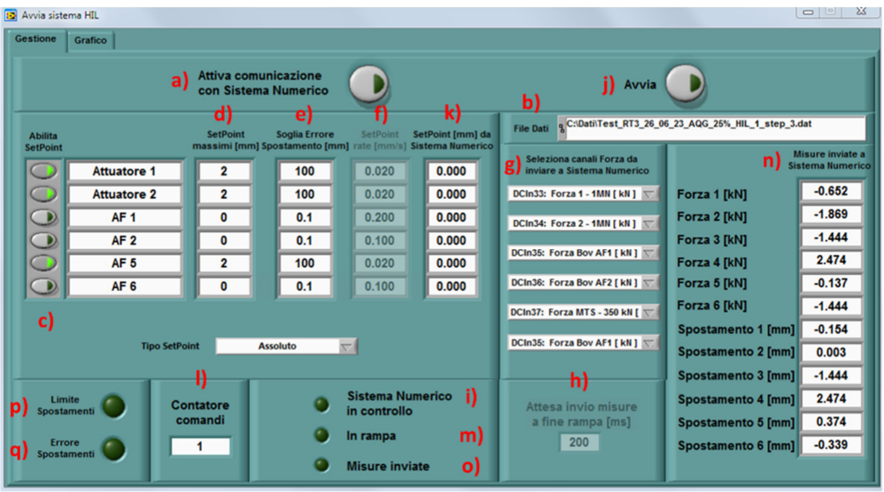

Figure 3.2.8. RT3 Hardware-In-the-Loop interface.

For each channel, the maximum displacement d) and the displacement errors e) interlock must be defined in order to pause the system if one of these is exceeded during the test. The load application-rate (or set point-rate) can be defined for each channel in the column f). In g), the channels assigned to the load cells installed on the hydraulic actuators must be defined. The correct definition of these channels is fundamental, to prevent an erroneous restoring force is introduced in the calculation. The time that the controller waits to send the data measured on the test specimen to the coordinator system can be specified in h). The connection between the coordinator system and the control system is established by the coordinator system. When the connection between the systems has been successfully established, the LED i) lights up. The test can now be started at any time by pressing the digital button j). This button can be used to pause, restart and stop the test.

The computed (target) displacement that the coordinator system sends to the control system, is listed in the column k) for the activated channels. In detail, the coordinator system sends a 6x1 displacement vector to the control system. Each vector variable is a data-type - floating point 64-bit with the unit of measurement mm and a precision of 0.000. Instead, the control system sends a 12x1 vector to the coordinator system where the first six rows contain the measured restoring forces, while the last six rows contain the measured displacements. The variable type and the precision are the same as in the coordinator system while the unit of measurement are kN for the restoring force and mm for the displacement.

The current integration step is indicated by the digital display l). When the LED m) lights up, the control system generates a ramp command to the actuator in order to achieve the computed displacement. The restoring force and the displacement measured on the test specimen are displayed in the column n) for the activated channels. The LED o) lights up when the control system sends the measured quantities to the coordinator system to end the loop. The computed displacements and the measured restoring forces can be monitored at each step using the graph included in the HIL interface (see Figure 3.2.9). The graph allows to combine the different variables in order to analyse the evolution of the test. If one of the interlocks defined in d) and e) is exceeded, the LEDs p) or q) light up and the system is paused. It can be restarted by increasing the size of the interlocks. The test ends when the integration of the accelerogram record has been completed or an interruption has occurred for dangerous situation. In this case, the test can be interrupted by first pressing the j) button to stop the test and then the a) button to interrupt the communication between the coordinator system and the control system.

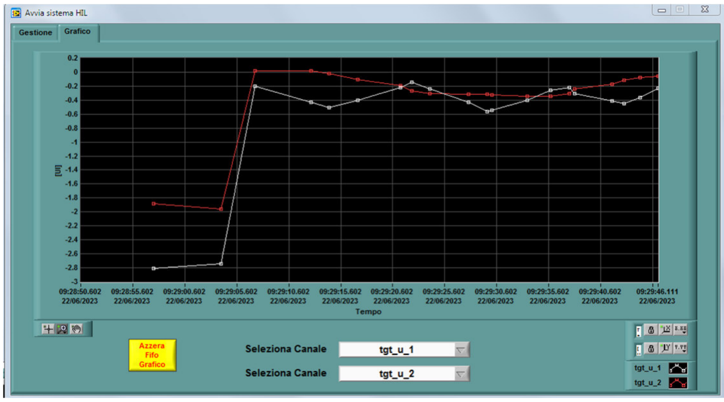

Figure 3.2.9. Graph provided in the HIL interface.

3.2.2 The coordinator system

Once the facility and the control system were provided in the CeSMA laboratory, the development of a code was required to perform PsD tests. The code was implemented in-house in MATLAB environment [57] enabling numerical analysis and experimental analysis (i.e., PsD test) to be performed. It consists of a total number of over 1500 rows and has a structure of seven scripts each with a specific function. Figure 3.2.10 a) shows the list of the script contained in the code. The "Source txt file", shown in Figure 3.2.10 b) contain the accelerogram record, the shadow curves, obtained from a numerical analysis and used as a prediction, and the additional functions.

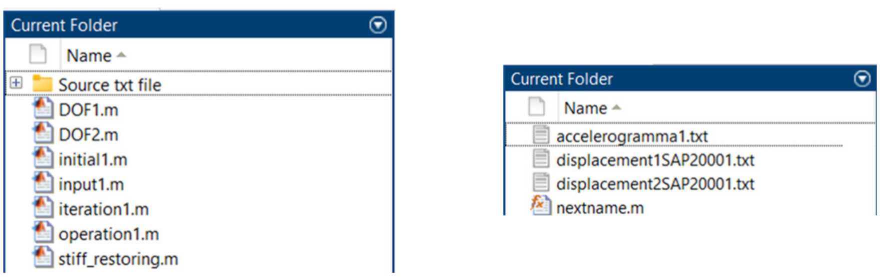

(a) (b)

Figure 3.2.10. (a) List of the scripts of the integration structure (b) Folder contents.

At this stage, the code is implemented for a multi-degree-of-freedom system (MDOF) with two DoFs. The number of DoFs can be increased up to six DoFs according to the total number of control channels implemented in the control system. The measurement units used in the algorithm are mm for the displacement, kN for the force and s for the time.

3.2.2.1 input1.m

The information required to perform the analysis (numerical and experimental) must be defined in the script input1.m. A set of indices (see Figure 3.2.11) allow to select the options contained in the code corresponding to a specific function. For instance, if the `analysis_index` is defined as zero, a numerical analysis is performed. In this case, the structural response is numerically simulated using the hysteretic laws implemented in the code. The law (i.e., elastic, elastic-plastic, hysteretic and pivot model [78]) can be selected defining the `behavior_index` according to the options reported in the comments (see Figure 3.2.11).

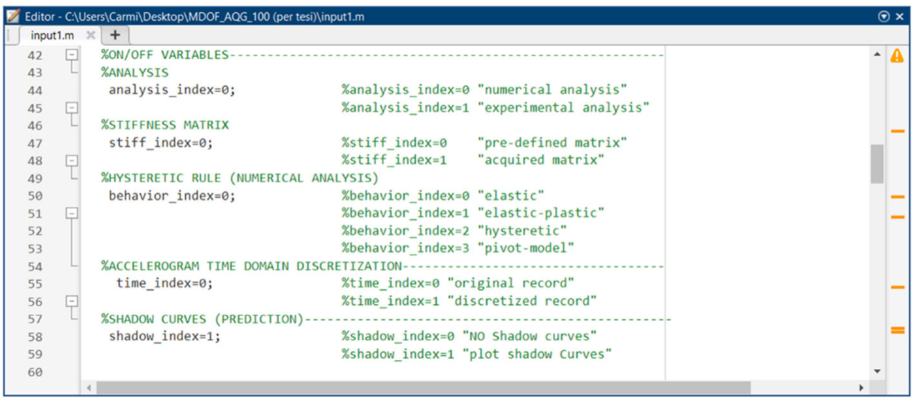

Figure 3.2.11. Test configuration variable and options implemented in input1.m.

To perform an experimental analysis, the `analysis_index` must be set to 1. The initial stiffness matrix $[K_0]$, required as input, can be evaluated preliminarily (`stiff_index=0`) or acquired from the specimen (`stiff_index=1`), using the function implemented in the operation1.m script. The code enables the analyses to be performed by using the time increment Δt of the original accelerogram record $\ddot{x}_g$ or a time increment defined for the discretization of the original record used for the integration of equation of motion. In particular, if `time_index=0`, the original record is used to perform the analysis. Otherwise, the accelerogram is discretized (`time_index=1`) using a linear interpolation according to the number of steps N defined as indicated in Figure 3.2.12. In addition, the analyses can be performed scaling the original record using an intensity scaling factor S. F.. However, discretizing the record increases the test duration due to the increase of the number of integration steps. This is because the Classical method is used as testing method.

The communication suite is implemented in the script input1.m. The information required for the connection between the coordinator system and the control system via UDP protocol are also defined in this script. In particular, the IP address and the port assigned to each system must be defined. In addition, the script creates an UDP object in the coordinator system to establish the communication with the control system. A communication timeout is also defined to stop the code if the communication between the two systems is interrupted when the test is ongoing.

Figure 3.2.12, shows the specimen properties and the time parameters defined in the script.

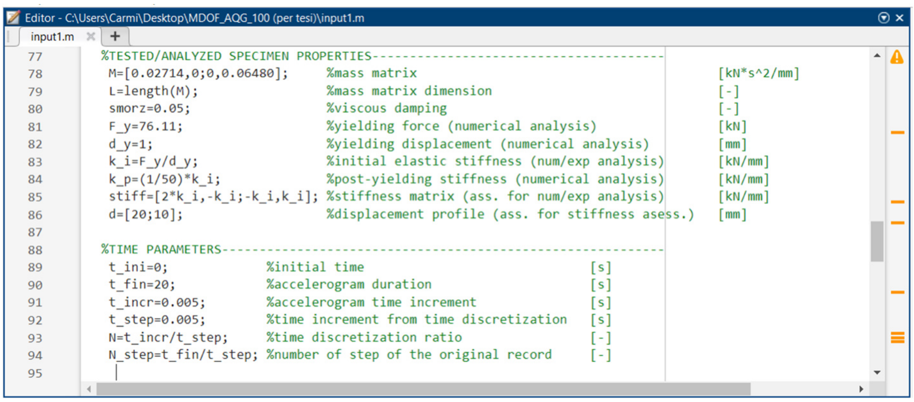


```
%TESTED/ANALYZED SPECIMEN PROPERTIES------------------------------------
 M=[0.02714,0;0,0.06480];     %mass matrix                                 [kN*s^2/mm]
 L=length(M);                 %mass matrix dimension                       [-]
 smorz=0.05;                  %viscous damping                             [-]
 F_y=76.11;                   %yielding force (numerical analysis)         [kN]
 d_y=1;                       %yielding displacement (numerical analysis)  [mm]
 k_i=F_y/d_y;                 %initial elastic stiffness (num/exp analysis) [kN/mm]
 k_p=(1/50)*k_i;              %post-yielding stiffness (numerical analysis) [kN/mm]
 stiff=[2*k_i,-k_i;-k_i,k_i]; %stiffness matrix (ass. for num/exp analysis) [kN/mm]
 d=[20;10];                   %displacement profile (ass. for stiffness asess.) [mm]

%TIME PARAMETERS--------------------------------------------------------
 t_ini=0;             %initial time                            [s]
 t_fin=20;            %accelerogram duration                   [s]
 t_incr=0.005;        %accelerogram time increment             [s]
 t_step=0.005;        %time increment from time discretization [s]
 N=t_incr/t_step;     %time discretization ratio               [-]
 N_step=t_fin/t_step; %number of step of the original record   [-]
```

Figure 3.2.12. Specimen properties and time parameters definition.

In particular, the dynamic properties of the specimen (mass matrix [M], stiffness matrix [K_0], viscous damping ζ) are defined. In addition, the displacement vector {x}, used to evaluate the initial stiffness of the specimen, is also defined. In numerical analyses, the characteristics of the selected law must be defined in order to simulate the structural behaviour. This is because the selected law requires the knowledge of the initial stiffness k_i, the displacement d_y and force F_y at yielding and the post-yielding stiffness ratio k_p is required.

In Figure 3.2.13 the initial condition vectors ($t = 0$ s) are defined. Generally, the analyses are performed starting with initial condition in which the displacement $\{x_0\}$, the velocity $\{\dot{x}_0\}$, and the acceleration $\{\ddot{x}_0\}$ vectors are assumed to be null.

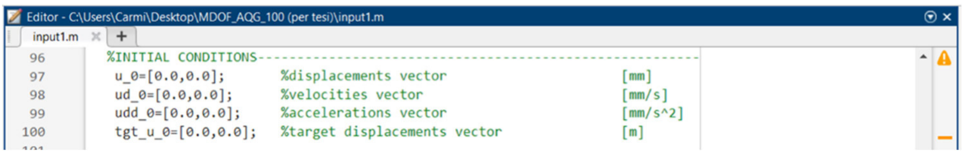


```
%INITIAL CONDITIONS-----------------------------------------------------------
 u_0=[0.0,0.0];         %displacements vector                       [mm]
 ud_0=[0.0,0.0];        %velocities vector                          [mm/s]
 udd_0=[0.0,0.0];       %accelerations vector                       [mm/s^2]
 tgt_u_0=[0.0,0.0];     %target displacements vector                [m]
```

Figure 3.2.13. Initial conditions and target displacement interlock definition.

For the experimental analyses, an interlock on the computed (target) displacement, sent to the controller system, is implemented in the code. This function immediately interrupts the code when one of the defined interlocks is exceeded during the analysis.

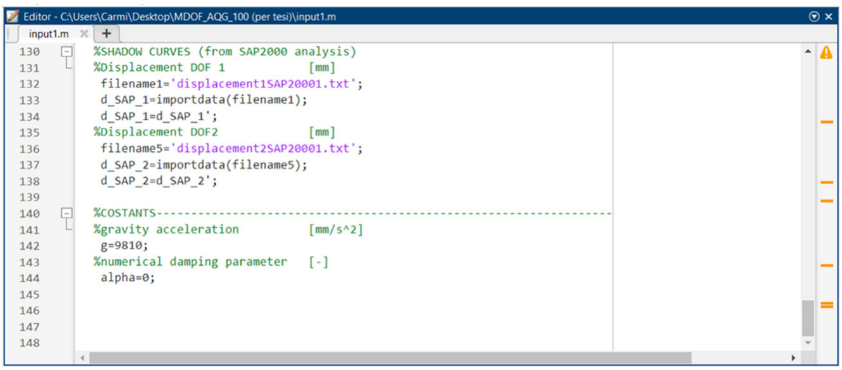


```
%SHADOW CURVES (from SAP2000 analysis)
%Displacement DOF 1              [mm]
 filename1='displacement1SAP20001.txt';
 d_SAP_1=importdata(filename1);
 d_SAP_1=d_SAP_1';
%Displacement DOF2               [mm]
 filename5='displacement2SAP20001.txt';
 d_SAP_2=importdata(filename5);
 d_SAP_2=d_SAP_2';

%COSTANTS-------------------------------------------------------------------
%gravity acceleration            [mm/s^2]
 g=9810;
%numerical damping parameter     [-]
 alpha=0;
```

Figure 3.2.14. Constants and shadow curves path definition.

In addition, it is possible to provide a series of shadow curves in the plot background as a prediction of the experimental response (`shadow_index=1`) or not (`shadow_index=0`). Figure 3.2.14 shows the last section of the script.

The path from it is possible to import the shadow curve files and the constant involved in the process is defined. In particular, the parameter α is set equal to zero (i.e., no numerical damping) to perform both numerical and experimental analyses.

3.2.2.2 operation1.m

In the script operation1.m, the preliminary operations required to perform the analyses are carried out. For the experimental analyses (`analysis_index=1`), the code prompt to the user to open the UDP port of the coordinator system created an UDP object in the MATLAB code. A message is displayed in the command windows confirming that the port has been opened successfully, thus the connection between the coordinator system and the control system can be established. Once the UDP port is open, it is possible to send a request to the control system in order to connect the systems sending a “start” message. If the message is correctly received, the control system sends a “Connessione stabilita” message to the coordinator system, which make a connection check and display the received message in the command window.

The evaluation of the initial stiffness matrix $[K_0]$ is necessary to perform both numerical and experimental analyses. If the stiffness matrix is evaluated preliminarily (`stiff_index=0`), the evaluation of the initial stiffness is not required and the evaluated matrix can be assigned to the structural system (Figure 3.2.15). Otherwise, the operation used to define the initial stiffness matrix $[K_0]$ depends on the type of analysis to be performed. In a numerical analysis, the initial stiffness matrix is numerically evaluated using the script initial1.m, recalled by the script operation1.m, presented successively.

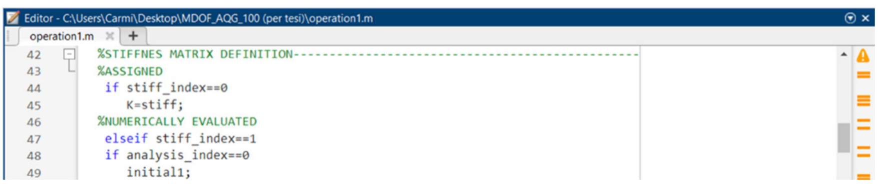

Figure 3.2.15. Initial stiffness matrix $[\mathbf{K_0}]$ definition options.

In an experimental analysis, the initial stiffness matrix $[K_0]$ can be experimentally evaluated, applying to the specimen the displacement profile {x} defined in input1.m. In particular, the displacement profile is sent through the communication suite to the controller to be imposed on the specimen by means of hydraulic actuators. The restoring force and the displacement measured from the specimen by means of load cells and displacement transducers, are sent to the coordinator system through the communication suite to calculate the secant stiffness $k_{m,n}$ (with $m = n$) at each DoF, as the ratio between the restoring force R_m and the imposed displacement x_m. The computed stiffnesses, are then used to assemble the initial stiffness matrix $[K_0]$ defined as input to perform the analysis. Figure 3.2.16 shows the method implemented in the script to assembly the stiffness matrix starting from the evaluated secant stiffnesses.

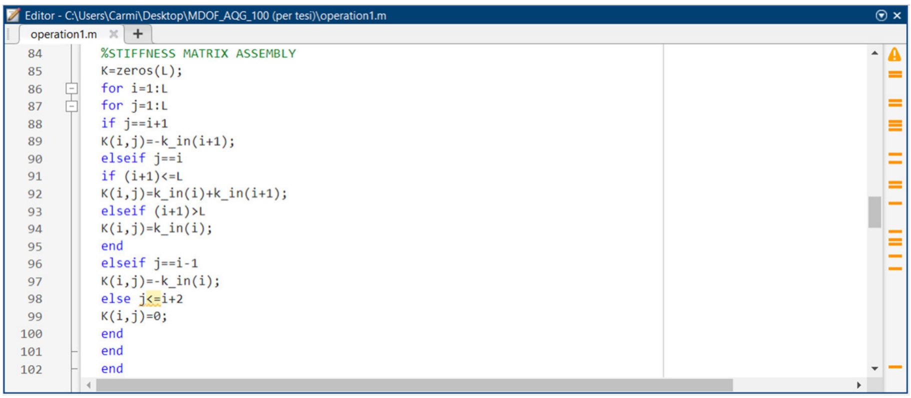

Figure 3.2.16. Initial stiffness matrix assembly method.

The evaluated stiffness matrix can be confirmed or discarded at the end of the operation. If the stiffness matrix is discarded, it is possible to repeat the evaluation, applying the defined displacement profile. This operation can be repeated until the stiffness matrix is confirmed by the user.

The eigen analysis is performed in the script for both analyses (Figure 3.2.17). The analysis starts with the definition of the eigenvalues and of the eigenvectors, in order to evaluate the natural periods T_0 and the natural frequencies f_0 of the structural system. However, the evaluated quantities do not represent an input mandatory to perform the analyses. In contrast, the definition of the viscous damping matrix [C] is mandatory required to perform the analysis if the viscous damping is not zero. In the code, the Rayleigh method is implemented to define the viscous damping matrix (see Figure 3.2.17).

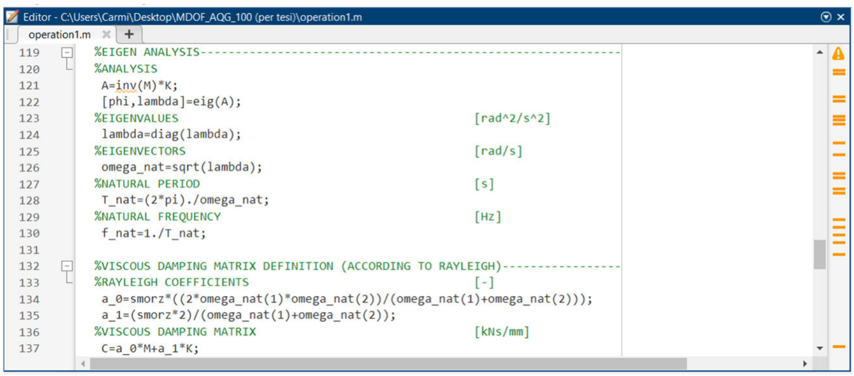


```
%EIGEN ANALYSIS---------------------------------------------------------
%ANALYSIS
 A=inv(M)*K;
 [phi,lambda]=eig(A);
%EIGENVALUES                                         [rad^2/s^2]
 lambda=diag(lambda);
%EIGENVECTORS                                        [rad/s]
 omega_nat=sqrt(lambda);
%NATURAL PERIOD                                      [s]
 T_nat=(2*pi)./omega_nat;
%NATURAL FREQUENCY                                   [Hz]
 f_nat=1./T_nat;

%VISCOUS DAMPING MATRIX DEFINITION (ACCORDING TO RAYLEIGH)----------------
%RAYLEIGH COEFFICIENTS                               [-]
 a_0=smorz*((2*omega_nat(1)*omega_nat(2))/(omega_nat(1)+omega_nat(2)));
 a_1=(smorz*2)/(omega_nat(1)+omega_nat(2));
%VISCOUS DAMPING MATRIX                              [kNs/mm]
 C=a_0*M+a_1*K;
```

Figure 3.2.17. Eigen analysis and viscous damping matrix [**C**] definition.

In the end section of the script, the numerical algorithm parameters and the time vector are defined. The parameters β and γ are calculated according to the expressions (2.11) and (2.12). The time vector has the length of the original accelerogram if it is not discretized. Otherwise, the length of the time vector depends on the time step increment chosen to perform the analysis.

3.2.2.3 iteration1.m

The script iteration1.m script is the main script from which the analyses is launched. When this script is run, it recalls first the input1.m script to read the input and then the operation1.m script to prepare the system to be ready to perform analysis. In addition, the properties of the figures and the plot implemented to visualize in real-time the analysis output can be defined in this script.

Once the system is ready, if the analysis is numerical the integration of the equation of motion starts automatically. Instead, if the analysis is experimental and the connection between the coordinator system and the control system has been successfully established, the process starts by pressing the j) button on the HIL interface of the control system (Figure 3.2.18).

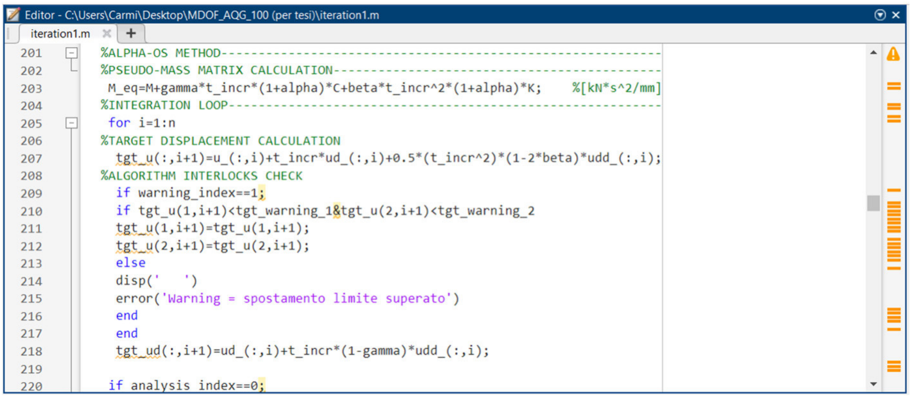

Editor - C:\Users\Carmi\Desktop\MDOF_AQG_100 (per tesi)\iteration1.m

```
%ALPHA-OS METHOD-------------------------------------------------------------
%PSEUDO-MASS MATRIX CALCULATION----------------------------------------------
 M_eq=M+gamma*t_incr*(1+alpha)*C+beta*t_incr^2*(1+alpha)*K;    %[kN*s^2/mm]
%INTEGRATION LOOP------------------------------------------------------------
 for i=1:n
%TARGET DISPLACEMENT CALCULATION
  tgt_u(:,i+1)=u_(:,i)+t_incr*ud_(:,i)+0.5*(t_incr^2)*(1-2*beta)*udd_(:,i);
%ALGORITHM INTERLOCKS CHECK
  if warning_index==1;
  if tgt_u(1,i+1)<tgt_warning_1&tgt_u(2,i+1)<tgt_warning_2
  tgt_u(1,i+1)=tgt_u(1,i+1);
  tgt_u(2,i+1)=tgt_u(2,i+1);
  else
  disp('   ')
  error('Warning = spostamento limite superato')
  end
  end
  tgt_ud(:,i+1)=ud_(:,i)+t_incr*(1-gamma)*udd_(:,i);

 if analysis index==0;
```

Figure 3.2.18. α-OS method and interlocks implemented in the iteration1.m script.

The numerical algorithm used to solve the equation of motion is the α-OS method [69] and the process is implemented according to the Figure 2.3.22. At the beginning of the integration, the algorithm calculates the target displacement vector $\{\tilde{x}\}$ to be imposed on the structural system. If the analysis is experimental type and the interlocks are defined in the code, the code verifies at each step if the calculated (target) displacements exceed the specified interlocks. However, only the interlocks defined in the control system are considered to perform the experimental analysis.

If the analysis launched is numerical type, the target displacement vector $\{\tilde{x}\}$ is sent to the corresponding DOFs.m scripts that numerically simulate the structural behaviour according to the law selected in the input1.m script. These scripts calculate the force and the stiffness for each DoF. In particular, the stiffness, intended as secant stiffness, is calculated as the ratio between the restoring force R and the applied displacement x. The secant stiffness evaluated at each floor is sent to the stiff_restoring.m script to assemble the stiffness matrix [K] and calculates the actual restoring force vector. This procedure is fundamental when the behaviour is nonlinear due to the stiffness matrix change. The DOF.m script and the stiff_restoring.m script, which constituted the numerical simulation suite, will be discussed successively.

If the analysis is experimental type, the target displacement vector $\{\tilde{x}\}$ is sent to the control system to be imposed on the test specimen by means of hydraulic actuators. In particular, the calculated displacement are the elements of the first two rows of the 6x1 vector that the coordinator system sends to the control system, by using the communication suite. Once the target displacements are applied by means of hydraulic actuators, the 12x1 vector that contains the restoring forces and the displacements measured on the specimen by means of load cells and displacement transducers is sent to the coordinator system, in order to calculate the next step.

The test outputs can be visualized in real-time using the interfaces shown in Figure 3.2.19 and Figure 3.2.20. Figure 3.2.19 contains the interface in which the accelerogram record, the displacement of each degree of freedom and the control errors, intended as difference between the sent displacement (target) and the received displacement (measured) are reported. The straight grey line represents the shadow curve provided for all the plot has except for the control error plot. The acceleration shadow curve represents the record selected as the input for the test, while the displacement shadow curves represent the results of numerical analysis perform to predict the experimental response. The straight red line shows the evolution of the test at every step of the integration. The red line traces the shadow curve during the test. In particular, the acceleration the red line gives information on the current status of the test, while the matching between the red line and the grey line for each DoF gives information on the reliability of the prediction analysis.

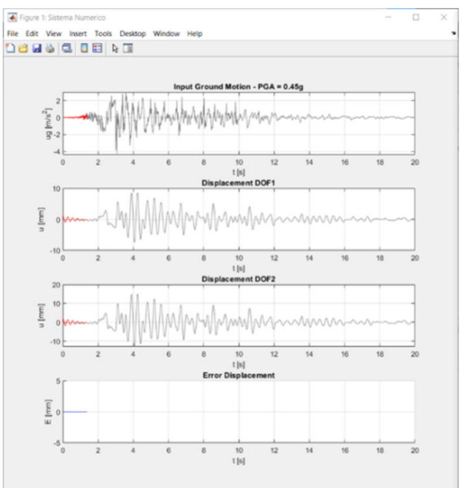

Figure 3.2.19. Real-time visualization output interface 1.

Figure 3.2.20 shows the interface in which the accelerogram record, the floor hysteresis and the global hysteresis are shown. It is possible to observe that the shadow curve is provided only for the accelerogram record for a clean view of the hysteresis graphs.

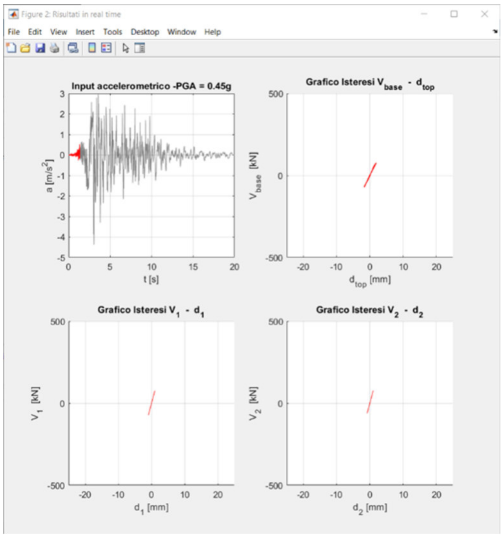

Figure 3.2.20. Real-time visualization output interface 2.

At the end of the experimental analysis, the code closing the UDP port to interrupt the connection between the coordinator system and the control system when the integration of the accelerogram record is successfully completed. In addition, independent of the analysis, the system prompt to the user to save the output of the integration in a .txt file.

3.2.2.4 initial1.m (numerical analysis)

The script initial1.m is recalled by the script operation1.m if the analysis launched is numerical type. It is a short script implement to evaluate the initial stiffness matrix [K_0] of the analysed MDOF system (Figure 3.2.21). First, the script calculates the restoring force vector {R} resulting from the imposed displacement profile {x}, defined in the script input1.m (see Figure 3.2.12).

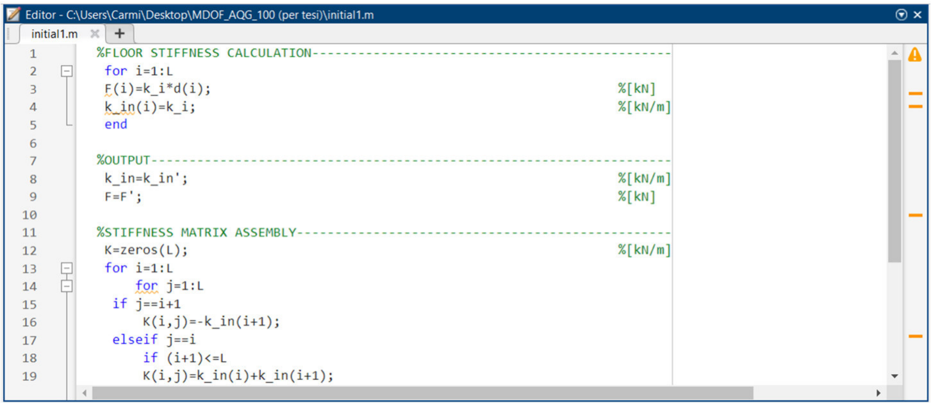


```
%FLOOR STIFFNESS CALCULATION------------------------------------------------
 for i=1:L
 F(i)=k_i*d(i);                                                        %[kN]
 k_in(i)=k_i;                                                          %[kN/m]
 end

%OUTPUT---------------------------------------------------------------------
 k_in=k_in';                                                           %[kN/m]
 F=F';                                                                 %[kN]

%STIFFNESS MATRIX ASSEMBLY--------------------------------------------------
 K=zeros(L);                                                           %[kN/m]
 for i=1:L
     for j=1:L
  if j==i+1
      K(i,j)=-k_in(i+1);
  elseif j==i
      if (i+1)<=L
      K(i,j)=k_in(i)+k_in(i+1);
```

Figure 3.2.21. Initial stiffness matrix $[\mathbf{K_0}]$ evaluation .

Then, the initial stiffness matrix $[K_0]$ is assembled using the approach presented in Figure 3.2.16, and used as input in the code to perform the analysis.

3.2.2.5 DOF.m and stiff_restoring.m (numerical analysis)

If the analysis is numerical type, the target displacement vector$\{\tilde{x}\}$ calculated in the integration loop is sent to the corresponding DOF.m script DoF, to calculate the force and the secant stiffness of each DoF according to the law selected to reproduce the structural behaviour (see Figure 3.2.22).

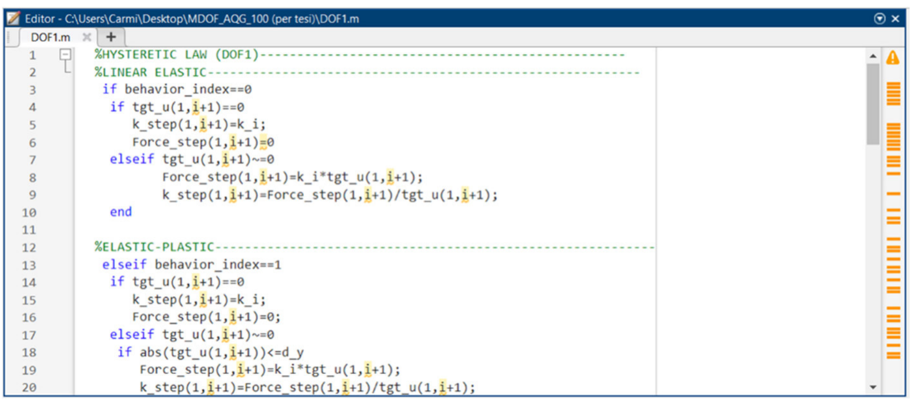


```
%HYSTERETIC LAW (DOF1)----------------------------------------------
%LINEAR ELASTIC-----------------------------------------------------
 if behavior_index==0
  if tgt_u(1,i+1)==0
     k_step(1,i+1)=k_i;
     Force_step(1,i+1)=0
  elseif tgt_u(1,i+1)~=0
         Force_step(1,i+1)=k_i*tgt_u(1,i+1);
         k_step(1,i+1)=Force_step(1,i+1)/tgt_u(1,i+1);
  end

%ELASTIC-PLASTIC----------------------------------------------------
 elseif behavior_index==1
  if tgt_u(1,i+1)==0
     k_step(1,i+1)=k_i;
     Force_step(1,i+1)=0;
  elseif tgt_u(1,i+1)~=0
   if abs(tgt_u(1,i+1))<=d_y
      Force_step(1,i+1)=k_i*tgt_u(1,i+1);
      k_step(1,i+1)=Force_step(1,i+1)/tgt_u(1,i+1);
```

Figure 3.2.22. Hysteretic law and DoF stiffness evaluation.

Figure 3.2.23 shows the laws implemented in the algorithm: a) elastic, b) elastic-plastic (monotonic), c) hysteretic, d) and pivot [78].

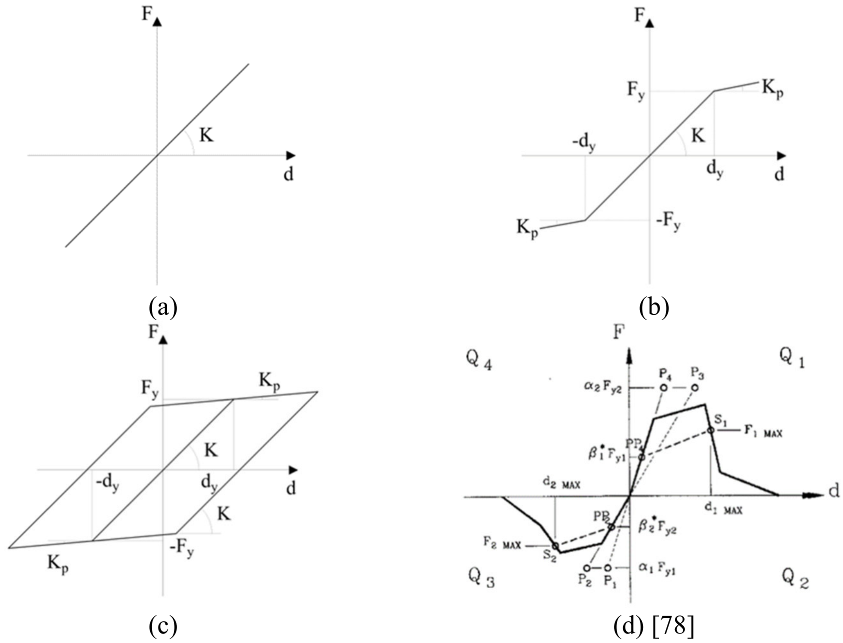

Figure 3.2.23. Hysteretic laws implemented in the DOF.m script.

The stiffnesses, evaluated as secant stiffness, are then sent to the stiff_restoring.m script in order to assemble the stiffness matrix and calculate the restoring force vector {R}. Finally, the computed restoring force vector is sent to the iteration1.m script to calculate to the next step of integration.

3.2.2.6 Numerical and experimental analysis framework

The MATLAB code developed for the CeSMA laboratory was conceived to conduct two different analyses: numerical (`analysis_index=0`) or experimental (`analysis_index=1`). The numerical algorithm used to solve the equation of motion is the α-OS method [69]. The numerical analysis allows the simulation of the structural response of a modelled multi-degree-of-freedom (MDOF) system using different hysteretic laws (Figure 3.2.23). The MDOF system is modelled as a system with lumped mass subjected to an accelerogram record $\ddot{x}_g$ selected as input. Figure 3.2.24 shows the framework implemented in the code to perform the numerical analysis of a 2-DoFs system. The analysis starts when the iteration1.m script is launched. This script calls the input1.m to load the information required to perform the test (Figure 3.2.12). Among these, the initial stiffness matrix $[K_0]$ can be assigned or numerically evaluated using the initial1.m script (`stiffness_index=1`). In particular, the operation1.m script recalls the initial1.m script to evaluate the stiffness matrix. In addition, the definition of the viscous damping matrix $[C]$ (mandatory to perform the analysis) and the eigen analysis are performed by the operation1.m script as preliminary operations so that the system is ready to start the analysis.

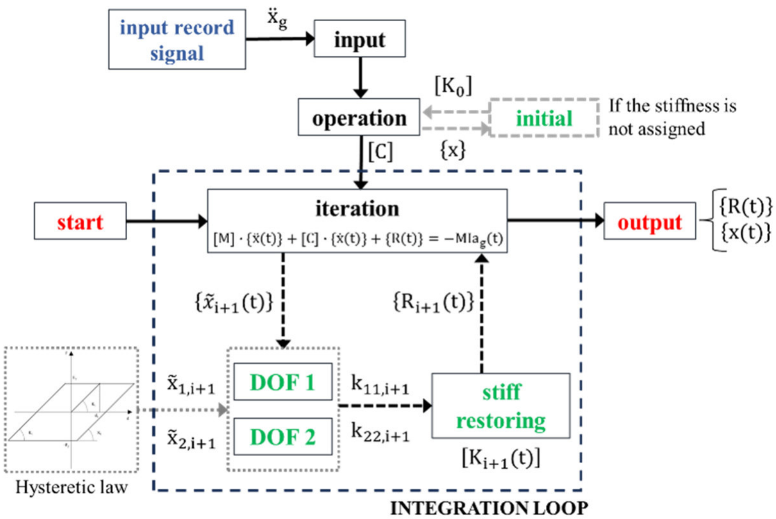

Figure 3.2.24. Numerical analysis framework implemented in the code.

The integration of the equation of motion starts with the calculation of the target displacement vector $\{\tilde{x}_{i+1}(t)\}$ to be imposed on the specimen. Each displacement, i.e., $\tilde{x}_{1,i+1}$ and $\tilde{x}_{2,i+1}$, is sent to the corresponding DOF.m script to calculate the floor force required to calculate the floor secant stiffnesses $k_{11,i+1}$ and $k_{22,i+1}$. The force is calculated according to the hysteretic law which was chosen to reproduce the structural behaviour (Figure 3.2.24). The calculated stiffnesses are sent to the stiff_restoring.m script to assemble the stiffness matrix $[K_{i+1}(t)]$ and calculate the restoring force $\{R_{i+1}(t)\}$ at each floor, which is required for the calculation of the next step. The real-time output visualization interface can also be used to visualize the result of the analysis during the execution. In addition, the output in terms of the restoring force vector {R(t)} and the displacement vector {x(t)} can be saved in a .txt file at the end of the analysis.

Figure 3.2.25 shows the framework implemented in the code to perform an experimental analysis. The framework allows to test a specimen which is physically built in the laboratory using the Classical PsD testing method. Therefore, the DOF.m and the stiff_restoring.m scripts are not required to perform the analysis since the response is acquired directly on the specimen.

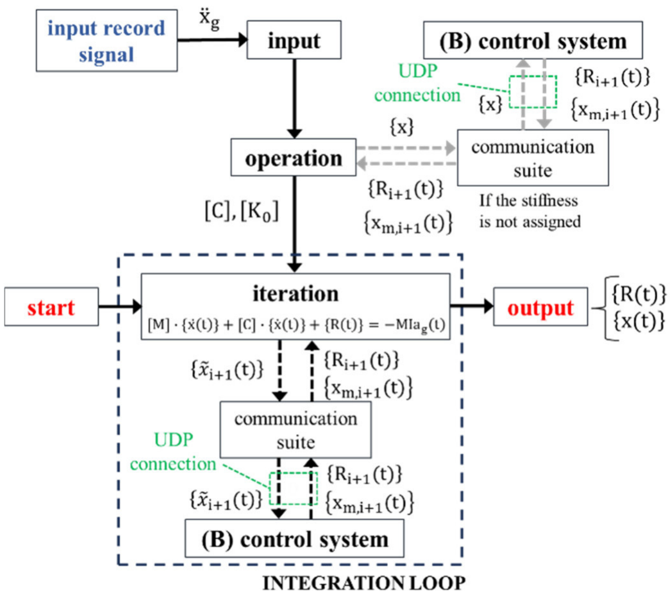

Figure 3.2.25. Experimental analysis framework implemented in the code.

The analysis starts launching the script iteration1.m. As with the numerical analysis, the properties of the specimen defined with the accelerogram record $\ddot{x}_g$ in the script input1.m are sent to the script operation1.m, with the exception of the stiffness matrix $[K_0]$. This matrix can be assigned in the input1.m script or assembled in the operation1.m script. In particular, the displacement profile {x} defined in the input1.m script is sent via the communication suite using the UDP protocol to the controller, to be imposed on the specimen by means of hydraulic actuators. Subsequently, the restoring force measured on the specimen at the imposed displacement, is sent to the operation1.m script to assembly the stiffness matrix and calculate the viscous damping matrix $[C]$ (if the damping is not zero), both of which are a mandatory input for performing the test.

The connection between the coordinator system and the control system is established by the operation1.m script. Once the connection has been successfully established, the experimental analysis (i.e., the PsD test) can be started by pressing the j) button in the HIL interface (Figure 3.2.8) on the control system. The test starts with the calculation of the target displacement vector (with dimension 6x1), which must be sent to the control system through the communication suite. The displacements received from the control system are imposed to the physical specimen using hydraulic actuators to measure the corresponding restoring force and the displacement applied using load cells and displacement transducers. The measured quantities are sent to the communication suite (as 12x1 vector) to calculate the next integration step. As can be seen in Figure 3.2.19 and Figure 3.2.20, the implemented code provides a real-time visualization output interface to visualize the test evolution. At the end of the test, the experimental results of the restoring force vector $\{R(t)\}$ and the displacement vector $\{x(t)\}$ can be saved in a .txt file at the end of the test.

Chapter 4

4. Case study building and substructuring approach

The first pseudo-dynamic experimental campaign in the CeSMA laboratory was carried out on a full-scale infilled reinforced concrete (RC) frame using the in-house developed code. The frame specimen, physically reproduced in the laboratory environment, was selected from a 4-storey infilled reinforced concrete building damaged by the 2009 L'Aquila earthquake. It was selected from the structural system as the most damaged perimetral frame ending with a corner column. This is because the aim of the research activities carried out in the laboratory regards the study of the interaction between the surrounding frame and the infill panel and its effects on the corner beam-to-column joint response to develop reliable numerical models. However, a substructuring approach was required to perform PsD tests in order to account for the contribution of the portion of the building that is not physically built in the laboratory. In this study, a simple substructuring approach is proposed in order to easily identify the source of potential errors in the PsD test.

This chapter presents the characteristics of the case study building, including the material properties and the reinforcement details, the nonlinear numerical building and frame models, along with the accelerogram record used as input to perform the experimental and the numerical analyses, the proposed substructuring approach and the considered assumptions, and the numerical validation of the substructuring approach using the results of the numerical analysis performed using the developed models.

4.1 The reference building: 4-storey existing infilled reinforced concrete (RC) building

4.1.1 Geometrical details

The case study building is selected from the database of RC buildings heavily damaged due to L'Aquila earthquake [3]. It is located in the L'Aquila municipality and consists of a four-floor building, with three walkable floors (from first to third), roof (fourth floor) and one floor basement. Figure 4.1.1 shows a view of the longitudinal direction (a) and of the transverse direction (b) of the case study building before the 2009 L'Aquila earthquake event, retrieved from Google Street View [79].

(a)

(b)

Figure 4.1.1. The case study building before the 2009 L'Aquila earthquake: (a) longitudinal direction; (b) transverse direction.

The plan view of the basement, the first floor and the roof, are shown in Figure 4.1.2, Figure 4.1.3 and Figure 4.1.4, respectively. Only the plan view of the first floor is reported since the characteristics of the third and fourth floor are identical. The cross-section of the building is shown in Figure 4.1.5. The building plan is rectangular with 15.60 m and 10.00 m sides. The storey height is about 3.20 m. It is regular in plan and elevation and was designed in the period 1972–1981 to withstand moderate seismic actions. The building relies on RC moment resisting frames available in the main directions of the building. In particular, the structural system consists of three frames in the longitudinal (x) direction, five frames in the transverse (y) direction and a staircase to vertical connect the building floors. The bay length is 4.40 m in the y direction while ranges from 3.10 m to 3.70 m in the x direction. The frames are composed of square columns 0.4 m side at all the floors, while the perimetral beams are rectangular with a width of 0.40 m and a height of 0.55 m and the inner and roof beams are rectangular with a width of 0.40 mm and a height of 0.20 mm.

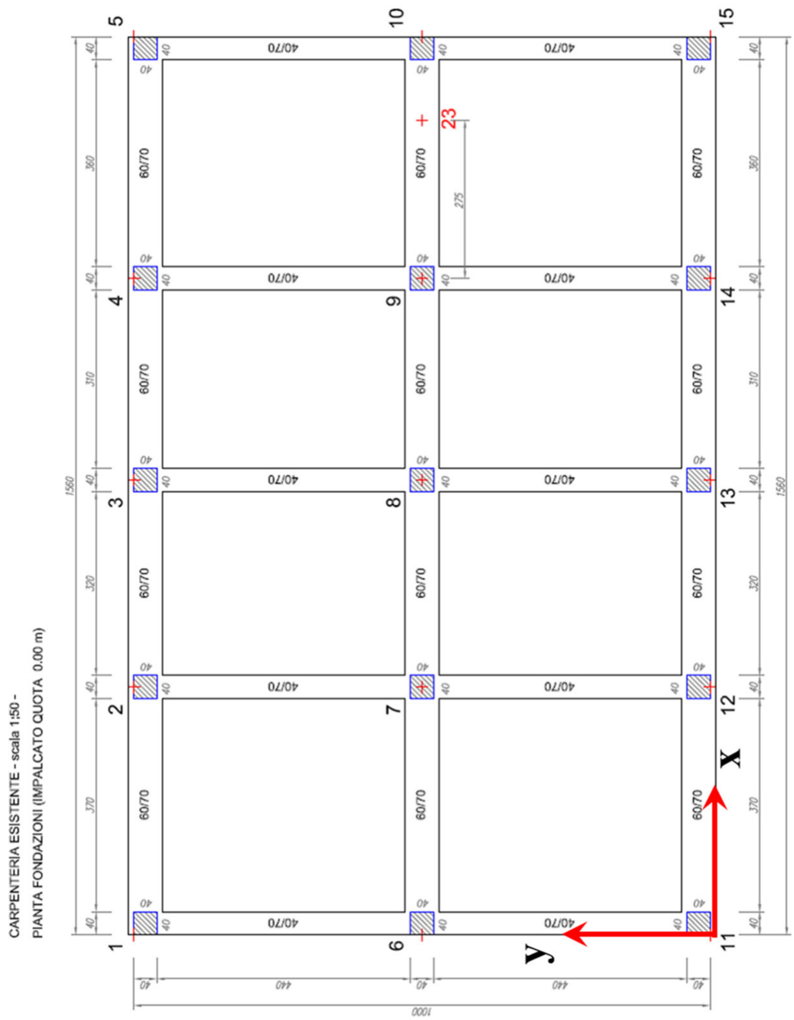

Figure 4.1.2. Case study building basement plan view.

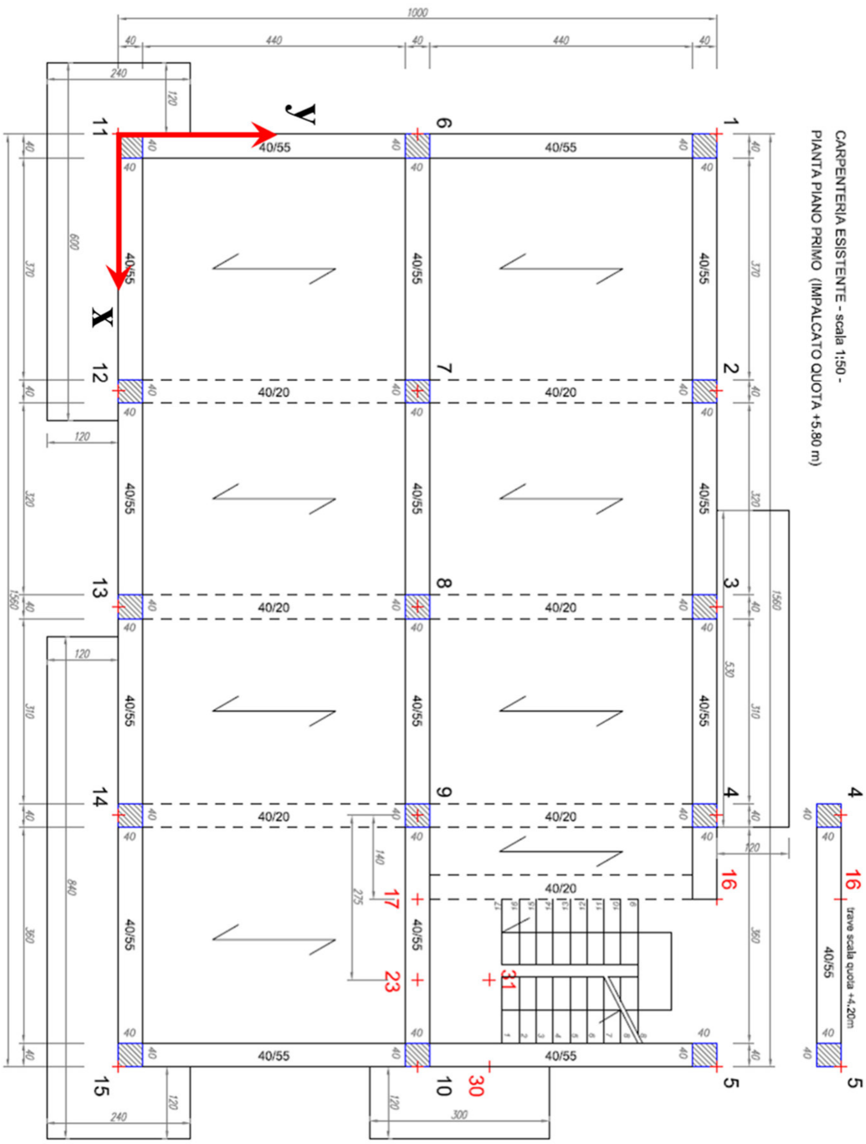

Figure 4.1.3. Case study building first floor plan view.

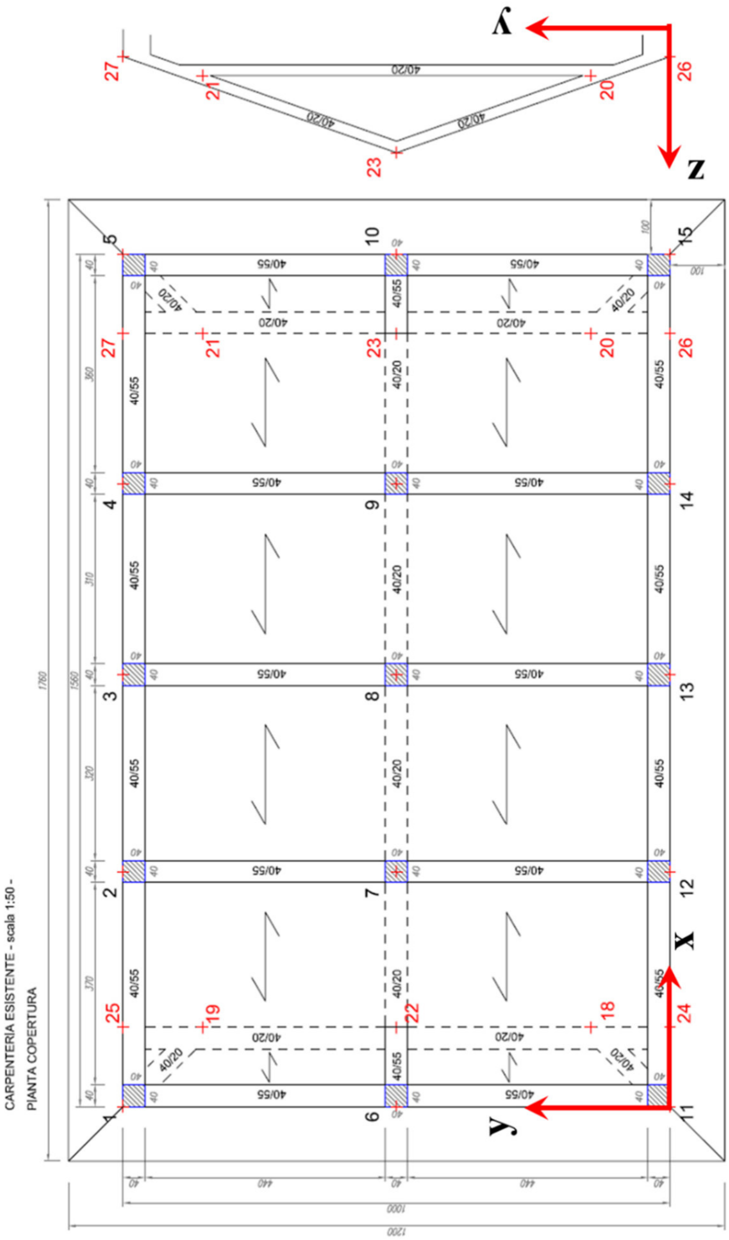

Figure 4.1.4. Case study building roof plan view.

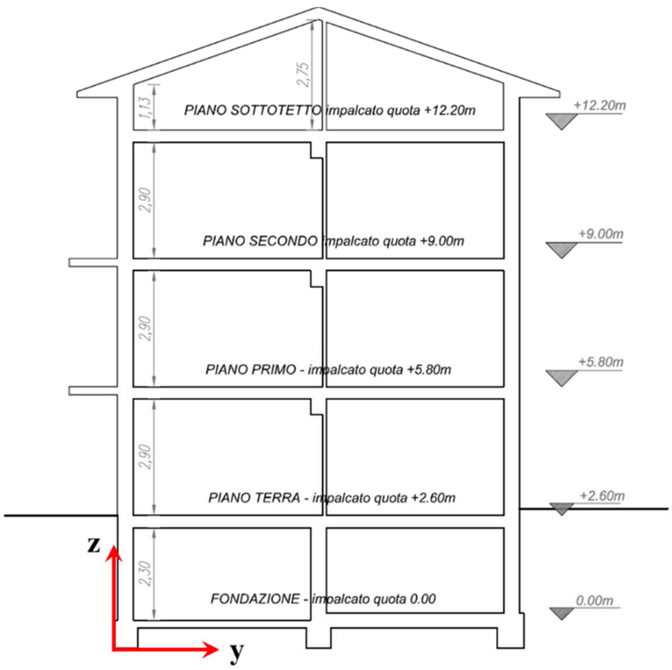

Figure 4.1.5. Case study building cross-section.

4.1.2 Material properties and reinforcement details

To identify the building geometry, the mechanical properties of the materials, the reinforcement details and the properties of the building envelope, post-earthquake inspection was conducted on the case study building. The material properties were characterized by means of destructive testing performed during the reconstruction process. For the purpose, two concrete cylinders and one steel rebar were taken from the structure. A compression test on the concrete specimens is performed to evaluate the compressive strength. The yielding tensile strength of the steel of which the bars were made was evaluated through a uniaxial tensile test. The concrete compressive strength was equal to 18 MPa while the mean yielding tensile of the bar was equal to 470 MPa.

The analysis of the reinforcement details outlined that the structural members were designed to sustain moderate seismic actions. The diameter of the longitudinal rebars and stirrups was

evaluated removing the concrete cover on some structural elements. The bars diameter identified for the was 16 mm for the longitudinal rebars and 8 mm for the stirrups. The number and the position of rebars in the elements cross-section and the stirrups spacing, were analysed using a Ground Penetrating Radar (GPR). The columns reinforcement consists of eight longitudinal bars equally distributed in the cross section and a stirrup spacing between 0.22 m to 0.34 m. The beams longitudinal reinforcement is different at every floor. The stirrup spacing evaluated on a limited number of beams was irregular and ranges from 0.12 m to 0.28 m. Therefore, also if the longitudinal reinforcement seems well designed to induce a weak-beam-strong column failure mechanism, poor transverse reinforcement characterized both the beams and the columns. The geometry of the cross-sections and a summary of the reinforcement details are reported in

Table 4.1.1.

The building envelope consist of infill realized with hollow clay brick infill walls. The infill panel consists of a double leaf, comprising an internal 120 mm leaf and external 80 mm leaf. Figure 4.1.6 shows the overturning of the external leaf of an infill panel located at the first floor. The bricks were positioned with horizontal holes and connected by 10 mm mortar layers. Two types of connections between the infills and the surrounding RC frame were observed during the inspections: the first made by using classic mortar on four layers (four sides); the second consist in a gap between the beam and the infill panel, resulting in a partial connection (three sides).

Figure 4.1.6. Infill panel overturning due to the 2009 L'Aquila earthquake.

Table 4.1.1. Cross-section and reinforcement details of columns and beams.

	Square Columns both directions			Beams												
				Direction X					Direction Y							
									Perimetral beams					Inner beams		
Storey	b (h) [mm]	$A_{s,t}$ ($A_{s,b}$)	ϕ_{st} (spac.) [mm]	b (h) [mm]	$A_{s,t}$ ($A_{s,b}$)			ϕ_{st} (spac.) [mm]	b (h) [mm]	$A_{s,t}$ ($A_{s,b}$)			ϕ_{st} (spac.) [mm]	v	$A_{s,t}$ ($A_{s,b}$)	ϕ_{st} (spac.) [mm]
-					Right	Center	Left			Right	Center	Left				
I	400 (400)	3ϕ16 (3ϕ16)	ϕ8 (300)	400 (550)	6ϕ16 (3-4ϕ16)	3ϕ16 (3-4ϕ16)	5-6ϕ16 (3-4ϕ16)	ϕ8 (270)	400 (550)	5-6ϕ16 (4-5ϕ16)	3ϕ16 (3-4ϕ16)	5-6ϕ16 (3-4ϕ16)	ϕ8 (270)	400 (200)	3ϕ16 (3ϕ16)	ϕ8 (270)
II	400 (400)	3ϕ16 (3ϕ16)	ϕ8 (300)	400 (550)	6ϕ16 (3-4ϕ16)	3ϕ16 (3-4ϕ16)	6ϕ16 (3-4ϕ16)	ϕ8 (270)	400 (550)	5-6ϕ16 (3-4ϕ16)	3ϕ16 (3ϕ16)	5-6ϕ16 (3-4ϕ16)	ϕ8 (270)	400 (200)	3ϕ16 (3ϕ16)	ϕ8 (270)
III	400 (400)	3ϕ16 (3ϕ16)	ϕ8 (300)	400 (550)	6ϕ16 (3-4ϕ16)	3ϕ16 (3-4ϕ16)	6ϕ16 (3-4ϕ16)	ϕ8 (270)	400 (550)	5-6ϕ16 (3-4ϕ16)	3ϕ16 (3ϕ16)	5-6ϕ16 (3-4ϕ16)	ϕ8 (270)	400 (200)	3ϕ16 (3ϕ16)	ϕ8 (270)
ROOF	400 (400)	3ϕ16 (3ϕ16)	ϕ8 (300)	400 (550)	6ϕ16 (3-4ϕ16)	3ϕ16 (3-4ϕ16)	6ϕ16 (3-4ϕ16)	ϕ8 (270)	400 (550)	5-6ϕ16 (3-4ϕ16)	3-6ϕ16 (3ϕ16)	5-6ϕ16 (3-4ϕ16)	ϕ8 (270)	400 (200)	3ϕ16 (3ϕ16)	ϕ8 (270)

where: b is the cross-section width; h is the cross-section height; $A_{s,t}$ is the top longitudinal reinforcement; $A_{s,b}$ is the bottom longitudinal reinforcement; ϕ_{st} is the diameter of transverse reinforcement; (spac.) is the spacing of transverse reinforcements

4.1.3 Observed damage

The post-earthquake surveys showed severe damage to the structural and non-structural components on the case study building (Figure 4.1.7). In the non-structural components, a significant degradation of the top layer of the mortar on some infills is observed, resulting in a partial connection (three sides) with the frame (see Figure 4.1.7). Significant diagonal cracking of the infills at the first two floors, were observed in both the main building directions along, as well as corner crushing and overturning of the panels. In contrast, no significant damage or zero damage was found on the non-structural components of the upper floors.

Figure 4.1.7. Case study building and observed damage to non-structural components.

Figure 4.1.8 shows the damage observed on the structural components with particular focus on the first floor. The shear cracking at the top end of the columns due to the infill-to-frame interaction was observed. In particular, the shear cracking of the corner joint belonging the selected frame is shown in

Figure 4.1.8 (a). The infill-to-frame interaction is clearer in Figure 4.1.8 (b), where the corner crushing of the bricks due to the infill-to-frame interaction can be observed.

(a)

(b)

Figure 4.1.8. Shear cracking at the top end of the columns observed during the inspections.

4.1.4 Accelerogram record

The accelerogram record represents a mandatory input to perform PsD tests. In the present study, the 2009 L'Aquila earthquake is selected as input according to the building site. An in-depth analysis of the signals recorded at five stations near the epicentral area is performed. In particular, the considered stations are indicated with the following tags: AQA, AQK, AQV, AQU and AQG.

Figure 4.1.9 shows the position of each station with respect to the building location. The accelerograms were recorded by each station in the North-Weast (N-W) direction, in the East-Weast (E-W) direction and in the vertical direction. The longitudinal direction (x) of the case study building, parallel to the frame selected to be tested, presents an angle of 9.5° with respect to the E-W direction (see Figure 4.1.10). Therefore, the original record should be manipulated to evaluate the actual acceleration acting in the direction parallel to the building.

Figure 4.1.9. Case study building and accelerometric stations locations.

However, the original accelerograms recorded by each station in the E-W direction are considered, avoiding the manipulation of the original records.

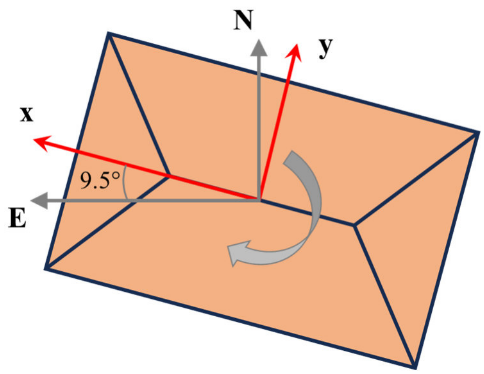

Figure 4.1.10. Inclination of the x direction of the building respect to the East direction in which the earthquake was recorded.

The acceleration response spectra of the records are depicted in Figure 4.1.11 along with the elastic code spectra calculated at the reference site, soil type B for 475 years (life safety, LS) and 975 years (collapse prevention, CP) return periods. These periods are calculated considering a reference life of 50 years, an importance class II (as suggested for ordinary buildings) and the probability of exceedance of 10% and 5% for LS and CP limit states, respectively.

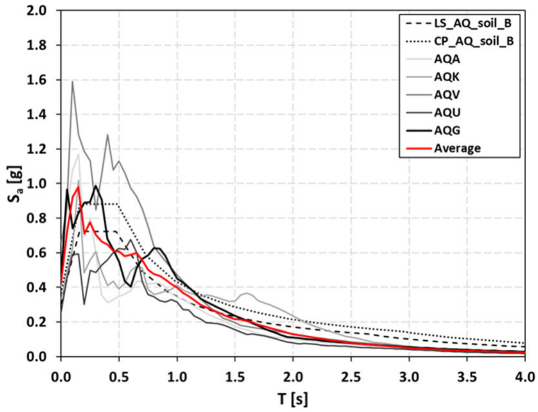

Figure 4.1.11. Acceleration response spectra of the 2009 L'Aquila earthquake and comparison with design spectra.

The design spectra were evaluated using the program "Spettri-NTC ver.1.0.3" [80] considering a viscous damping ζ of 5%. The peak ground acceleration (PGA) of each record is summarized in Table 4.1.2 along with the PGA obtained from the INGV ShakeMap of the L'Aquila 2009 earthquake at the site of the building. The PGA of the records ranges from a minimum of 0.260 g (AQU) to a maximum of 0.546 g (AQV).

Table 4.1.2. Summary of the peak ground acceleration (PGA) recorded by each station.

Station	AQA	AQK	AQV	AQU	AQG	Shake Map
PGA [g]	0.402	0.353	0.546	0.260	0.446	0.451

Figure 4.1.12 shows a close-up on the range of variation of the fundamental period of vibration of the case study building obtained by using the linear numerical model presented successively. The figure shows that the signal recorded by the AQG station is the closest to the code spectra and to the average spectra of the recorded signals. Furthermore, the peak ground acceleration (PGA) of this record is about 0.45 g that correspond to the PGA obtained from the INGV ShakeMap of the L'Aquila 2009 earthquake at the site of the building.

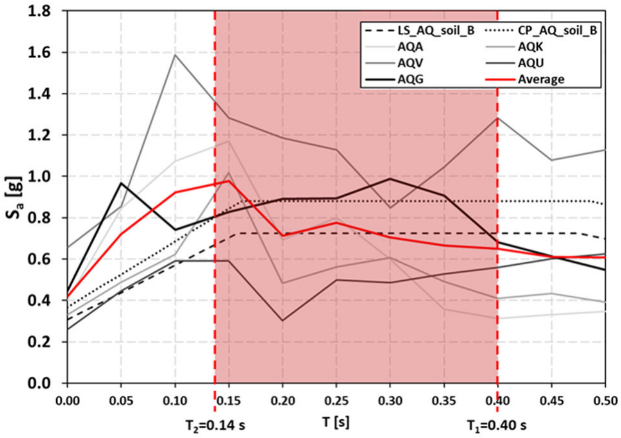

Figure 4.1.12. Acceleration response spectra of the 2009 L'Aquila earthquake and comparison with design spectra in the range 0.00 s-0.50 s.

The same approach is used considering the displacement response spectra of the records along with the design spectra (see Figure 4.1.13). The displacement design spectra are defined considering the same assumptions made above for the definition of the acceleration design spectra.

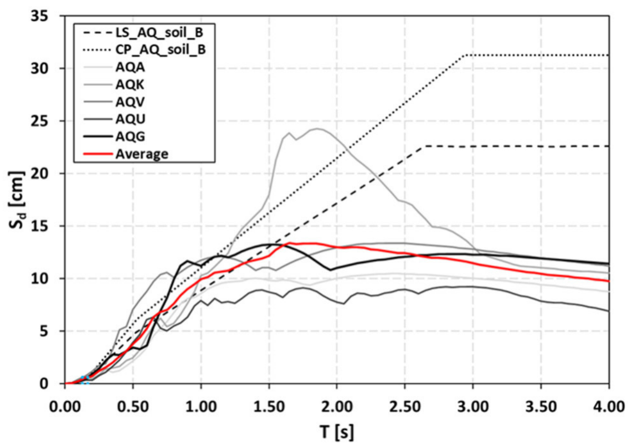

Figure 4.1.13. Displacement response spectra of the 2009 L'Aquila earthquake and comparison with design spectra.

Figure 4.1.14 shows the close-up on the same interval defined in Figure 4.1.12. As a result, the displacement response spectra of the signal recorded by the AQG station is the closest to the design spectra and to the average spectra of the recorded signals.

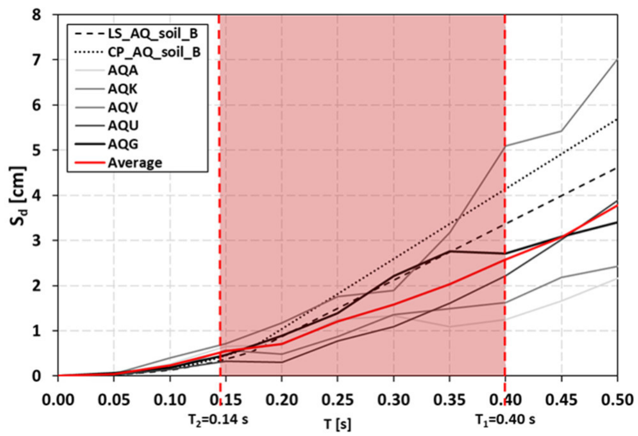

Figure 4.1.14. Displacement response spectra of the 2009 L'Aquila earthquake and comparison with design spectra in the range 0.00 s-0.50 s.

In turn, the AQG signal recorded in E-W direction is used for the tests. The original record, with a duration of 100 s, is shown in Figure 4.1.15. It is shortened to 14 s by removing the tails at low acceleration demand.

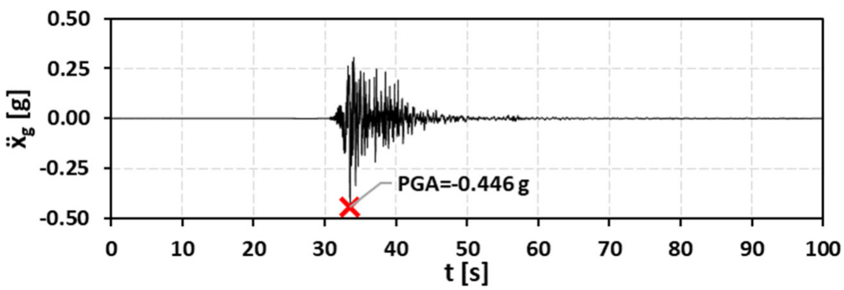

Figure 4.1.15. The AQG E-W 2009 L'Aquila earthquake original record.

This is to have a reasonable duration of the test at large intensities. In particular, the 0.0 s - 30.5 s and the 44.5 s -100 s time interval were removed while a zero accelerations interval was left in the part of the record to be used at beginning of PsD tests as reference to verify the stability of the control system.

The modified AQG accelerogram record, along with the displacement record, is shown in Figure 4.1.16.

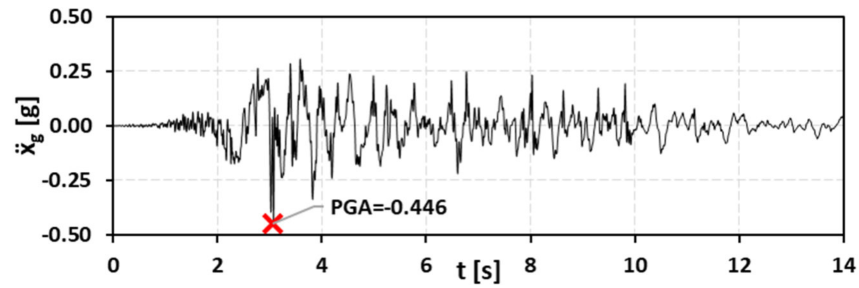

(a)

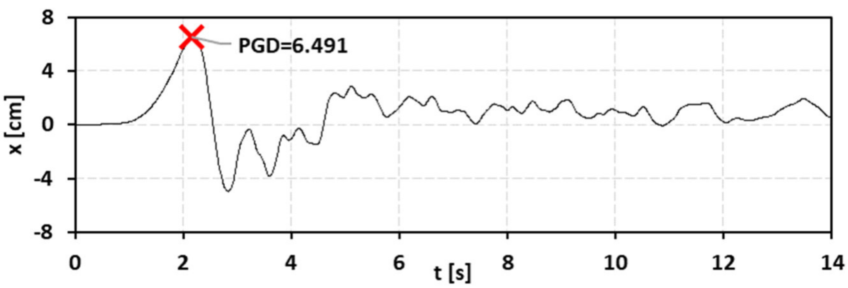

(b)

Figure 4.1.16. (a) The modified E-W AQG accelerogram record; (b) the corresponding displacement record.

Finally, a baseline correction is applied to the record and the matching with the original record in terms of acceleration and displacement response spectra is checked. Figure 4.1.17 shows the comparison between the original record and the modified record in terms of acceleration and displacement response spectra. From the figure, it can be observed that the analyzed spectra completely match.

The record used as input, is scaled to perform PsD tests and numerical analyses with increasing intensities (i.e. 10%, 25%, 50%, 60%, 75%, 100%, 125%, 150%), allowing to account for the stiffness degradation and of the progressive damage.

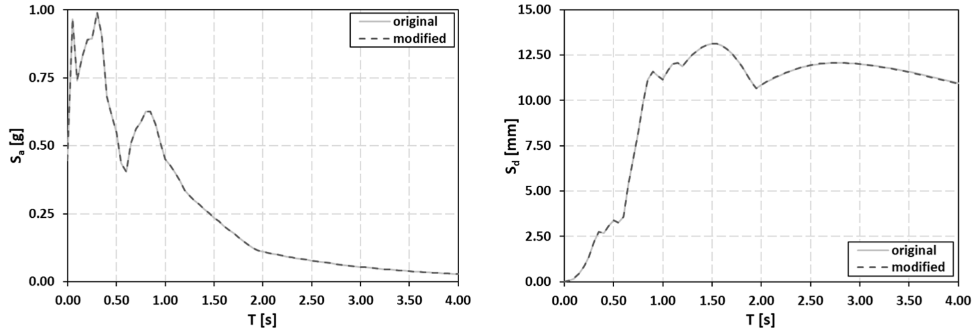

(a) (b)

Figure 4.1.17. Comparison between the original record and the modified record in terms of acceleration and displacement response spectra.

4.1.5 Building nonlinear model

To estimate the building response and verify the following hypothesis on the test substructuring, three different numerical models of the case study building were developed in the SAP 2000 environment [56]. A linear model was developed to conduct a modal analysis. A nonlinear model to conduct static nonlinear analyses (pushover), then refined with definition of hysteretic rules for structural components and infills to conduct nonlinear time histories (NLTHs).

The linear model is realized considering both the contribution of RC members and infills. The RC members are modeled with their central axis, while a three-strut model proposed by Chrysostomou et al. [81] is used for the infills; see Figure 4.1.18. The base columns are considered fixed at the base, thus neglecting the contribution of the foundation. The floor masses are lumped at the center of the floor. A diaphragm restraint is used to connect all the joints of the same floor, thus considering the floor rigid in its own plane. The stairs are modeled with linear elastic shell elements rigidly connected to the columns and floors. The floors' mass m_i is estimated by means of a gravity load analysis, considering dead loads and live loads in the seismic combination defined according to the EC8 [82]. They are equal to 254 tons at first and second floors, 221 tons at the third floor and 132 tons at the fourth floor.

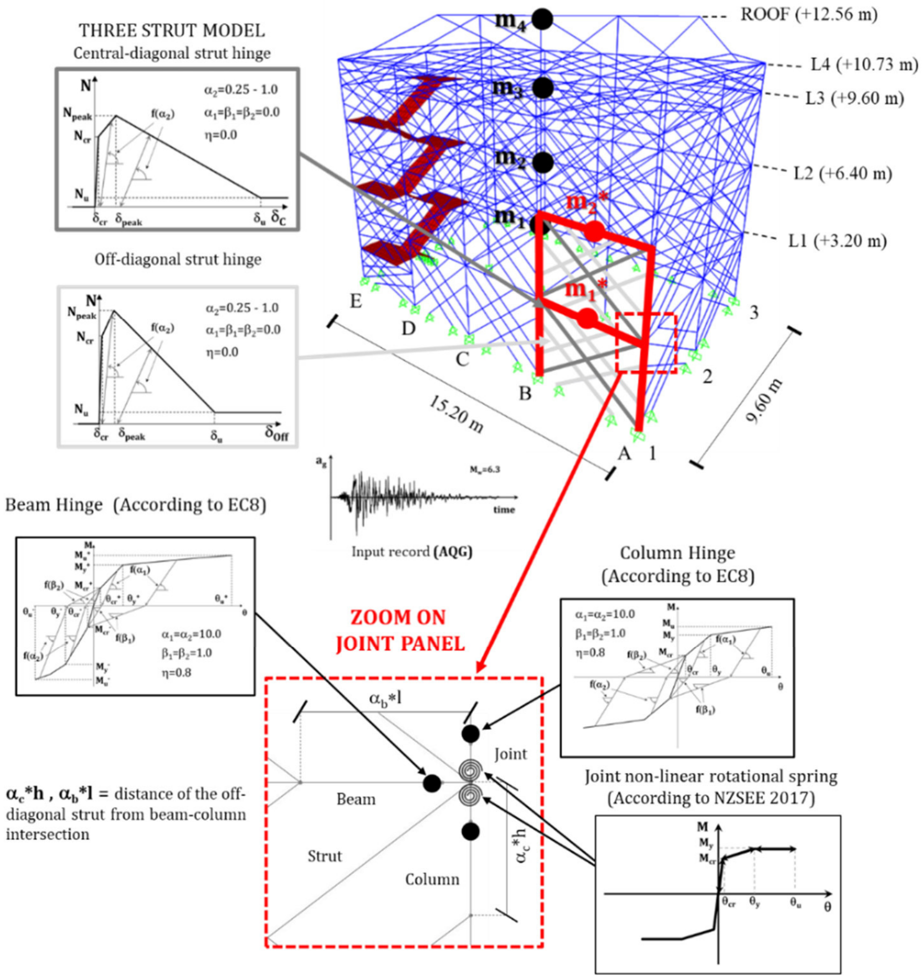

Figure 4.1.18. Numerical model of the infilled RC building and of the frame substructure.

The three struts model [81] consists of a central-diagonal strut and two off-diagonal struts acting only in compression to account for the infill-to-frame interaction. The force of the central strut is transmitted to the beam-column joint while the force of the off-diagonal struts is transmitted both on the column and on the beam of the surrounding frame. The distance of the connection point of the diagonal off-struts from beam-column joint $\alpha_c \cdot h$ and $\alpha_b \cdot h$ (Figure 4.1.19) was estimated according to El-Dakhakhni et al. [83] using the following expressions (4.1) and (4.2):

$$\alpha_c h = \sqrt{\frac{2(M_{pj} + 0.2M_{pc})}{t_m\, f'_{m-0}}} \leq 0.4\, h \tag{4.1}$$

$$\alpha_b l = \sqrt{\frac{2(M_{pj} + 0.2M_{pb})}{t_m\, f'_{m-90}}} \leq 0.4\, l \tag{4.2}$$

where α_c is the ratio of the column contact length to the height of the column and α_b is the ratio of the beam contact length to the length to the span of the beam; h is the column height and l the beam span; M_{pj} the minimum of the column's, the beam's or connection's plastic moment capacity referred to as the plastic moment capacity of the joint; M_{pc} and M_{pb} the column and the beam plastic moment capacities; t_m the thickness of the infill panel; f'_{m-0} and f'_{m-90} the compressive strength of the masonry panel parallel and normal to the bed joint.

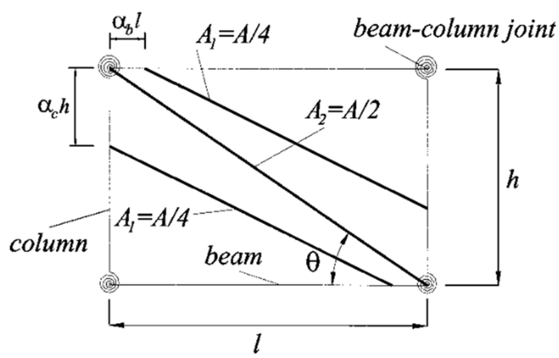

Figure 4.1.19. The concrete masonry-infilled model approach proposed by El-Dakhakni et al. [83].

The width b_m of the struts cross-section is defined according to the method proposed by Stafford Smith [84] (4.3) :

$$b_m = [0.175(\lambda h_m)^{-0.4}]d_m \tag{4.3}$$

where h_m is the height of the infill panel, d_m is the length of the diagonal strut, and λ is the stiffness ratio which takes into account of the relative stiffness of the masonry panel to the frame, defines as (4.4):

$$\lambda = \sqrt[4]{\frac{E_m t_m \sin 2\theta}{4E_c I_c h_m}} \tag{4.4}$$

with E_m, the elastic modulus; θ the angle between the diagonal and base of the infill panel; E_c and I_c the elastic modulus and the moment of inertia of the columns. This method allows to define the width of a single strut in order to calculate the area of the cross-section with thickness t_m. However, the three-struts model is used to reproduce the response of the infill. Therefore, a method is required to distribute the single strut cross-section area among the three struts taking into account for the diagonal length of each strut (i.e., central-diagonal and off-diagonal) and maintaining the strength and stiffness of the original single strut. This method is presented successively.

The evaluation of the initial elastic stiffness of the RC and infill members model is mandatory in the building model to perform a modal analysis. It is evaluated based on the cross-sectional area, on the length of the element and on the elastic modulus of the material of which each member is made. According to the experimental test conducted on the material used to realize the frame specimen, the materials properties assumed in the numerical model of the building are: concrete mean compressive strength f_{cm} of 18 MPa; steel rebars mean yielding stress f_{ym} of 535 MPa; infill mean compressive strength parallel to holes f_{m-0} of 2.59 MPa; infill mean compressive strength normal to holes f_{m-90} of 1.91 MPa; mean elastic modulus E_{m-0} of infill parallel to holes of 4445 MPa; mean shear modulus G_m of infill of 1063 MPa; mean shear strength τ_{cr} of infill of 0.35 MPa. More details on the material properties characterization are discussed in 5.1.1.

A lumped plasticity approach is used to simulate the nonlinear behaviour of the RC members and of the infills. Figure 4.1.20 shows a 1-bay-1-storey infilled RC frame used as reference to support the discussion. The plastic hinges of the RC elements are located at the end of the elastic elements and are characterized according to the Eurocode 8 prescriptions [85]. In the characterization of the M-θ relationship, the rotation at cracking, yielding and ultimate states and related bending moment are defined.

The nonlinear behaviour of the infills is characterized considering a three-strut model [81] acting only in compression. The struts axial hinge is located at the centre of the elastic element. The relationship proposed by Panagiotakos and Fardis [8] in terms of interstorey shear-displacement is used to characterize the response of the equivalent strut considering cracking, peak and residual strength.

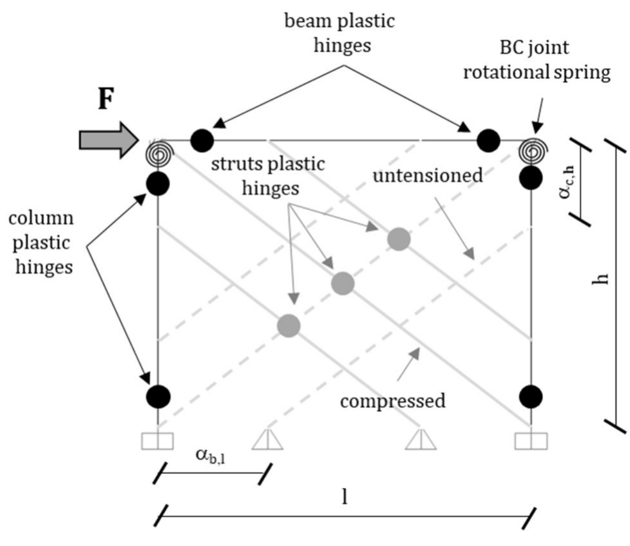

Figure 4.1.20. 1-bay-1-storey reference infilled RC frame.

Figure 4.1.21 shows the relationship proposed by the authors. It is a multilinear curve in monotonic loading with an initial elastic stiffness K_{el} defined as (4.5):

$$K_{el} = \frac{G_m l_m t_m}{h_m} \tag{4.5}$$

and a cracking shear V_{cr} equal to (4.6):

$$V_{cr} = \tau_{cr} l_m t_m \tag{4.6}$$

where G_m and τ_{cr} are the shear modulus and the cracking stress of the infill panel measured in a diagonal compression test of the infill panel. The cracking displacement d_{cr} is then calculated as the ratio between the elastic stiffness K_{el} and the cracking shear V_{cr} (4.7):

$$d_{cr} = \frac{V_{cr}}{K_{el}} \tag{4.7}$$

Based on the (4.5), the elastic modulus of the infill panel is evaluated as (4.8):

$$E_m = \frac{K_{el} d_m}{A_m \cos \theta^2} \tag{4.8}$$

with d_m the length of the strut and A_m the cross-section area calculated as (4.9):

$$A_m = b_m t_m \tag{4.9}$$

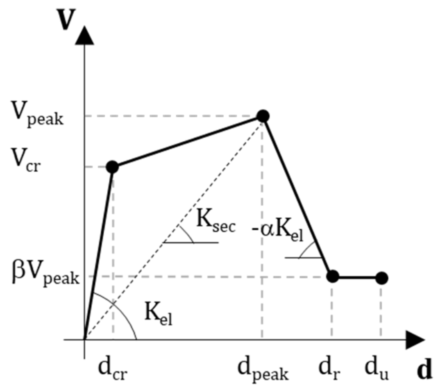

Figure 4.1.21. Interstorey shear-displacement relationship proposed by Panagiotakos and Fardis [8] for the equivalent strut model.

The post-cracking hardening branch is characterized of a peak shear V_{peak} evaluated as (4.10):

$$V_{peak} = 1.3\,\tau_{cr} l_m t_m \tag{4.10}$$

and is limited to a peak displacement d_{peak} equal to (4.11):

$$d_{peak} = \frac{V_{peak}}{K_{sec}} \tag{4.11}$$

where the secant stiffness K_{sec} is calculated according to Mainstone [86] (4.12):

$$K_{sec} = \frac{E_m b_m t_m}{d_m} \cos\theta^2 \tag{4.12}$$

The third branch of the envelope is a degrading branch with a stiffness equal to $-\alpha K_{el}$, to the achievement of a residual shear equal to βV_{peak}. The parameters α and β used in this study are 0.03 and 0.01 according to the range of values proposed by the authors. The displacement d_r corresponding to the residual shear βV_{peak} is evaluated by geometric assumptions, while the ultimate displacement d_u is calculated three times larger than the displacement d_r.

Once the interstorey shear-displacement envelope has been defined for each infill panel [8], the strength and stiffness distribution into the three struts (i.e., central-diagonal and off-diagonal struts) can be performed. The approach proposed by Chrysostomou et al. [81] and recently validated by Verderame et al. [6] based on experimental tests is used for the purpose. Figure 4.1.22, shows a reference scheme reported in [87] demonstrating that the envelope curve evaluated for the equivalent strut is recovered if the contribution of each struct in the three struts model are combined.

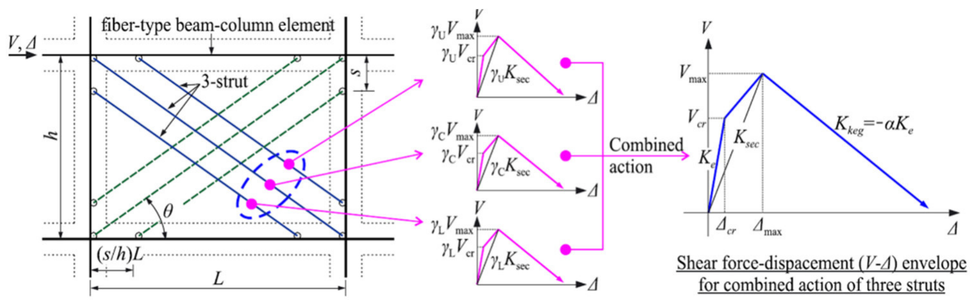

Figure 4.1.22. Three-strut model of infill panel reference scheme reported in [87].

The approach used for the strength and stiffness distribution, depending on the eccentricity of off-diagonal struts and the central-diagonal strut through the parameter α_{off} defined as the ratio between the end-point of the lower off-diagonal strut z_c and the height of the infill panel h_m (4.13):

$$\alpha_{off} = \frac{z_c}{h_m} \tag{4.13}$$

with z_c calculated according to the Figure 4.1.23, as the difference between the column height and the contact length to the height of column (4.14):

$$z_c = h - \alpha_c h \tag{4.14}$$

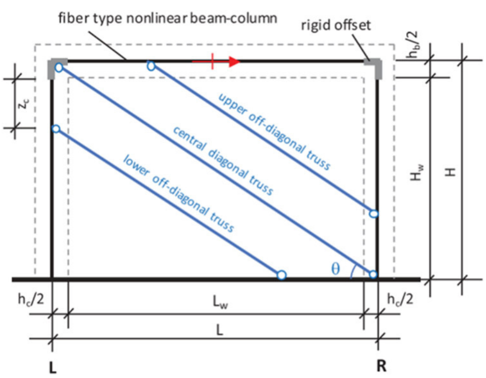

Figure 4.1.23. Definition of the end-point of the lower off-diagonal strut $\mathbf{z_c}$ [6].

The axial stiffness of the central strut k_c and the corresponding displacement d_c can be calculated starting from the knowledge of the stiffness K of the equivalent strut and the corresponding displacement d in the horizontal direction, using the following expressions (4.15) and (4.16):

$$k_c = \frac{K}{\cos^2\theta} \cdot \gamma_c \tag{4.15}$$

$$d_c = d \cdot \cos\theta \tag{4.16}$$

where γ_c represents the portion of the lateral load absorbed by the central-diagonal strut according to Jeon et al. [87]:

$$\gamma_c + 2\gamma_{off} = 1 \tag{4.17}$$

with γ_{off} the portion of the lateral load absorbed by the off-diagonal struts. In this study, γ_c and γ_{off} were assumed to be 0.35 and 0.33 according to the authors. The stiffness of the off-diagonal struts k_{off} and the corresponding displacement d_{off} can be evaluated assuming the hypothesis of linear deformed shape of the columns suggested by Chrysostomou et al. [81], as in (4.18) and (4.19):

$$k_{off} = \frac{K - k_c \cdot \cos^2\theta}{2(1-\alpha)^2 \cdot \cos\theta^2} = \frac{K(1-\gamma_c)}{2(1-\alpha)^2 \cdot \cos^2\theta} \tag{4.18}$$

$$d_{off} = d \cdot \cos\theta \cdot (1-\alpha) \tag{4.19}$$

Finally, the axial load acting N_c in the central diagonal and off-diagonal struts N_{off} can be calculated according to (4.20) and (4.21):

$$N_c = k_c \cdot d_c = \left(\frac{K}{\cos^2\theta} \cdot \gamma_c\right) \cdot (d \cdot \cos\theta) = \frac{K \cdot d}{\cos\theta} \cdot \gamma_c = \frac{V}{\cos\theta} \cdot \gamma_c \tag{4.20}$$

$$\begin{aligned} N_{off} = k_{off} \cdot d_{off} &= \frac{K(1-\gamma_c)}{2(1-\alpha)^2 \cdot \cos\theta^2} \cdot \big(d \cdot \cos\theta \cdot (1-\alpha)\big) \\ &= \frac{K(1-\gamma_c)}{2(1-\alpha) \cdot \cos^2\theta} \cdot d = \frac{V}{\cos\theta} \frac{(1-\gamma_c)}{2} \frac{1}{(1-\alpha)} \end{aligned} \tag{4.21}$$

In this way, it is possible to define the axial stiffness, the axial load and the corresponding displacement of the points necessary to define of the backbone curve of each diagonal strut (i.e., central strut and off-struts). The backbone curve represents the $N - d$ relationship assigned to the plastic hinge to reproduce the nonlinear behaviour of the infill panels in the nonlinear building model.

The correct definition of the cross-sectional area of struts is a fundamental to proper reproduce the initial elastic stiffness of the infill panel in the modal analysis. The area A_m calculated with (4.9) cannot be divided equally among the three struts. Therefore, the area assigned to each strut in the numerical model must be defined correctly. In this study, the cross-section area of each strut is defined according to the length of the diagonal strut d_m, the elastic modulus E_m (4.8) and the evaluated axial stiffness k_c or k_{off}, as (4.22):

$$A_{c\,(off)} = \frac{d_{m,c\,(off)} \cdot k_{c\,(off)}}{E_m} \tag{4.22}$$

The nonlinear behaviour of beam-column joint is reproduced using a rotational spring (Figure 4.1.18) with M-θ relationship characterized according to the suggestion of the NZSEE guidelines for the seismic assessment of existing buildings [88]. It consists in the definition of two rotational springs located immediately at the top and bottom of the centre of the joint. In addition, the M-θ relationship is represented by a monotonic curve.

The nonlinear building model is then refined to include hysteretic response of RC members and infill struts. A pivot model [85] is selected because it allows to capture the pinching effect typical of poorly detailed non-ductile members. Figure 4.1.24 shows the pivot hysteretic model reported in Dowell et al. [78]. The P_1 and P_4 points represent the primary pivot points which control the amount of softening expected with increasing displacement, while the points PP_2 and PP_4 represent the pinching pivot point which fix the degree of pinching following a load reversal.

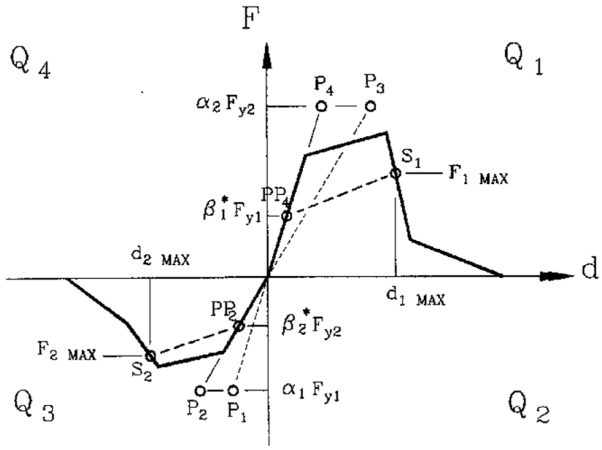

Figure 4.1.24. Pivot hysteresis model [78].

The parameters used to characterize this model are the following [89]:

- α_1 which locates the pivot point for unloading to zero from positive force. Unloading occurs toward a point on the extension of the positive elastic line, but at a negative force value of α_1 times the positive yield force.
- α_2 which locates the pivot point for unloading to zero from negative force. Unloading occurs toward a point on the extension of the negative elastic line, but at a positive force value of α_2 times the negative yield force.
- β_1 which locates the pivot point for reverse loading from zero toward positive force. Reloading occurs toward a point on the positive elastic line at a force value of β_1 times the positive yield force, where $0.0 < \beta_1 \leq 1.0$. Beyond that point, loading occurs along the secant to the point of maximum previous positive deformation on the backbone curve.

- β_2 which locates the pivot point for reverse loading from zero toward negative force. Reloading occurs toward a point on the negative elastic line at a force value of β_2 times the negative yield force, where $0.0 < \beta_2 \leq 1.0$. Beyond that point, loading occurs along the secant to the point of maximum previous negative deformation on the backbone curve.
- η which determines the amount of degradation of the elastic slopes after plastic deformation, where $0.0 < \eta \leq 1.0$.

In addition, the pinching pivot points, initially fixed, move towards the origin once the strength degradation has occurred. In particular, the value of β_i is equal to:

$$\beta_i^* = \beta_i \quad (d_{max} \leq d_{peak}) \tag{4.23}$$

$$\beta_i^* = \frac{F_{max}}{F_{peak}} \beta_i \quad (d_{max} \geq d_{peak}) \tag{4.24}$$

The parameters adopted for the RC members were calibrated on cyclic experimental tests on RC members and infilled RC frames subjected to cyclic loads [6] available in literature studies. The hysteretic law of the infill strut is reproduced using the pivot model using only the α_2 parameter as suggested in Cavaleri and Di Trapani [5], while the other parameters are set to zero. This is because, the parameters α_1 and β_1 are null since the infill panels does not provide any contribution in terms of tensile strength. In addition, from the experimental test on the infilled frame has been observed that the system does not gain stiffness at load reversal until the whole plastic deformation is recovered. Therefore, based on this assumption the β_2 parameter is also null. In this study, the α_2 parameter was experimentally calibrated and set equal to 0.5. The calibration of this parameter will be discussed successively in the Chapter 5.

4.2 The proposed substructuring approach

4.2.1 From the building to the laboratory: 1-bay 2-storey infilled RC frame

Due to limitation in the height of the laboratory reaction wall and to avoid the scaling of the specimen, only the most damaged frame is selected from the case study existing building and reproduced in full-scale in the laboratory environment to perform the PsD tests. It is a perimetral frame ending with a corner column. Only the first two stories, where most of the earthquake damage is located, have been constructed in laboratory (see Figure 4.2.1).

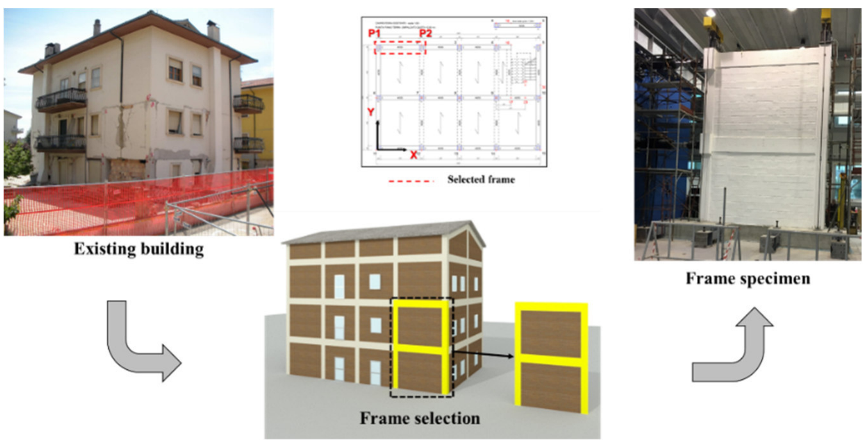

Figure 4.2.1. Frame selection from the existing infilled RC building.

The PsD testing procedure requires the definition of the mass matrix [M] and the initial stiffness matrix $[K_0]$ as well as the rules for combining the different floor stiffnesses to assemble the initial stiffness matrix. Therefore, a reliable substructuring approach is needed to define the mass matrix [M] starting from the global building masses m_i and assuring that the displacement applied on the frame prototype are comparable with those applied on the same frame when considering that the whole building is subjected to the earthquake shaking (see Figure 4.2.3), guaranteeing the following condition (4.25):

$$d_1^* = d_1 \quad \text{and} \quad d_2^* = d_2 \tag{4.25}$$

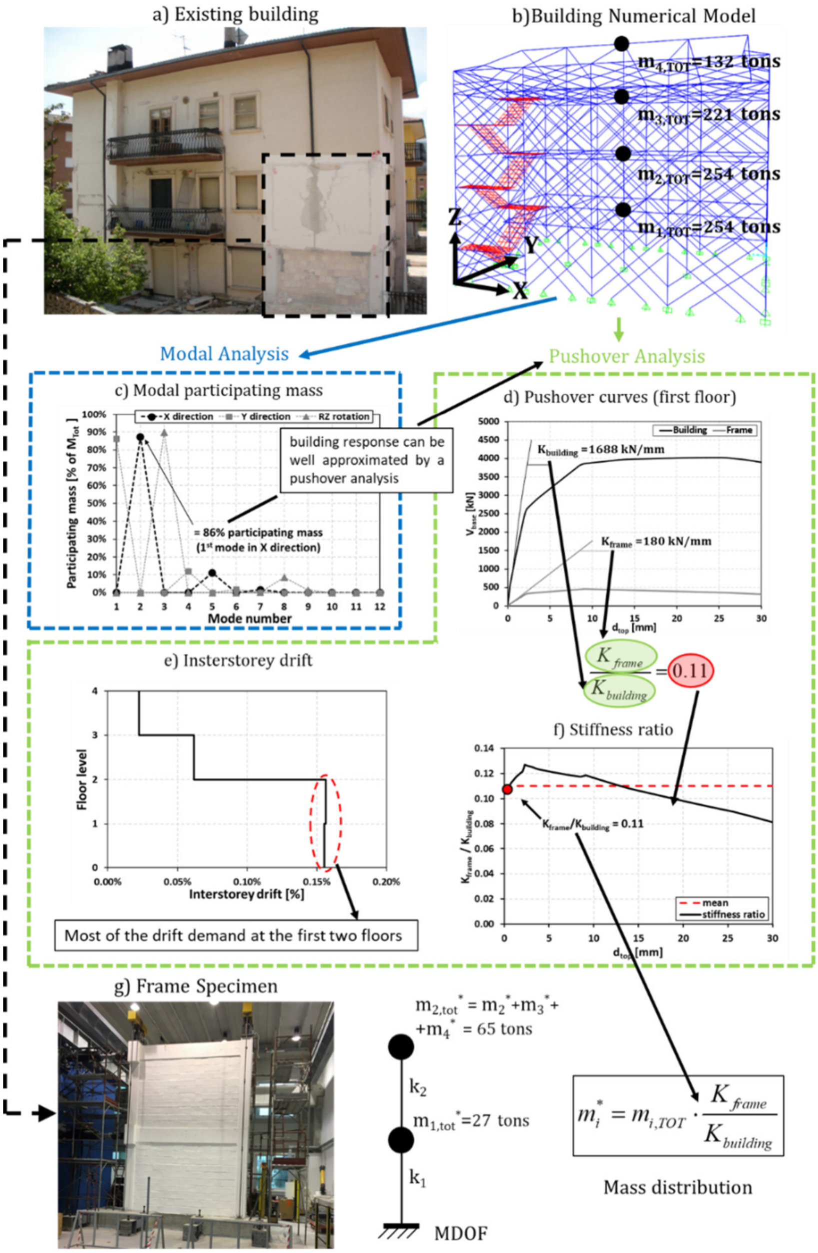

Figure 4.2.2. Case study building and substructuring procedure.

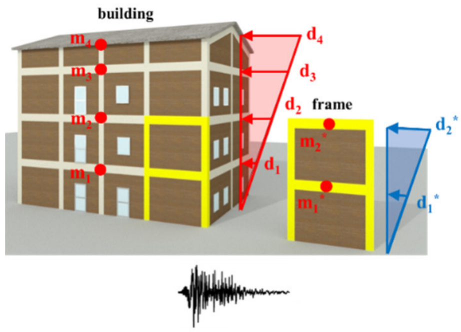

Figure 4.2.3. Displacement profile acting on both structural systems during earthquake event.

The substructuring approach relies on the results of a modal analysis considering the initial stiffness of structural members and infills and of a nonlinear static analysis on an infilled numerical model. Then the proposed substructuring approach and the related assumptions are verified comparing the results of nonlinear time history analysis (NLTH) at building and frame level. Figure 4.2.2 shows the substructuring procedure and the corresponding analysis used for the purpose.

First a modal analysis of the linear building model is performed considering the initial stiffness of the structural members and infills. The results show that the participating mass ratio to first mode is significantly higher than the other modes (about 86%; see Figure 4.2.2 c); thus, the building response can be well approximated by a pushover analysis with floor displacements applied all in the same direction. The mode shapes of the nonlinear building model are shown in Figure 4.2.4 and Figure 4.2.5.

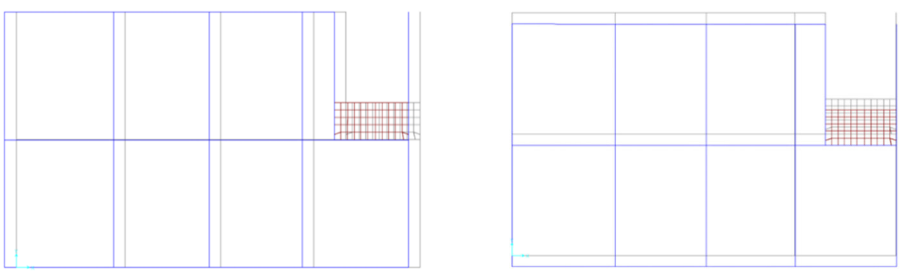

(a) (b)

Figure 4.2.4. Building model translational mode shapes: 1st mode along x; 2nd mode along y.

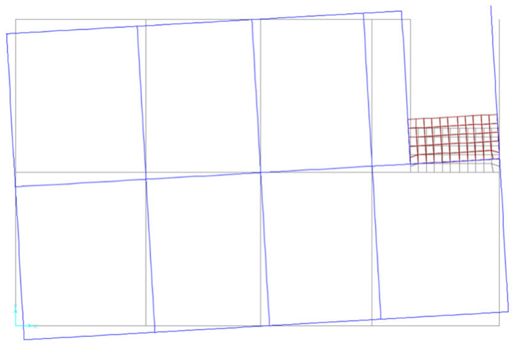

Figure 4.2.5. Building model torsional mode shape around z.

Based on this assumption, a pushover analysis is performed to evaluate the lateral response of the building and of the selected frame. A unitary force F is applied at the first level in the direction of the selected frame to obtain the response of a single floor (see Figure 4.2.6). This was repeated for all the other floors restraining the lateral displacement of the lower floors. The response of the base floor is reported in Figure 4.2.2 d), and it is representative of all other floors due to the similarities in geometry and reinforcement details of columns, beams and infills.

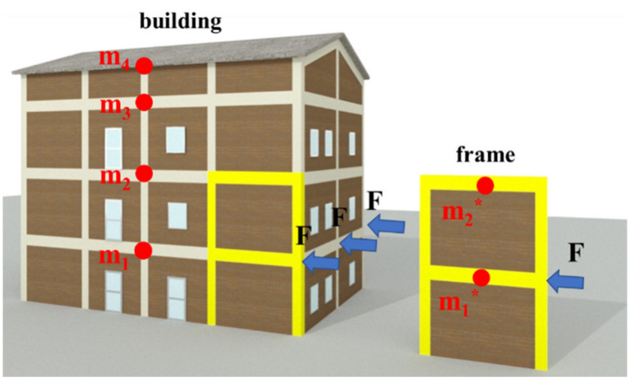

Figure 4.2.6. Nonlinear static analysis performed on both numerical models applying a unitary force at first level.

As a result of these analyses, two different substructuring approaches can be used: the first consists in the implementation of a full building model in the coordinator system (Figure 3.2.1) reproducing the contribution of the portion of the building not available in the laboratory by means of a numerical model (hybrid testing); the second one consists in the definition of the mass matrix of the frame built in the laboratory considering the portion of the seismic force effectively carried by that frame basing on the results of numerical analyses. In this study, the second approach was preferred because it allows to better control the stability of the algorithm and a direct identification of possible errors. These aspects are of paramount importance considering that this was the first testing program carried out with the proposed PsD testing infrastructure.

Thus, as shown in the Figure 4.2.2 g) the mass, $m^*_{i,TOT}$, attributed to the case study frame is the product of the total floor mass m_i and a distribution coefficient equal to 0.11 (evaluated as the ratio of the initial stiffness of frame k_{frame} and that of the whole building $k_{building}$, see Figure 4.2.2 f). This coefficient was calculated at imposed top displacement d_{top} of 0.56 mm where the building and frame behave mostly elastic. The variability of this ratio within the range of the imposed top displacement is reported in Figure 4.2.2 f). It is shown that the mean ratio $k_{frame}/k_{building}$ is very close to the one calculated in the elastic range (i.e. 0.11). This study relies on the assumption that the contribution of the selected 1-bay 2-storey frame in the global building response can be represented by the response of the frame alone considered as non-interactive with surrounding members. This assumption was checked comparing the contribution in terms of base shear $V_{base,building}$ of the frame measured from a global analysis of the entire building and the total base shear of the frame alone $V_{base,frame}$ under the same imposed top displacement. A difference of about the 10% confirms the reliability of this assumption. Furthermore, the masses of the third and the fourth floor are lumped at the second floor assuming that these two floors behave as rigid. This assumption is supported by the drift distribution resulted from the nonlinear static analysis on the building model in which the uppers floor exhibited very small deformations (see Figure 4.2.2 e) and by the damage observed in-situ showing that the last two floors were characterized by negligible damage (Figure 4.1.7). Accordingly, the portion of the total mass attributed to the studied frame at the first, $m^*_{1,TOT}$, and second level, $m^*_{2,TOT}$, are equal to 27.0 tons and 65.0 tons (calculated as the sum of masses, m^*_2, m^*_3 and m^*_4 respectively). The mass matrix defined as input to perform the PsD test on the substructure frame is reported in (4.26). The portion of these masses belonging to the test frame is about 23.6 tons and 14.1 tons for the first and second floor, respectively.

$$[\mathrm{M}^*] = \begin{bmatrix} \mathrm{m}^*_{1,\mathrm{TOT}} & 0 \\ 0 & \mathrm{m}^*_{2,\mathrm{TOT}} \end{bmatrix} = \begin{bmatrix} 27.0 & 0 \\ 0 & 65.0 \end{bmatrix} \text{ [tons]} \tag{4.26}$$

It is worth remembering that the initial stiffness matrix $[\mathrm{K}_0]$ of the tested frame is evaluated at the beginning of each test since it depends on the stiffness degradation and damage evolution.

The building model was used to conduct nonlinear time history analysis. To account for the damage evolution, strength and stiffness degradation with the increasing earthquake intensity a unique acceleration time history including all the scaled AQG records (from 10% to 150% intensity) in row is used as input. The record is applied at the base of the model in the direction parallel to the frame. The analysis results and the numerical validation of the proposed substructuring approach are discussed in the paragraph 4.2.3.

4.2.2 Frame nonlinear model

Figure 4.2.7 shows the nonlinear model developed in SAP2000 environment [56] of the full-scale infilled RC frame physically built in the laboratory environment. In this figure, it is possible to observe that the frame nonlinear model is modelled in the same way as the building model. In fact, a lumped plasticity approach is used to reproduce the nonlinear response of beams, columns and infills. The plastic hinges of beam and columns are characterized according to the suggestion of the Eurocode 8 [85] modelling the cracking, yielding and a perfectly plastic response up to the ultimate rotation. The infill lateral response is reproduced using the model of the equivalent struts proposed by Panagiotakos & Fardis [8] then distributed in a three-strut model using the procedure proposed by Chrysostomou et al. [81]. It is worth mentioning in advance that the top off-strut is omitted in the model used to reproduce the response of the frame F2_3S_M. This aspect will be explained in 5.2.2.

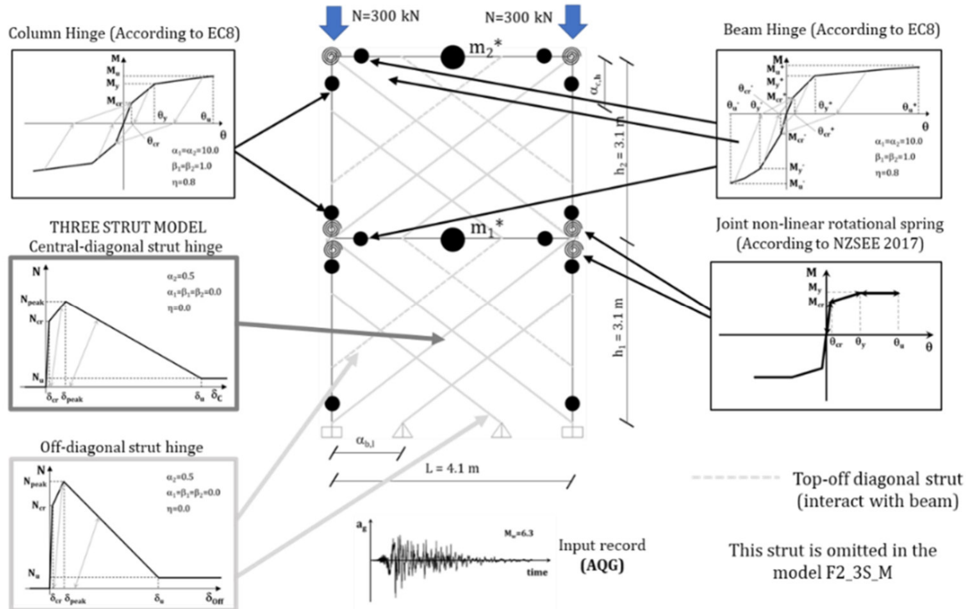

Figure 4.2.7. Frame nonlinear model.

The hysteresis model adopted to reproduce the RC members and infill panels hysteretic behaviour is the pivot model [78]. The nonlinear response of beam-column joints is reproduced by using a double hinge model [90] where the nonlinear response (cracking and peak) is characterized as suggested in the NZSEE 2017 [88]. The material properties considered for each material are those used for the building nonlinear model reported in 4.1.5. Details on the geometry and mechanical characterization of the plastic hinges are reported in Figure 4.2.7.

In Table 4.2.1, the force-deformation law, the hysteresis law and the related parameters implemented in the numerical models are summarized. As seen for the building nonlinear model, the parameter α_2 of the infill Pivot model is set equal to 0.5. The calibration of this parameter will be successively discussed in 5.2.1.

Table 4.2.1. Modeling assumptions and related parameters.

geometrical and nonlinear model			force-deformation relationship	hysteresis	
member	nonlinear element	location		Model	parameters
columns	rotational plastic hinges	at member ends	Moment-Rotation according to Eurocode 8	pivot	α1=10 α2=10 β1=1 β2=1 η=0.8
beams	rotational plastic hinges	at member ends	Moment-Rotation according to Eurocode 8	pivot	α1=10 α2=10 β1=1 β2=1 η=0.8
infills	three struts with axial hinge	at member centre	according to Panagiotakos and Fardis (1996)	pivot	α_2 = 0.5
beam-column joints	two rotational springs	above and below the joint centroid	according to NZSEE (2017)	multilinear elastic	-

4.2.3 Numerical validation

The validation of the adopted substructuring approach is carried out comparing the results in terms of the displacement at the second floor obtained from NLTH analysis performed on the building and frame numerical model (see Figure 4.2.8).

The record of the 2009 L'Aquila earthquake (AQG record in E-W direction) is used as input. Then, an acceleration history consisting of the scaled AQG records (i.e., 10%, 25%, 50%, 75%, 100%, 125% and 150%) in row is used as input for the analysis and applied in the direction parallel to the frame.

Figure 4.2.8 shows the approach used to validate the proposed substructuring approach. The reliability of the substructuring approach is validated by comparing the results of the NLTH analyses performed on the building and frame numerical model to verify that the displacement applied on the frame prototype are comparable with those applied on the same frame, according to the (4.25) when considering that the whole building is subject to the earthquake shaking (Figure 4.2.8).

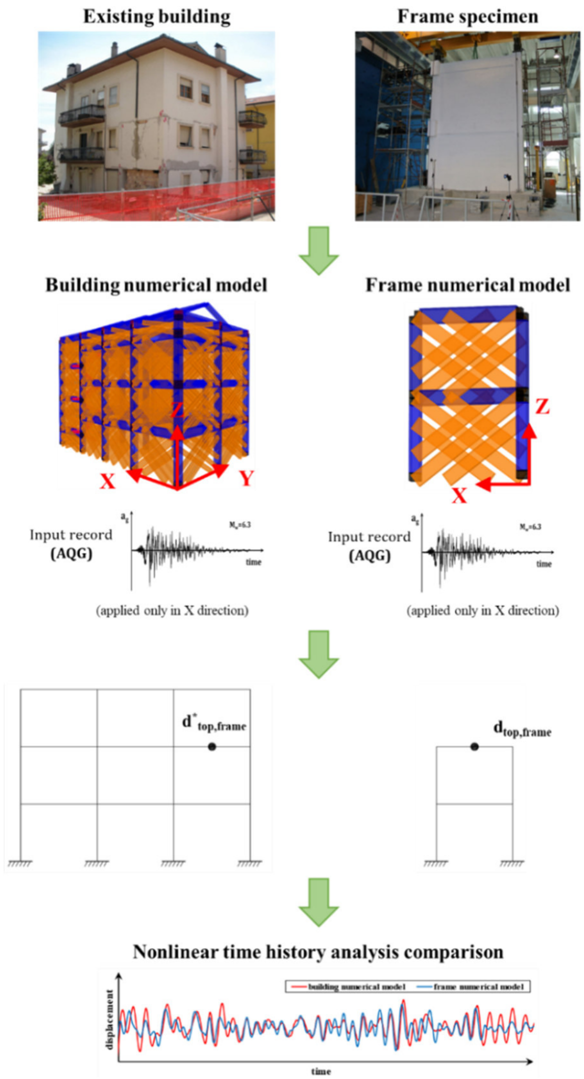

Figure 4.2.8. Validation of numerical result of nonlinear time history analysis.

The comparison in terms of the displacement response under the 50% of the earthquake intensity is reported in Figure 4.2.9. The comparison shows a good agreement in terms of absolute maximum displacement.

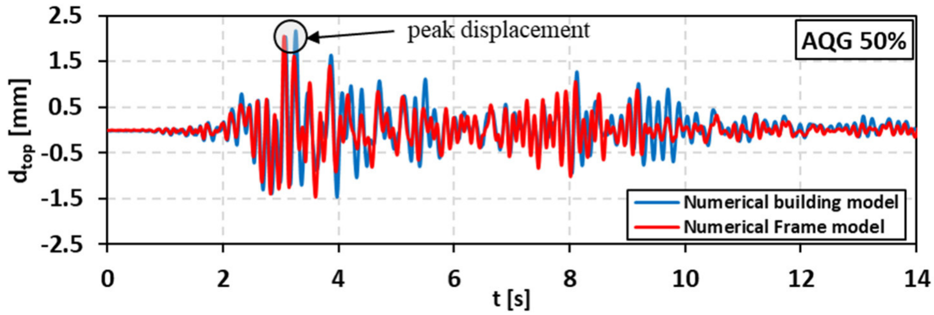

Figure 4.2.9. Comparison between the numerical results obtained from the building and the frame numerical models in terms of top displacement $\mathbf{d_{top}}$ at intensity of 50%.

The same comparison is performed for all the other earthquake intensities, and it is reported in Figure 4.2.10 in terms of the ratio $d_{top,frame}/d^{*}_{top,frame}$ of the displacement at the top of the selected frame.

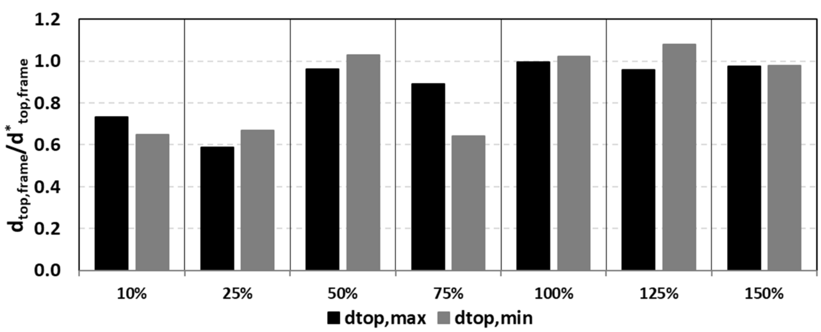

Figure 4.2.10. Comparison between the numerical results obtained from the building and the frame numerical models in terms of top displacement $\mathbf{d_{top}}$ at all the intensities.

The results show that the agreement between the displacements in both directions increases with increasing intensity. At the intensity of 10% and 25% of the AQG record, it is observed that the displacement ratio is lower than unity (from 0.59 to 0.73) meaning that the displacement at the top of the frame recorded in the frame model is lower than the one recorded in the building model. When the intensity increases (from 50% to 150%), the displacement ratio is close to 1.00 showing the good matching between the frame model with mass substructuring and the whole building model.

Figure 4.2.11 shows the time history at 100% of AQG in terms of displacement demand at the second floor obtained from the numerical models. A good matching can be observed between the displacement demand at the second floor obtained from the numerical frame model and building model. The two responses are in good agreement for all the duration of the earthquake.

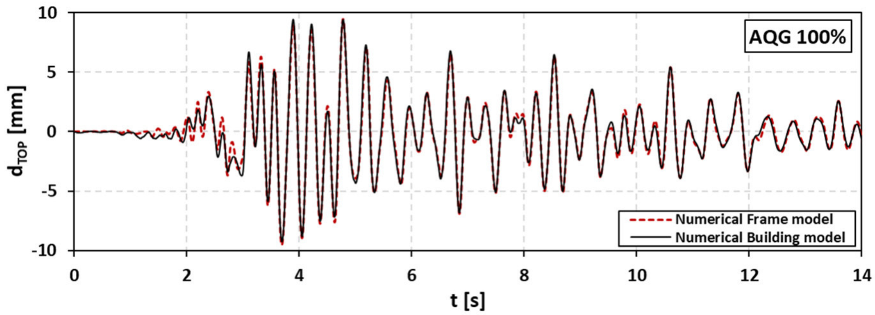

Figure 4.2.11. Comparison in terms of displacement demand $\mathbf{d_{top}}$ at the second floor from numerical models.

Figure 4.2.12 shows the results in of ratio $V_{base,frame}/V^{*}_{base,frame}$ of the base shear in the positive and negative directions for all the earthquake intensities.

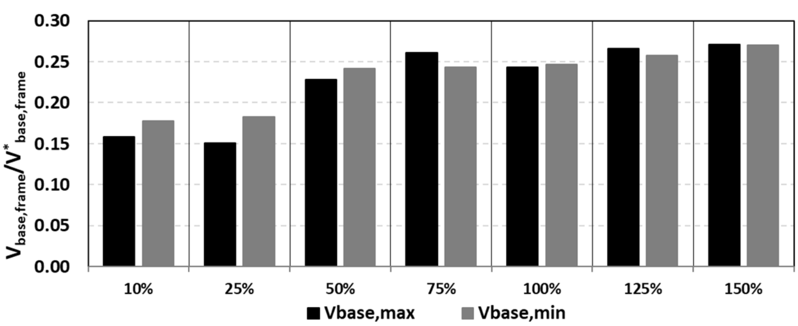

Figure 4.2.12. Comparison between the numerical results obtained from the building and the frame numerical models in terms of base shear $\mathbf{V_{base}}$ at all the intensities.

The figure shows that the base shear ratio increases as the intensity of the AQG record increases. In this case, $V^{*}_{\text{base,frame}}$ is evaluated as the sum of the shear forces at the base of the outer frame of the building from which the reference frame was extracted (see Figure 4.2.1). Since the geometry and the reinforcement details of the members belonging to the outer frame are the same, as discussed in 2, a uniform base shear distribution between the different frames can be assumed. This assumption is confirmed by Figure 4.2.12 which shows a base shear ratio of 0.25, starting from 50% to 150% of the intensity.

Based on the results of the numerical analyses, it can be concluded that the proposed substructuring approach is accurate and reliable for medium-to-high intensity earthquakes. Although some differences can be observed in terms of peak displacement demand, they are negligible, and this confirms the reliability of the adopted substructuring approach. Accordingly, the previously defined mass matrix (4.26) was implemented in the PsD framework to perform the experimental tests on the infilled RC frame prototype.

Chapter 5

5. Experimental tests on full-scale infilled reinforced (RC) frames

The most damaged frame belonging to the case study building was selected and reproduced in the CeSMA laboratory environment to perform PsD tests. It consists of a perimetral frame ending with a corner column. Only two stories were reproduced in the laboratory environment due to the limitation of laboratory dimensions. Therefore, a simplified substructuring approach was proposed and numerically validated to define the mass matrix to be assigned to the substructured frame accounting for the contribution of the remaining portion of the whole building. The L'Aquila 2009 accelerogram recorded in the E-W direction by the AQG station was selected as input. The response of three frames with three different infill-to-frame connections was investigated during the tests. In addition, the damage of the structural and non-structural members was assessed. The experimental results were used both to experimentally validate the substructuring approach and to calibrate the parameters of the hysteretic rule adopted to reproduce the nonlinear behaviour of the infill panels. They are also compared to the numerical results obtained from the analysis performed on the nonlinear building model. Then, the pivot model with the calibrated parameter was successively implemented in a regional scale loss-assessment framework.

In this Chapter, the characteristics of the test set-up and of the frame specimens are presented. Then, the analysis of test results and along with the experimental validation of the substructuring approach are discussed. The results are compared with those obtained from NLTH performed using the nonlinear building model. Finally, the calibration of the pivot model and the implementation in a framework for the regional scale seismic-loss assessment are presented.

5.1 Experimental program

5.1.1 Test set-up

The test set-up realized in the CeSMA laboratory to perform PsD tests on full-scale infilled RC frames is shown in Figure 5.1.1 a). It is installed on the reaction wall and the strong floor available in the laboratory (see 2.3.2). The set-up is equipped with two hydraulic actuators (Figure 3.1.6) to impose the displacement at both floors. The actuators are fixed to the reaction wall by means of a steel plate and pre-stressed bars designed to withstand the maximum load of the actuators (i.e., 1200 kN).

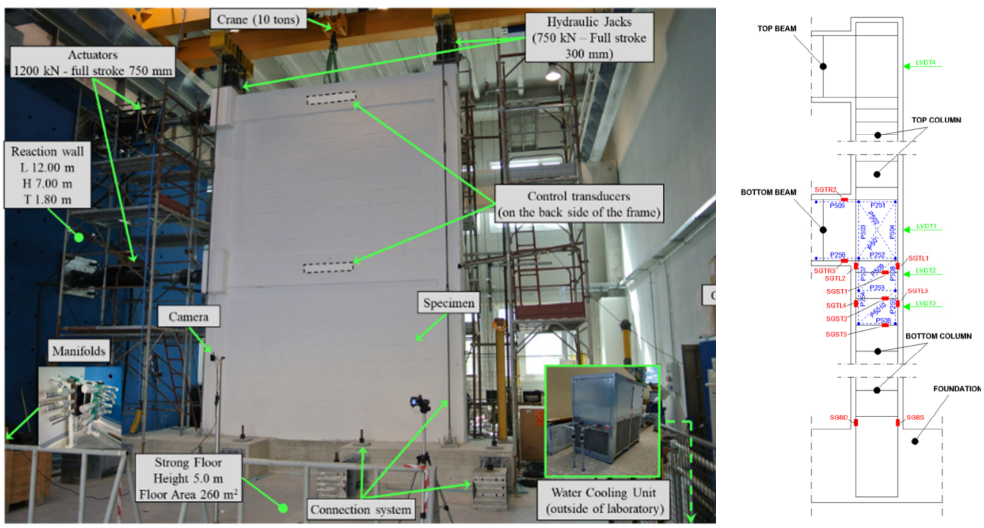

(a) (b)

Figure 5.1.1. Full-scale infilled RC frame test set-up (a) and layout instrumentation (b).

The foundation system is conceived to prevent the sliding between the foundation and the strong floor. Eight bars positioned in the holes properly realized on the foundation (Figure 5.1.2, a) were pre-stressed with 40 tons to clamp the foundation to the strong floor. An additional system (Figure 5.1.2, b) is provided to prevent the sliding. It consists of a HE 260 B steel profile embedded in the foundation connected to a composed steel profile placed externally. Each external profile is clamped to the strong floor using bars pre-stressed with 40 tons. This system allows to apply at the base of the specimen a maximum shear force of 1200 kN (i.e., the capacity load of a single actuator) avoiding the sliding of the foundation (see Figure 5.1.2).


(a)


(b)

Figure 5.1.2. Connection system to provide the foundation clamping (a) and to avoid sliding (b).

The vertical load is applied using two hydraulic jacks (Figure 3.1.8) positioned at the top end of the columns. The jacks apply the vertical load on the specimen through the connection system realized for the purpose. It consists of a steel beam located at the top of the columns, a couple of steel plates fixed to the foundation and two bars. The bars are connected to both the beam and the foundation. The hydraulic jack contrasts on a steel beam linked to the specimen foundation by means of the two pinned bars to apply the axial load. The system is designed to apply on the specimen a vertical load of 750 kN (i.e., the hydraulic jacks load capacity).

The hydraulic actuators are connected to the specimen using an alternative system respect to those available in other experiments. The system is conceived to avoid the confinement of the right beam-column joint, the object of this study, which can influence the response and the damage exhibited by this component. It is designed to avoid the punching of the joint for which a cross-section enlargement is provided. The system consists of a steel joint embedded during the cast in the left beam-column joint. It is made of two plates connected between them using UPN 120 steel profiles welded on both plates. On each profile, a series of bolts and steel bars are provided to improve the grip between the steel joint and the concrete. In addition, six bolts are provided to connect the actuator to the steel joint. Figure 5.1.3 shows a picture of the steel joint installed on the actuator before the cast. The system is designed to transfer to the specimen a load approximately of 500 kN at each interstorey, which is the maximum predicted for the test specimen at the second floor.

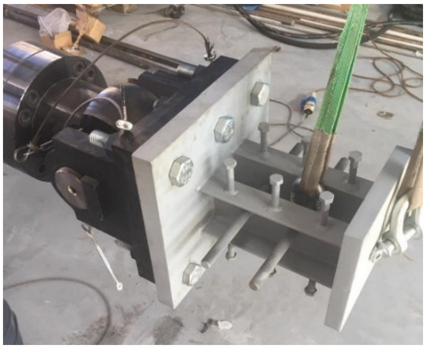

Figure 5.1.3. Steel joint embedded in the concrete for the connection of the hydraulic actuator.

According to Figure 5.1.1, the displacement imposed on the specimen is measured by two displacements Temposonics transducers (Figure 3.1.10) placed on a reference frame and installed at the mid-span of beam of each floor. The hydraulic actuators and jacks are supplied by an oil pump system (Figure 3.1.4 (a)) equipped with a water-cooling unit (Figure 3.1.4 (b)). The devices are connected to the pumping system through the manifolds (see Figure 5.1.1). Figure 5.1.1 (b) shows the instrumentation installed on the tested frame monitor global and local deformations as well as strain on internal reinforcement during the tests. It consists of high precision LVDTs, classic LVDT (in green), potentiometers (in blue) and strain gauges (in red) used which measures are recorded by the DAQ system shown in Figure 3.1.11

5.1.2 Test specimen

The frame prototype consists of a 1-bay-2-storey infilled RC frame reproduced in full-scale in the CeSMA laboratory environment. It is 4.10 m wide and 6.30 m height with a foundation of 0.56 m (i.e., total height of 6.86 m). The interstorey height is of 3.10 m at each floor. The clear interstorey height and the clear bay length are 2.55 m and 3.70 m, respectively. Figure 5.1.4 shows the geometry and the reinforcement details of the test specimen

[91]. The foundation was designed as rigid to remain elastic under the maximum allowable actions transmitted by the superstructure. The columns cross-section is square with a side of 0.40 m. It is reinforced with eight bars of 16 mm equally distributed within the cross-section. The beam cross-section is rectangular with a width of 0.40 m and an height of 0.55 m. The longitudinal reinforcement consists of a top layer with six bars of 16 mm diameter and a bottom layer of four bars with the same diameter. Three of the top bars are bended according to the reinforcement observed on the case study building during the post-earthquake inspection.

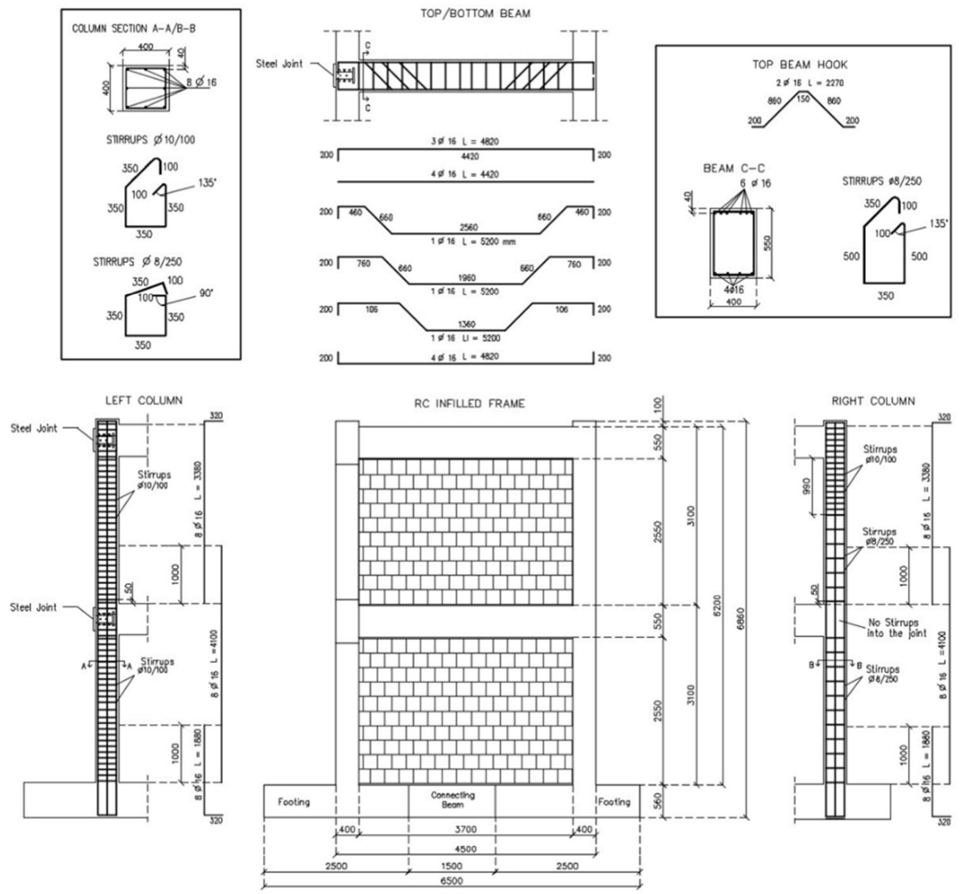

Figure 5.1.4. Infilled RC frame geometry and reinforcement details.

Figure 5.1.5 shows the reinforcement beam detail realized on the frame specimen. This detail was commonly used in the design practice of the time to increase the shear strength at the beam-ends. The transverse reinforcement consists of stirrups with a diameter of 8 mm for the beams and of 8 and 10 mm for the columns. The stirrups spacing is of 0.25 m on the beams while it is variable on the columns.

Figure 5.1.5. Bended longitudinal bars of the first-floor beam.

The left column presents a stirrup with a diameter of 10 mm and a spacing of 0.10 m. This is because the diameter and the spacing of the left column were designed to avoid any local brittle failure in shear or punching shear and allow the load transfer at the right column during the test. In addition, steel profiles and cross-section enlargement reinforced with horizontal and vertical stirrups with a diameter of 10 mm were used in correspondence of the joints of the left column to avoid local punching failure due to concentrated loads transmitted by the hydraulic actuators. Figure 5.1.6 show the reinforcement details of the cross-section enlargement along with the steel joint. The same transverse reinforcement (i.e., diameter and spacing) is used only in the top mid-height of the right column and into the joint at the second floor to avoid local failures. The right column presents at the first-floor and at the mid-height of the second-floor a transverse reinforcement with a stirrups of 8 mm and a spacing of 0.25 m. In this way, the structural weaknesses are concentrated in the right joint of the first floor in which no stirrups can be found as commonly done in the Italian design practice until the end of the past century. Therefore, only the response of the right joint of the first floor was investigated.

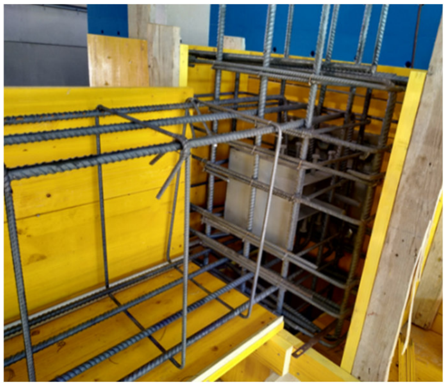

Figure 5.1.6. Beam-left column joint enlargement reinforcement details.

To investigate the infill-to-frame connection at both the floors, two different frames, labelled as F1 and F2, were built in the laboratory. For the purpose, three different connections were realized: full connection with a perfect bond between frame and infill; full connection with a good bond between frame and infill; partial connection with a gap between the beam and top side of the infills. For the first frame, F1_4S_M+A, a full connection on four sides (4S) by using the classic mortar (M) with the addition of a flexible adhesive (A) placed between the mortar and the concrete surface is used. On the second frame, two different connections by using classic mortar (M) applied on three (3S) or four sides (4S) are used. For the F2_3S_M specimen, a 5 mm gap between the bottom side of the beam and the infill top surface was realized during the fabrication, while for the F2_4S_M specimen the connection is identical to that used for the F1_4S_M+A unless the use of the adhesive.

Table 5.1.1. PsD test matrix.

Specimen	Frame	f_{cm} [MPa]		Infill-to-Frame Connection				
		1st floor	2nd floor	Materials	Top	Bottom	Left	Right
F1_4S_M+A	F1	8	8	Mortar and adhesive	x	x	x	x
F2_3S_M	F2	19	14	Mortar	5 mm gap	x	x	x
F2_4S_M	F2*	19	14	Mortar	x	x	x	x

*tested after F2_3S_M

In Table 5.1.1 the test matrix is reported, while an overview of the tested frames with details on the infill-to-frame connection is reported in Figure 5.1.7.

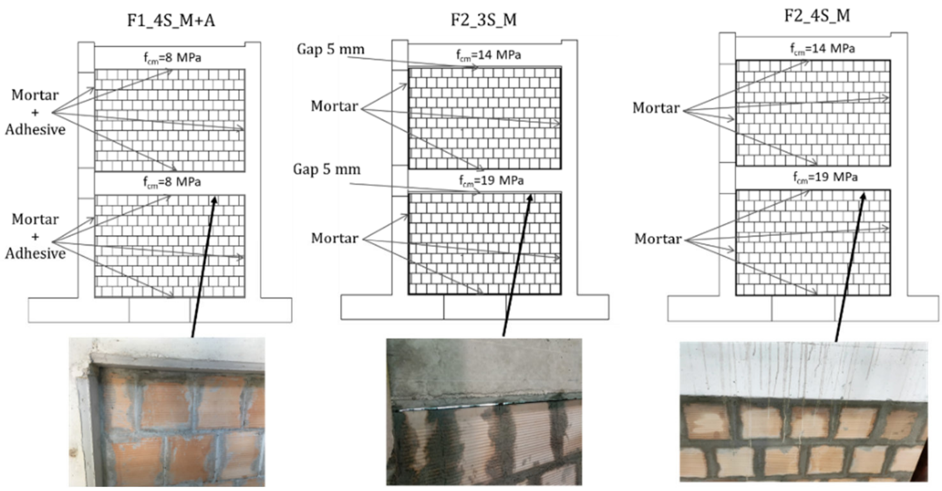

Figure 5.1.7. Detail of the infill-to-structure connection in the three tests.

The material used to realize the frames were selected according to the results of the material characterization discussed in the Chapter 4 for the reference building. Compression tests were carried out at 28 days on the concrete cylinder realized during the cast of the foundation, the first and second floors. A concrete compressive strength of 8 MPa resulted for the frame F1 on each floor, while a compressive strength of 19 MPa and 14 MPa was obtained for the frame F2 at the first and the second floors, respectively. The compressive strengths reported here are the same used for the definition of the properties of the concrete in both the numerical models. The foundation is characterized by a concrete compressive strength of about 27 MPa. The longitudinal and the transverse reinforcement of each frame were realized using deformed bars made of the same steel. From the direct tensile test performed on steel bars resulting a mean yielding stress of 535.3 MPa, 471.2 MPa and 504.6 MPa, a mean ultimate stress is of 641.2 MPa, 607.1 MPa, 504.6 MPa, a mean yielding strain 0.0028, 0.0028, 0.0026 and mean ultimate strain of 0.021, 0.012, 0.021 for the 16 mm, 10 mm and 8 mm bars, respectively. It is worth to note that the tensile strength of 535 MPa is used as properties of the steel bars in the numerical models.

The infill panel fabricated on the frames consists of a single layer realized using a brick with holes oriented horizontally and a thickness of 0.20 m. It is different from the infill panel observed during the post-earthquake inspection on the case study building (see 2), but it has been verified that the contribution in the lateral response is the same of the first one. The properties of the panel are required as input to modelling the nonlinear response of the infill according to the model presented in 4.1.5. An in-depth testing program was carried out to characterize mechanical properties of both components (i.e., brick and mortar) and infill panels for which, compression tests with the load applied parallel or orthogonal to holes as well as in the diagonal direction were carried out on three masonry wallets per each direction. Figure 2.1.1 shows the compression test with load applied orthogonal to holes (a) and in the diagonal direction (b).

In Table 5.1.2, the results of the tests performed on the bricks and on the wallets are summarized. Among these, the mean elastic modulus parallel to holes E_{m-0}, the mean compressive strength parallel (f_{m-0}) and orthogonal (f_{m-90}) to holes and the mean shear strength τ_{cr}, and modulus G_m are previously implemented in the numerical models. The adhesive used for the connection of the F1_4S_M+A specimen is a Portland cement-based mixture with a bond strength on a concrete surface of about 1 MPa improved adding a polymeric resin to the mixture.

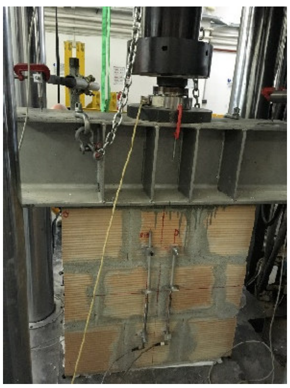

(a)

(b)

Figure 5.1.8. Compressive test on masonry wallets with load applied: (a) orthogonal to holes; (b) in diagonal direction.

Table 5.1.2. Results of the mechanical characterization tests on infills (mean of three tests).

mortar	mean flexural strength	[MPa]	3.39
bricks	mean compressive strength	[MPa]	11.76
	dimension (lenght x height x thickness)	[mm]	250 x 200 x 250
	void ratio	[%]	66%
	compressive strength (// to holes)	[MPa]	1.90
	compressive strength (⊥ to holes)	[MPa]	3.05
masonry wallette (three course)	dimension (lenght x height x thickness)	[mm]	770 x 770 x 200
	compressive strength (// to holes), f_{m-0}	[MPa]	2.59
	compressive strength (⊥ to holes), f_{m-90}	[MPa]	1.91
	elastic modulus (// to holes), E_{m-0}	[MPa]	4445
	elastic modulus (⊥ to holes), E_{m-90}	[MPa]	5186
masonry wallette (five course)	dimension (lenght x height x thickness)	[mm]	1290 x 1290 x 200
	shear strength, τ_{cr}	[MPa]	0.34
	shear modulus, G_w	[MPa]	1063

5.1.3 Testing procedure

The full-scale infilled RC frames with different infill-to-frame connections were tested using the PsD testing method. The mass matrix [M] assigned to the frame was defined using the numerically validated substructuring approach (see 4.2). The initial stiffness matrix $[K_0]$ is evaluated at beginning of every test to account for the damage evolution and the corresponding stiffness degradation. The viscous damping is set at 5% and the viscous damping matrix is evaluated according to Rayleigh method (see 3.2.2). It is important to emphasise that in this work the additional viscous damping is introduced to compensate for a possible negative equivalent damping due to control errors. The accelerogram used for the test is the 2009 L'Aquila earthquake recorded in the E-W direction by the AQG station (see 4.1.4). In particular, the accelerogram was scaled to different intensities (i.e., 10%, 25%, 50%, 75%, 100%, 125% and 150%) using a scaling factor to allow the assessment of the frame response and progressive damage. At this stage, only in-plane actions were considered, thus neglecting the influence of out-of-plane loads. At the top of the column a vertical (or axial) load of 300 kN was applied by means of hydraulic jacks and kept constant during the tests.

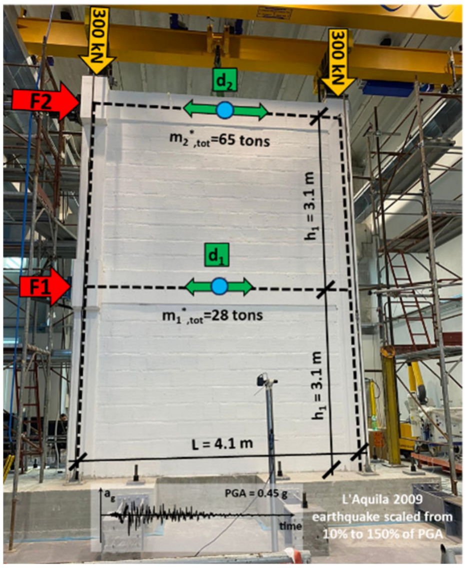

Figure 5.1.9. Testing procedure for PsD tests.

The PsD tests were performed using the testing framework implemented in the CeSMA laboratory 3.2. The testing method used is the Classical (or step) method (see 2.3.4). The equation of motion is solved using the α-OS splitting method presented in 2.3.5. The parameter α, which is used to define the numerical damping, is set equal to zero. The testing procedure used for the tests is presented in the previous Figure 3.2.1. The computed displacement profile is applied to the specimen and the recorded displacements and the restoring forces at each level are recorded by means of Temposonics high precision transducers installed at the mid-span of the beams and load cells installed on the actuators. The recorded measures are used by the coordinator system to update the stiffness matrix before moving to the following step of the record. This allows to reproduce the actual displacement demand of the earthquake considering the strength and stiffness degradation that is significant in existing infilled RC buildings.

5.1.4 Analysis of results

Three experimental campaigns for a total of twenty tests were carried out on the two frames. Among these, nineteen tests were performed using the PsD testing method to characterize the response at increasing earthquake intensity. The intensity was increased at every test until a clear failure of the infills is identified or the peak strength is achieved. The results of each PsD test account for the damage and the stiffness degradation occurred during the previous test. On the F1_4S_M+A specimen a pushover test was carried out to characterize the damage at larger displacement demand. The test was conducted using a pre-defined load pattern in displacement control for safety reason since a marked shear crack interested the first-floor column. The load pattern was conceived to impose a displacement at second floor double of the one at first floor. In Table 5.1.3 a summary of the test performed for each frame is reported. The experimental results are presented in terms of interstorey displacement, hysteretic response, and observed damage. The results of the experimental analysis are summarized in Table 5.1.4, Table 5.1.5 and

Table 5.1.6 along with a description of the observed damage and the related damage states (DSs) classified according to Cardone and Perrone [92].

Table 5.1.3. Experimental test type performed on each frame specimen.

Specimen	PsD								Pushover
	10%	25%	50%	60%	75%	100%	125%	150%	
F1_4S_M+A	x	x	x	x	x	x			x
F2_3S_M	x	x	x		x	x	x		
F2_4S_M	x	x	x		x	x	x	x	

The results in terms of interstorey displacement/drift are shown in Figure 5.1.10. The displacements imposed on the specimen at each floor, given as d_1 and d_2, are recorded as a measure of global frame displacement using Temposonics high precision transducers (Figure 3.1.10) installed on the beam mid-span. The imposed displacement is positive $(+)$ when the specimen is pulled, while it is negative $(-)$ when the specimen is pushed.

Table 5.1.4. Summary of the test results and observed damage for the F1_4S_M+A specimen.

ID [-]	Intensity [%]	PGA [g]	Floor [-]	Peak interstorey displacement [mm]		Peak Drift [%]		Maximum Storey Shear [kN]		Observed damage	Damage State [92]
				+	-	+	-	+	-		
F1_4S_M+A	10%	0.045	1	0.1	0.13	0.004	0.005	64	81	No damage	DS0
			2	0.21	0.08	0.01	0.003	83	34	No damage	DS0
	25%	0.112	1	0.34	0.22	0.01	0.01	144	132	No damage	DS0
			2	0.32	0.21	0.01	0.01	136	80	No damage	DS0
	50%	0.223	1	0.82	0.58	0.03	0.04	259	268	No damage	DS0
			2	1.07	0.73	0.02	0.03	222	171	Hairline cracking at the infill-to-beam connection	DS0
	60%	0.268	1	1	1.33	0.04	0.05	290	337	Null damage	DS0
			2	2.08	1.49	0.08	0.06	229	204	Infill-frame separation	DS1
	75%	0.335	1	1.76	3.16	0.07	0.12	325	398	Light diagonal cracking of infill	DS1
			2	2.84	4.00	0.11	0.16	228	297	Light diagonal cracking of infill	DS1
	100%	0.446	1	4.93	4.64	0.19	0.18	395	396	Significant diagonal cracking of infill - Column shear cracking due to infill action	DS2
			2	7.05	5.67	0.28	0.22	291	307	Significant diagonal cracking of infill	DS2
	Pushover	-	1	13.6	-	0.53	-	498	-	Wide diagonal cracking of infill - Concrete cracking at beam-to joint and column-to-joint interface at floor 1	DS2
			2	13.87	-	0.54	-	290	-	Significant diagonal cracking of infill	DS2

Table 5.1.5. Summary of the test results and observed damage for the F2_3S_M specimen.

ID [-]	Intensity [%]	PGA [g]	Floor [-]	Peak interstorey displacement [mm]		Peak Drift [%]		Maximum Storey Shear [kN]		Observed damage	Damage State [92]
				+	-	+	-	+	-		
F2_3S_M	10%	0.045	1	0.15	0.14	0.01	0.01	38	39	No damage	DS0
			2	0.14	0.10	0.01	0.00	37	20	No damage	DS0
	25%	0.112	1	0.55	0.50	0.02	0.02	102	103	No damage	DS0
			2	0.35	0.39	0.01	0.02	71	70	No damage	DS0
	50%	0.223	1	2.21	2.74	0.09	0.11	189	224	Infill-frame separation - Light diagonal cracking of infill	DS1
			2	1.61	1.56	0.06	0.06	148	163	No damage	DS0
	75%	0.335	1	4.65	3.42	0.18	0.13	230	220	Light diagonal cracking of infill	DS1
			2	4.81	2.50	0.19	0.10	183	135	Light diagonal cracking of infill	DS1
	100%	0.446	1	7.53	4.88	0.30	0.19	275	234	Significant diagonal cracking of infill and crushing of corners	DS2
			2	7.95	5.18	0.31	0.20	221	172	Significant diagonal cracking of infill and crushing of corners	DS2
	125%	0.558	1	9.45	6.73	0.37	0.26	290	287	Crushing of some bricks	DS2
			2	10.39	8.90	0.41	0.35	240	212	Crushing of some bricks	DS2

Table 5.1.6. Summary of the test results and observed damage for the F4_3S_M specimen.

ID [-]	Intensity [%]	PGA [g]	Floor [-]	Peak interstorey displacement [mm]		Peak Drift [%]		Maximum Storey Shear [kN]		Observed damage	Damage State
				+	-	+	-	+	-		
F2_4S_M	10%	0.045	1	0.06	0.07	0	0	44	37	No damage	DS0
			2	0.06	0.15	0	0.01	32	48	No damage	DS0
	25%	0.112	1	0.25	0.21	0.01	0.01	87	80	No damage	DS0
			2	0.3	0.28	0.01	0.01	69	69	No damage	DS0
	50%	0.223	1	0.65	0.67	0.03	0.03	166	188	Hairline cracking at the infill-to-beam connection	DS0
			2	1.21	0.87	0.05	0.03	122	140	Infill-frame separation	DS1
	75%	0.335	1	1.83	2.28	0.07	0.09	212	302	Light diagonal cracking of infill	DS1
			2	2.32	2.48	0.09	0.1	173	221	Light diagonal cracking of infill	DS1
	100%	0.446	1	3.47	3.31	0.14	0.13	305	349	Significant diagonal cracking of infill	DS2
			2	4.17	3.98	0.16	0.16	232		Significant diagonal cracking of infill	DS2
	125%	0.558	1	8.44	5.7	0.33	0.22	409	391	Significant diagonal cracking of infill – Column shear cracking due to infill action	DS2
			2	10.29	6.62	0.4	0.26	330	312	Significant diagonal cracking of infill	DS2
	150%	0.669	1	13.25	10.41	0.52	0.41	389	359	Wide diagonal cracking of infill and crushing of some bricks Concrete cracking at beam-to joint interface	DS2/DS3
			2	15.93	10.2	0.62	0.4	342	299	Wide diagonal cracking of infill and crushing of some bricks	DS2/DS3

The peak displacement is achieved between 2.0 s and 4.0 s for all the intensities and all frames (Figure 5.1.10). In addition, a period elongation with increasing intensity can be observed for each frame at each floor. This effect is due to the damage evolution of the tested specimens. The analysis of the interstorey displacement time histories and the damage assessment of the specimens, with increasing intensity, allow to explain the elongation of the period. In this analysis, the interstorey drift is to be understood as the absolute maximum interstorey drift. During the first two runs at 10% and 25% of AQG (PGA of 0.045 g and 0.112 g and drift of 0.01%) all tested frames exhibited a null damage (DS0) at each floor. The specimen F1_4S_M exhibited a hairline crack at 50% of AQG (PGA of 0.223 g) at the connection between the infill and the beam of the second floor at a drift of 0.03%. This damage is classified as DS0 since it interested a limited length of the beam and could be detected only with a close inspection. During the fourth run at 60% of AQG (PGA of 0.268 g and drift of 0.05% and 0.08%), a clear separation between the infill panel and the surrounding frame (DS1) was observed on both floors. A light diagonal cracking of the infill at each floor was exhibited by the frame at the 75% of AQG (PGA of 0.355 g and drift of 0.12% and 0.16%). Figure 5.1.11 shows for each frame the damage on the whole specimen and on the first-floor e beam-column joint of the right. Figure 5.1.11 a) shows the presence of multiple inclined cracks in the infill panels starting from the bottom of the beam or at the top of the column for the F1_4S_M+A specimen. The crack pattern is due to the use of a flexible adhesive with good bond strength to realize the connection between the infill and the beam. During the final run to 100% of AQG (PGA of 0.446 g and a drift of 0.19% and 0.28%), the width of the infill diagonal cracks raised (DS2) allowing the infill struts to fully develop and peak strength to be achieved. This led to a significant increase in shear forces on the second storey and consequently to an increase in the base shear up to 395 kN. This action, carried by the struts developed in the infill panel of the first floor, was transferred to the top end of the right column and resulted in the development of diagonal shear cracks under an imposed positive (pulling) displacement of 4.93 mm and a corresponding drift of 0.19%. Figure 5.1.11 b) shows the crack pattern at the top end of the right column of the first floor. The test campaign was concluded with a pushover test by pulling the frame under displacement control. In this test, the interstorey drift was at 0.53% and 0.54% on the first and the second floors, respectively, to have clear evidence of the damage.

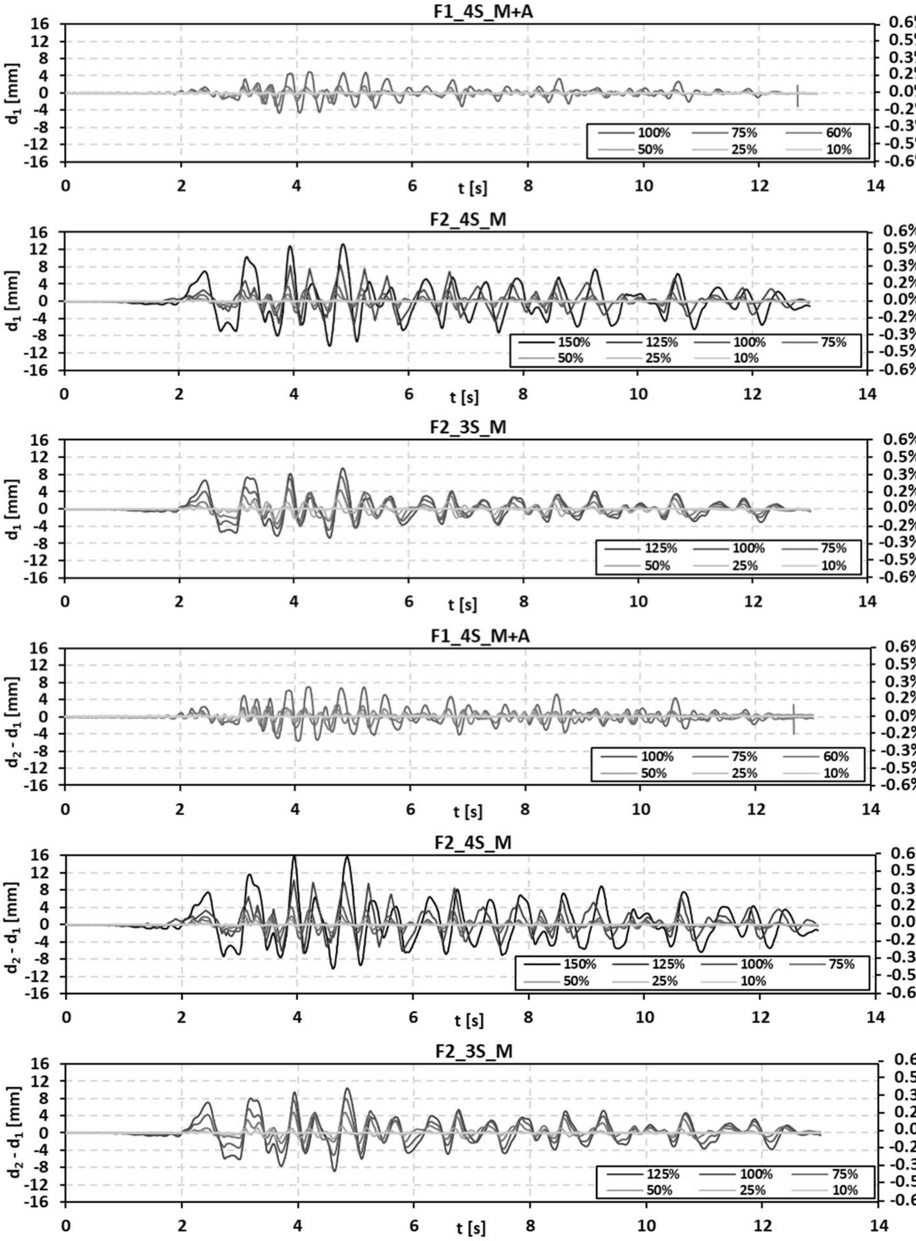

Figure 5.1.10. Interstorey displacement/drift demand at each floor of the three tested frames.

As a result, the crack width of the infill panels increased and more cracks developed at the beam-to-joint and column-to joint interface leading to an increase in base shear up to 498 kN. It is worth noting that the observed damage leading to the decrease in the lateral stiffness of the frame with consequent period elongation.

The specimen F2_3S_M present a gap of 5 mm between the infill and the beam interface at each floor. The gap was realized for scientific purposes only, to quantify the contribution of the infill panels transmitted to the column by friction. During an earthquake, this configuration may occur in case of a low-quality or slim mortar joint at the top of the infill significantly degraded under in-plane and out-of-plane loads. Due to this gap, the specimen has a deformability higher than the F1_4S_M+A frame, resulting in a drift demand about three times larger. As a result, the infill-to-frame separation and light diagonal cracking of the infill at the first floor (DS1) was anticipated at the run to 50% of AQG (PGA of 0.223 g and a drift of 0.11% and of 0.06%). Subsequently, the frame also exhibited diagonal cracking on the second floor during the run to 75% of AQG (PGA of 0.335 g and a drift of 0.18% and 0.19%). The size of the diagonal cracks increased significantly (DS2) during the run to 100% of AQG (PGA of 0.446 g and drift of 0.30% and 0.31%). Figure 5.1.11 c) shows the two major cracks per each direction together along with the diagonal strut and the onset crushing of the corner bricks. Corner crushing was clearly observed during the final run to 125% of AQG (PGA of 0.558 g and drift of 0.37% and 0.41%). In addition, a flexural crack developed at the beam-joint interface (see Figure 5.1.11, d).

The specimen F2_4S_M exhibited response similar to the specimen F1_4S_M+A frame up the 50% of AQG. This is due the fact that the infill panels were bonded on four sides to the frame by means of a classic mortar. The infill-frame separation (DS1) was observed in this run (PGA of 0.223 g and drift of 0.03% and 0.05%) followed by the light diagonal cracking of the infills during the run to 75% of AQG (PGA of 0.335 g and drift of 0.07% and 0.09%). The width of the infill cracks increases at 100% of AQG (PGA of 0.446 g and drift of 0.14% and 0.16%), where a significant diagonal crack (DS2) was observed. Figure 5.1.11 e) shows that multiple diagonal cracks developed starting from the bottom of the beam as seen for the specimen F1_4S_M+A. The full development of the infill strut was observed during the run to 125% of AQG (0.558 g and drift of 0.16% and 0.33%), resulting in a significant increase of the shear force transmitted to the top of the right column. Consequently, shear cracks were observed at the top end of the column when a positive (pulling) displacement was imposed. Figure 5.1.11 e) shows that a sub-horizontal shear crack was observed along with the crushing of some bricks. It is important to note that the shear crack pattern at the top end of the right column of the specimen F2_4S_M is different from the crack pattern observed in Figure 5.1.11 b) for the specimen F1_4S_M. During the final run to 150% of AQG (PGA of 0.669 and drift of 0.52% and 0.62%), the peak strength of the infilled frame was achieved, followed by a significant strength degradation. As a result, the infill panels were severely damaged. Wide diagonal cracks formed and most of the infill bricks in contact with the bottom of the beam were crushed. According to Cardone and Perrone [92], an intermediate DS was assigned between DS2 and DS3, as the surface of the crushed bricks was less than 30% of the total infill area.The results in terms of hysteretic response are shown in Figure 5.1.12, Figure 5.1.13 and Figure 5.1.14. In particular the hysteretic response in terms of interstorey shear vs displacement are shown in Figure 5.1.12 and Figure 5.1.13, while the response in terms of base shear V_{base} vs top displacement d_{top} is shown in Figure 5.1.14. The response of the specimen F1_4S_M+A from 10% to 50% of AQG (PGA from 0.045 g to 0.223 g) is linear elastic. According to the damage observed during these runs, no stiffness reduction occurred during the test while a negligible energy dissipation is observed (see Figure 5.1.12 a), Figure 5.1.13 a) and Figure 5.1.14, a). A significant decrease in stiffness was observed at 60% of AQG (PGA of 0.268 g) due to the separation between the infill panel and the surrounding frame at the second floor (see Figure 5.1.13 (a)) and at 75% of AQG (PGA of 0.335 g) due to cracking of the infill (Figure 5.1.12, a). The maximum peak strength at the first floor (-398 kN) was achieved at this stage. During the final run to 100% of AQG the peak strength in the positive and negative directions on the second floor was achieved (291 and −307 kN) although the trend of the strength in the positive direction was still growing. For this reason, and to have clear evidence of the failure mode, a final test in displacement control (pushover) was performed to achieve the peak shear also in the positive direction. In this test, the frame exhibited a peak strength about 498 kN on the first floor at a corresponding drift demand of 0.50%. Furthermore, a slight strength loss can be observed in Figure 5.1.12 a). Regarding the energy dissipation it is quite small during all the tests due to the marked pinching typical of brittle failures representative of the infill panels.

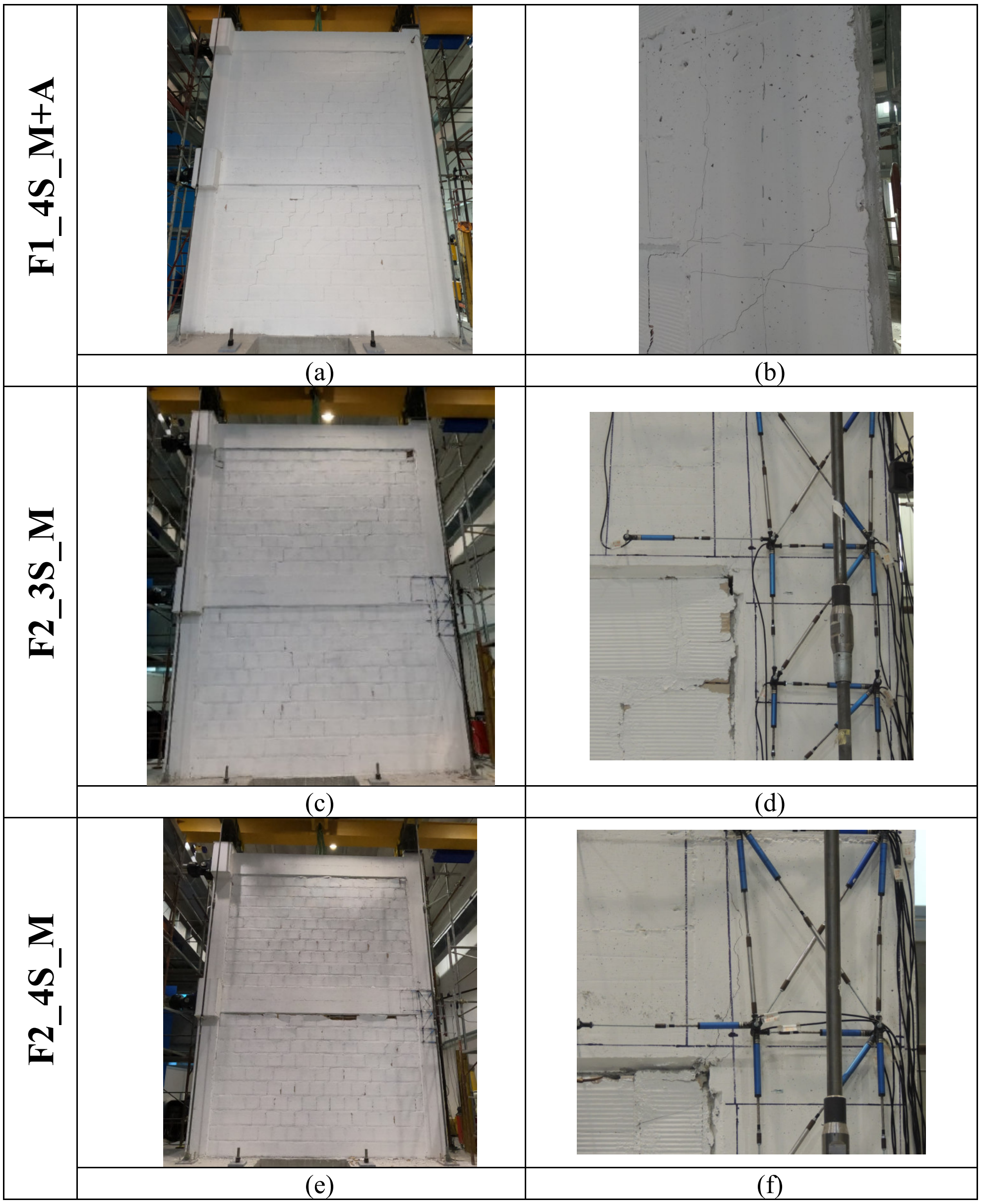

Figure 5.1.11. Observed damage on the infilled RC frame at the end of the tests. F1_4S_M+A: global view (a); close-up on the first floor right joint (b); F2_3S_M: global view (c); close-up on the first floor right joint (d); F2_4S_M: global view (e); close-up on the first floor right joint.

The response of the frame F2_3S_M is linear elastic during the first two runs to 10% and 25% of AQG (see Figure 5.1.12 b), Figure 5.1.13 b) and Figure 5.1.14, b). At 50% of AQG, a stiffness degradation was observed due to the infill-to-frame separation followed by the light diagonal cracking of the infill panels. The maximum strength was achieved at this stage with subsequent strength reduction at both floors. This is due to the presence of a 5 mm of gap between the bottom interface of the beam and the infill, which allowed the slipping of the infill along column (clearly visible after the infill-frame separation). As a result, the post-cracking lateral stiffness of the specimen is significantly reduced if compared to specimen F1_4S_M+A, resulting in a larger displacement demand. The presence of the gap also reduced the shear force that is transferred to the top end of the right column avoiding the shear cracking. The diagonal crack width of the infills increased during the run to 75% and 100% of AQG, resulting in a clear development of the infill strut. The slight increase in the floor strength observed in the graphs is related to the sliding between the infill panels and the column surface. During the final runs to 100% and 125%, the base shear remained almost constant, reaching a peak strength of about 290 kN achieved with a drift demand of about 0.37%. At these stages the crushing of corner bricks was observed, leading to the full development of the strength of the diagonal strut. The maximum strength of the specimen F2_3S_M is significantly lower (approximately 40%) than the maximum strength observed for the specimen F1_4S_M+A with a full infill-frame connection. In addition, the hysteresis shown in Figure 5.1.12 b), Figure 5.1.13 b), and Figure 5.1.14 b) outlines a pinching effect and a reduced energy dissipation. The hysteretic responses of the specimen F2_4S_M are shown in Figure 5.1.12 c), Figure 5.1.13 c), and Figure 5.1.14 c). As for the other specimens, the response is elastic during the first two runs to 10% and 25% of AQG. The stiffness degradation starts due to the separation of the infill and frame, which is observed at the second floor during the run to 50% of AQG and at the first floor during the early stages of the run to 75% of AQG. Due to the different infill-to-frame connection realized on the two frames, a significant strength increase with a lower stiffness was observed in the response respect to the specimen F1_4S_M+A. During the run to 125% of AQG the peak strength was achieved at both floors in the positive and negative load directions. The strength is 409 kN (at 0.33 % drift) and -391 kN (at 0.22% drift) at the first floor and 330 kN (at 0.40% drift) and -312 kN (at 0.26% drift) at the second floor.

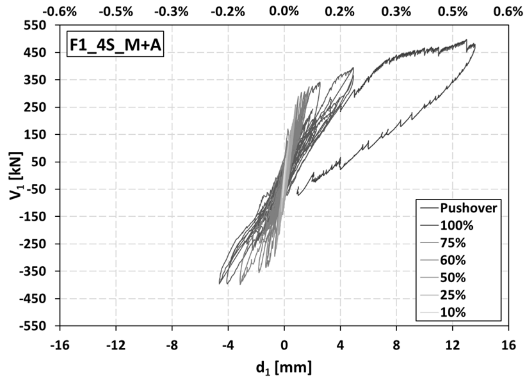

(a)

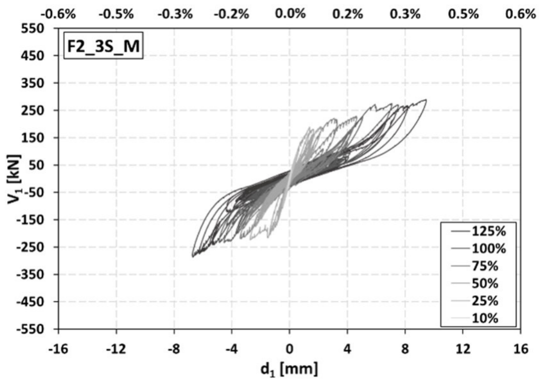

(b)

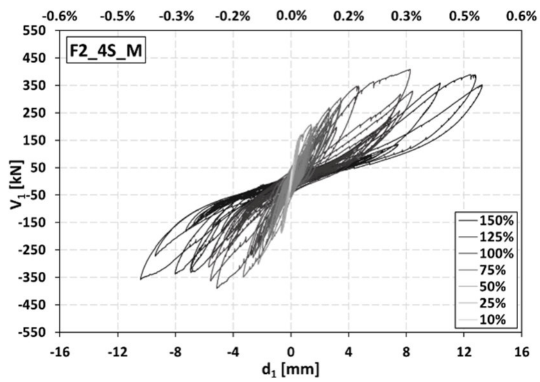

(c)

Figure 5.1.12. First floor hysteretic response at increasing intensity of the tested frames.

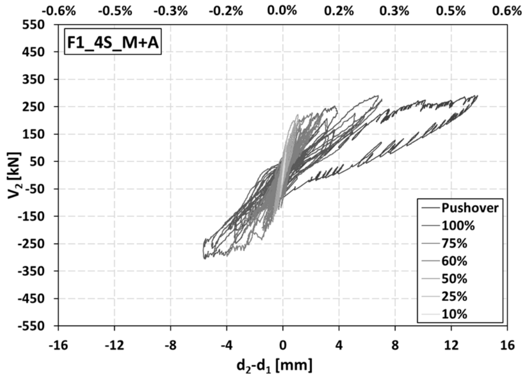

(a)

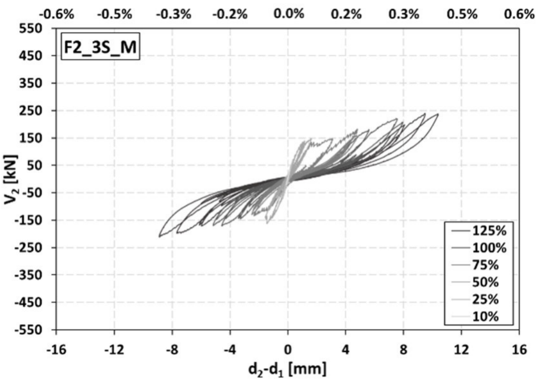

(b)

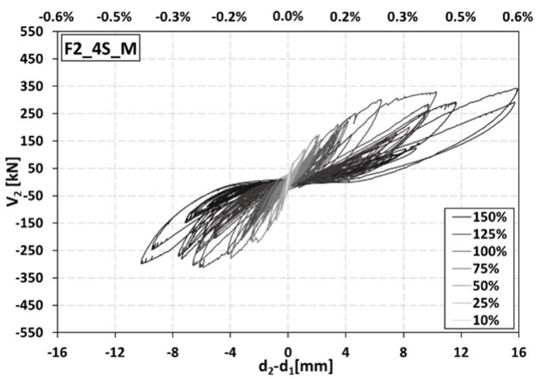

(c)

Figure 5.1.13. Second floor hysteretic response at increasing intensity of the tested frames.

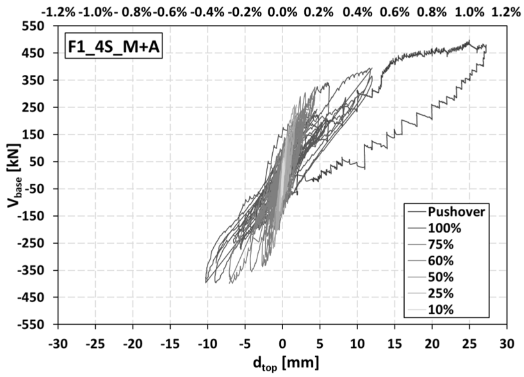

(a)

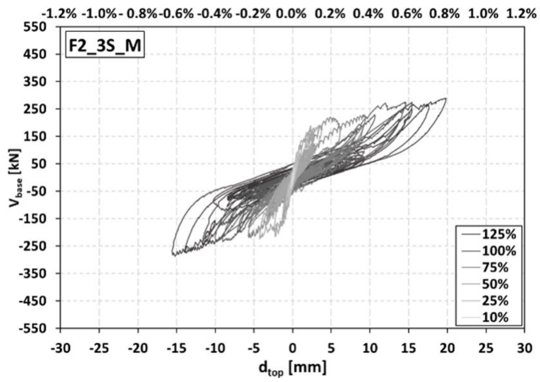

(b)

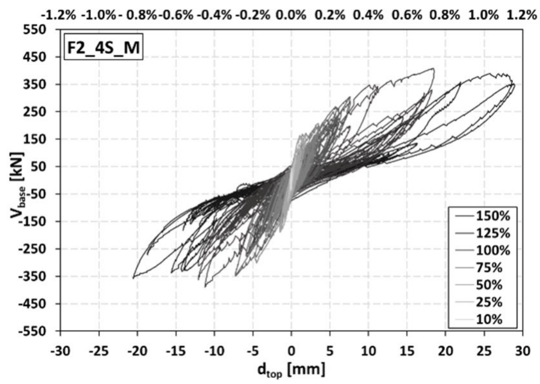

(c)

Figure 5.1.14. Global hysteretic response at increasing intensity of the tested frames.

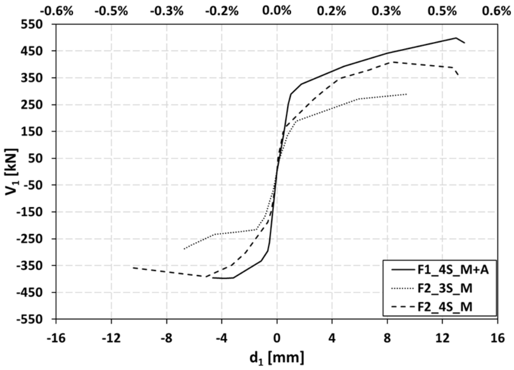

(a)

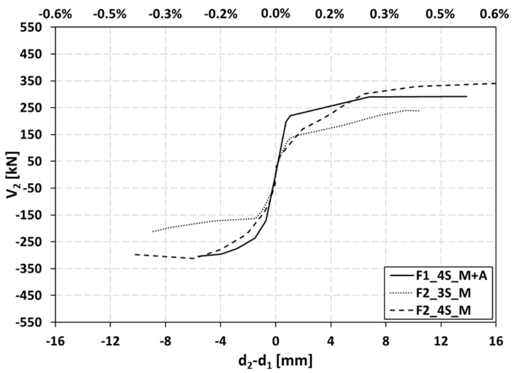

(b)

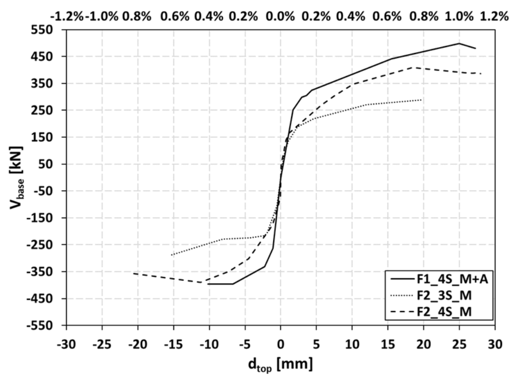

(c)

Figure 5.1.15. Comparison of the backbone curves of the tested frames: first floor a); second floor b); global response c).

The maximum strength at the second floor in positive direction slightly increased to 342 kN (at 0.62% drift) during the run to 150% of AQG. However, the strength in the negative loading direction decreased at both floors and in the positive loading direction at first floor. This is due to the crushing of bricks at the top of the infills.

The backbone curves regarding the first floor, the second floor and the global response for the three tested specimens (F1_4S_M+A, F2_3S_M, and F2_4S_M) are reported in Figure 5.1.15. The results are also compared in terms of maximum imposed top displacement, d_{top}, vs the peak ground acceleration, PGA, of the imposed ground motion in Figure 5.1.16.

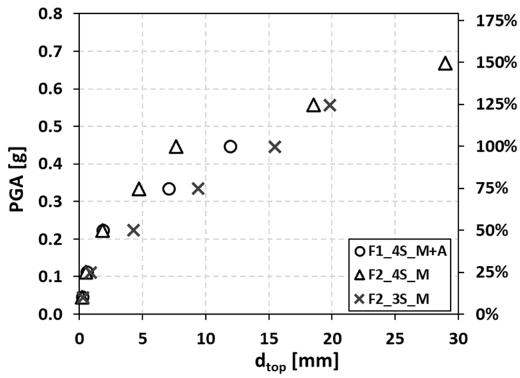

Figure 5.1.16. Experimental results in terms of top displacement $\mathbf{d_{top}}$ vs imposed PGA.

The comparison of the hysteretic global responses shows that at low intensity earthquakes (i.e.<50% AQG, PGA<0.223 g), the specimen F1_4S_M+A has strength and stiffness higher than the other specimens (see Figure 5.1.15). This is due to the full infill-to-structure connection with mortar and an improved bond adhesive on the four sides. On the other side, the specimen F2_3S_M has the lowest strength and stiffness because of the gap between the top of the infill and the beam. The specimen F2_4S_M, where a classic connection on four sides with mortar is used, has an intermediate behaviour. The displacement demand on the three specimens is similar (see Figure 5.1.16).

On the F2_3S_M and F2_4S_M specimens, the infill-frame separation is achieved during the run to a PGA of 0.223 g (50% AQG). This led to a significant stiffness degradation and increasing displacement demand (see Figure 5.1.15) only in F2_3S_M specimen. A displacement demand double than other specimens was measured during the test on F2_3S_M specimen due to the gap between the infill and the beam. Such an increase can be clearly observed at a PGA of 0.335 g (75% of AQG) and 0.446 g (100% of AQG), where the displacement demand of the specimen F2_3S_M is about the double of the specimen F2_4S_M remarking the role of the infill-to-frame connection in the lateral response of infilled RC frames. The specimen F1_4S_M+A showed an intermediate behaviour between the other specimens. The full connection and the flexibility of the mortar allowed to delay the infill-to frame separation respect to the F2_4S_M specimen that was observed during the run to 0.335 g (75% AQG).

It is worth mentioning that the contribution of the frame becomes significant only after the infill-to frame separation. At the 75% and 100% of AQG the displacement demand of F1_4S_M+A specimen is larger than F2_4S_M specimen due to the reduced stiffness of the RC frame related to a low-quality concrete. The three tested frames exhibited a moderate damage to the infills with significant diagonal cracking at 100% of the AQG. At this stage the specimen F1_4S_M+A showed a marked shear crack at the top of the ground floor column due to the infill-to-structure interaction. By increasing the earthquake intensity to 125%, the specimens F2_3S_M showed crushing of some bricks of the infill, while the specimen F2_4S_M showed a sub-horizontal shear crack at the top of the ground floor column due to the interaction with the infill strut.

5.1.5 Test verification and experimental validation of the proposed substructuring approach

The experimental results presented in the previous paragraph are used for the test verification and the validation of the proposed substructuring approach (4.2). Regarding the test verification, a first tentative consists in the analysis of the evolution of the stiffness of the specimen with the increasing earthquake intensity and the assessment of its dynamic properties used by the PsD algorithm. This allows to have insights on the reliability of simple multi degree of freedoms (MDOFs)-based numerical models in predicting the displacement demand imposed during the PsD tests. The adopted procedure is summarized in Figure 5.1.17. It consists in the estimation of the secant stiffness, k_{sec}, and the dissipated energy E associated to the cycle at the maximum displacement demand d_{max} at each run (see Figure 5.1.17, a). They are used to calculate the fundamental period of vibration of the specimen, T_1, and the equivalent viscous damping, ζ_{eq}.

Table 5.1.7. Comparison of experimental and analytical results.

Intensity [%]	PGA [g]	Specimen [-]	T_1 [s]	ζ_{eq} [%]	$S_{d,T1}$ [mm]	d_{top}^{exp} [mm]	$S_{d,T1}/d_{top}^{exp}$ [-]
10%	0.045	F1_4S_M+A	0.106	5.00%	0.18	0.24	0.77
		F2_4S_M	0.107	5.00%	0.18	0.21	0.86
		F2_3S_M	0.152	5.00%	0.46	0.27	1.68
25%	0.112	F1_4S_M+A	0.113	5.00%	0.45	0.63	0.71
		F2_4S_M	0.140	5.00%	0.87	0.52	1.65
		F2_3S_M	0.171	5.00%	1.24	0.88	1.42
50%	0.223	F1_4S_M+A	0.141	16.08%	1.18	1.86	0.63
		F2_4S_M	0.178	20.60%	1.75	1.85	0.94
		F2_3S_M	0.260	14.30%	4.39	4.28	1.03
75%	0.335	F1_4S_M+A	0.230	14.09%	6.47	7.12	0.91
		F2_4S_M	0.242	16.60%	5.88	4.73	1.24
		F2_3S_M	0.344	17.50%	10.05	9.41	1.07
100%	0.446	F1_4S_M+A	0.300	20.72%	9.66	11.97	0.81
		F2_4S_M	0.278	17.80%	8.7	7.63	1.14
		F2_3S_M	0.404	12.50%	17.63	15.47	1.14
125%	0.558	F1_4S_M+A	-	-	-	-	-
		F2_4S_M	0.379	15.30%	20.76	18.52	1.12
		F2_3S_M	0.441	13.50%	22.76	19.83	1.15
150%	0.669	F1_4S_M+A	-	-	-	-	-
		F2_4S_M	0.463	10.00%	35.26	28.96	1.22
		F2_3S_M	-	-	-	-	-
						Mean	1.08
						COV (%)	27.2

Once that the floor stiffness is obtained, a modal analysis by using two degrees of freedom lumped mass linear model is performed to calculate T_1. The equivalent damping, ζ_{eq}, is calculated by using the analytical formulation proposed by Naeim and Kelly [93]:

$$\zeta_{eq} = \frac{E}{2 \cdot \pi \cdot F_{max} \cdot d_{max}} \tag{5.1}$$

where F_{max} is the maximum strength. A summary of the experimental and numerical results is reported in Table 5.1.7.

Figure 5.1.17 d) shows the period elongation with the increasing earthquake intensity. The period is sensitive to the stiffness of the frame and its variability depends on the infill-to-structure connection and damage level. The F1_4S_M+A has the shortest period until the achievement of the infill-frame separation at 75% of AQG. It ranges from 0.106 s (at 10%) to 0.230 sec (at 75%). On the other side, the specimen F2_3S_M has the longest period ranging from 0.152 sec (at 10%) to 0.441 sec (at 125%). The specimen F2_4S_M specimen exhibited an intermediate response with a period ranging from 0.107 sec (at 10%) to 0.463 sec (at 150%). Thus, the results in terms of fundamental period computed considering the peak-to-peak secant stiffness confirm the role of the infill-to-frame connection on the lateral stiffness of the tested specimens.

These periods are here used to estimate the spectral displacement demand, S_{d,T_1}, computed by using the damped elastic spectra (Figure 5.1.17, e) and then compared in Figure 5.1.18 with the maximum absolute recorded top displacement d_{top}^{exp} in order to assess the reliability of the proposed PsD procedure. The results are also reported in Table 5.1.7 along with the $S_{d,T_1}/d_{top}^{exp}$ ratio.

In general, a good agreement can be found between the spectral displacement demand computed and the maximum displacement demand recorded during the test (mean = 1.08 and CoV = 27.2%) with points well aligned along the 45° line. At low-intensity earthquakes (i.e. 10% and 25% of AQG) the accuracy is quite low, and this is related to the difficulties in estimating the secant stiffness and the energy dissipation due to jagged hysteretic response. Indeed a 5% damping is assumed at these stages. This is particularly true at the initial stages of a test because of the high stiffness of the specimen that makes significant the contribution of higher modes.

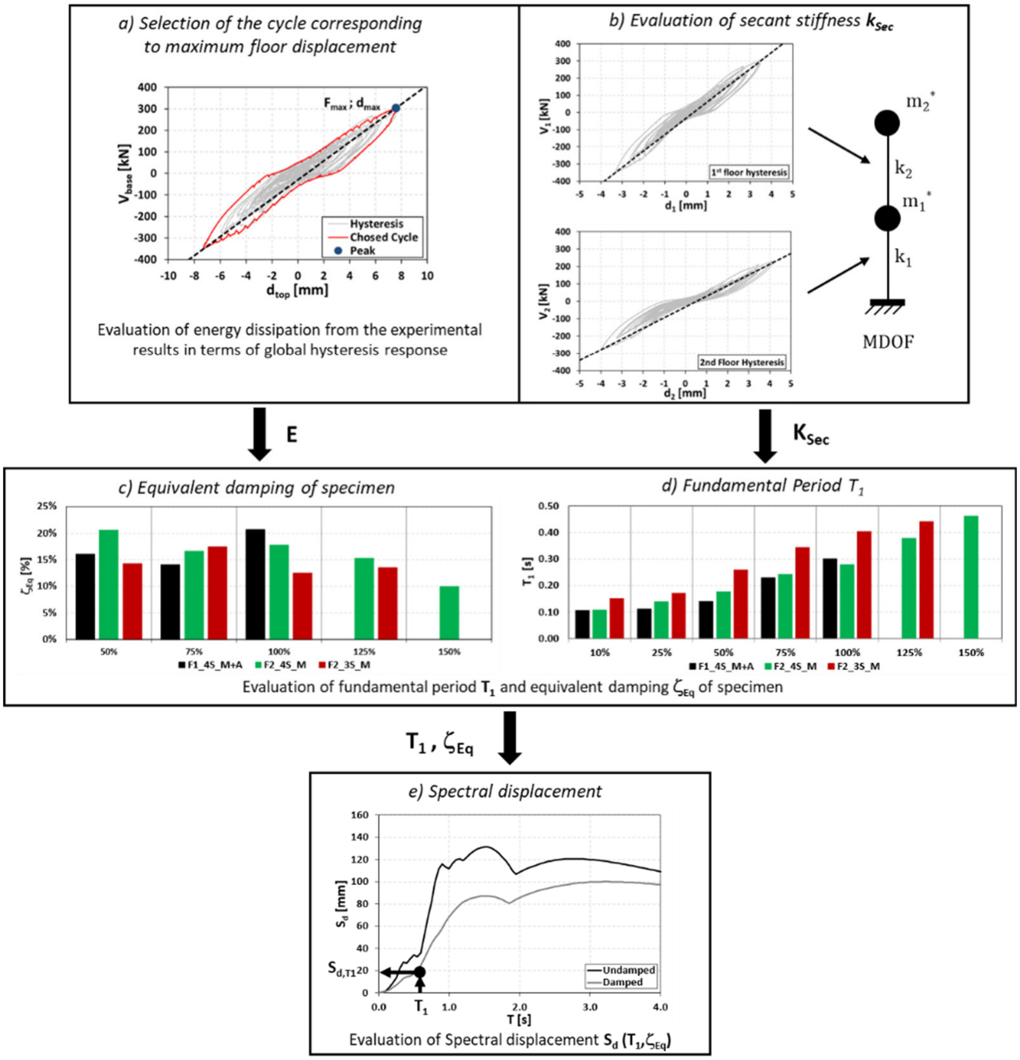

Figure 5.1.17. Analytical procedure to estimate the dynamic properties of the tested specimens and predict the spectral displacement demand.

Increasing the earthquake intensity to 50/75/100% of AQG, the stiffness of the specimens degrades due to the infill-to structure detachment and diagonal cracking. The magnitude of the imposed displacement increases, and a good agreement can be found with the spectral displacement. At late stages of the test on the specimens F2_4S_M and F2_3S_M the spectral displacement demand, S_{d,T_1}, is higher than the experimental top displacement of about 15% on average. Therefore, the results confirm the reliability of simple MDOFs-based numerical models in predicting the displacement demand imposed during the PsD tests.

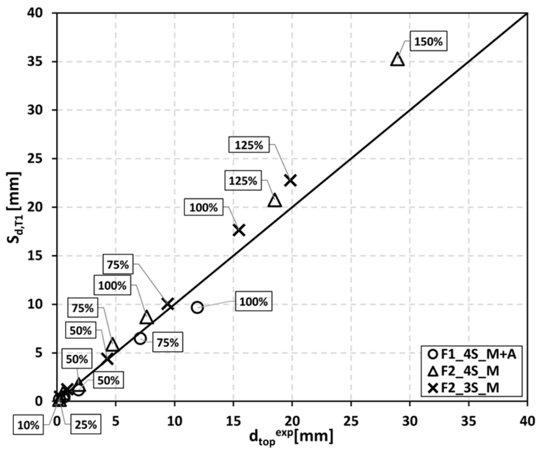

Figure 5.1.18. Comparison between spectral displacement demand, $\mathbf{S_{d,T_1}}$, and imposed displacement during the test, $\mathbf{d_{top}^{exp}}$.

To validate the substructuring approach, only the results of the specimens F1_4S_M+A and F2_4S_M are considered. These frames are characterized by an infill-to-frame connection fabricated through a classic mortar (M) or mortar plus a flexible adhesive (M+A) applied on the four sides (4S) of the infills. The experimental results obtained from the PsD tests are compared to the results obtained from the analysis carried out using the nonlinear building model. In particular, as seen for the numerical validation, the reliability of the substructuring approach is validated by comparing the results of the NLTH analysis performed on the building with the results of the experimental tests to verify that the displacement applied on the frame prototype are comparable with those applied on the frame specimens, according to the (4.25) when considering that the whole building is subject to the earthquake shaking (Figure 5.1.19).

Figure 5.1.20 shows the comparison between the numerical and the experimental results. At 50% of the earthquake intensity a good agreement between the experimental and numerical result is observed in a period ranging between 2 to 4 seconds when the positive and negative peak displacements are achieved, while after 6 second a clear mismatch between the numerical model and the F1_4S_M+A specimen is observed. In fact, the F1_4S_M+A specimen appear less stiff than the F2_4S_M due to the presence of the flexible adhesive not accounted in the model. The agreement between the numerical and experimental results of F2_4S_M is better over the entire duration of the earthquake.

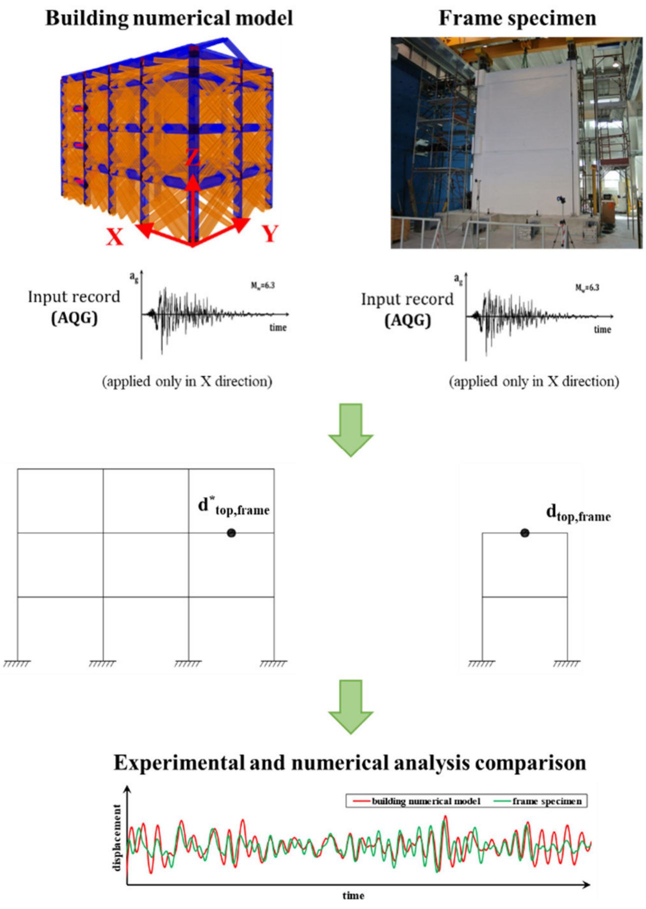

Figure 5.1.19. Comparison of experimental and numerical results for the validation of the proposed substructuring approach

The matching of the results increases significantly at 100% of the considered input signal record. Indeed, a good matching between the shape of the displacement histories can be observed. Nevertheless, the peak displacements are achieved at the same time step, and the signals are in phase throughout the duration of the input record. This matching increases as the intensity of the earthquake increases. Also in this case the specimen F1_4S_M+A showed high displacement demand due to its reduced stiffness.

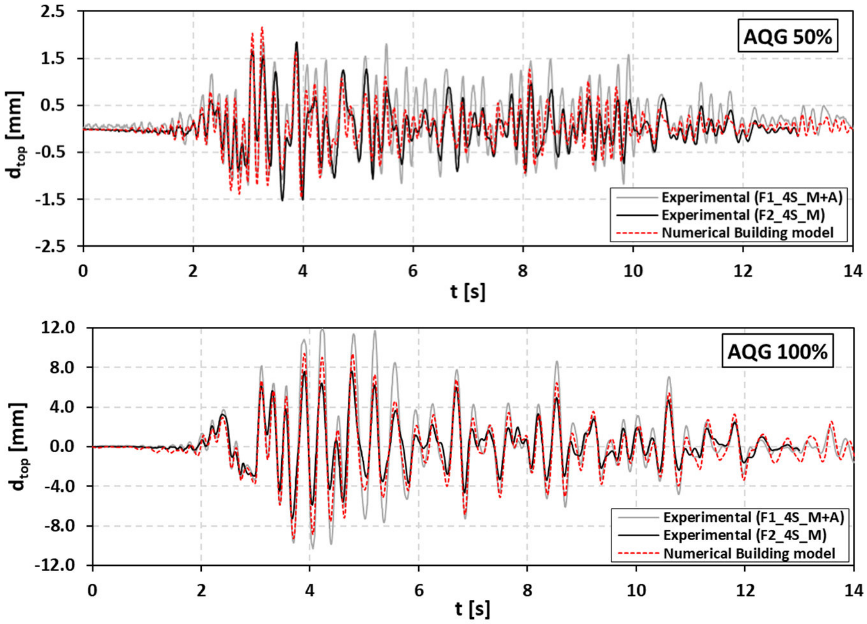

Figure 5.1.20. Comparison of experimental results on the prototype frame and numerical results at building level for the 50% and 100% of the L'Aquila 2009 earthquake.

Based on the comparison with experimental results, it can be concluded that the proposed substructuring approach is suitable for application in PsD tests on infilled RC structures due to the high stiffness of the infill that makes the distribution of strength and stiffness quite regular in the building plan and height. However, this accuracy may change significantly when moving to RC structures with higher deformability. Indeed, the localization of plastic deformation or damage in a specific portion or component of the building may significantly change the distribution of dis-placement demand. In this case more refined substructuring approaches (i.e. hybrid symulations) are needed.

5.2 Nonlinear modeling: calibration and validation

5.2.1 Model calibration

The nonlinear frame model illustrated in 4.2.2 is used and emphasis is given, in this paragraph, to the calibration of the hysteretic response of the infill struts. It is worth remembering that a three-strut model developed according to Chrysostomou et al. [81], with struts acting only in compression, is selected to reproduce the experimental response of the infill of the specimens F1_4S_M+A and F2_4S_M. In the numerical model of the F2_3S_M, the top off-strut acting on the beam is neglected, to account for the presence of 5 mm gap between the beam and the top end of the infill. The pivot model [78], implemented in the SAP2000 [56], used to reproduce the hysteretic response of the infill struts is shown in Figure 5.2.1.

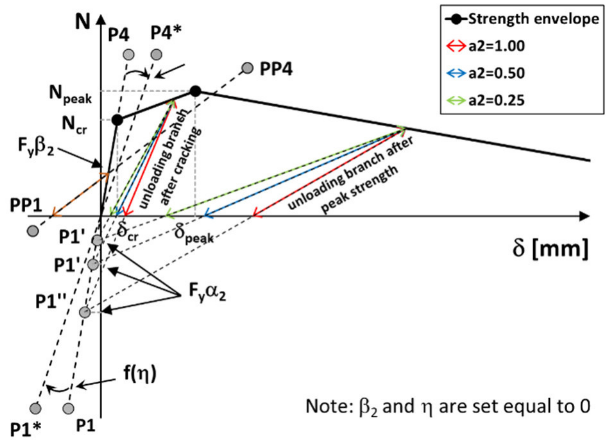

Figure 5.2.1. Hysteretic Pivot model adopted to reproduce the infill nonlinear response.

As already discussed in 4.1.5, because it is assumed that the infill struts act only in compression, the hysteretic response is governed only by the parameter α_2. According to Cavaleri and Di Trapani [5], the authors observed experimentally that the infilled frame does not gain stiffness until the whole plastic deformation is not recovered; thus, β_2 can be assumed equal to zero.

To calibrate the α_2 parameter, nonlinear time history analyses (NLTH) are performed using the previously developed numerical model (see Figure 4.1.18). To account for the damage evolution, strength and stiffness degradation with the increasing earthquake intensity an unique acceleration time history including all the scaled AQG records (from 10% to 150% intensity) in row is used as input. The same floor masses used during the PsD test are lumped at first and second level. The parameter α of the integration method (Hilber et al. [66]) is set to zero according to that used during the PsD tests. The numerical results are compared in terms of displacement time histories and global hysteresis to calibrate and validate the developed models. More iterations are performed to increase the matching between the numerical and experimental results. In the first iteration, α_2 is set equal to 0.25 as suggested by Cavaleri and Di Trapani [5]. Although the comparison in terms of the hysteretic response shows a reasonable match (see Figure 5.2.2, a), it can be clearly observed that unloading stiffness of the numerical model is smaller than the experimental one. Therefore, several iterations are performed changing α_2 parameter until the best match between the numerical and the experimental results is achieved (e.g. Figure 5.2.2 a), b) and c). The best matching is obtained considering $\alpha_2 = 0.50$ (see Figure 5.2.2, c).

5.2.2 Comparison of experimental and numerical results

The comparison between the numerical and the experimental results is performed in terms of top displacement d_{top} histories, backbone curve and assessed damage. A summary of the comparison in terms of displacement, considering the two most representative earthquake intensities (i.e. AQG 50% and AQG 100%, representing the onset of first cracking and moderate/severe damage to the infills, respectively), is reported in Figure 5.2.3 and Figure 5.2.4. The experimental results are represented with a continuous black line, while the dashed red line represents the numerical ones. Overall, the proposed numerical models well match the experimental response for the three different tested specimens. However, major differences in the model accuracy can be found varying the reference intensity (i.e. 50% or 100% of AQG) and the specimen because of the different infill-to-structure connection.

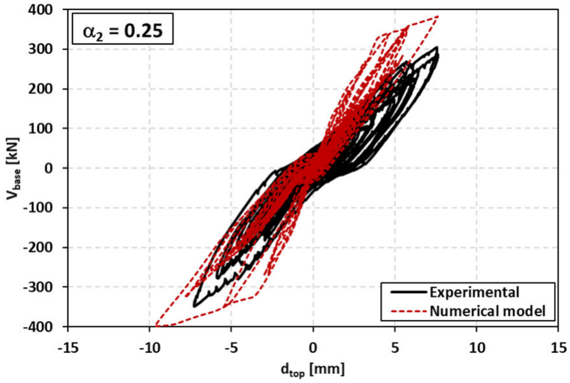

(a)

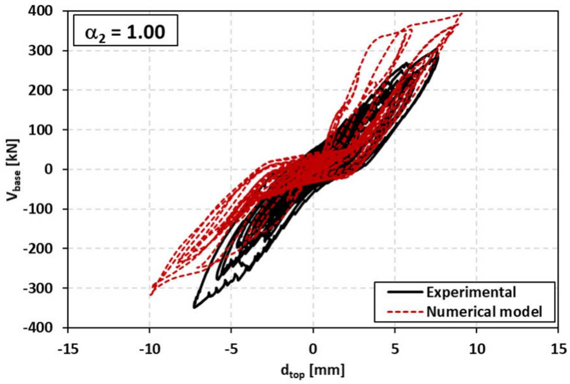

(b)

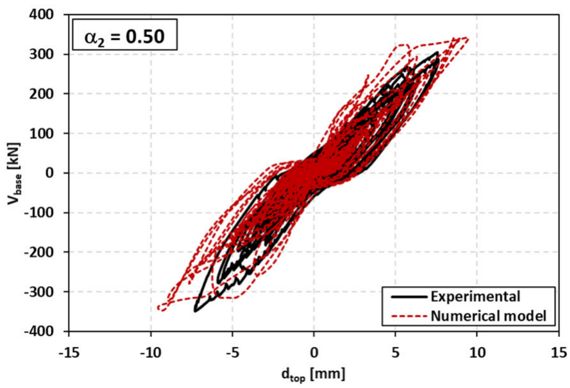

(c)

Figure 5.2.2. Calibration of $\boldsymbol{\alpha_2}$ parameter.

At onset of the first cracking, 50% of AQG (see Figure 5.2.3), the numerical model well captures the response of the specimen F1_4S_M+A and F2_4S_M where the infill is fully connected to the RC frame. The matching is satisfactory between 2.0 sec and 4.0 sec where the peak displacement is achieved. In the post-peak response, the numerical model of the F1_4S_M+A frame underpredict the experimental displacement, while the latter is well predicted by the numerical model of the F2_4S_M specimen. With reference to the specimen F2_3S_M, the proposed model is capable of capturing the negative peak displacement in the time range 0.0–3.0 s, while a clear mismatch can be observed after 4.0 s. This demonstrates that the model is not capable of reproducing the nonlinearities related to infill-to-frame separation where a gap at the top of the beam is available.

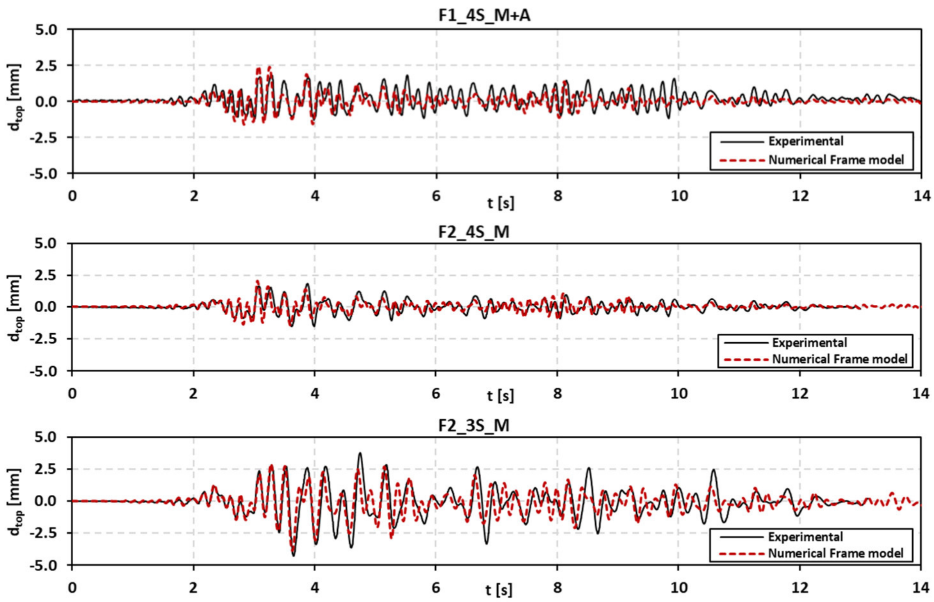

Figure 5.2.3. Comparison between experimental and numerical results in terms of top displacement $\mathbf{d_{top}}$ at 50% of AQG.

In Figure 5.2.4, the same comparison is reported at the intensity of 100% of the AQG record. A remarkable matching can be observed for the first two specimens, F1_4S_M+A and F2_4S_M, where the infills were initially fully connected to the RC frame. The numerical model can capture the peak strength and the stiffness degradation with high accuracy. The results are almost overlapped also during the entire duration of the record, showing the capabilities of the proposed model to account for the damage evolution at high intensity of the earthquake. By contrast, the proposed model is less accurate when compared with the results of the F2_3S_M specimen. Although a reasonable accuracy can be found at the first stages of the test until the achievement to of the first peak displacement (around 4.0 s), the matching decreases for the following steps. The numerical model is stiffer and cannot well predict the experimental displacement demand. This because a strut model cannot reproduce the slip of the infill along the column surface that is exacerbated by the lack of a contact with the beam.

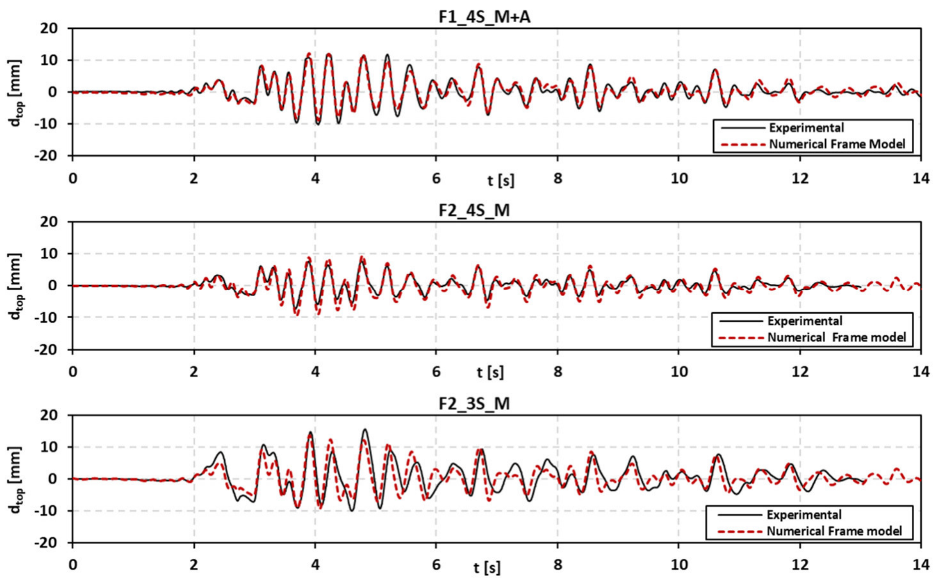

Figure 5.2.4. Comparison between experimental and numerical results in terms of top displacement $\mathbf{d_{top}}$ at 100% of AQG.

Further discussion on the model accuracy can be made comparing the experimental hysteretic responses with pushover curves and numerical hysteresis and their variability with the different infill-to-structure connection. For this scope, pushover analyses have been performed by using the proposed numerical models of the frame specimens and applying the floor displacement recorded during the tests. In Figure 5.2.5 the numerical pushover curves are compared with the experimental hysteresis in terms of storey shear (V_1 or V_2) vs. interstorey displacement (d_1 or $d_2 - d_1$).

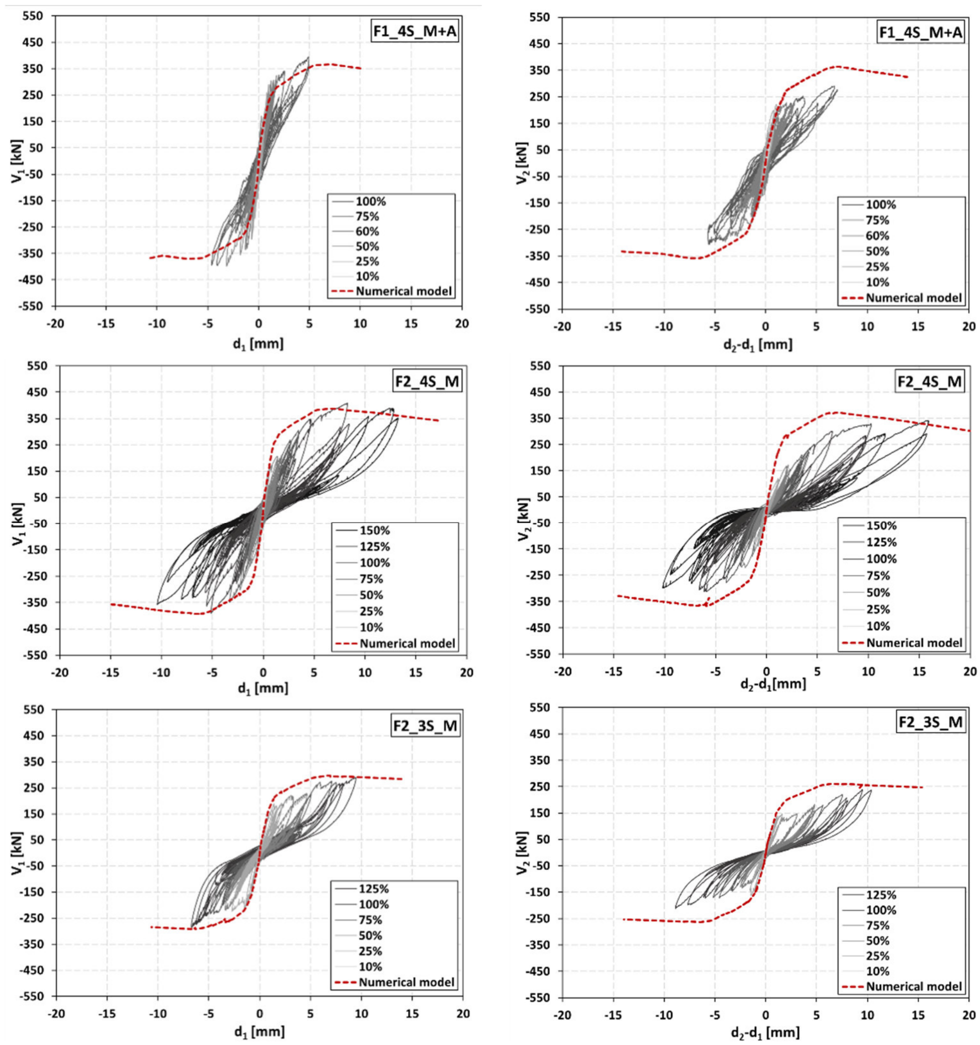

Figure 5.2.5. Comparison between 1st and 2nd floor hysteresis and pushover curves.

The comparison shows a satisfactory agreement between the proposed numerical model that relies on the infill model proposed by Panagiotakos and Fardis [8]. This model well captures the response of the F2_4S_M specimen where a classic mortar is used for the infill-frame connection. Although the peak strength and the initial stiffness are well approximated at both the floors, a significant underestimation of post-cracking stiffness can be observed. This can be related to the strength and stiffness degradation due to cyclic loads that cannot be considered in the pushover analyses.

With reference to the F1_4S_M+A test, where the infill-to-frame connection was fabricated by using a layer of adhesive in addition to a classic mortar, this model well captures the initial stiffness, while it slightly underestimates the peak strength at the first floor.

A good agreement can be found also comparing the results of the numerical model with the experimental response of the specimen F2_3S_M. It is worth remembering that, in this model (see Figure 4.2.7), the top off-diagonal strut was omitted to account for the 5 mm gap between the infill and the bottom of the beams.

All the numerical models well simulate the experimental response of the first floor, although the experimental peak strength is achieved in correspondence of a displacement demand lower than the experimental one. At the second floor the numerical model underestimates the experimental strength and stiffness, mostly in the positive pulling direction. In all the three specimens the strength of the second floor is underestimated of about 5% to 20%.

Following the calibration of the α_2 parameter, performed in the previous section, the α_2 is set equal to 0.50. Here the experimental and numerical results in terms of the global hysteresis of the specimen at 100% of the AQG record are compared in Figure 5.2.6 to have further information on the accuracy of the proposed model varying the infill-to-structure connection.

A good agreement between experimental and analytical results can be found in terms of peak strength, peak displacement and stiffness for the two tests with infills connected to the frame on four sides (i.e. F1_4S_M+A and F2_4S_M, see Figure 5.2.6 a), b). In particular, the numerical model of the F1_4S_M+A specimen underestimates the peak strength of about 5% and 14% in the negative and positive load direction, respectively. In terms of top displacement demand, the numerical model well predict the experimental one in the positive load direction, while in the negative direction it under-estimates the top displacement of about the 15%.

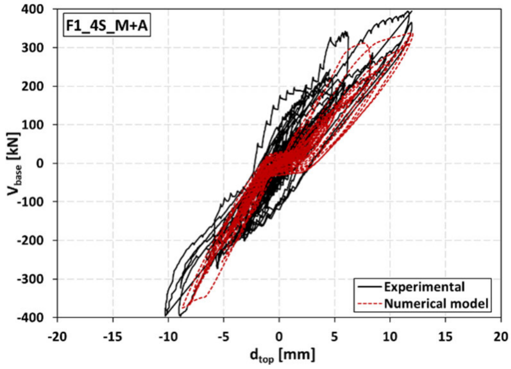

(a)

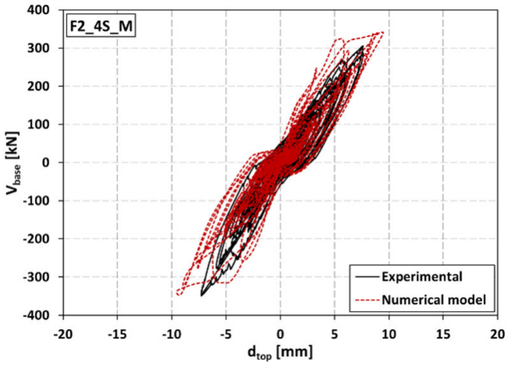

(b)

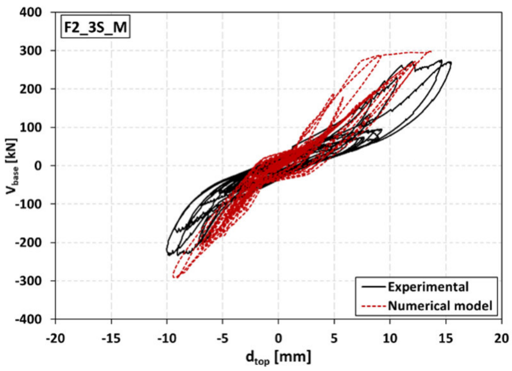

(c)

Figure 5.2.6. Comparison between experimental and numerical results in terms of global hysteresis at 100% of AQG record for the: (a) F1_4S_M+A, (b) F2_4S_M and (c) F2_3S_M test specimen.

With reference to the F2_4S_M specimen, the shape of the numerical hysteresis is very similar to the experimental one (see Figure 5.2.6, b). A good matching can be found in terms of peak strength, while the displacement demand is overestimated of about the 30% and 25% in the negative and positive load direction, respectively. The proposed numerical model does not capture the global hysteretic response of the F2_3S_M specimen. The numerical model is stiffer than the specimen, and the peak strength is overestimated of about the 8% and 25% in positive and negative load directions, respectively. This is because the proposed numerical model where specifically calibrated on the experimental tests on infilled frame with a full infill-to-frame connection.

Based on the comparison between experimental and numerical results and on the in-situ observation on the actual infill-frame connection, the numerical model of the F2_4S_M frame is selected and extended at building level.

The numerical model of the building proposed in Chapter 4 (see Figure 4.1.18) is here updated based on the parameters of the hysteretic response previously calibrated (i.e. $\alpha_2 = 0.5$). The updated model is used to perform a NLTH analyses by using the same input used in the experimental tests (i.e. an unique record created by assembling the AQG record of the 2009 L'Aquila earthquake scaled from 10% to 150% of the original intensity). Then, the numerical results of the building model are compared with those recorded during the experimental tests.

The comparison between the numerical results of the building model and the experimental ones is performed in terms of the displacement recorded in the middle of the 2nd-floor beam of the selected perimetral frame (see Figure 4.1.18). The comparison is reported in Figure 5.2.7 at intensity of 50% and 100% of AQG. This allows to assess the accuracy of the substructuring assumptions needed to conduct PsD tests on a single portion of the building (the selected two-storey frame), by comparing the experimental results at frame level with the simulated numerical response of the entire building.

At 50% of the earthquake intensity a satisfactory agreement can be observed in terms of the maximum recorded displacement (around 3.0 s in the positive load direction). However, the building response is stiffer than the experimental one and a clear mismatch can be observed in the following stages. This because in the experimental test the damage is concentrated in the physical specimen and, in turn, extended to all the other portion of the building. In the building model, and probably in the reality, only some portions of the building are damaged at low intensity, and this is clearly the reason of such a difference.

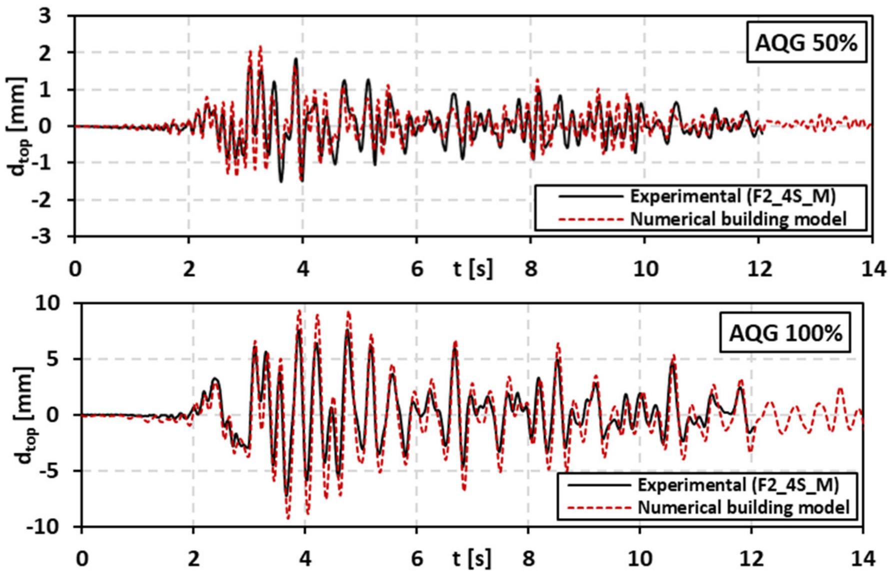

Figure 5.2.7. Comparison between building model and experimental results in terms of displacement at the 2nd floor at 50% and 100% of AQG record.

The matching of the results increases significantly at 100% of the considered earthquake intensity. Indeed, a good matching between the shape of the displacement histories can be observed. The numerical model overestimated the experimental displacement demand at frame level of about 15%. Nevertheless, the peak displacements are achieved at the same time step, and the signals are in phase for all the duration of the record. This matching increase when the increasing intensity of input. Therefore, it can be concluded that the adopted substructuring assumption, although they are quite basic, allowed to reproduce the numerical response of the entire building response with a satisfactory agreement.

It is worth mentioning that such simple substructuring assumptions were preferred to more complex ones (e.g. hybrid simulations) in order to easily identify the sourced of possible errors in the PsD tests.

In conclusion, the numerical model of the entire building is used to predict damage on perimetral infills. Such damage is then compared with that detected on the case-study building by in-situ inspection in the aftermath of the earthquake. To this end, the results obtained from the NLTH analysis performed under the 100% of the AQG record of the L'Aquila earthquake are used to estimate the interstorey drift at the different levels and in the two main building directions. The drift-based damage classification proposed by Del Gaudio et al. [94] is used to assign a damage state (DS) to each of the perimetral infills. It relies on the definition of the DS proposed by Cardone and Perrone [92]. Four different DSs can be defined for the infills and partitions: Infill-to-frame detachment or light diagonal cracking in partition and infills (DS1); Diagonal cracking with crack width ranging between 1 mm and 2 mm (DS2); Detachment of large plaster area and significant sliding in mortar joints, crushing and spalling of bricks units in 30% of the panel area (DS3); In-plane or out-of-plane global collapse of the infill (DS4). DS0 is assigned to infills that experienced a null damage. In this procedure, the damage states are set a defined as function of interstorey drift ratio at the peak strength (IDR_{peak}), by using the parameter α_i representing the ratio of the IDR at the i-th damage state and the IDR_{peak}. The α_i ratios for the four different DSs suggested by Del Gaudio et al. [94] are based on a database of the experimental tests on hollow clay brick infill realized without opening on reduced scale or full-scale 1-storey infilled RC frames. The ratio α_1 at DS1 is equal to 0.25, while α_2 is equal to 1.0, thus making the IDR at DS2 equal to IDR_{peak}. α_3 and α_4 are set equal to 2.50 and 4.10 for the DS3 and DS4, respectively.

The DS attributed to the actual damage that the building experienced during the 2009 L'Aquila earthquake is assessed according to the Cardone and Perrone [92]. Thus, by using the available photographic documentation, a DS is assigned to each of the perimetral infills as showed in Figure 5.2.8 (left). Considering the west and south face, the major damage (DS3 and DS4) is located at ground floor infills, where the corners crushing and partial or total collapse of some panels can be observed. The damage experienced by the structure decreases at the first floor for both faces, where diagonal crack and failure of some bricks is detected (DS2). Finally, a null or slightly damage (DS0 and DS1) is observed in the last floor of the building on both sides. Therefore, on average, the damage states can be considered as DS3 at the ground level, DS2 at the first floor and DS0 at the last floor. The most severe damage, total collapse of the panel (DS4) occurred in the

5–10 bay, located on the ground floor. Figure 5.2.8 shows that the collapse of both panels (internal and external) makes the staircase visible. On the same floor, the external panel infill collapse occurred in the bay 1–2 (south face) and in the bay 10– 15 (west face). The less damaged perimetral infills are detected at the last floor, particularly in the 5–10 for the west face and 1–2 bay, 4–5 bay for the south face.

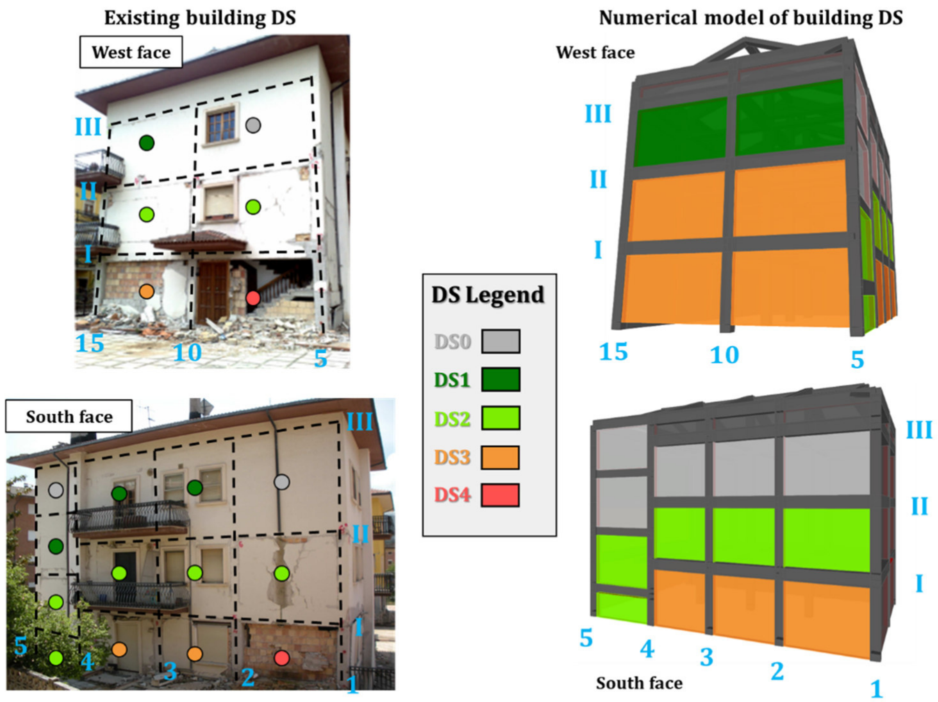

Figure 5.2.8. Damage assessment: existing building (left); numerical model of the building (right).

The predicted DSs by using the proposed numerical models and different damage classification available in literature (Del Gaudio et al. [94]; Magenes and Pampanin [90]; Sassun et al. [95]) are reported in Table 5.2.1. These damage classifications are preferred to classic drift-based ones (Cardone and Perrone [92]; Chiozzi and Miranda [96]; Liu et al. [97]), since they allow to account for the infill-to-infill variability as function of the mechanical response of the different struts. The direct comparison with the results obtained by using the damage classification proposed by Del Gaudio et al. [94] is showed in Figure 5.2.8 (right). Overall, a quite good matching can be observed between the observed and predicted damage.

Table 5.2.1. Comparison of damage predicted by using different approaches.

Side	Bay	Floor	Observed	Del Gaudio et al. [94]	Sassun et al. [95]	Magenes & Pampanin [90]
South view	1-2	I	DS4	DS3	DS1	DS1
		II	DS2	DS2	DS1	DS1
		III	DS0	DS0	DS1	DS1
	2-3	I	DS3	DS3	DS1	DS1
		II	DS2	DS2	DS1	DS1
		III	DS1	DS0	DS1	DS1
	3-4	I	DS3	DS3	DS1	DS2
		II	DS2	DS2	DS1	DS1
		III	DS1	DS0	DS1	DS1
	4-5 (stair)	I/2	DS2	DS2	DS1	DS1
		I	DS2	DS2	DS1	DS1
		II	DS1	DS0	DS1	DS1
		III	DS0	DS0	DS1	DS1
North view	5-10	I	DS4	DS3	DS2	DS2
		II	DS2	DS3	DS2	DS2
		III	DS0	DS1	DS1	DS1
	10-15	I	DS3	DS3	DS2	DS2
		II	DS2	DS3	DS2	DS2
		III	DS1	DS1	DS1	DS1

The numerical model tends to underestimate the predicted damage on some of the ground floor infills because the out-of-plane response of the infill panel is neglected. Indeed, a DS3 is predicted for ground floor infills in both the directions, while some of them experienced an out-of-plane failure falling within the DS4. More refined numerical models including the out-of-plane response are needed to improve the matching with the observed damage. The predicted damage on perimetral infills of the first floor is a DS2 well matching the observed. The numerical model slightly underestimates the DS at the last floor, where a DS0 is predicted by the numerical model while some of the infills experienced a slight cracking with infill-to frame separation typical of a DS1.

According to Magenes and Pampanin [90], the DSs are defined as a function of the axial strain in the diagonal compressive strut ε_w. This damage classification was later refined by Sassun et al. [95] by using a large database of experimental data on single-bay single-storey RC frames with different infill types (vertically or horizontally hollowed bricks, single or double panel, different mortar properties). The comparison of infills damage predicted using the three different damage measures is reported in Table 5.2.1. It shows that the strain-based damage measures underestimate the DSs of infills at different levels of the building for both the South and East face. These differences can be mainly attributed to the differences between the characteristics of the infills used in the definition of the DSs (e.g. solid clay bricks, hollow clay bricks with vertical holes) and those available on the case study building (i.e. vertical or horizontal holes, single or double panels, with or w/o openings), as also outlined by Del Gaudio et al. [94].

5.2.3 Model simplification for regional scale loss-assessment

The refined model of the building is simplified to be implemented in the loss-assessment framework developed to perform simulation at a regional scale, shown in Figure 5.2.9. The framework is an extension of the framework proposed by Natale [98]. The proposed framework relying on the PEER PBEE [99] framework and the loss-assessment analyses carried out using the FEMA-58 [100]. It consists of eight steps: building definition, hazard analysis, structural analysis and seismic performance assessment, estimation of the Engineering Demand Parameters (EDPs), evaluation of damage and losses, identification of potential weaknesses, design of the retrofit alternatives, estimation of the actual cost of the intervention, calculation of the annual savings and pay-back-time (PBT). The whole procedure is implemented in a MATLAB code to provide to designers a simple tool to evaluate the benefits of different retrofit solutions and calculate the related PBT without performing sophisticated calculations. The code consists of different scripts representing the steps of the described framework. More details can be found in Natale [98].

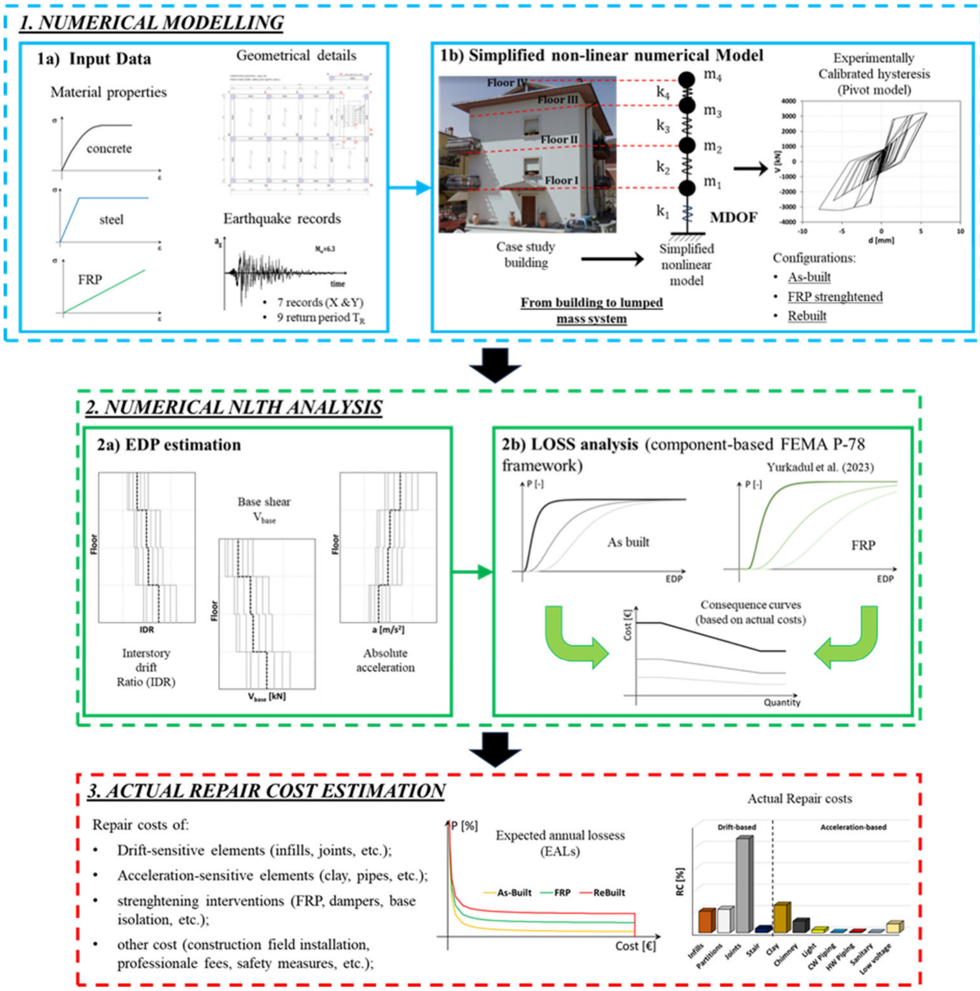

Figure 5.2.9. MATLAB framework for the seismic loss assessment

The structural analysis is performed in the script "numerical integration" [98] using NTLHs analysis relying on a simplified 2D model to determine the EDPs. A set of 14 acceleration records is scaled for different return periods (from 30 to 2475 years) to be imposed to the model. The equation of motion is solved using the α-OS method [69]. The model consists of an MDOF system with mass lumped at each floor. The characteristics and dynamic properties of the building, from which the model is built into the code, are defined in the "input" and "dynamic" scripts. Two different configurations of the building are implemented to perform the analysis: base isolated and fixed-base. In the framework presented in this thesis (Figure 5.2.9) for the loss-assessment, the fixed-base building configuration is considered for the purpose. However, the response of the structural members is assumed to be linear elastic in the proposed framework for this configuration. This is because, it is implemented to study the buildings for which the collapse is governed by brittle failures. Therefore, the implementation of the model obtained from the simplification of the refined model is fundamental to extend the proposed framework to perform the structural analysis accounting for the nonlinear response of buildings.

The simplified model consists of an MDOF system with masses lumped at floor level. The nonlinear response of each storey is reproduced using a single non-linear spring reproducing the previously calibrated pivot model [78]. The stiffness and the strength of each floor are modelled considering the contribution of the RC columns and the infill panels. The envelope curve representing the shear-displacement capacity of each floor is calculated considering the lateral capacity of the infills, partitions, and columns. Figure 5.2.10 shows the information defined in the input script, already implemented, and the "backbone" script added in the proposed framework to implement the simplified model. The envelope curves associated to each storey of the bare building are defined in the script "input. The curve is obtained by performing a pushover analysis using the numerical model of the bare building. The analysis is performed by imposing a target displacement for a selected floor while the other floors are kept fixed. This operation is repeated for all the floors to obtain all the envelope curves.

The envelope curve of infills is defined for each floor in the script backbone starting from the characteristics of infill panels (i.e., h_m, t_m, E_m, G_m and τ_{cr}) defined in the script input (see Figure 5.2.10). The length of the diagonal strut d_m and the angle between the diagonal strut and to the horizontal plane θ are evaluated for each panel (i.e., for all the floors and bays) to define the width of the strut cross-section b_m and the stiffness ratio λ according to (4.3) and (4.4). These parameters are necessary to evaluate the secant stiffness K_{sec} according to Mainstone (4.12) [86].

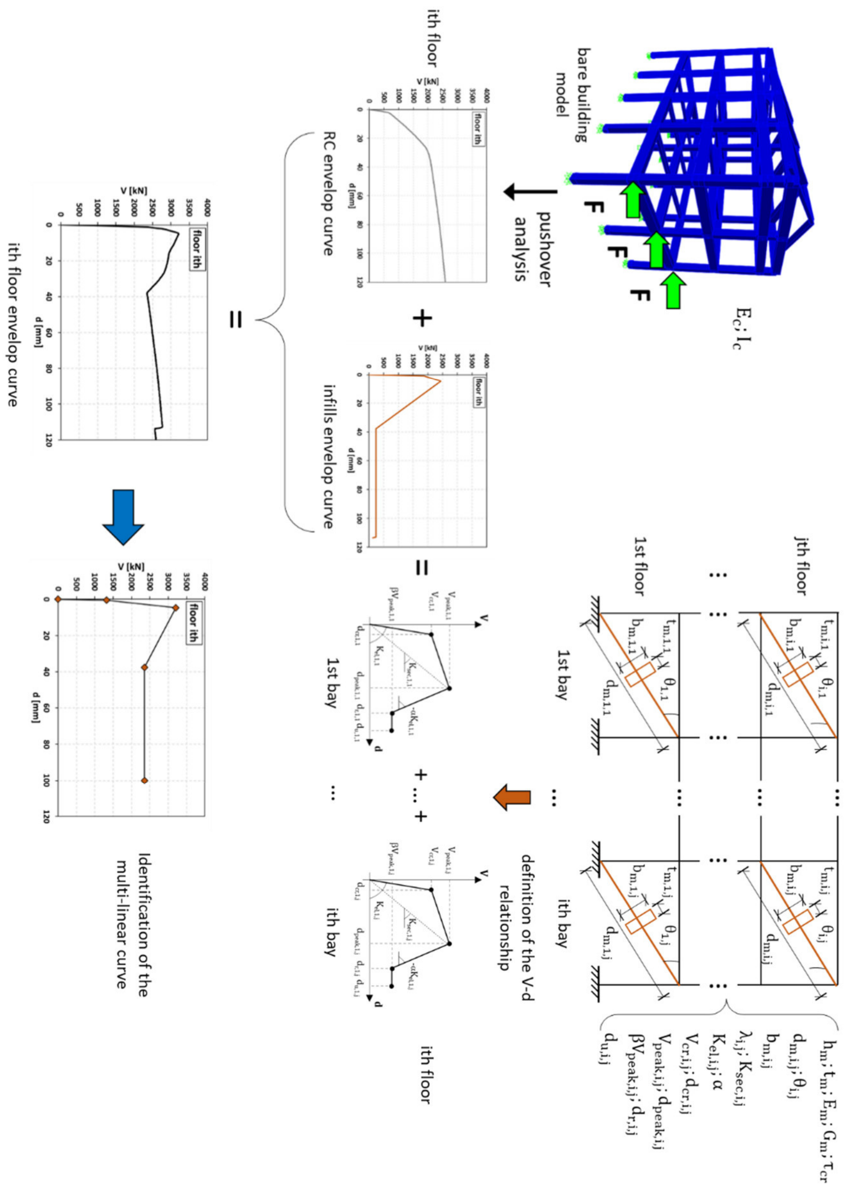

Figure 5.2.10. Additional Script and input added in the framework proposed by Natale [98].

The response of each infill panel (of each bay at each floor) is modelled as an equivalent strut with shear-displacement relationship characterized to according to Panagiotakos and Fardis [8]. The characterization of this relationship require the definition for each panel of the elastic stiffness K_{el} (according to (4.5)), the shear and the displacement at cracking ($V_{cr}; d_{cr}$) (according to (4.6) and (4.7)), at peak ($V_{peak}; d_{peak}$) (according to (4.10) and (4.11)), the residual strength ($\beta V_{peak}; d_r$), the corresponding stiffness ($-\alpha K_{el}$), and the ultimate displacement (d_u), as indicated in 4.1.5. Then, the envelope curve of infills of each floor is obtained as the sum of the shear-displacement relationship characterized for each infill panel of the same floor.

The envelope curve of the ith floor is obtained as the sum of the envelope curve of infills and RC columns evaluated for the selected floor (see Figure 5.2.10). This operation is repeated for all the floor to characterize the envelope curves of the buildings. In Figure 5.2.10 the envelope curves reported in the graphs account only for the positive region. It is worth mentioning that in the framework the behaviour of each floor is assumed to be symmetric.

From the envelope curves defined for each floor, the multi-linear curve used to reproduce the hysteretic response of the building are characterized. The definition of the multi-linear curve of each floor consists in the identification, from the envelope curves, of the cracking, the peak, the residual, and the ultimate points according to the model proposed by Panagiotakos and Fardis [8].

The peak point is defined as the point of the envelope curve with maximum shear (i.e., V_{peak}). The displacement at peak d_{peak} is the displacement corresponding to the peak shear V_{peak}. The ultimate and the residual point are defined starting from the peak point. The residual shear is evaluated as βV_{peak} and the corresponding residual displacement d_r is evaluated from geometrical assumption considering that the stiffness of the degrading branch is equal to $-\alpha K_{el}$ (Figure 4.1.21). The ultimate displacement d_u is calculated as three times larger than the displacement d_r. The parameters α and β used are 0.03 and 0.01 according to the range of values proposed by the authors.

The identification of the cracking point is the most critical because it defines the initial elastic stiffness K_{el}, the displacement of first cracking and the slope between the cracking and the peak strength that is crucial to accurately reproduce the stiffness degradation after cracking. To this end, an energetic approach is implemented in the framework.

In Figure 5.2.11 the straight blue line represents the envelope curve while the straight black curve with dots represents two branches of the multi-linear curve that must be defined. The definition of the cracking point starts with the calculation of the energy E under the blue curve in the displacement interval between zero and the peak displacement d_{peak}. The remaining part of the envelope curve is neglected. The energy under the blue line is evaluated using geometrical assumptions.

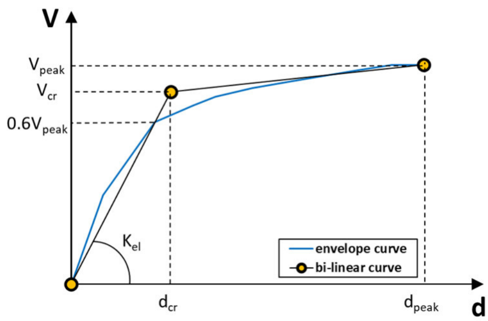

Figure 5.2.11. Energetic approach used for the definition of the displacement at cracking .

The initial elastic stiffness K_{el} is evaluated as the ratio between $0.6V_{peak}$, defined according to Italian Standard code NTC 2018 [101], and the displacement corresponding at this shear value $d(0.6V_{peak})$. Then, the displacement at cracking is defined assuming that the energy E under the blue line is equal to the energy under the black line considering that the initial elastic stiffness is fixed to be equal to K_{el} (see Figure 5.2.11). The corresponding shear cracking V_{cr}, is obtained by multiplying the defined displacement d_{cr} with the initial elastic stiffness K_{el}. Once the multi-linear envelope is defined for each floor, the previously calibrated pivot model [78] is implemented in the MATLAB code to reproduce the hysteretic response of each floor to perform NTLH analyses. In this way, the simplified model is implemented in the framework to perform loss-assessment at regional scale.

The simplified nonlinear model implemented in the seismic loss assessment framework (Figure 5.2.9) was validated by comparing the results in terms of interstorey drift (IDR) and interstorey shear (V) with those obtained from the numerical analysis performed with the nonlinear building model. The dynamic properties (mass, stiffness, and damping) of the model are the same as those previously defined for this model. The analysis consists of a NLTH analysis performed using as input the original signal of the 2009 L'Aquila earthquake (PGA of 0.45 g) recorded by the AQG station in the E-W direction. Figure 5.2.12 shows the comparison of the results.

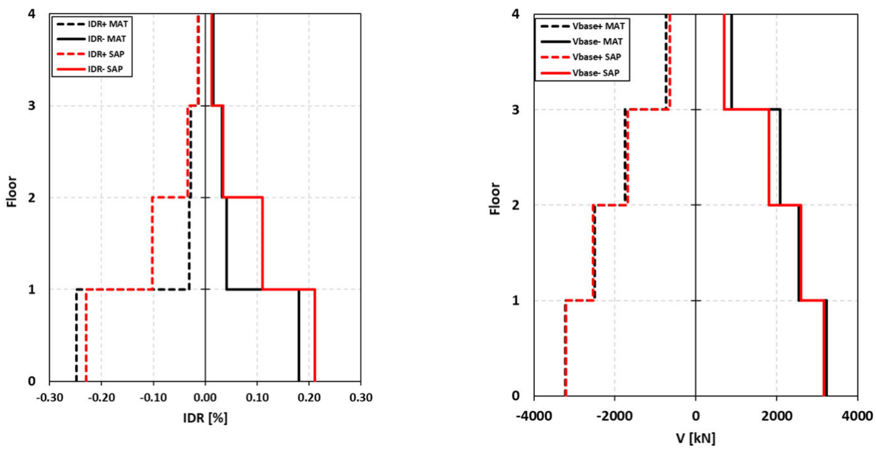

Figure 5.2.12. Comparison between the results obtained from the simplified framework and the refined numerical model in terms of IDR and interstorey shear for 100% of the L'Aquila 2009 earthquake.

In Table 5.2.2 and Table 5.2.3, the percentage difference between the EDPs resulting from the two models is reported. The results show that at the 1st, 3rd, and 4th storey the IDR differs between the two models by 8%, -18%, and -4% in the negative direction and -15%, -5%, and 26% in the positive direction. At the 2nd storey, the IDR of the simplified model differs from that of the refined model of 69% in the negative direction and -63% in the positive direction. Therefore, the simplified model provides a lower IDR than the refined model on the 2nd storey. This result can be attributed to the tendency of the lumped mass system adopted for the simplified model to localize most of the building deformations on the 1st storey.

Figure 5.2.12 also shows the comparison of the results in terms of the interstorey shear V for all the stories. A difference of 1% in the negative direction and 2% in the positive direction is observed at the 1st storey and the 2nd storey. The difference increases on the 3rd and the 4th storey, with a difference of 4% and 15% in the negative direction and of 16% and 26% in the positive direction. Despite these slight differences, the two models are in agreement between them.

Table 5.2.2. Summary of the comparison of between the numerical results in terms of IDR from the MATLAB and SAP2000 models

Floor	MATLAB		SAP2000		$\Delta_{MAT/SAP2000}$	
	Interstorey drift (IDR)					
	-	+	-	+	-	+
-	%		%		%	
1	0.248	0.181	0.23	0.212	8%	-15%
2	0.031	0.041	0.102	0.111	-69%	-63%
3	0.028	0.033	0.034	0.034	-18%	-5%
4	0.013	0.016	0.014	0.013	-4%	26%

A summary of the comparison of the results obtained from the NLTH analysis in terms of interstorey drift IDR and shear V and the difference between the two models is shown in Table 5.2.2 and Table 5.2.3.

Table 5.2.3. Summary of the comparison of between the numerical results in terms of interstorey shear from the MATLAB and SAP2000 models

Floor	MATLAB		SAP2000		$\Delta_{MAT/SAP2000}$	
	Interstorey shear (V)					
	-	+	-	+	-	+
-	kN		kN		%	
1	3228	3232	3208	3169	1%	2%
2	2503	2549	2535	2599	-1%	-2%
3	1752	2085	1687	1802	4%	16%
4	741	880	646	696	15%	26%

Chapter 6

6. Study on control errors and test reliability

The PsD testing method allows to reproduce the effects of real earthquakes on a reduced or full-scale structural system physically built in the laboratory environment. The method is usually used to overcome the limitations in the pre-defined loading protocols of the quasi-static test and of the maximum payload of the shaking table. However, to guarantee that the displacement imposed on the specimen corresponds to the actual displacement experienced by the structure during the earthquake, the reliability of the test must be assessed, and the presence of errors investigated. The main sources of errors are related to the control errors and the experimental errors. This study focuses on the control errors related, since the effects of other experimental errors and their consequences are better known and controlled [67]. The control errors, discussed in 2.3.6, strictly depend on the gain parameters of the PID algorithm [43] as well as on the λ time scale factor [36] defined in the control system.

In this Chapter, the testing framework implemented in the European Laboratory for Structural Assessment (ELSA) of the Joint Research Centre (JRC) at the European Commission is presented along with the new bench set-up, PONYBENCH, used to carry out the research activities. The effects of the control parameters (i.e., P, I and λ) on the response are investigated and the optimum set of control parameters was identified. The dynamic properties of the specimen are identified by dynamic snap-back (SnB) tests. Based on the test results of the SnB and PsD tests the dynamic properties were identified the methods presented in the Chapter 2. Finally, the SnB test is reproduced using a PsD test to investigate the reliability of this method to reproduce the dynamic response of the specimen.

6.1 The European Laboratory for Structural Assessment (ELSA) of the Joint Research Centre (JRC) at the European Commission

6.1.1 Testing infrastructure

In this Chapter the control system used to perform PsD tests, the ELSAREC, is presented. The PsD testing infrastructure of the ELSA laboratory is presented in Chapter 2. Figure 6.1.1 shows the configuration of the testing framework in which the control system is included. The control system uses EtherCAT technology and consists of a master unit, monitoring units, slave boxes and an I/O mushroom. A bus wire starts from the master unit and connect this one to the slave boxes with a linear or radial scheme. The master unit is constituted by a master box, on which the I/O mushroom is connected, and a master PC which consents to define the control parameters and to manage all the devices installed on a test set-up. In addition, it runs the algorithms implemented to carry out the tests (cyclic, dynamic and pseudo-dynamic), the input data, and allows to visualize in real-time the feedback of all the DoFs separately. The I/O mushroom allows to start, pause and restart the test by an on/off switch, and shut-down the pumping system for safety reason.

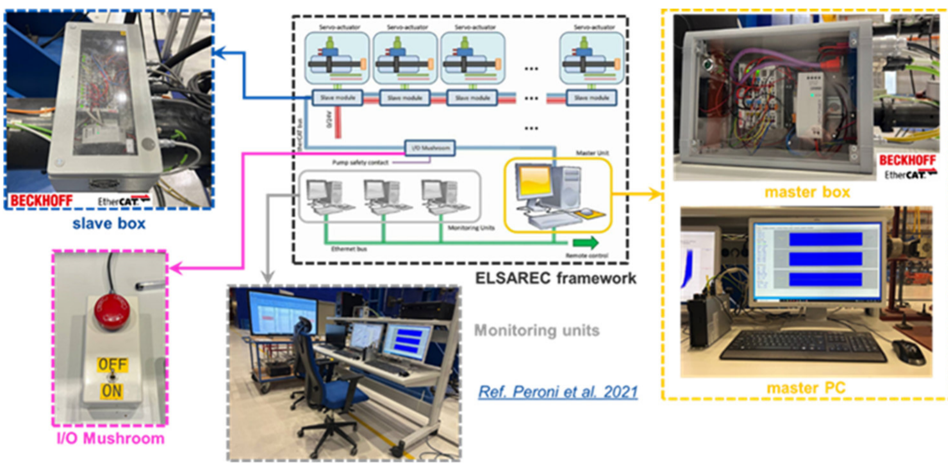

Figure 6.1.1. ELSAREC framework.

The slave boxes are connected through an EtherCAT bus wire to the master box to be managed by the master unit and powered by a 0/24V supply wire. Two different configurations are conceived for the slave box. The first configuration allows to manage the DoFs and to visualize the fed-back of the instruments installed on the hydraulic actuators. The second configuration representing the data acquisition (DAQ) used to record the measurements of the instruments installed on the specimen. The monitoring units allow to visualize contemporary the feedback of each DoF. They are connected to the master box using an Ethernet bus wire. In this way, the response of each DoF can be monitored at every time allowing to check for the presence of issue or errors in the response. Furthermore, the measurement recorded by the instruments (inclinometers, displacement transducers, laser, strain gauges, accelerometers, etc.) installed on the specimen and connected to the slave boxes can be visualized in the monitoring units adding in the main interface the window corresponding to the selected instrument. More details on the ELSAREC control system can be found in Peroni et al. [102].

Figure 6.1.2 shows the comparison between the ELSAREC controller and a commercial controller. The commercial controller is a ready-to-use system with a sample rating of 1-2 kHz which can control up to 30 DoFs (or axes) without requiring a specific employee to perform the tests and to implement the algorithms.

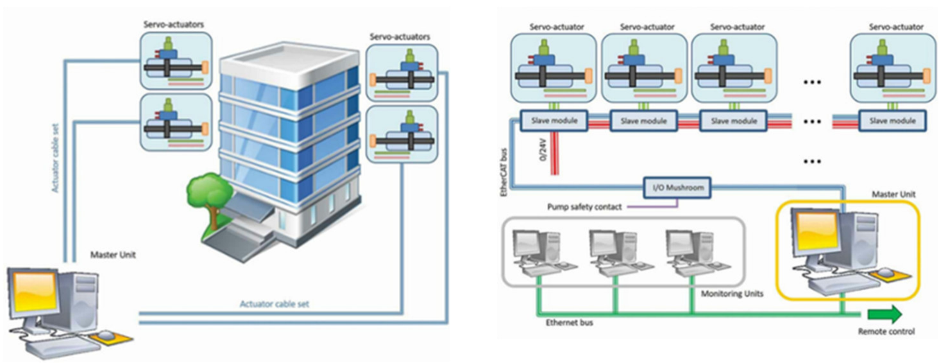

(a) (b)

Figure 6.1.2. Comparison between ELSAREC controller (a) and commercial controller (b) [102].

However, the system is too much expensive while when the characteristics of the set-up or testing methodology must be changed, a new contract must be developed with the provider with additional costs and time delay.

On the other hand, the ELSAREC controller allows to increase the number of DoFs simultaneously managed by the control system without additional costs. This consents the testing framework to be adapted to different test set-ups and to be used for different testing methods. The wiring system is improved due to the possibility of install the slave boxes near to the instruments. The algorithms used to perform the tests and the control system are implemented in an industrial PC for which specific performances are not required. Despite these advantages, specific skills are necessary for programming and the maintenance of the control system.

6.1.2 The test set-up for demonstration, training, research and knowledge handover: the PONYBENCH

The new bench test set-up, PONYBENCH, is shown in Figure 6.1.3. It consists of a single-bay, two-storey 3D structure relying on steel columns connected by two rigid steel slabs.

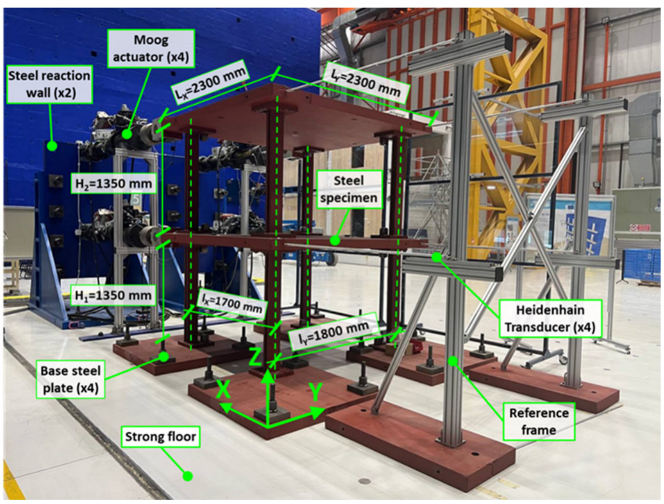

Figure 6.1.3. The PONYBENCH test set-up.

Each slab is 0.10 m thick with a mass of 4126 kg. The columns of the ground floor are connected at the bottom end to a steel plate while the top end is connected to steel slab by means of bolted connections. Each plate is fixed to the strong floor by means of four 36 mm diameter Dywidag bars pre-stressed with 50 tons each. On the second floor, the columns are connected at both ends to the slab of first and second level by means of bolted connections.

The column cross-section consists of four separated rectangular steel profiles 70 mm width and 30 mm height (see Figure 6.1.4). All the columns are oriented with the weakest direction (with the minimum moment of inertia along the load direction, X). The interstorey height is 1.35 m, and the clear height of columns is 1.17 m. The slabs are 2.30 m x 2.30 m x 0.10 m and considered infinitely rigid due their high thickness. The bay length is 1.70 m and 1.80 m in the X and Y directions, respectively. The specimen is in its bare configuration (Orig) is depicted in Figure 6.1.3. It was designed to withstand a maximum displacement in X direction of 14.50 mm. To avoid the columns yielding, this value is used as interlock in the control system to switch-off the pumping system when the displacement threshold is achieved. The bare configuration can be modified installing diagonal V-shaped steel braces connected to the steel floor by means of configurable steel springs that can be used to increase the stiffness or add additional damping.

The experimental set-up consists of two steel reaction walls fixed to the strong floor by means of six bars Dywidag of 36 mm. Two Moog actuators (one on each level) with 500 mm peak to peak stroke ($\pm$ 250 mm) and a load capacity of 500 kN (50 tons) are installed on each reaction wall. Each actuator is equipped with a Moog servo valve with a capacity of 38 l/min and a Maywood load cell with a capacity of 500 kN (50 tons) for measuring the restoring force. The mounted actuators can apply the load only in the X direction (translational). The actuators located at the same level can be coupled to apply to the specimen a translational, torsional or translational plus torsional displacement to the specimen. The displacement imposed on the specimen is measured by four displacement Heidenhain transducers (two on each level) with a stroke length of 520 mm installed on a Bosh-Rexroth aluminium frame. The transducer axis is coincident with the load axis of the actuator positioned on the steel reaction walls on the opposite side.

The PONYBENCH was used in the research activities carried out at ELSA, to identify the dynamic properties of the specimen by dynamic snap-back test and to investigate the effects of the control parameters on the experimental response by PsD tests. In addition, the dynamic SnB test is reproduced through PsD test to assess the reliability of the PsD testing method to reproduce the dynamic response of the specimen.

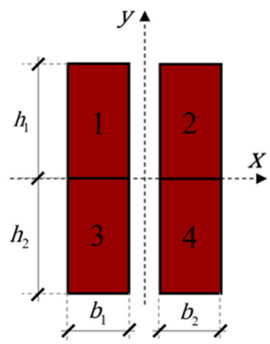

Figure 6.1.4. Column cross-section.

6.2 Experimental program

6.2.1 Numerical models

The SnB and PsD tests require the definition of an idealized numerical model representative of the tested specimen. Two different models were adopted for the SnB tests and PsD tests. The models are also used to perform a modal analysis in order to predict the test results. Figure 6.2.1 shows the model referred as Orig4T adopted for the SnB tests (dynamic and PsD).

The term “Orig” stands for original bare structure configuration while the term “4T” stands for 4 tons, which is approximately the real mass of the steel floor slabs. The model consists of a 1-bay-by-1-bay, two-storey structure lumped mass model with mass (DoFs) lumped (placed) at the load application point of each actuator. The column rotation at both ends is negligible since the floors are assumed to be infinitely rigid due to the high thickness of the slabs.

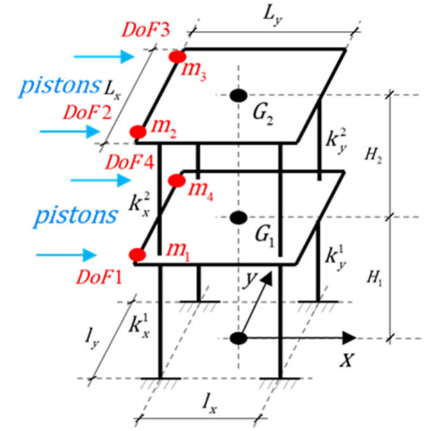

Figure 6.2.1. Numerical model of the SnB tests (Orig4T).

Four mode shapes are identified for the model Orig4T (see Figure 6.2.2). The first and the third modes are translational along X (weakest) direction while the second and the fourth modes are torsional around the Z axis (vertical).

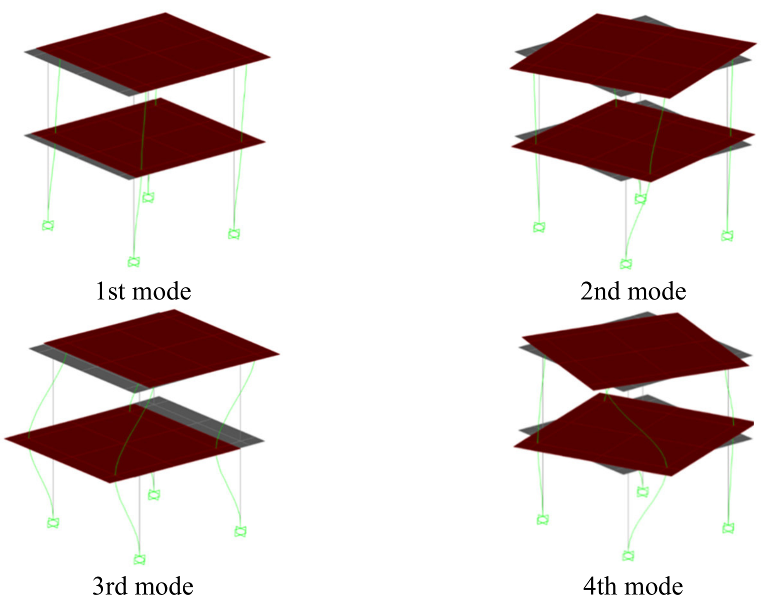

Figure 6.2.2. Translational and torsional mode shapes of the Orig4T model.

The geometrical dimension of the model corresponds to the dimensions of the specimen. Indeed, the bay length in X direction l_x is 1.70 m while the bay length in Y direction l_y is 1.80 m. The interstorey height is 1.17 m at both floors (i.e., H_1 and H_2). The slabs are 2.3 m x 2.3 m in plan ($L_x = L_y$). The thickness of the slabs and of the end plates of the columns is neglected in the model to consider only the deformable portion of the structure. The theoretical mass of the slab is assumed to be 4126 kg (i.e. the real mass of the slabs).

The idealized model Orig8T used for the PsD tests is shown in Figure 6.2.3. The differences from the previous model Orig4T are the number of DoFs, which has been reduced from four to two DoFs and placed at the centre of the two slabs, and the mass, which has been increased to about 8 tons. Since the load is applied in the X direction, only two translational mode shapes along the X direction are considered for this model.

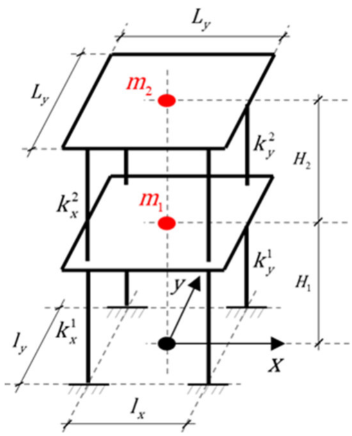

Figure 6.2.3. Numerical model of the PsD tests (Orig8T).

The definition of the mass matrix [M] and the stiffness matrix [K] is a mandatory input to perform the tests and the numerical analysis. The definition of the viscous damping matrix [C] is not considered in the solution of the equation of motion since the hysteretic damping already considered is the kind of damping normally observed for classical construction materials under seismic loading.

The translational mass $[M_x]$ of the physical specimen in the X direction is defined as (6.1):

$$[M_x] = \begin{bmatrix} m_1 & 0 \\ 0 & m_2 \end{bmatrix} = \begin{bmatrix} 4126 & 0 \\ 0 & 4126 \end{bmatrix} \text{ [kg]} \tag{6.1}$$

In addition, the torsional mass matrix $[M_\theta]$ is also evaluated to analyse the torsional mode shapes. Considering that the elements of the matrix m_1 and m_2 represent the physical mass of each slab, the matrix $[M_\theta]$ is evaluated as (6.2):

$$[M_\theta] = \left(\frac{L_x^2 + L_y^2}{12}\right) \cdot \begin{bmatrix} m_1 & 0 \\ 0 & m_2 \end{bmatrix} = \begin{bmatrix} 3638 & 0 \\ 0 & 3638 \end{bmatrix} \text{ [kgm}^2\text{]} \tag{6.2}$$

From these matrices, the mass matrix $[M_{x\theta}]$ is defined as (6.3):

$$[M_{x\theta}] = \begin{bmatrix} [M_x] & [0] \\ [0] & [M_\theta] \end{bmatrix} = \begin{bmatrix} 4126 & 0 & 0 & 0 \\ 0 & 4126 & 0 & 0 \\ 0 & 0 & 3638 & 0 \\ 0 & 0 & 0 & 3638 \end{bmatrix} \text{ [kg; kgm}^2\text{]} \tag{6.3}$$

reflecting the contributions of the two translational and two torsional mode shapes. However, the DoFs of the model Orig4T are placed on the load application point of the actuators, while the mass matrix $[M_{x\theta}]$ is defined respect to the mass lumped at the centre of each floor. To convert the matrix $[M_{x\theta}]$ in a coordinate system in which the displacements are considered along the axes of the four actuators, a transformation matrix [T] is defined as (6.4) according to the reference scheme reported in Figure 6.2.4. In this scheme, the counterclockwise rotation is assumed to be positive.

$$u_p = T \cdot u_{x\theta} \Leftrightarrow \begin{bmatrix} u_{p1} \\ u_{p2} \\ u_{p3} \\ u_{p4} \end{bmatrix} = \begin{bmatrix} 1 & 0 & -L_y/2 & 0 \\ 0 & 1 & 0 & -L_y/2 \\ 0 & 1 & 0 & L_y/2 \\ 1 & 0 & L_y/2 & 0 \end{bmatrix} \cdot \begin{bmatrix} d_{xI} \\ d_{xII} \\ \theta_I \\ \theta_{II} \end{bmatrix} \tag{6.4}$$

The transformed mass matrix used as input for the model to perform modal analysis and the PsD snap-back tests is defined as (6.5):

$$[M_p] = (T^{-1})^T \cdot [M_{x\theta}] \cdot T^{-1} \Leftrightarrow [M_p] = \begin{bmatrix} 1941 & 0 & 0 & 122 \\ 0 & 1941 & 122 & 0 \\ 0 & 122 & 1941 & 0 \\ 122 & 0 & 0 & 1941 \end{bmatrix} [\mathrm{kg; kgm^2}] \tag{6.5}$$

The model Orig8T adopted for the PsD tests require the definition of the mass matrix as input. The translational mass matrix $[M_{x,PsD}]$ has the diagonal elements m_1 and m_2 assumed to equal double the mass of the slab (i.e., 8152 kg). This assumption is possible for the mass since it can be numerically simulated for each DoF while to change stiffness the configuration of the test set-up must be changed.

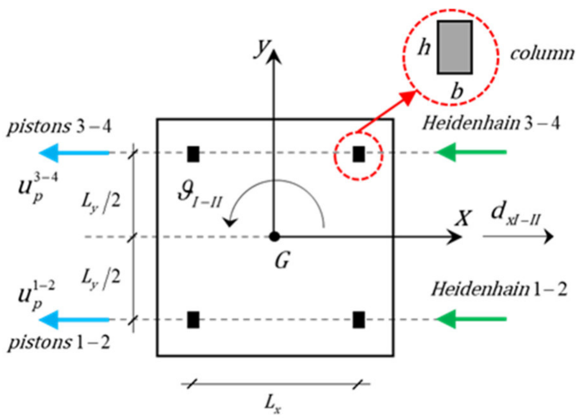

Figure 6.2.4. Reference scheme for the definition of the transformation matrix [**T**].

In this way, the natural frequencies of the specimen are shifted into a more typical range for civil engineering structures. The mass matrix $[M_{x,PsD}]$ evaluated as input for the model Orig8T is reported below in (6.6).

$$[M_{x,PsD}] = \begin{bmatrix} m_{1,PsD} & 0 \\ 0 & m_{2,PsD} \end{bmatrix} = \begin{bmatrix} 8152 & 0 \\ 0 & 8152 \end{bmatrix} \text{ [kg]} \tag{6.6}$$

The modal shapes considered in the model Orig8T are only translational according to the load which is applied only in X direction (i.e., no torsion is considered in the model).

The stiffness matrix is also required as input for all the presented models. The stiffness matrix $[K_x]$ of the physical specimen in the X direction is defined with reference to the simplified model reported in Figure 6.2.5, in which the rotation at both ends of the columns is assumed negligible due to the thickness of the slab.

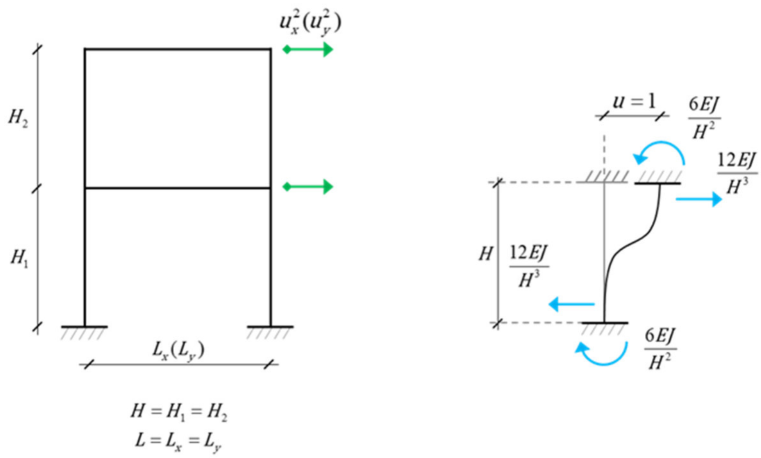

Figure 6.2.5. Simplified model considered to define the PONYBENCH lateral stiffness $\mathbf{k_x}$.

According to Figure 6.2.5, the lateral stiffness k_x of the single column in the X direction is calculated as (6.7):

$$k_x = \frac{12 \cdot E \cdot J_x}{H^3} = 991 \left[\frac{kN}{m}\right] \tag{6.7}$$

while the elements $k_{x,ij}$ of the translational stiffness matrix $[K_x]$ reported in (6.8) are evaluated applying an unitary displacement at one floor while the other is kept fixed, as shown in Figure 6.2.6.

$$[K_x] = \begin{bmatrix} k_{x,11} & k_{x,12} \\ k_{x,21} & k_{x,22} \end{bmatrix} = \begin{bmatrix} 7930 & -3965 \\ -3965 & 3965 \end{bmatrix} \left[\frac{kN}{m}\right] \tag{6.8}$$

The defined matrix $[K_x]$ represents the stiffness matrix assigned as the input to the Orig8T model to perform modal analysis and compare the frequencies of the identified mode shapes with those evaluated from the post-processing of the PsD test results.

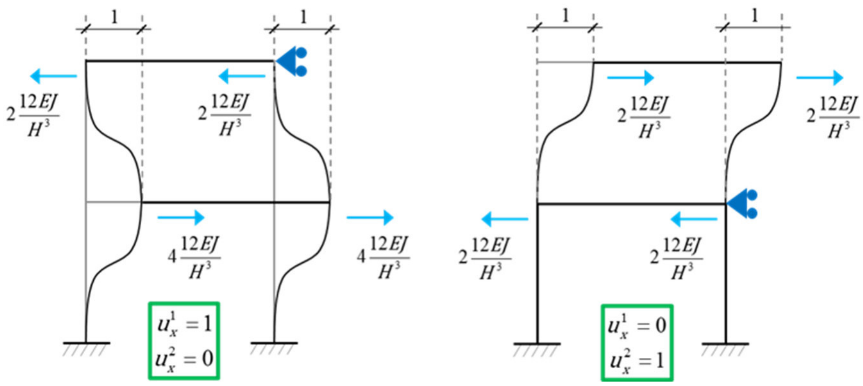

Figure 6.2.6. Reference scheme for the definition of the stiffness matrix $[\mathbf{K_x}]$.

To evaluate the torsional modes, the torsional stiffness matrix $[K_\theta]$ is required as input in the modal analysis. The elements $k_{\theta,ij}$ of the torsional stiffness matrix are defined applying a unitary rotation at one floor while the other was kept fixed. According to Figure 6.2.7, the torsional stiffness matrix $[K_\theta]$ is defined as (6.9):

$$[\mathrm{K}_\theta] = \begin{bmatrix} \mathrm{k}_{\theta,11} & \mathrm{k}_{\theta,12} \\ \mathrm{k}_{\theta,21} & \mathrm{k}_{\theta,22} \end{bmatrix} = \begin{bmatrix} 37801 & -18900 \\ -18900 & 18900 \end{bmatrix} [\mathrm{kNm}] \qquad (6.9)$$

The stiffness matrix $[\mathrm{K}_{x\theta}]$, is defined combining the matrices (6.8) and (6.9) with respect to the centre of the mass (6.10):

$$[\mathrm{K}_{x\theta}] = \begin{bmatrix} [\mathrm{K}_x] & [0] \\ [0] & [\mathrm{K}_\theta] \end{bmatrix} = \begin{bmatrix} 7930 & -3965 & 0 & 0 \\ -3965 & 3965 & 0 & 0 \\ 0 & 0 & 37801 & -18900 \\ 0 & 0 & -18900 & 18900 \end{bmatrix} \left[\frac{\mathrm{kN}}{\mathrm{m}}; \mathrm{kNm}\right] \qquad (6.10)$$

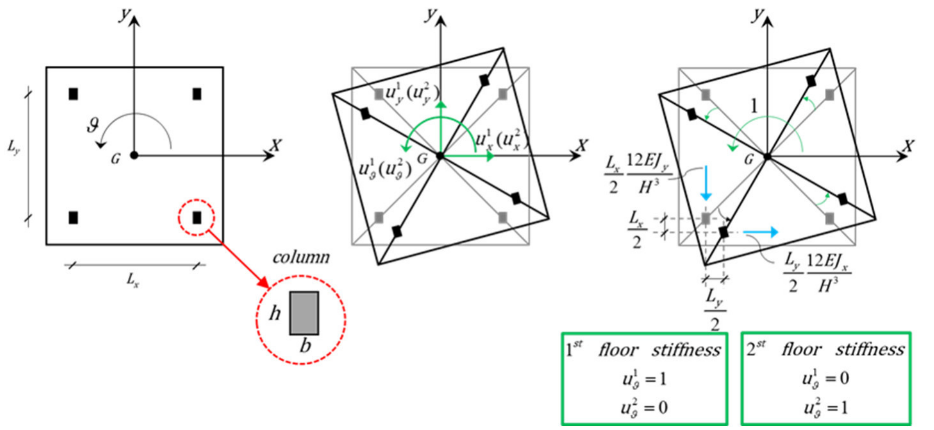

Figure 6.2.7. Reference scheme for the definition of the stiffness matrix $[\mathbf{K}_\theta]$.

As seen for the mass matrix, the stiffness matrix $[\mathrm{K}_{x\theta}]$ is then transformed with respect to the actuators position using the transformation matrix [T] (6.11):

$$[K_p] = (T^{-1})^T \cdot [K_{x\theta}] \cdot T^{-1} \Leftrightarrow [K_p] = \begin{bmatrix} 11433 & -5716 & 3734 & -7468 \\ -5716 & 5716 & -3734 & 3734 \\ 3734 & -3734 & 5716 & -5716 \\ -7468 & 3734 & -5716 & 11433 \end{bmatrix} \left[\frac{kN}{m};\right] \tag{6.11}$$

Once the mass matrix and the stiffness matrix of each model are defined, a modal analysis is performed to evaluate the mode shapes and the corresponding frequencies. The results of the analyses are then compared with the frequencies obtained from the post-processing of the test results. The modal analyses are carried out using the models Orig4T and Orig8T. In the first model the mass matrix $[M_p]$ (6.5) and the stiffness matrix $[K_p]$ (6.11) are used to identify both translational and torsional modes. In the second model the mass matrix $[M_{x,PsD}]$ (6.6) and the stiffness matrix $[K_x]$ (6.8) are used to identify the translational modes only. In Table 6.2.1 a summary of the results of the modal analyses is reported along with the type of tests, the type of model, the mass matrix and the stiffness matrix used for the model, the number of DoFs, the type of mode and the related frequencies.

Table 6.2.1. Modal analysis results.

to predict test type	model details			number of DoFs	mode direction	frequency [Hz]			
	model	[M]	[K]			mode 1	mode 2	mode 3	mode 4
PsD	Orig8T	$[M_x]$ (6.6)	$[K_x]$ (6.8)	2	X	2.156	5.645	n.d.	n.d.
SnB	Orig4T	$[M_p]$ (6.5)	$[K_p]$ (6.10)	4	X - θ	3.049	7.090	7.983	18.562

6.2.2 Testing procedure

The testing sequence comprises the dynamic snap-back (SnB) test performed to identify the dynamic properties of the PONYBENCH, and the pseudo-dynamic tests (PsD) to study the effects of the control errors on the response. Then, a PsD snap-back test is performed to evaluate the reliability of the PsD testing method to reproduce the dynamic response of the specimen. At the beginning of each test, all the instruments are reset except for the PsD snap-back test in which an initial displacement is imposed on each DoF by the hydraulic actuators to reproduce the initial boundary conditions of the specimen. In Table 6.2.2 the test matrix of the experiment carried out on the PONYBENCH is reported. The table contains the following information:

- Test ID: test identification name.
- Type of numerical model: Orig4T or Orig8T (see 6.2.1).
- Type of load: free vibration of accelerogram.
- Intensity and interval of the record.
- Control parameters: l, P and I which can be constant (CO) or variable (VB).
- Notes and additional information.

Table 6.2.2. PONYBENCH experiments.

test ID	model	input			parameter			notes
		load	intensity	interval	λ	P	I	
SnB	Orig4T	free vibration	10 mm	-	-	-	-	dynamic snapback test
PSnB*	Orig4T	free vibration	-	-	200 (CO)	2.0 (CO)	100 (CO)	PsD snapback test. Reproduction of test SnB
PsD1	Orig8T	Amatrice EQ	5%	6-9 s	200 (VB)	0.5 (CO)	100 (CO)	λ variable. P, I constant
PsD2	Orig8T	Amatrice EQ	5%	6-9 s	200 (CO)	0.5 (VB)	100 (CO)	P variable. λ and I constant
PsD3	Orig8T	Amatrice EQ	5%	6-9 s	200 (CO)	0.5 (CO)	50 (VB)	I variable. λ and P constant

(CO) constant

(VB) variable

(*) The test PSnB is carried out imposing the proper DoFs displacement and velocity defined through the analysis of the results of the tests SnB as initial conditions.

The PsD tests are carried out on the PONYBENCH test set-up to study the control parameters. The range of values and the effect of their change on the response of the control system are investigated. The occurrence of frequency and damping distortion in the response is expected when the time scale factor λ decreases while the gain parameters P and I are kept constant. The same result is to be expected when the gain parameter P decreases. This is due to the proportionality of this parameter with the control error. In contrast, the occurrence of the control errors is to be expected when the gain parameter I increase due to the integrative relationship with the errors.

6.2.2.1 Dynamic Snap-back (SnB) test

The dynamic snap-back test consists in pulling the specimen at a specified target displacement increasing the level of force, until a fragile connection is broken releasing the structure that is left free to vibrate. The target displacement imposed to the specimen (10.00 mm) is selected as fraction of 70% of the maximum allowable displacement u_x^{adm} (14.50 mm) reported in 6.1.2, considering a safety factor of 1.5. This kind of test is performed to identify the dynamic properties and the mode shapes of the specimen. The load is applied in one side using its actuator installed on a reaction wall and connected to the structure through a steel bar with a section properly designed for the purpose (fragile connection), while the other actuators are detached from the specimen. The specimen is pulled at the first floor rather than at the second one in order to increase the response of the higher modes. Figure 6.2.8 shows the test set-up realized to perform the dynamic SnB test installed on the actuator connected to the specimen.

The test set-up is equipped with two struts used to limit the target displacement, while the load applied by the actuator is transferred on the reaction wall using the cylinder of the actuator itself as a bearing. The gap between the specimen and the struts is regulated by two nuts that allow to stop the structure when the target displacement is achieved. In this way, the actuator continues to pull the tension rod until its fracture maintaining constant the imposed displacement.

Once the dynamic SnB test is performed, the test set-up was removed, and all the actuators are connected to the structure to carry out the PsD snap-back test. The aim of the test is to reproduce the dynamic response of the specimen observed in the snap-back test. The initial conditions (displacement and velocity) of the PsD test are obtained through the analysis of the results obtained from the dynamic SnB test.

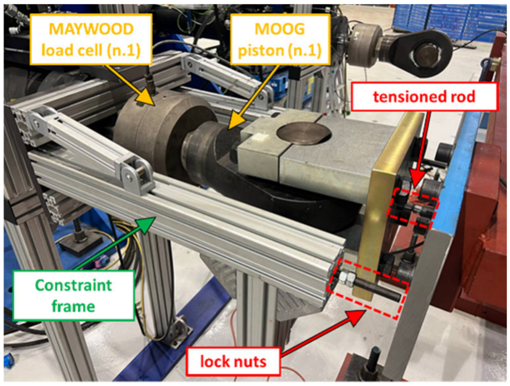

Figure 6.2.8. Dynamic snap-back (SnB) test set-up.

6.2.2.2 Pseudo-dynamic (PsD) tests

The PsD tests were performed to study the control errors and to identify the optimum set of control parameters. It is worth remembering that the control errors are defined as the difference between the computed (target) displacement and the measured (imposed) displacements. The effects of time scale factor λ [19] (which gives information about the test speed) and proportional and integrative gain parameters P and I on the experimental response are investigated. The tests consist of several stages, in which the accelerogram selected is repeated at every stage, while the value of factor λ and P and I parameters changed from stage to stage.

The load is applied only in the X direction, using as accelerogram from the 2016 Central Italy Amatrice earthquake. This record was selected as it is representative of the natural accelerograms commonly used in the full-scale tests conducted at ELSA. The original record has a peak ground acceleration (PGA) of 5.22 m/s^2 and a length of 25.0 s (see Figure 6.2.9).

For convenience, a time window between 6.0 s to 9.0 s (with a length of 3.0 s) of the original record was selected. The selection criteria consisted of identifying a short length accelerogram with an energy content that could excite the relevant modes and eventually repeat it several times. The accelerations of this record are scaled by a factor of 5% in order to limit the response in the elastic range avoiding the maximum allowable displacement of 14.50 mm to be achieved. Thus, the record presents a PGA equal to 0.26 m/s^2.

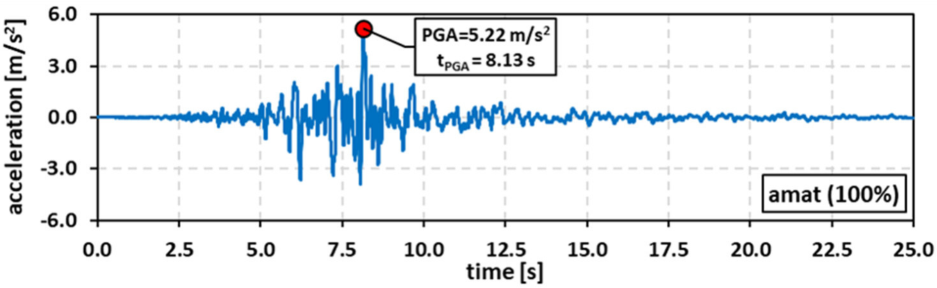

Figure 6.2.9. Amatrice accelerogram record.

The test was performed using the continuous method [36] (see 2.3.4) and an explicit Newmark algorithm for the equation of motion solution (see 2.3.5). The mass matrix $[M_{x,PsD}]$ defined as (6.5) for the idealized model Orig8T is selected as input. The direction of application of the load determines the identification of only two translational mode shapes along the X direction for this specimen.

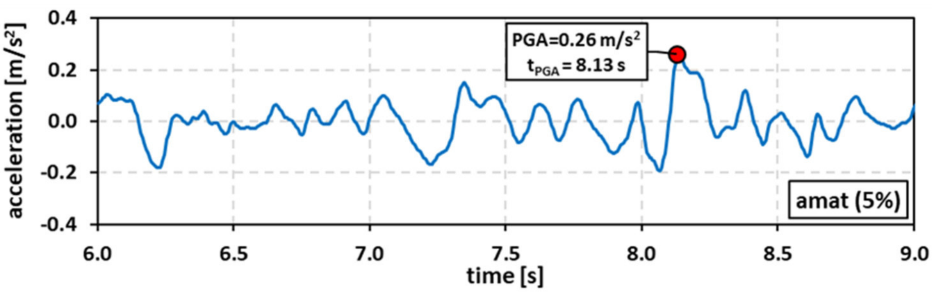

Figure 6.2.10. Accelerogram record used as input for the PsD tests.

6.2.3 Analysis of results

6.2.3.1 Dynamic and pseudo-dynamic snap-back test

The results in terms of displacement time histories measured for each DoF are reported in Figure 6.2.11. The test data is recorded by the controller using an acquisition with a pre-trigger and a maximum time window of 40 s. Despite the test duration is greater than the acquisition duration (greater than 60 s), the amount data recorded during the test is satisfying for the purpose. The displacement measured at breaking time for the DoF1 was 10.31 mm, with an error of 0.03% with respect to the imposed one. Thus, the tensioned bar was correctly designed to break at a target displacement of 10 mm. In addition, the maximum force recorded on the actuator connected to the specimen at the instant in which the tension rod beaks setting the specimen in free vibration is 111.5 kN.

The displacement measured by the transducers at the breaking time are 10.31 mm, 10.41 mm, 7.97 mm and 7.93 mm for the DoFs 1, 2, 3, and 4. The position of each DoF corresponds to the position of the DoFs in the model Orig4T (Figure 6.2.1). The results show a difference between the displacement of the DoFs 1 and 4, which are located on the north side of the specimen and the DoFs 2 and 3, which are located on the south side is observed. This is due to the presence of a torsional deformation induced because the specimen is pulled by a single actuator placed at the first floor of the north side (i.e., imposing an unbalanced load). Consequently, the torsional modes are introduced in the structural response.

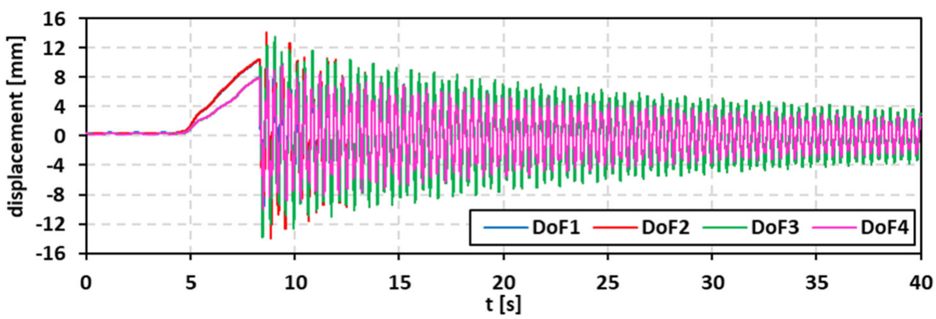

Figure 6.2.11. Displacement time histories measured for each DoF.

The frequencies of the modal shapes identified for the physical specimen are evaluated using the Filter model [19] presented in 2.3.6, from the displacement measured by the Heidenhain transducers for each DoF. The experimental results are compared with those obtained from the modal analysis performed using the idealized model Orig4T. In Table 6.2.3 the comparison between the experimental and the numerical results is reported.

Table 6.2.3. Comparison between the frequencies of the modes numerically and experimentally evaluated.

type of analysis		num.	exp.	Δ [%]
frequency [Hz]	mode 1	3.049	2.737	11%
	mode 2	7.090	6.050	17%
	mode 3	7.983	7.200	11%
	mode 4	18.562	16.200	15%

The frequencies evaluated from the tests are equal to 2.737 Hz, 6.050 Hz, 7.200 Hz and 16.200 Hz for the first translational, the first torsional, the second translational and the second torsional modes, respectively. The frequencies assessed from the modal analysis differ from these by 11.4%, 17.2%, 10.9% and 14.6%, respectively. It is worth noting that the results can be influenced by the accuracy of the mass matrix $[M_p]$ (6.5) and the stiffness matrix $[K_p]$ (6.11) defined for the model Orig4T.

The dynamic snap-back test is then reproduced with a pseudo-dynamic test to investigate the reliability of the PsD testing method to reproduce the dynamic response of the specimen. The set-up realized to perform the SnB test is removed, and all the actuators are connected to the specimen to perform the test. A preliminary PsD test was performed to analyse the matching between the experimental frequencies obtained from the results of both tests (i.e., SnB and PsD). The results of the preliminary test, suggest that the elements of the mass matrix need to be adjusted by the factors of 1.0973 (translational mass) and of 1.2633 (torsional mass) in attempt to match the results of the SnB test. Therefore, the mass matrix $[M_p]$ defined for the Orig4T model is adjusted with these factors.

The initial conditions in terms of displacements and velocities for each DoFs are a mandatory input to perform the PsD snap-back test. The conditions are defined from the analysis of the displacement time histories reported in Figure 6.2.11. The time step corresponding to the “breaking time” is not selected to define the initial conditions. This is due to the fact that when the displacement is so far from zero, the prepositioning prior to the start of the test may cause a stress relaxation. Therefore, a time step at which the displacement of each DoF is close to zero is selected. In Table 6.2.4 the initial conditions used as input to perform the test are reported. In this case, the velocity is evaluated as the differentiation of the displacement.

Table 6.2.4. PsD snap-back test initial conditions.

DoF	1	2	3	4
d_0 [mm]	0.049	0.704	0.42	-0.223
v_0 [m/s]	-0.249	0.001	-0.213	-0.224

The comparison between the results of the dynamic and pseudo-dynamic snap-back tests in terms of identified frequencies is reported in Figure 6.2.12.As for the SnB test, the frequencies are identified using the Filter model [19]. The difference between the frequencies identified for the PsD test respect to those identified for the SnB test is evaluated for each mode in terms of frequencies average error Δf_{av}, calculated as (6.12):

$$\Delta f_{av} = \text{mean}\left(\sum_i \frac{f_{PsD,i} - f_{SnB,i}}{f_{SnB,i}}\right) [\%] \tag{6.12}$$

with i being the single time step varying the averaging interval. In Figure 6.2.12, the averaging interval (i.e., white background portion) represents the time window in which each mode is present in the structural response. It is worth noting that for the 1st mode the entire time window has been considered. In addition, the average error Δf_{av} is reported near the title.

The results show that the average error evaluated for the 1st and the 3rd modes (translational) is lower than 1% while increase up to about 4% in the case of the 2nd and the 4th modes (torsional). Therefore, the PsD testing method is able to well reproduce the translational modes. However, this is not the case for the torsional frequencies. This could be due to the fact that the torsional modes are less present in the response which makes less accurate their measurement and identification.

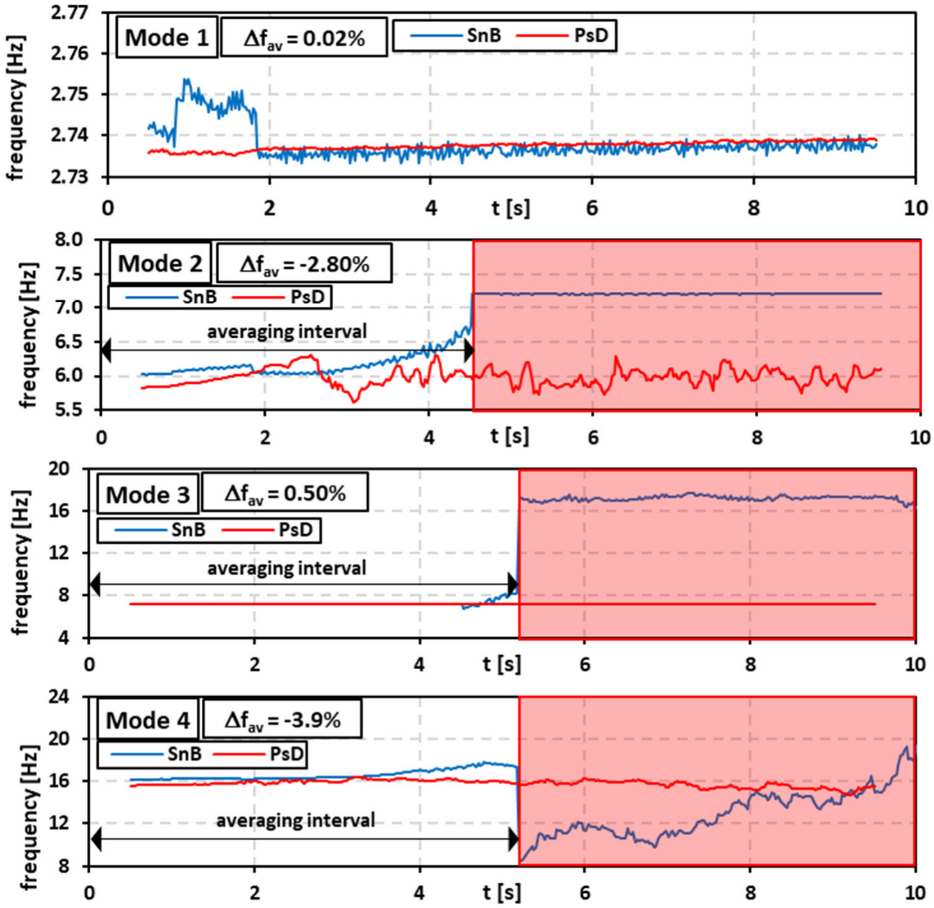

Figure 6.2.12. Comparison of the frequencies identified for the dynamic and pseudo-dynamic snap-back tests.

6.2.3.2 Pseudo-dynamic tests

The proposed test matrix for pseudo-dynamic tests (PsD) is conceived to investigate the effects of the control errors on the reliability of the results and to identify the range of use of the PID gain parameters. Considering the Table 6.2.2, the test performed during the test campaign are the following:

- test PsD1: the test is performed to study the effects of the test speed on the control stability and reliability of the test results. The λ factor is variable during the tests, with an initial value of 200, whereas the control gain parameters, P and I, are constant and set equal to 0.5 and 100, respectively.

- test PsD2: the test is performed to study the effects of the proportional gain P parameter on the control stability and the reliability of the test results. The P parameter is variable during the tests, with an initial value of 0.5, whereas the integrative gain parameter I and the λ factor are constant and set equal to 100 and 200, respectively.

- test PsD3: the test is performed to study the effects of the integrative gain I parameter on the control stability and the reliability of the test results. The I parameter is variable during the tests, with an initial value of 50, whereas the proportional gain parameter P and the λ factor are constant and set equal to 0.5 and 200, respectively.

Figure 6.2.13 shows the results in term of measured displacement and applied force time histories of the 1st and the 2nd floor for the PsD1 test. The test consists in seven stages, in which the accelerogram shown in Figure 6.2.10 is repeated at every stage, while the value of time scale factor λ is decreased from 200 to 25.

During the first stage (from 0 s to 3 s, with λ = 200) a peak displacement of 2.10 mm and 3.75 mm is achieved in the pulling (positive) direction at the 1st and 2nd floor. In the opposite direction (i.e., pushing or negative) the peak displacement applied to the specimen is -2.48 mm and -3.79 mm at 1st and 2nd floor. Thus, the maximum and minimum displacement applied to the structure can be considered symmetric.

At the second stage (from 3 s to 6 s) the test speed is increased, decreasing the λ value to 140. The peak displacement at 1st floor increased by 12% and 5%, for the pulling and pushing directions, respectively, while an increment on average of 16.5% is observed in both directions at the 2nd floor.

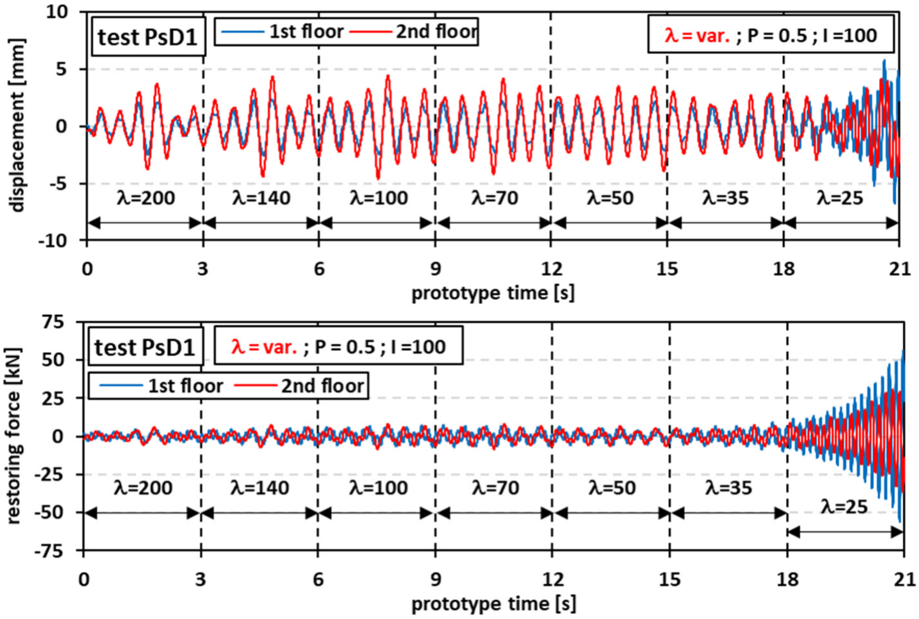

Figure 6.2.13. Results in terms of displacement and applied force for the 1st and 2nd floors.

In the time interval between 3 s to 12 s, the maximum and the minimum displacement applied at each floor remains constant, although the test speed is increased (λ changed from 140 to 70). The difference of the maximum or minimum displacement observed between two stages is smaller than 10%. Thus, the specimen reached a stationary response dominated by the presence of the 1st mode since the displacements of both floors are in phase with each other.The structural response changes when the λ factor is decreased from 50 to 25. A displacement decrement is observed at the 2nd floor during the 12-18 s time interval (λ from 50 to 35), while an increment is observed at the 1st floor. During the final stage (from 18 s), the λ factor is set equal to 25 and the 2nd mode appears and grows in the structural response in an unstable manner. The displacement diverges very fast at both floors, achieving a displacement amplitude greater than those observed during the first stage (especially at 1st floor). Note that this instability regards only the (apparent) structural response while the control stability, which is characterised by much higher frequencies, is not lost. In the cases of control instability, high-frequency noise may be heard and the displacements and forces may reach out-of-limit values in just a few control samplings (a few milliseconds of real time).

A similar response is observed also for the applied force time history (Figure 6.2.13). In this case, the 2nd mode is visible much earlier during the test. The instability starts at 18 s with λ equal to 35, when the test became very fast, as seen in the displacement time history. However, the divergence observed at the end of the test (12-18 sec) in the terms of displacement time history is clearer in the case of the applied force. This structural behaviour is related to the occurrence of an apparent negative damping ratio in the 2nd mode, as discussed later. The result shows that the response has become visibly unstable both for displacement and for applied force. In addition, the reliability of the results is questionable as well as the physical meaning of the response. Even though the control was still stable, the test is interrupted at 21 s with λ factor of 25 i.e. when the error limit (intended as the difference between the imposed and the measured displacement) defined in the control system is exceeded. In Figure 6.2.14, the response in terms of frequencies of the specimen identified using the Spatial model [19], is reported for the 1st and the 2nd modes.

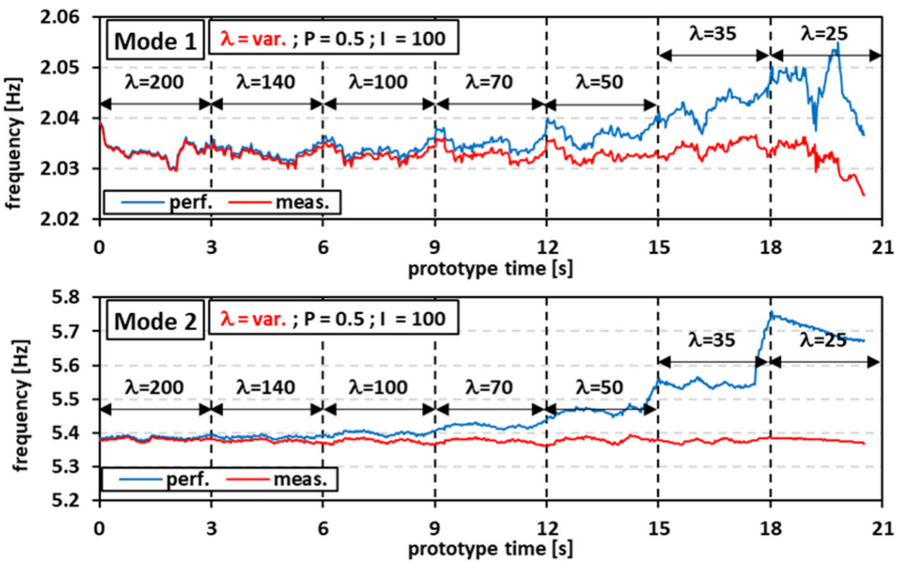

Figure 6.2.14. Frequencies of the 1^{st} and 2^{nd} modes identified using the Spatial model **[19]**.

The frequencies are computed from the measured and the reference displacement. Frequency values equal to 2.033 Hz and 5.377 Hz, obtained as the average of the frequencies identified during the first stage of the test (i.e. when λ equals to 200) from the measured displacement, are estimated for the 1st and the 2nd modes, respectively. On the other hand, the frequencies computed through the modal analysis carried out using the model Orig8T are 2.156 Hz and 5.645 Hz, as reported in Table 6.2.1. Therefore, the numerical model predicted the experimental frequencies, with a difference of 6.5% and 4.9% for the 1st and 2nd modes, respectively. The results show that the maximum difference is of 0.02 Hz for the 1st mode. This confirm that the instability is mainly associated to the higher mode. Indeed, the difference increases in the case of the 2nd mode, up to more than 0.3 Hz for λ equal to 25 due to a frequency distortion introduced by the control error.

Figure 6.2.15 shows the damping ratio identified using the Spatial model [19] for both the 1st and the 2nd modes.

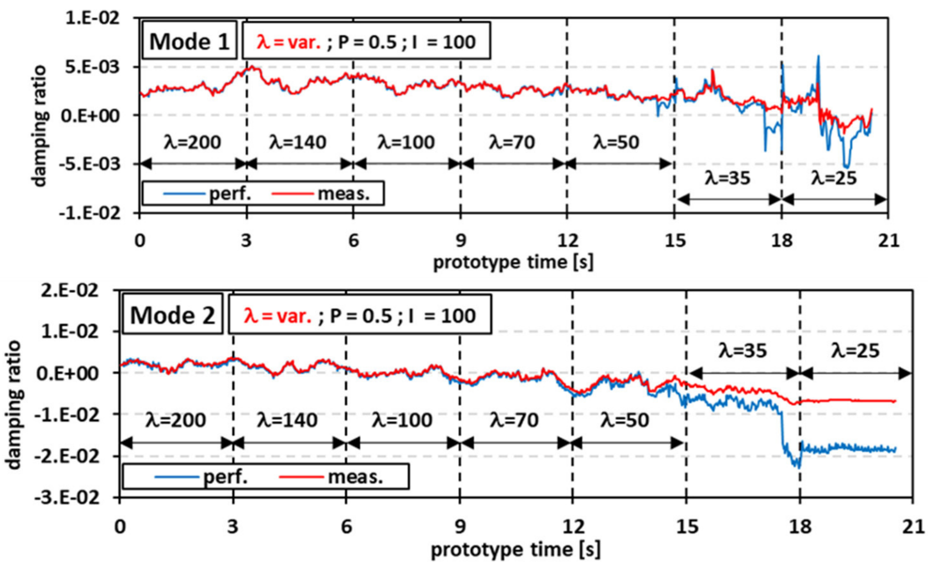

Figure 6.2.15. Damping ratio of the 1st and 2nd modes identified using the Spatial model **[19]**.

The damping ratio computed from the measured displacement and the reference displacement is close to zero in both cases. The results (Figure 6.2.15) show that the difference in terms of damping is smaller than 8.00E-4 in the case of the 1st mode. For the 2nd mode, the differences decrease to a minimum value of -0.012, when the instability occurred. In addition, the Figure 6.2.15 shows that the damping ratio computed from the reference displacement decreases to a negative value about -0.02 in the case of the 2nd mode. This result explains the divergence observed in terms of the displacement, the applied force at the end of the test. Note that for the case of a specimen with a larger physical (or added viscous) damping, these damping distortions may not yet induce instability but they may compromise the reliability of the performed test and it is important to detect them in advance.

The results of the test PsD2 in terms of displacement time histories along with the applied force time histories for the 1st and the 2nd floor are reported in Figure 6.2.16.

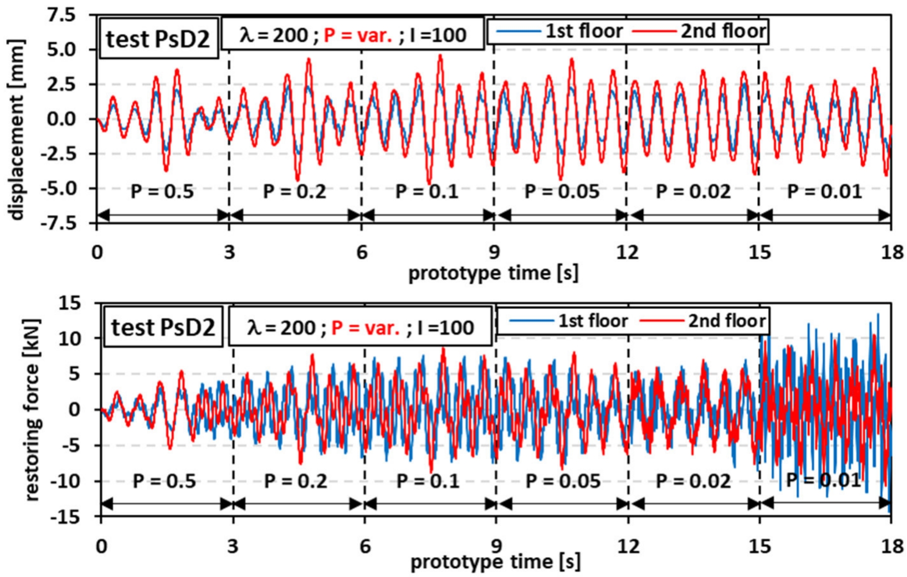

Figure 6.2.16. Results in terms of displacement and applied force for the 1st and 2nd floors.

The test approach is the same used for the PsD1 test. Therefore, the PsD2 test consist of six stages, in which the proportional gain parameter P decreases from 0.5 to 0.01 during the test. The accelerogram applied at the base of the specimen is the same used for the previous tests. It is repeated at every stage considering the same intensity (Figure 6.2.10).

The gain parameter P is set equal to 0.5 at the beginning of the test. The peak displacement achieved during the 0 to 3 s time interval on the 1st and 2nd floor in the pulling (positive) and the pushing (negative) direction has the same amplitude of those observed in the case of PsD1 test. Furthermore, the dominance of the 1st mode in the response is clear because the displacements of both floors were in phase during the test.

Looking at the applied force signal, the response is noisy at the end of the first stage of the test (P = 0.5). This happens because the proportional gain parameter P directly influences the control errors. In addition, this noise is also related to the presence of the 2nd mode in the response, it can be noted that the applied forces are out of phase between the two stories.

The displacement at both floors increases in the second stage, i.e. 3 to 6 s time interval when P is set equal to 0.2. The same situation is observed also for the applied force. Then, the amplitude of the response remains constant (stationary) from 6 s to 12 s (P =0.2 - 0.05) to then slightly decrease between 12 s and 15 s (P = 0.02).

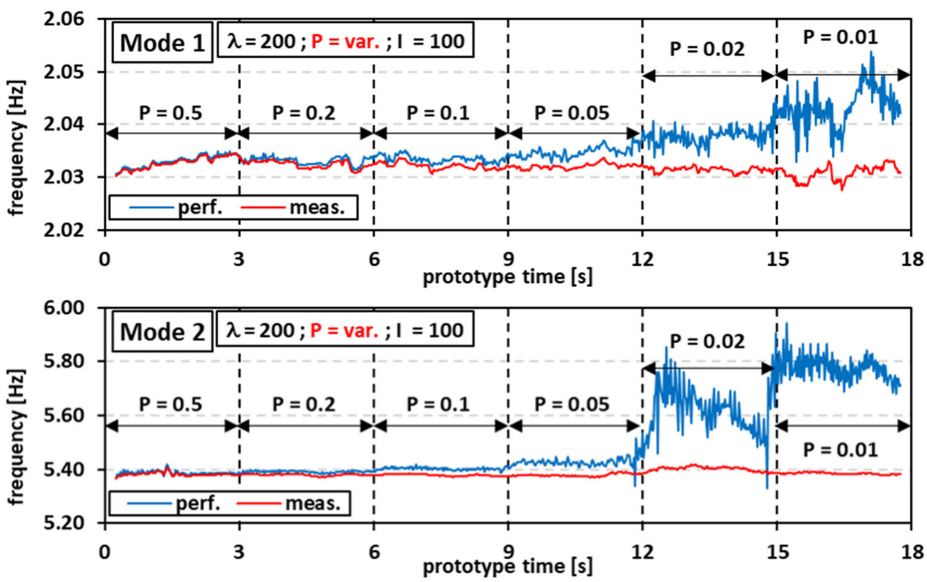

Figure 6.2.17. Frequencies of the 1st and 2nd modes identified using the Spatial model **[19]**.

During the final stage of the test (i.e. 15 to 18 s time interval with P = 0.01), the response, as it is visible in the applied force graph, is unstable because of the control errors with induced negative damping ratio in the response. Contrarily, the instability is not evident in the case of the displacement Figure 6.2.16. Finally, the test is interrupted due to the exceeding of the error limit set in the control system.

As for the PsD1 test, the response in terms of frequencies of the specimen, is reported in Figure 6.2.17 for the 1st and the 2nd modes. The frequencies are identified using the Spatial model [19] from the measured and the reference displacement. The results show that the frequencies identified for the 1st and the 2nd modes are identical to those evaluated for the PsD1 test. However, the frequencies time histories identified for the 1st and the 2nd modes appear noisier. This effect could be related to the proportionality of the gain parameter P to the errors. The maximum difference in terms of frequencies are 0.3 Hz and 0.02 Hz for the 1st and the 2nd mode, respectively. Therefore, the results of the PsD1 and the PsD2 tests confirm that the frequency distortion introduced by control errors is mainly associated to the higher mode.

Figure 6.2.18 shows the damping ratio identified for the 1st and the 2nd mode. The damping ratio is computed from the measured and the reference displacements using the Spatial model [19]. It is possible to observe that, as for the PsD1 test, the damping ratio is close to zero in both cases.

The results (Figure 6.2.18) shows that the difference in terms of damping ratio is smaller than 0.01 for the 1st mode. This is because the control errors are related to the higher modes. The damping ratio computed from the measured displacement for the 2nd mode is almost constant and slightly over zero for all the test duration. Contrarily, the damping ratio computed from the performed displacement oscillated between negative and positive values after the firsts 12 s (i.e. stage 5 and 6), achieving a minimum damping ratio of -0.06 (i.e., -6%) in the time interval when the gain parameter P equals 0.02.

According to Figure 6.2.18, the difference of the damping ratio is close to zero at the beginning of the test (P = 0.5) and remains small achieving its maximum value of 0.001 for P equal to 0.05. Thereafter, the damping ratios computed from the measured displacements are greater than those computed from the reference displacements for P from 0.2 to 0.05. At the end of the test, the difference decreases to -0.004 and -0.006 for P equal to 0.02 and 0.01. Thus, the damping ratio becomes negative, due to the occurrence of the control error. These results are consistent with those observed for the displacement and applied force response.

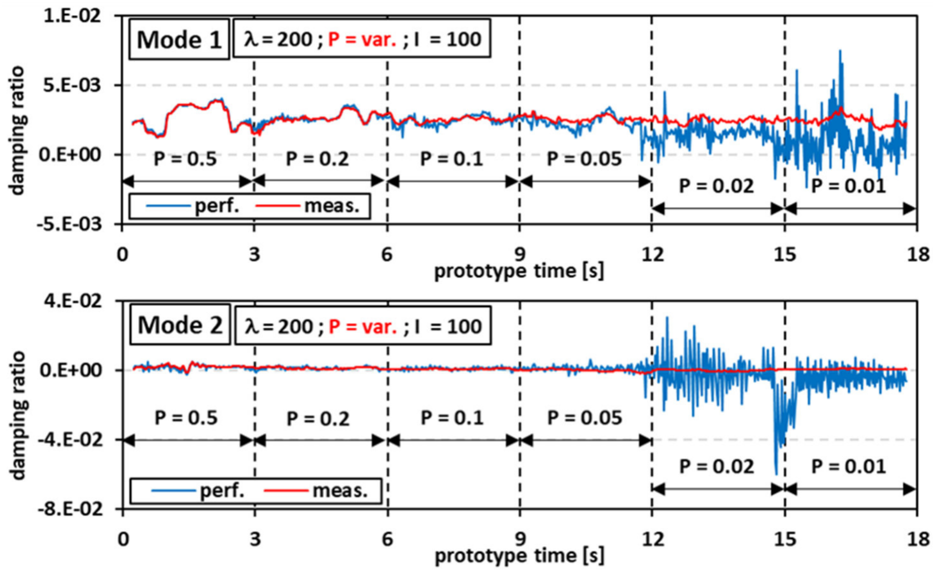

Figure 6.2.18. Damping ration of the 1st and 2nd modes identified using the Spatial model **[19]**.

Figure 6.2.19 shows the results in terms of time histories of the measured displacement and applied force for the PsD3 test. The test consists in seven stages, in which a different value of the integrative gain parameter I is defined ranging between 50 and 5000. The accelerogram used as input is presented in 0. The test is interrupted after about 19 s because the displacement error limit defined in the control system is exceeded.

The displacement time history retraces the results already seen in the previous tests (PsD1 and PsD2). Indeed, the Figure 6.2.19 shows that the peak displacement in the pulling and pushing direction increased at the 1st and 2nd floor passing from the first (I=50) to the second (I=100) test stage. Then, the amplitude remains constant for the next test stages (I=200-500), while the displacement decrement started at I equal to 1000. The same response is observed for the force applied to the specimen.

During the test final stage (I=5000) the test is interrupted due to the occurrence of the control error. In Figure 6.2.19, the restoring force increased indefinitely because of the negative damping ratio. The same response is observed in the case of displacement, although it is limited in amplitude.

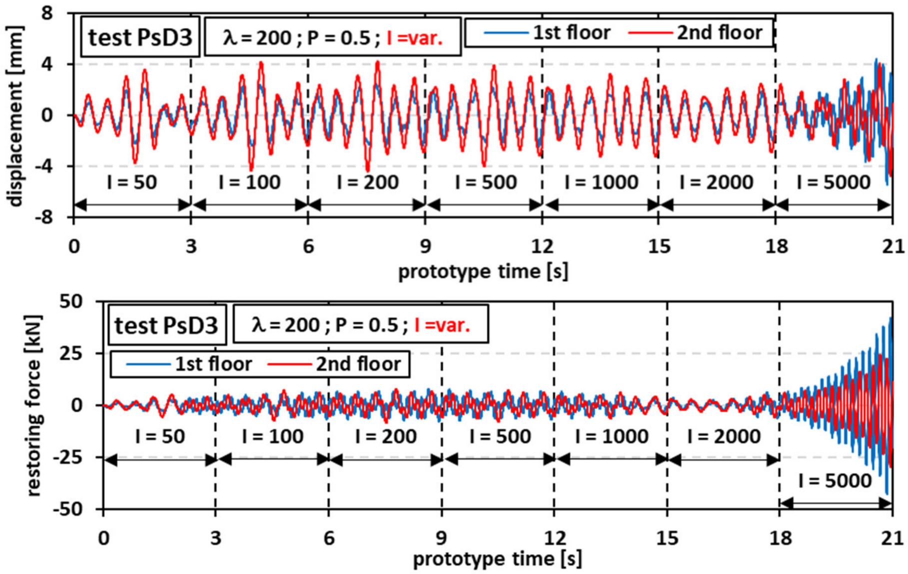

Figure 6.2.19. Results in terms of displacement and applied force for the 1st and 2nd floors.

The 1st mode dominated the displacement response up for I up to 2000 (the displacements of the 1st and 2nd floor were in phase with each other) while a more significant contribution of the 2nd mode is observed during the last stage of the test. On the other hand, the force is totally dominated by the 2nd mode (the forces of the 1st and 2nd floor were out of phase with each other), which then made the system unstable during the test final stage.

The frequencies of the 1st and 2nd mode of the system identified using the Spatial model [19] from the measured and performed displacement are reported in Figure 6.2.20.

The frequencies identified for the 1st and the 2nd modes are identical to those evaluated for the PsD1 and the PsD2 test. A difference smaller than 0.1 Hz is observed between the frequency identified from the performed (computed) and the measured displacement for the 1st mode. The difference increases up to about 0.2 Hz for the 2nd mode. This is because the control errors are related to the higher modes (i.e., the 2nd mode).

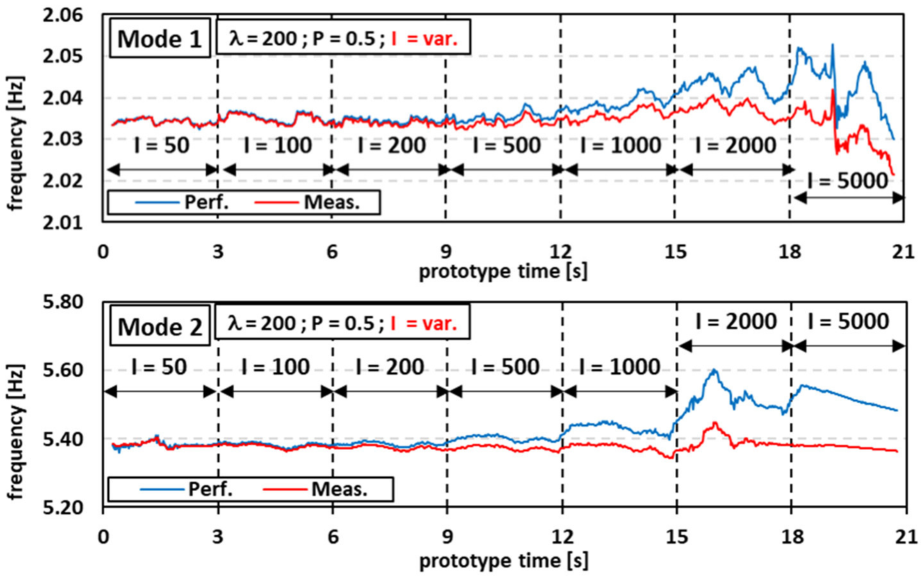

Figure 6.2.20. Frequencies of the 1st and 2nd modes identified using the Spatial model **[19]**.

The damping ratio identified using the Spatial model [19] for the 1st and the 2nd modes are reported in Figure 6.2.21.

The results show that the difference between the red and the blue lines for the 2nd mode is low for I smaller than 500. In particular, the values are close to zero during all the test stages. Then, the difference started to decrease (increase in absolute sense) for I larger than or equal to 1000, achieving a value of -0.026. Thus, significant control errors are already present for I equal to 1000 and led the system to instability when I equals 5000. In contrast, the difference of the damping ration is negligible for the 1st mode.

According to the prediction the control errors affected the response when the test speed increases (up to λ =25), when the proportional gain parameter decreases (up to P=0.01) or when the integrative gain parameter increases (up to I=5000). The effects of the control error consisted in a frequency and damping distortion with introduction of a negative damping ratio.

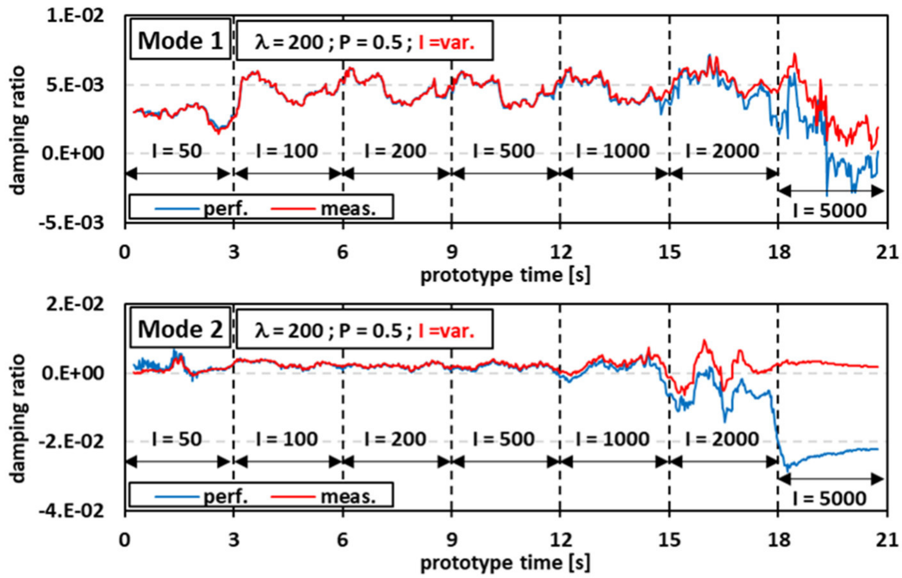

Figure 6.2.21. Damping ratio of the 1st and 2nd modes identified using the Spatial model **[19]**.

Chapter 7

7. Conclusions

This thesis discusses the research activities conducted to implement and validate the pseudo-dynamic testing method for seismic performance assessment of full-scale multi-storey structures at the Laboratory of testing on real-scale STRUcTures (LaSTRUT) within the center CeSMA of the University of Napoli Federico II. In particular, it focused on the following aspects and goals: i) effectiveness of the pseudo-dynamic (PsD) testing method compared to the other available testing methods; ii) development of a reliable PsD testing framework to enable the researchers to study the response of full-scale multi-storey infilled RC structures under seismic excitations; iii) development and validation of a simplified substructuring approach to perform PsD tests on a portion of an entire structural system; iv) assess the influence of infills in the lateral response of infilled RC structures; v) calibrate refined numerical models on the test results to numerically reproduce the nonlinear response of the entire buildings under dynamic loads; vi) study the effects of the control errors on the reliability of the test. With reference to these goals, the main findings can be summarized as follows.

The PsD testing framework implemented in the LaSTRUT of the CeSMA allows to conduct full-scale experimental tests on building prototypes or substructures to assess seismic performance under imposed record motions. The Classical (or Step) method is implemented to perform PsD tests. An in-house coordinator software is developed in the MATLAB environment. It guarantees the communication with the control system at each step of the test to impose the displacements to the physical specimen. The proposed PsD testing framework was validated performing experimental tests on three different multi-storey infilled RC frames varying the infill-to-frame connection. The outcomes of the experimental tests can be summarized as follows:

- The developed testing framework allows to reproduce the earthquake effects in terms of damage to structural and non-structural components consisting in marked diagonal cracking and crushing of some bricks of the infills and shear cracking at the end of the column. This is in satisfactory agreement with the damage observed on the real structure;
- The stiffness and the strength of the infilled frame increases when the degree of the infill-to-structure connection increases (i.e. moving from a three-side connection with mortar and gap at bottom of the beam to a full connection with mortar and to a full connection with mortar and adhesives). As a consequence, the specimens exhibited a lower drift demand while a reduced damage is attained at a fixed intensity;
- The use of a flexible adhesive at the infill-to-frame interface allows to have a better loading transfer from the structure to the infill with a strength increase ranging between 10% and 30%. On the other hand, the strength increase leads to an increase of the shear force transferred to the structural components that resulted in the shear cracking at the top of the column due to the infill-to-strut interaction.

The results of PsD tests are used to validate the proposed substructuring approach. This approach, based on simplified stiffness-based assumptions, is preferred to more complex ones to easily identify the sources of potential errors in the PsD tests. The approach is preliminarily validated using the results of NLTHs analysis performed using the nonlinear models of the building and the frame. Then the results of the NLTH analysis performed using the refined building model are compared to the experimental results. The outcomes of the preliminary and the experimental validation can be summarized as follows:

- The proposed stiffness-based substructuring approach allows to significantly simplify a complex problem and enable the testing of the most damaged frame under reliable seismic load protocols;
- The preliminary numerical analyses show a good matching between the displacement demand at the top of the selected frame and the displacement demand recorded during NLTHs performed with the

entire building model. This confirms the numerical validation of the proposed approach;

- The comparison in terms of top displacement demand between the numerical and experimental results shows that the adopted substructuring assumption, allows to reproduce the numerical response of the entire building response with a satisfactory agreement.

The experimental results are also used to calibrate and validate the hysteretic pivot model used to reproduce the nonlinear response of infills at frame level. In particular, three frame models are proposed to account for the different infill-to-frame connection. The frame model is then extended at the building level to predict the nonlinear response of buildings under imposed record motions. The refined model is simplified to be implemented in a framework for the loss-assessment at regional scale. It was numerically validated by comparing the results of a NLTH analysis performed using this model and the refined model. The comparison of the experimental and the numerical results useful to calibrate and validate the models showed that:

- The proposed numerical frame models well reproduced the response of the frame with a full connection with classic mortar (i.e., F2_4S_M). However, the additional strength provided using a flexible adhesive in the infill-to-frame connection of the F1_4S_M+A specimen is not captured by this model. For this reason, the numerical model of the F2_4S_M frame is selected and extended at the building level;
- The proposed numerical does not capture the response of the specimen F2_3S_M fabricated with a gap of 5 mm between the infill and the beam. Indeed, the comparison between the numerical and the experimental results shows a clear mismatch demonstrating that the model is not able to reproduce the slip of the infill along the column surface that is exacerbated by the lack of a contact with the beam;
- The predicted DSs by using the proposed numerical models at the building level and by using the damage classification available in literature are in good agreement with the actual earthquake damage.

- The numerical model tends to underestimate the predicted damage on some of the ground floor infills since out-of-plane response has been neglected in the model.
- The simplified model underestimated the IDR on the 2nd floor due to the damage concentration at the ground floor;
- In terms of interstorey shear, although slight differences are observed, the simplified model and the refined model are in agreement between them.

Finally, to study the effects of errors on the test reliability and to improve UNINA PsD testing framework, research activities are conducted at the European Laboratory of Structural Assessment (ELSA) at the Joint Research Centre (JRC) of the European Commission. In particular, PsD tests are performed on a new bench test set-up, the PONYBENCH, to investigate the influence of the control parameters and the testing method on the experimental response. The dynamic properties of the test specimen are defined through a dynamic snap-back test (SnB) successively reproduced using the PsD testing method. The outcomes of the experimental activities can be summarized as follows:

- The new bench test set-up, conceived for demonstration, training, research and knowledge handover, allows the researchers perform dynamic and pseudo-dynamic tests, to study the effects of the control errors on the experimental response.
- The results of the Snb reproduced using a PsD test show that the PsD testing method is able to reproduce the translational frequencies. In contrast, the torsional frequencies are not well reproduced. This limitation can be related to the fact that the torsional modes are less present in the response. Therefore, the measurement and the identification of these modes are less accurate;
- The results of PsD tests show that a distortion is introduced in the response frequencies and damping when lower values of the time scale factor λ (which means increasing the test speed), lower values of P or higher values of I are used. The distortion is clearly observed at the high modes and can be critical if it shift the damping ratio to negative values, resulting in an unstable response.

According to the research activities conducted on the study of effects of errors on the test reliability, further developments will be implemented in the new version of the coordinator software to improve the performances of the UNINA PsD testing framework. Further research effort is needed to simulate the effects of out-of-plane actions on infills, in particular the test setup should be adapted to include a further series of actuator that may impose equivalent inertial forces on the infills.

Bibliography

[1] C. Del Vecchio, M. Di Ludovico and S. Pampanin, "Repair costs of existing rc buildings damaged by the l'aquila earthquake and comparison with FEMA P-58 predictions," *Earthquake Spectra,* vol. 34, no. 1, pp. 237-263, 2018.

[2] P. Ricci, F. De Luca and G. M. Verderame, "6th April 2009 L'Aquila earthquake, Italy: Reinforced concrete building performance," *Bulletin of Earthquake Engineering,* vol. 1, no. 285-305, p. 9, 2011.

[3] M. Di Ludovico, A. Prota, C. Moroni, G. Manfredi and M. Dolce, "Reconstruction process of damaged residential buildings outside historical centres after the L'Aquila earthquake: part II—"heavy damage" reconstruction," *Bulletin of Earthquake Engineering,* vol. 15, no. 2, pp. 693-729, 2017.

[4] F. Di Trapani, V. Bolis, F. Basone and M. Preti, "Seismic reliability and loss assessment of RC frame structures with traditional and innovative masonry infills," *Engineering Structures,* vol. 208, 2020.

[5] L. Cavaleri and F. Di Trapani, "Cyclic response of masonry infilled RC frames: Experimental results and simplified modeling," *Soil Dynamics and Earthquake Engineering,* vol. 65, pp. 224-242, 2014.

[6] G. M. Verderame, P. Ricci, M. T. De Risi and C. Del Gaudio, "Experimental Assessment and Numerical Modelling of Conforming and Non-Conforming RC Frames with and without Infills," *Journal of Earthquake Engineering,* vol. 00, no. 00, pp. 1-42, 2019.

[7] A. Furtado, T. Ramos, H. Rodrigues, A. Arede, H. Varum and P. Tavares, "In-plane response of masonry infill walls: experimental study using digital image correlation," *Proceedia Engineering,* vol. 114, pp. 870-876, 2015.

[8] T. Panagiotakos and M. Fardis, “Seismic response of infilled RC frame structures,” in *Proceedings of the 11th World Conference on Earthquake Engineering*, Acapulco, Mexico, 1996.

[9] C. Del Vecchio, M. Di Ludovico, A. Balsamo and A. Prota, “Seismic Retrofit of Real Beam-Column Joints Using,” *Journal of Structural Engineering,* vol. 144, no. 5, pp. 1-12, 2018.

[10] M. Nakashima, T. Nagae, R. Enokida and K. Kajiwara, “Experiences, accomplishments, lessons, and challenges of E-defense—Tests using world's largest shaking table,” *Japan Architectural Review,* vol. 1, no. 1, pp. 4-17, 2018.

[11] G. Maddaloni, M. Di Ludovico, A. Balsamo, G. Maddaloni and A. Prota, “Dynamic assessment of innovative retrofit techniques for masonry buildings,” *Composites Part B: Engineering,* vol. 147, pp. 147-161, 2018.

[12] G. Maddaloni, *LE TAVOLE VIBRANTI BIASSIALI DEL CRdC AMRA: PROCEDURE DI CALIBRAZIONE E PROGETTO DI UN SISTEMA DI ISOLAMENTO,* 2008.

[13] H. M. Aktan and A. M. ASCE, “Pseudo-dynamic testing of structures,” *Journal of Engineering Mechanics,* vol. 112, no. 2, pp. 183-197, 1986.

[14] P. Pegon and A. Pinto, “Pseudo-dynamic testing with substructuring at the ELSA laboratory,” *Earthquake Engineering and Structural Dynamics,* vol. 29, no. 7, pp. 905-925, 2000.

[15] M. Nakashima, “Hybrid simulation: An early history,” *Earthquake Engineering and Structural Dynamics,* vol. 49, no. 10, pp. 1-14, 2020.

[16] J. Carrion and B. F. Spencer, “Model-based Strategies for Real-time Hybrid testing,” *NSEL Report Series,* p. 211, 2007.

[17] F. J. Molina, G. Magonette and P. Pegon, “Assessment of Systematic Experimental Errors in Pseudodynamic Tests,” in *12th European Conference on Earthquake Engineering*, 2002.

[18] M. Nakashima, H. Kato and E. Takaoka, “Development of real-time pseudo dynamic testing,” *Earthquake Engineering & Structural Dynamics,* vol. 21, no. 1, pp. 79-92, 1992.

[19] F. J. Molina, G. Magonette, P. Pegon and B. Zapico, “Monitoring damping in pseudo-dynamic tests,” *Journal of Earthquake Engineering,* vol. 15, no. 6, pp. 877-900, 2011.

[20] M. Di Ludovico, G. M. Verderame, A. Prota, G. Manfredi and E. Cosenza, “Cyclic Behaviour of Nonconforming Full-Scale RC Columns,” *Journal of Structural Engineering,* vol. 140, no. 5, 2014.

[21] C. Del Vecchio, M. Di Ludovico, A. Balsamo, A. Prota, G. Manfredi and M. Dolce, “Experimental Investigation of Exterior RC Beam-Column Joints Retrofitted with FRP Systems,” vol. 18, no. 4, p. 04014002, 2014.

[22] ASCE/SEI, “Seismic rehabilitation of existing buildings,” *ASCE/SEI,* 2007.

[23] A. C. I. (ACI), "Code requirements for load testing of concrete members of existing buildings", ACI 437, Farmington Hills, MI., 2012.

[24] R. Park and T. Paulay, “Behaviour of reinforced concrete external beam-column joints under cyclic loading,” in *Proceedings of the 5th World Conference on Earthquake Engineering*, Rome, 1973.

[25] V. V. Bertero, D. Rea, S. Mahin and M. B. Atalay, “Rate of loading effects on uncracked and repaired reinforced concrete members,” in *Proceedings of the 5th World Conference of Earthquake Engineering*, Rome, 1973.

[26] L. M. Megget, “Cyclic behaviour of exterior reinforced concrete beam-colum joints,” *Bulletin of the New Zealand Society for Earthquake Engineering,* vol. 7, no. 1, pp. 27-47, 1974.

[27] L. Di Sarno, C. Del Vecchio , G. Maddaloni and A. Prota, “Experimental response of an existing RC bridge with smooth bars,” *Engineering Structures,* vol. 136, pp. 355-368, 2017.

[28] E. Coelho, A. Campos Costa, P. Candeias, M. J. Falcao Silva and L. Mendes, "Shake table tests of a 3-storey irregular RC structure," in *S eismic Pe rformance A ssessment and R ehabilitation of Existing Buildings* , Ispra, 2005.

[29] G. Magliulo, C. Petrone, V. Capozzi, G. Maddaloni, P. Lopez, R. Talamonti and G. Manfredi, "Shake table tests on infill plasterboard partitions," *The Open Construction and Building Technology Journal,* vol. 6, no. 1, pp. 155-163, 2012.

[30] L. Van Den Einde, J. P. Conte, J. I. Restrepo, R. Bustamante, M. Halvorson, T. C. Hutchinson, C.-. Ta Lai, K. Lotifzadeh, J. E. Luco, M. L. Morrison, G. Mosqueda, M. Nemeth, O. Ozcelik, S. Restrepo, A. Rodriguez, P. B. Shing, B. Thoen and G. Tsampras, "NHERI@UC San Diego 6-DOF Large High-Performance Outdoor Shake Table Facility," *Frontiers in Built Environment,* vol. 6, pp. 1-21, 2021.

[31] F. Graziotti, U. Tomassetti, S. Kallioras, A. Penna and G. Magenes, "Shaking table test on a full scale URM cavity wall building," *Bulletin of Earthquake Engineering,* vol. 15, no. 12, pp. 5329-5364, 2017.

[32] M. G. Durante, L. Di Sarno, G. Mylokanis, C. A. Taylor and A. L. Simonelli, "Soil–pile–structure interaction: experimental outcomes from shaking," *Earthquake Engineering and Structural Dynamics,* vol. 45, pp. 1041-1061, 2015.

[33] J. Donea, G. Magonette, P. Negro, M. EERI, P. Pegon, A. Pinto and G. Verzeletti, "Pseudodynamic capabilities of the ELSA laboratory for earthquake testing of large structures," *Earthquake Spectra,* vol. 12, no. 1, pp. 163-180, 1996.

[34] G. M. Calvi, A. Pavese, P. Ceresa, F. Dacarro, C. G. Lai and C. Beltrami, "Design of a large-scale dynamic and pseudo-dynamic testing facility," 2005, Pavia, IUSS Press.

[35] S. Okamoto, Y. Yamazaki, T. Kaminosono, M. Nakashima and H. Kato, "Techniques for large scale testing at BRI large scale structure test laboratory," *Building Research Institute, Ministry of Construction,* no. 101, p. 83, 1983.

[36] P. Pegon, F. J. Molina and G. Magonette, “Continuous Pseudo-dynamic Testing at ELSA,” in *Hybrid Simulation: Theory, Implementation and Applications*, Taylor & Francis, 2008, pp. 79-88.

[37] F. J. Molina, G. Magonette, P. Pegon, P. Negro and A. Pinto, “Pseudo-Dynamic Testing . Evolution of the Method and the Testing Facilities,” in *Sísmica 2010 - 8º Congresso de Sismologia e Engenharia Sísmica*, 2010.

[38] O. Mercan and J. M. Ricles, “NEES@ Lehigh: Real-time hybrid pseudodynamic testing of large-scale structures,” in *Hybrid simulation: Theory, implementation and application*, London, Uk, Taylor & Francis, 2008.

[39] O. Mercan and J. Ricles, “Real-time hybrids pseudo-dynamic testing of large-scale structures,” in *Hybrid simulation: Theory, implementation and applications* , 2008.

[40] B. Stojadinovic, J. P. Moehle, S. A. Mahin, K. Mosalam and J. F. Canny, “NEES EQUIPMENT SITE AT THE UNIVERSITY OF CALIFORNIA, BERKELEY,” in *Proceedings of 13th World Conference on Earthquake Engineering*, Vancouver, Canada, 2004.

[41] “Università di Trento - Dipartimento di Ingegneria Civile Ambientale e Meccanica - Ricerca - Materials and Structural Testing,” [Online]. Available: https://www.dicam.unitn.it/126/materials-and-structural-testing.

[42] C. French, A. E. Schultz, J. F. Hajjar and C. K. Shield, “MULTI-AXIAL SUBASSEMBLAGE TESTING (MAST) SYSTEM: DESCRIPTION AND CAPABILITIES,” in *3th World Conference on Earthquake Engineering*, Vancouver, 2004.

[43] C. L. Phillips and R. D. Habord, Feedback control systems, Simons & Schuster Inc., 1995.

[44] P. B. Shing, M. EERI, M. Nakashima and O. S. Bursi, “Application of Pseudodynamic Test Method to Structural Research,” *Earthquake Spectra,* vol. 12, no. 1, pp. 29-55, 1996.

[45] K. Takanashi, "Nonlinear earthquake response analysis of structures by a computer-actuator on-line system," *Bulletin of Earthquake Resistant Structure Research Center,* vol. 8, 1975.

[46] K. Takanashi and M. Nakashima, "Japanese Activities on On-Line Testing," *Journal of Engineering Mechanics,* vol. 113, no. 7, pp. 1014-1032, 1987.

[47] K. Takanashi and K. Ohi, "Earthquake response analysis of steel structures by rapid computer-actuator on-line system, (1) a progress report, trial system and dynamic response of steel beams," *Bull. Earthquake Resistant Struct. Research Center (ERS),* vol. 16, pp. 103-109, 1983.

[48] S. Dermitzakis and S. Mahin, "Development of substructuring techniques for," Berkeley, 1985.

[49] E. Watanabe, T. Kitada, S. Kunimoto and K. Nagata, "Parallel pseudodynamic seismic loading test on elevated bridge system through the internet," in *The Eight East Asia-Pacific Conference on Structural Engineering and Construction*, Singapore, 2001.

[50] G. Mosqueda, B. Stojadinovic and S. Mahin, "Geographically distributed continuous hybrid simulation," in *Proceedings of the 13th World Conference on Earthquake Engineering*, Vancouver, 2004.

[51] G. Mosqueda, B. Stojadinovic and S. Mahin, "Real-Time Error Monitoring for Hybrid Simulation. Part II: Structural Response Modification due to Errors," *Journal of Structural Engineering,* vol. 133, no. 8, pp. 1109-1117, 2007.

[52] G. Magonette, "Development and application of large-scale continuous pseudo-dynamic testing techniques," *Philosophical Transactions of the Royal Society A,* vol. 359, no. 1786, pp. 1771-1799, 2001.

[53] M. Nakashima, K. Ishii, S. Kamagata, H. Tsutsumi and K. Ando, "Feasibility of pseudo dynamic test using substructuring techniques," in *Proceedings of Ninth World Conference on Earthquake Engineering*, Tokyo, 1988.

[54] A. Pinto, P. Pegon, G. Magonette and G. Tsionis, “Pseudo-dynamic testing of bridges using non-linear substructuring,” *Earthquake Engineering and Structural Dynamics,* vol. 33, no. 11, pp. 1125-1146, 2004.

[55] F. McKenna, “OpenSees: A Framework for Earthquake Engineering Simulation Computing in Science and Engineering,” 2011.

[56] “SAP2000. Static and Dynamic Finite Element Analysis of Structures,” C.S.I. Computers and Structures Inc.

[57] “MATLAB 2022b,” The Mathworks Inc., Natick. Massachuetts.

[58] M. Nakashima , “Development , potential , and limitations of real-time online (pseudo-dynamic) testing,” *Philosophical Transactions of the Royal Society A,* vol. 359, no. 1786, pp. 1851-1867, 2001.

[59] S. Mahin, P. Shing, C. Thewal and R. Hanson, “Pseudo-dynamic test method - current status and future directions,” *Journal of Structural Engineering,* vol. 115, no. 8, pp. 2113-2128, 1989.

[60] O. Kwon and V. Kammula, “Model updating method for substructure pseudo-dynamic,” *Earthquake engineering & structural dynamics,* vol. 42, pp. 1971-1984, 2013.

[61] A. M. Reinhorn, M. V. Sivaselvan, Z. Liang and X. Shao, “REAL-TIME DYNAMIC HYBRID TESTING OF STRUCTURAL SYSTEMS,” in *13 th World Conference on Earthquake Engineering*, Vancouver, Canada, 2004.

[62] G. Abbiati, O. S. Bursi, E. Cazzador, R. Ceravolo, Z. Mei, F. Paolacci and P. Pegon, “Pseudo-Dynamic Testing Based on Non-linear Dynamic Substructuring of a Reinforced Concrete Bridge,” in *Experimental Research in Earthquake Engineering* , 2015, pp. 83-99.

[63] M. Lamperti Tornaghi, G. Tsionis, P. Pegon, F. J. Molina, M. Peroni, M. Korzen, N. Tondini, P. Covi, G. Abbiati, M. Antonelli and B. Gilardi, “Experimental study of braced steel frames subjected to fire after

earthquake," in *17th World Conference on Earthquake Engineering*, Sendai, Japan, 2020.

[64] S. Kallioras, D. A. Pohoryles, D. Bournas, F. J. Molina and P. Pegon, "Seismic performance of a full-scale five-storey masonry-infilled RC building subjected to substructured pseudodynamic tests," *Earthquake Engineering and Structural Dynamics,* vol. 52, no. 12, pp. 3649-3678, 2023.

[65] N. M. Newmark, "A method of computation for structural dynamics," *Journal of Engineering Mechanics,* pp. 67-94, 1959.

[66] H. Hilber, T. Hughes and R. Taylor, "Algorithms in Structural Dynamics," *Earthquake Engineering and Structural Dynamics,* vol. 5, pp. 283-292, 1977.

[67] S. Mahin and P. Shing, "Pseudodynamic Method for Seismic Testing," *Journal of Structural Engineering,* vol. 111, no. 7, pp. 1482-1503, 1985.

[68] M. Nakashima, T. Kamisono, M. Ishida and K. Ando, "Integration technique for substructure pseudodynamic test," in *Proc. 4th U.S. National Conference on Earthquake Engineering*, 1990.

[69] D. Combescure and P. Pegon, "A-Operator Splitting time integration technique for pseudo dynamic testing Error propagation analysis," *Soil Dynamics and Earthquake Engineering,* vol. 16, pp. 427-443, 1997.

[70] C. Thewalt and M. Roman, "Performance Parameters for Pseudodynamic Tests," *Journal of Structural Engineering,* vol. 120, no. 9, pp. 2768-2781, 1994.

[71] F. J. Molina, A. Bosi, P. Pegon, G. Magonette and A. Pinto, "Error study of a hybrid testing system of structures through a state-space model," in *15th World Conference on Earthquake Engineering (15WCEE)*, Lisboa, 2012.

[72] D. J. Ewins, Modal Testing: Theory and Practice, Somerset, UK: Taunton Research Studies Press.

[73] M. H. Hayes, Statistical Digital Signal Processing and Modelling, New York: John Wiley, 1996.

[74] O. S. Kwon, N. Nakata, A. S. Elnashai and B. F. Spencer, "A Framework for Multi-Site Distributed Simulation and Application to Complex Structural Systems," *Journal of Earthquake Engineering,* vol. 9, no. 5, pp. 741-753, 2005.

[75] A. Schellenberg, S. Mahin and G. Fenves, "Advanced Implementation of Hybrid Simulation," Pacific Earthquake Engineering Research Center, Berkeley, California, 2009.

[76] C. Del Vecchio, M. Di Ludovico, A. Fiorillo, G. M. Verderame, A. Prota, G. Manfredi and E. Cosenza, "The pseudo-dynamic testing facility at UNINA : preliminary test on a RC frame," 2020.

[77] N. Instruments, "Labview," Austin, Texas, USA, 2000.

[78] R. K. Dowell, F. Seible and E. L. Wilson, "Pivot Hysteresis Model for Reinforced Concrete Members," *ACI STRUCTURAL JOURNAL,* no. 95, pp. 607-617, 1998.

[79] Google, "Google Street View," [Online]. Available: https://www.google.com/streetview/.

[80] C. S. d. L. Pubblici, "Spettri NTC ver. 1.0.3," 2012 .

[81] C. Chrysostomou, P. Gergely and J. Abel, "A SIX-STRUT MODEL FOR NONLINEAR DYNAMIC ANALYSIS OF STEEL INFILLED FRAMEs," *International Journal of Structural Stability and Dynamics,* vol. 3, no. 335-353, p. 2, 2002.

[82] CEN, *Eurocode 8: Design of structures for earthquake resistance - Part 1: General rules, seismic actions and rules for buildings,* 2005 .

[83] W. El-Dakhakni, M. Elgaaly and A. Hamid, "Three-Strut Model for Concrete Masonry-Infilled Steel Frames," *Journal of Structural Engineering,* vol. 129, no. 2, pp. 177-185, 2003.

[84] B. Staffor Smith and J. Riddington , "The design of masonry-infilled steel frames for bracing structures," *The Structural Engineering,* vol. 56, no. 1, pp. 1-7, 1978.

[85] CEN, *Eurocode 8: Design of structures for earthquake resistance - Part 3: Assessment and retrofitting of buildings.,* 2005.

[86] R. J. Mainstone, "On the stiffnesses and strengths of infilled frames.," *Proc. Inst. Civil. Eng.,* pp. 57-90, 1971.

[87] J. Jeon, J. Park and R. DesRoches, "Seismic fragility of lightly reinforced concrete frames with masonry infills," *EARTHQUAKE ENGINEERING & STRUCTURAL DYNAMICS,* vol. 44, pp. 1783-1803, 2015.

[88] NZSEE/MBIE, *The seismic assessment of existing buildings: Technical guidelines for engineering assessments. Part c–Detailed seismic assessment,* 2017.

[89] C. &. S. Inc., "SAP2000 Reference Manual," 2016.

[90] S. Pampanin, G. Magenes and A. Carr, "Modelling of Shear Hinge Mechanism in Poorly Detailed RC Beam-Column Joints," in *fib 2003 Symp. "Concrete Str. Seism. Reg."*, 2003.

[91] C. Del Vecchio, M. Di Ludovico, G. M. Verderame and A. Prota, "Pseudo-dynamic tests on full-scale two storeys RC frames with different infill-to-structure connections," *Engineering Structures,* vol. 266, 2022.

[92] D. Cardone and G. Perrone, "Developing fragility curves and loss functions for masonry infill walls.," *Earthq Struct,* vol. 9, pp. 257-279, 2015.

[93] F. Naeim and M. Kelly, Design of seismic Isolated structures: From theory to practice, Hoboken, New Jersey: John Wiley and Sons, 1999.

[94] C. Del Gaudio, M. T. De Risi, P. Ricci and G. M. Verderame, "Empirical drift-fragility functions and loss estimation for infills in reinforced concrete frames under seismic loading," *Bulletin of Earthquake Engineering,* vol. 17, no. 3, pp. 1285-1330, 2019.

[95] K. Sassun, T. Sullivan, P. Morandi and D. Cardone, "Characterising the in-plane seismic performance of infill masonry," *Bulletin of the New Zealand Society for Earthquake Engineering,* vol. 49, no. 1, pp. 98-115, 2016.

[96] A. Chiozzi and E. Miranda, "Fragility functions for masonry infill walls with in-plane loading," *Earthquake Engineering and Structural Dynamics,* vol. 46, no. 15, pp. 2831-2850, 2017.

[97] C. Liu, B. Liu, X. Wang, J. Kong and Y. Gao, "Seismic Performance Target and Fragility of Masonry Infilled RC Frames under In-Plane Loading," *Buildings,* vol. 12, no. 8, pp. 1-16, 2022.

[98] A. Natale, EFFECTIVENESS AND ECONOMIC FEASIBILITY OF BASE ISOLATED SEISMIC RETROFIT SOLUTIONS FOR BUILDINGS AND INFRASTRUCTURES, Università degli Studi di Napoli Federico II, Italy, 2022.

[99] K. Porter, "An Overview of PEER's Performance-Based Earthquake Engineering Methodology," in *Proceedings of the 9th International Conferenc on Applications of Statistics and Probability in Civil Engineering*, 2003.

[100] A. -. A. T. C. FP-58, Next-generation Seismic Performance Assessment for Buildings, Volume 1 - Methodology, Washington, DC: Fed Emerg Manag Agency, 2012a .

[101] M. D. NTC, Norme Tecniche per le Costruzioni, 2018.

[102] M. Peroni, P. Pegon, F. J. Molina and P. Buchet, "Ethernet-Based Servo-Hydraulic Real-Time Controller and DAQ at ELSA for Large Scale Experiments," *Journal of Earthquake Engineering,* vol. 26, no. 15, pp. 7657-7688, 2022.

[103] V. Drosos and I. Anastasopoulos, "Shaking table testing of multidrum columns and portals," *Earthquake Engineering and Structural Dynamics,* vol. 43, pp. 1703-1723, 2014.

[104] M. Nakashima, T. Akazawa and H. Igarashi, “Pseudo-dynamic testing using conventional testing devices,” *Earthquake engineering and structural dynamics,* vol. 24, pp. 1409-1422, 1995.

[105] F. Taucer and G. Franchioni, “Directory of European Facilities for Seismic and Dynamic Test in Support of Industry,” *Cooperative Advancements in Seismic and Dynamic,* vol. 6, 2005.

Author’s publications

1. C. Molitierno, C. Del Vecchio, M. Di Ludovico, A. Prota, “Validation of pseudo-dynamic testing protocol through full-scale tests on two-storey infilled reinforced concrete frame”, Proceedings of the 2nd fib Italy YMG Symposium on Concrete and Concrete Structures, Rome, Italy, 109-116, 2021.
2. C. Molitierno, C. Del Vecchio, M. Di Ludovico, A. Prota, “In-plane response of two storeys infilled reinforced concrete frame using a pseudo-dynamic testing framework”, Proceedings of the 14th fib International PhD Symposium in Civil Engineering, Rome, Italy, 581-587, 2022.
3. C. Molitierno, C. Del Vecchio, M. Di Ludovico, A. Prota, “Pseudo-dynamic Tests and Numerical Modelling for Damage Analysis of Infilled RC Frames”, Journal of Earthquake Engineering, 27:16, 4549-4574, DOI: 10.1080/13632469.2023.2183048.
4. C. Molitierno, C. Del Vecchio, M. Di Ludovico, A. Balsamo, A. Prota, “Analysis of the experimental response of a two-storey frame retrofitted with thermal insulation coat”, Proceedings of the 3rd fib Italy YMG Symposium on Concrete and Concrete Structures, Turin, Italy, 109-116, 2023.